Institut für Physik und Astronomie

Experimentalphysik

Interaction of azobenzene containing surfactants with plasmonic nanoparticles

Dissertation
zur Erlangung des akademischen Grades
"**doctor rerum naturalium**"
(Dr. rer. nat.)
in der Wissenschaftsdisziplin "Experimentalphysik"

eingereicht an der
Mathematisch-Naturwissenschaftlichen Fakultät
der Universität Potsdam

von

Liudmila Lysyakova

Gutachter: Prof. Dr. Svetlana Santer
PD Dr. Marina Grenzer
Prof. Dr. Ilko Bald

Potsdam, den 13.04.2017

Abstract

The goal of this thesis is related to the question how to introduce and combine simultaneously plasmonic and photoswitching properties to different nano-objects. In this thesis I investigate the complexes between noble metal nanoparticles and cationic surfactants containing azobenzene units in their hydrophobic tail, employing absorption spectroscopy, surface zeta-potential, and electron microscopy.

In the first part of the thesis, the formation of complexes between negatively charged laser ablated spherical gold nanoparticles and cationic azobenzene surfactants in trans- conformation is explored. It is shown that the constitution of the complexes strongly depends on a surfactant-to-gold molar ratio. At certain molar ratios, particle self-assembly into nanochains and their aggregation have been registered. At higher surfactant concentrations, the surface charge of nanoparticles turned positive, attributed to the formation of the stabilizing double layer of azobenzene surfactants on gold nanoparticle surfaces. These gold-surfactant complexes remained colloidally stable. UV light induced trans-cis isomerization of azobenzene surfactant molecules and thus perturbed the stabilizing surfactant shell, causing nanoparticle aggregation. The results obtained with silver and silicon nanoparticles mimick those for the comprehensively studied gold nanoparticles, corroborating the proposed model of complex formation.

In the second part, the interaction between plasmonic metal nanoparticles (Au, Ag, Pd, alloy Au-Ag, Au-Pd), as well as silicon nanoparticles, and cis-isomers of azobenzene containing compounds is addressed. Cis-trans thermal isomerization of azobenzenes was enhanced in the presence of gold, palladium, and alloy gold-palladium nanoparticles. The influence of the surfactant structure and nanoparticle material on the azobenzene isomerization rate is expounded. Gold nanoparticles showed superior catalytic activity for thermal cis-trans isomerization of azobenzenes. In a joint project with theoretical chemists, we demonstrated that the possible physical origin of this phenomenon is the electron transfer between azobenzene moieties and nanoparticle surfaces.

In the third part, complexes between gold nanorods and azobenzene surfactants with different tail length were exposed to UV and blue light, inducing trans-cis and cis-trans isomerization of surfactant, respectively. At the same time, the position of longitudinal plasmonic absorption maximum of gold nanorods experienced reversible shift responding to the changes in local dielectric environment. Surface plasmon resonance condition allowed the estimation of the refractive index of azobenzene containing surfactants in solution.

Zusammenfassung

Das Ziel dieser Arbeit ist mit der Fragestellung verwandt, wie plasmonische und photoschaltende Eigenschaften in Nano-Objekten simultan herbeigeführt und kombiniert werden können. Diese Arbeit untersucht Komplexe aus Edelmetall-Nanoteilchen und kationischen Tensiden, deren hydrophober Teil Azobenzol enthält, mithilfe von Absorptionsspektroskopie, Oberflächen-Zeta-Potentialen und Elektronenmikroskopie.

Im Teil 1 wird die Bildung von Komplexen aus negativ geladenen, Laser ablatierten, sphärischen Goldnanopartikeln und kationischen Azobenzol-haltigen Tensiden in trans-Konfiguration untersucht. Es wird gezeigt, dass die Zusammensetzung des Komplexes stark vom Tensid-Gold Molverhältnis abhängt. Bei bestimmten Molverhältnissen wurde beobachtet, dass sich die Partikel selbst zu Nanoketten zusammensetzten und aggregieren. Bei höheren Tensid-Konzentrationen wurde die Oberflächen-Ladung der Nanopartikel positiv, erklärt durch das Formen einer stabilen Doppel-Schicht von azobenzolhaltigen Tensiden auf der Gold-Oberfläche. Diese Gold-Tensidkomplexe bleiben kolloidal stabil. UV-Licht induziert eine Trans-Cis Isomerisation von Azobenzoltensidmolekülen und stört somit die stabilisierenden Tensidhüllen, welche die Nanopartikelaggregation bewirken. Die Ergebnisse der Silber- und Silikonnanopartikel decken sich mit den Ergebnissen der ausführlich untersuchten Goldnanopartikel, was den vorgeschlagenen Mechanismus der Komplexbildung bekräftigt.

Im Teil 2 wird die Wechselwirkung zwischen plasmonischen Metallnanopartikeln und Cis-Isomeren der Azobenzol beinhaltenden Verbindungen adressiert. Die Studie beinhaltet Gold, Silber, Palladium, Gold-Silber und Gold-Palladium Legierungen, und außerdem Silikonnanopartikel, und eine Serie von Azobenzol-Derivaten. Cis-Trans thermale Isomerisation von Azobenzolen wurde verbessert in der Gegenwart von Gold, Palladium und Gold-Palladium legierten Nanopartikeln. Der Einfluss der Tensidstruktur und Nanopartikelmaterialien auf die Isomerisationsrate wird erläutert. Goldnanopartikel zeigen eine hervorragende katalytische Aktivität für die thermale Cis-Trans Isomerisation von Azobenzolen. In einem gemeinsamen Projekt mit Theoretischen Chemikern haben wir demonstriert, dass ein möglicher Mechanismus der Elektronentransfer von der absorbierten Azobenzolhälfte zur Goldoberfläche ist.

Im Teil 3 werden die Komplexe zwischen Goldnanostäbchen und Azobenzol-haltigen Timethylammoniumbromide mit verschiedenen Endlängen UV-Licht und blauem Licht ausgesetzt, was eine Trans-Cis und Cis-Trans Isomerisation von Tensiden induziert. Zur gleichen Zeit erfährt das longitudinale plasmonische Absorptionsmaximum von Goldnanostäbchen eine reversible Verschiebung als Reaktion auf die Änderungen in der lokalen dielektrischen Umgebung. Die Oberflächenplasmonenresonanzbedingung erlaubte die Bestimmung des Brechungsindex von Azobenzol-haltigen Tensiden in wässeriger Lösung.

Contents

1. Introduction

1.1. Azobenzene photoswitches

1.1.1. Azobenzene containing surfactants

Surfactant is the abbreviation for “surface active agent”. These are amphiphilic molecules of low molecular weight, including a part that is soluble in a fluid (solvent) and a part insoluble in this solvent. When the solvent is water, the soluble part is called the hydrophilic part, the insoluble part is called hydrophobic. The hydrophilic part is usually a polar headgroup, the hydrophobic part (tail) may have linear or branched structure, and the length of the chain in the tail can be varied. Depending on the headgroup, surfactants may be ionic or non-ionic. Ionic surfactants dissociate in solution. The charge that the headgroup obtains after dissociation determines whether the surfactant is cationic (positive charge), anionic (negative charge) or zwitterionic (both charges).

The properties of surfactants are well studied. Their applications include a wide range of fields, such as textiles, foods, plastics, petroleum production, chemical industry, medicine and the every-day worldwide application as detergents and soaps.[1,2]

Surfactant molecules tend to adsorb at surfaces and interfaces. For instance at water-air interface, surfactant molecules orient in a way that their hydrophobic tails point towards air, while polar hydrophilic headgroups remain in water. Such adsorption provides the reduction of surface tension and the free energy of the interface. In solution, the reduction of free energy of the system is achieved via removing hydrophobic tails from contact with water (hydrophobic interactions). Thereby individual surfactant molecules self-assemble into dynamic aggregates in solution, so-called micelles. Surfactant molecules exchange between a micelle and bulk solution. In water surfactant micelles are formed with polar headgroups exposed to the aqueous medium and enclosing withdrawn hydrophobic tails that avoid contacts with water.

Micelle formation (micellization) is governed by the concentration of free surfactant unimers (unassociated surfactant molecules). The concentration at which micelles start to form is called the critical micelle concentration (CMC). This is the main characteristic of surfactant self-assembly. CMC depends mainly on the surfactant chemical structure, but also on the cosolutes and the properties of the solvent, for instance ionic strength or temperature. Ionic strength implies the presence of salt in solution. In the case of ionic surfactants, counter-ions of salt inhibit electrostatic repulsion between ionic headgroups of surfactant unimers. This influences hydrophobic interactions and changes the enthalpy-entropy balance in the system.[3–5]

There’s an increasing interest in smart materials, which properties can be controlled by external stimuli, such as pH,[6] magnetic field,[7] and light.[8] Light-responsive devices most widely employ azobenzene containing materials.[9] The most peculiar property of the azobenzene chromophores is their reversible photoisomerization between the trans- and cis- geometric isomers, which allows photoswitching of chemical, mechanical, electronical, and optical properties of the azobenzene containing systems. For instance, azobenzene photoswitching has been employed to control the properties of photonic crystals,[10] refractive index of an optical device,[11] topography of polymer layers.[12,13]

Shinkai[14] pioneered incorporation of the azobenzene units into surfactant structures and demonstrated photocontrol of micellar catalysis. The azobenzene group was first integrated next to the head group. Later, incorporating the azobenzene group into the surfactant hydrophobic tail improved its solubility in water.[15]

Having the azobenzene group in the hydrophobic tail, a surfactant molecule carries a dipole in azobenzene cis-conformation, while in trans-conformation its dipole moment is negligible. Therefore, irradiation with light enables manipulation of the surfactant hydrophobicity, and in turn its solubility in water, micellization and interactions with other objects in aqueous medium.

For instance, the use of azobenzene containing surfactant in the surfactant-mediated synthesis of gold nanoparticles allowed the photocontrol over the shape of the resulting particles.[16]

Azobenzene-containing cationic surfactants caused the shrinking of dispersed in water hydrogel microparticles.[17,18] Under UV irradiation the particles swelled as the surfactant molecules isomerized into the more hydrophilic cis- state and unbound from the hydrogel.[19,20] Under blue light, microgel particles shrank upon the rebinding of more hydrophobic trans-surfactant molecules.

DNA conformation was manipulated by light via the use of azobenzene containing cationic surfactants.[2] In compact state DNA can be delivered into target cells, but its further decompaction is required. Light was reported to serve a trigger for DNA conformation using azobenzene containing trimethylammonium bromide surfactants.[21,22,23,24,25]

Azobenzene containing trimethylammonium bromides were also employed to render polymer brushes photosensitive, so that their topography could be controlled by light,[26,27,28] and to compact-decompact single end-grafted DNA molecules.[29]

This thesis demonstrates that versatile applications of photosensitive azobenzene containing surfactants can be extended toward manipulating properties of “solid” nanoobjects, such as metal nanoparticles.

1.1.2. Azobenzene trans-cis isomerization

Azobenzene molecule (IUPAC name: diphenyldiazene) is composed by two phenyl rings separated by an azo bond (N=N). It is the most studied photoswitch. The derivatives of the molecule are usually referred to as the class of azobenzene compounds or simply azobenzenes. The spectroscopic character of azobenzenes is affected by substituents on the azobenzene rings.[30]

Rau [31] described three spectroscopic classes of azobenzenes, differing in the absorption spectra and therefore their prominent colors: azobenzene-type molecules with yellow color, aminoazobenzenes having orange color, and pseudo-stilbenes with red color (**Figure 1.1**). Aminoazobenzenes and pseudo-stilbenes typically absorb in the visible range. The focus of this work is on azobenzene-type molecules with yellow color and a strong absorption band in the UV range. Their spectroscopic properties are similar to the parental azobenzene molecule, which will be described below. Modulating the substitution pattern of the azobenzene unit can shift their absorption bands into visible range.[32,33]

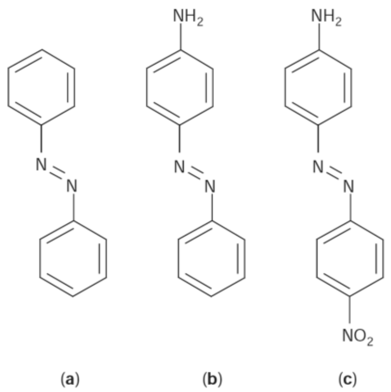

Figure 1.1. Spectroscopic classification of azobenzene molecules: (a) azobenzenes, (b) aminoazobenzenes, and (c) pseudo-stilbenes. The figure is taken from Ref. 34.

Azobenzenes assume one of the two isomeric states: the thermodynamically stable trans- (or E; from the German *entgegen*) and the metastable cis- (or Z; from the German *zusammen*). Azobenzene unit can reversibly interconvert between these configurations upon absorption of a photon of incident light without side reactions. Azobenzene photoisomerization is schematically shown in **Figure 1.2.**

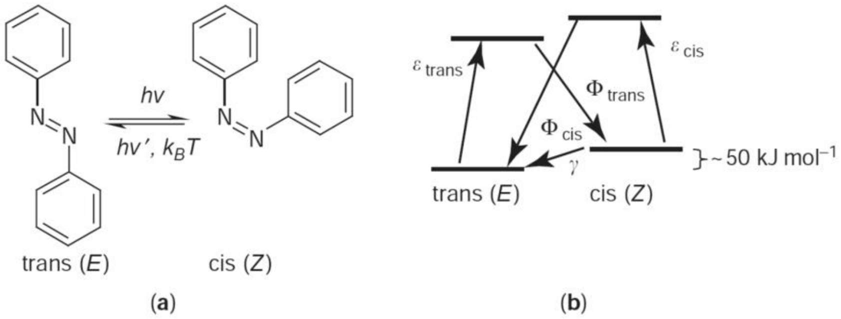

Figure 1.2. (a) Schematic of azobenzene conversion between trans- and cis- conformation via photoisomerization and cis-trans thermal relaxation. (b) Simplified state model for azobenzenes. Trans-cis and cis-trans photoisomerization occurs with the formation of photoexcited states. Cis-azobenzenes can relax into the more stable trans-form thermally. The figure is the replica from Ref. 34.

In the dark, azobenzenes are to be found in the stable trans-state. Upon illumination with the wavelength within the absorption band of the trans-isomer (UV range for azobenzene-type molecules), trans-azobenzenes convert into cis-isomers. Irradiation with light (*i. e.* photon absorption) of a wavelength corresponding to the absorption band of cis-isomer (visible range), initiates the back cis-trans transition. Both trans-cis and cis-trans photoisomerizations occur on the timescale of picoseconds [35,36,37] and are fully reversible.

The alternative way of the azobenzene cis-trans transition is thermal relaxation on a timescale strongly dependent on the ring substitution and local environment. The metastable cis-isomer spontaneously reverts to the trans- form in the absence of light. The lifetime of cis-isomers is usually on the order of hours and days for azobenzene-type molecules in solution. The incorporation of bulky ring substituents hinders thermal relaxation; heating accelerates it.[9]

Azobenzene bulk systems under illumination reach photostationary states composed by mixed trans- and cis- isomers.[38] The composition of a photostationary state is dictated by the chemical substitution on azobenzene chromophores, incident wavelength of light, irradiation duration and intensity, temperature and the matrix (solution, molecular assembly, monolayer, polymer etc.).[9] In the dark, azobenzene photostationary states can be considered all-trans, as the cis-fraction is below most detection limits. Under UV irradiation, photostationary states of azobenzen-type molecules predominantly consist of their cis-isomers. In the case of light-induced trans-cis transitions, the effects of trans-cis photoisomerization, thermal cis-trans relaxation, and possible cis-trans photoconversion contribute into the steady-state composition after irradiation.

Importantly, azobenzene photoisomerization is accompanied by dramatic changes in geometry and dipole moment of molecules. The bent cis- conformation is more bulky than the extended trans- conformation. Bending from trans- to cis- configuration decreases the distance between 4,4'- ring substituents by one third from ~9 to ~6 Å. Moreover, in the trans- configuration lone electron pairs on the nitrogen atoms are pointing to opposite directions. For the unsubstituted azobenzene, the dipole moment of the trans-isomer is 0 Debye (no dipole moment). Upon trans-cis isomerization, due to the bent shape of the cis isomer, molecular dipole moment increases to 3 Debye.[39,40,41] Dipole moments of azobenzene derivatives are usually higher by roughly 1 Debye for both isomers.[42]

Spectral properties of azobenzene

Figure 1.3 schematically shows absorption spectra of azobenzenes. The solid line demonstrates spectral properties of the parental unsubstituted azobenzene molecules, determined by the following three types of electron transitions. Firstly, φ-φ* transitions localized in benzene rings result in the absorption bands in the region 230 – 240 nm for both isomers. Secondly, the strong π-π* absorption band of trans-azobenzene is centered at 314 nm, and at 280 nm for the non-planar cis-isomer. The π-π* absorption band if the most strongly dependent on the substitution pattern. Finally, the n-π* transitions exhibit the absorption band in the visible range. The n-π* transitions are allowed in cis-form, but formally symmetry forbidden in the trans-isomer and therefore possess a low intensity n-π* band at 440 nm in the trans-state.[30]

Absorption spectra of azobenzenes are sensitive to aggregation. When azobenzene dipoles are aligned head-to-tail, forming so-called J-aggregates, bathochromic (red) shift occurs in the spectra as compared with the spectra of individual chromophores. Parallel alignment of the dipoles (head-to-head) is called H-aggregates and induces hypsochromic (blue) shift in the absorption spectrum.[43] Stacking interactions between the rings can additionally stabilize aggregates of azobenzene molecules. Single-chain surfactants with azobenzene unit in the hydrophobic tail tend to form bilayer assemblies in water.[44] At concentrations exceeding CMC, 10-nm hypsochromic shift of π- π* absorption maximum was registered, consistent with the formation of H-aggregates.[5]

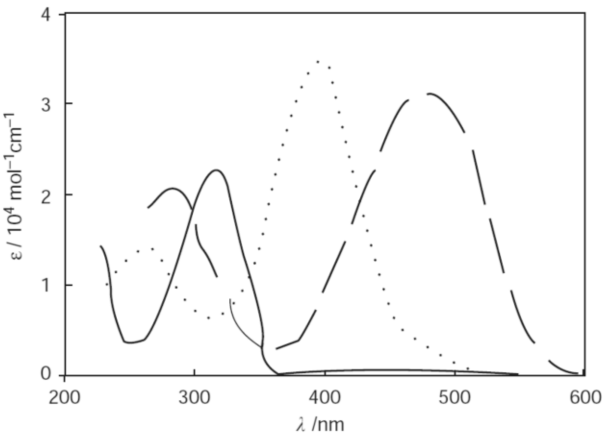

Figure 1.3. Schematic of typical absorption spectra of azobenzenes in trans-conformation. The azobenzene-type molecules (solid line) have a strong absorption band in the UV range, while the aminoazobenzenes (dotted line) and pseudo-stilbenes (dashed line) typically absorb in the visible range. The figure is taken from Ref. 9.

Isomerization Mechanisms

The yield of photoisomerization and the rate of thermal isomerization of azobenzene depend on the isomerization mechanism. The possible mechanisms of azobenzene trans-cis isomerization are shown in **Figure 1.4**. The first main mechanism is a rupture of the N=N π-bond and a rotation around the N–N bond. The second main mechanism is inversion (rehybridization) through a semilinear and hybridized transition state.[31] In the rotation, the C–N–N–C dihedral angle changes, while the N–N–C angle remains fixed at 120°. In the inversion, the C–N=N–C dihedral angle remains 0°, while one N=N–C angle increases to 180°. In the rather recent studies,[45] concerted inversion and inversion-assisted rotation have been proposed as additional isomerization mechanisms. In the concerted inversion, both N=N–C bond angles increase to 180°, so that the linear transition state has no dipole moment. In inversion-assisted rotation, large changes in the C–N–N–C dihedral angle occur simultaneously with smaller changes in the N–N–C angles. All the four mechanisms predict photostationary states consisting of both isomers. Experimental results usually cannot be explained by a single mechanism.

Determining for the photo- and thermal isomerization mechanism are the structure of the molecule (substituents, initial cis *vs.* trans isomeric form), environment (solvent polarity and viscosity, temperature and pressure), and irradiation wavelength.[46,45] Substituents influence isomerization through steric and electronic effects. In push-pull azobenzenes, photoisomerization is dominated by the rotation. Azobenzene-type molecules behave similar to the unsubstituted azobenzene.

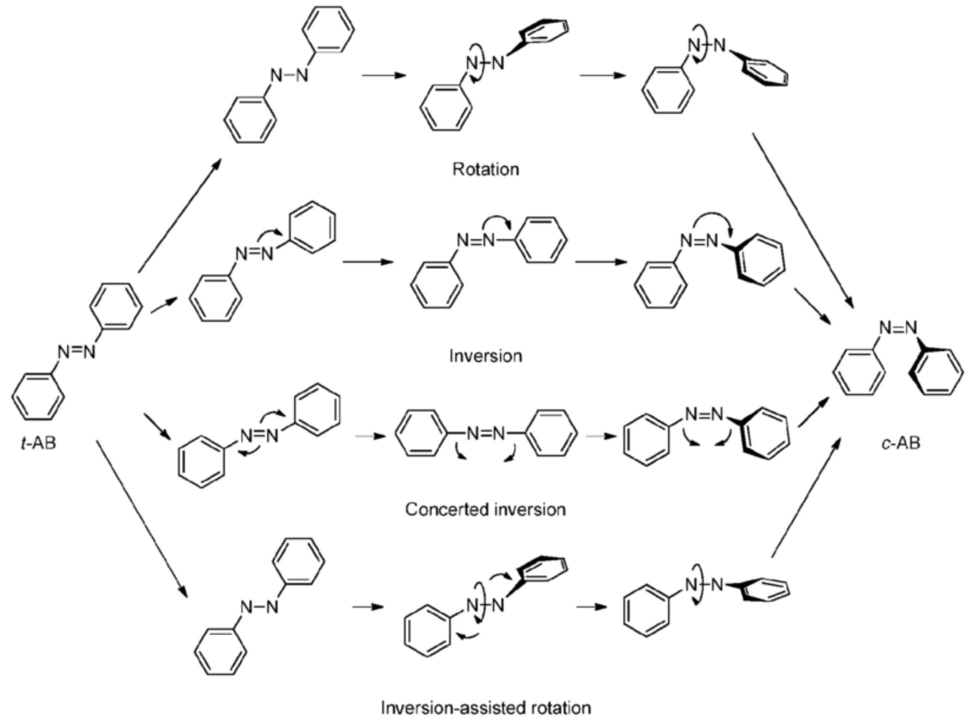

Figure 1.4. Possible mechanisms of azobenzene trans-cis isomerization. Replica from Ref. 45.

For the isomerization of the azobenzene groups within the backbone of an amorphous polymer[47] via the rotation mechanism, the estimated required minimum free volume is the volume of a sphere of 4.5 Å in radius, *i. e.* about 0.38 nm^3. Viscous solvents and bulky substituents typically hinder rotation. The inversion mechanism requires much less free volume than the rotation (around 0.13 nm^3) and therefore this mechanism can be expected in the conditions with steric hindrance: in restricted azobenzenes and in rigid matrices. In azobenzene and its derivatives without any restrictions, rotation mechanism is not excluded.

The concerted inversion was found to be energetically unfavorable mechanism for trans-cis azobenzene isomerization. Rotation and inversion isomerization mechanisms can be competing in diazene derivatives, what remains the widely accepted explanation for the wavelength dependence of the photoisomerization quantum yield. Azobenzene photoisomerization is suggested to proceed via inversion upon illumination in visible range (n-π* excitation), and through the rotation mechanism under π-π* excitation (UV light). The majority of studies suggest that cis-trans azobenzene photoisomerization follows rotation mechanism.

Thermal relaxation

Substituents and solvent properties can influence the mechanism of azobenzene thermal isomerization in solution.

Thermal isomerization in amino-azobenzenes depends on the position of substituents and solvent properties, which indicates a rotation-dominated mechanism.[45] For instance, thermal isomerization of 4-hydroxyazobenzene proceeds faster in polar solvents compared to non-polar ones. Isomerization rates depend on solvent polarity but not viscosity.

The specific mechanism of cis-trans thermal isomerization of azobenzene-type molecules, studied in this work, is still being discussed, but the inversion mechanism is favoured.[45] The rate of the azobenzene-type thermal isomerization is independent of solvent properties and bulky substituents. Acidic pH can accelerate the thermal cis-trans isomerization. Calculations suggest multiple mechanisms dominated by the concerted inversion. Azobenzene derivatives with strong electron-acceptor substituents such as NO_2 group undergo faster thermal isomerization.

The azobenzene thermal back-relaxation is generally a first-order kinetic process in solutions of small molecules and polymers. In some cases, the multiexponential decay occurs, reflecting isomerization processes in differently confined local environments.

For instance, in amphiphilic azobenzene containing copolymers in solution self-assembling of hydrophobic groups leads to phases with aggregated azobenzene groups. Thermal relaxation in such systems occurs in the biexponential fashion, corresponding to the anomalously fast relaxation of constrained and relatively slow relaxation of unaggregated azobenzene groups. Since the thermal relaxation decay rate was found to depend on the solvent quality and the composition of the polymer, it was suggested as a probe of local environments with different free volumes.[48]

For the thermal cis-trans isomerization of the polymer with azobenzene units in its main chains,[47] two rates were found below the glass transition temperature. The faster process was attributed to the reorientation of the azobenzene moieties in contact with the glassy matrix. The slower process was attributed to the relaxation of the azobenzene back to its trans conformation.

In another example, azobenzene containing molecules readily trans-cis photoisomerized in multilayer thin films. The back cis-trans thermal relaxation kinetics had two contributions originating from different degrees of strain in the films. The faster relaxation rate was likely from the isomerization of cis-isomers with more strain and less free volume.[49]

1.1.3. Photoswitching of azobenzene self-assembled monolayers

Azobenzene containing ligands can form self-assembled monolayers (SAMs) on planar and curved surfaces of noble metals. The formation of covalently bound SAMs on gold surfaces is comprehensively studied using thiols.[42] Due to the dipolar interactions between azobenzene groups, azobenzene-modified alkyl thiols are densely packed on gold surfaces, what exhibits a pronounced blue shift of the π-π^* absorption band of azobenzene units corresponding to the formation of H-aggregates.[50,51]

Two factors are important for the photoswitching of azobenzenes on metal surfaces. On the one hand, substrate-induced quenching of the azobenzene photoisomerization can occur.[52,53] Since the quenching of the azobenzene excited state by metal core is distance-dependent, the length of the alkyl linker between the terminal azobenzene unit and gold surface affect the photoreactivity of SAMs of azobenzene functionalized thiols on gold clusters.[54] The linker between the metal surface and the azobenzene unit should be therefore long enough to allow its photoisomerization.

On the other hand, dense packing sterically limits photoswitching. The lack of spatial conformational freedom necessary for azobenzene isomerization leads to its suppression in SAMs chemically bound to a gold surface. All strategies toward improving the photochemical activity of azobenzene containing thiol SAMs on planar gold surfaces relied on the free volume generation for azobenzene isomerization. One way to achieve this is the "dilution" of azobenzene ligands by adding plain alkyl ligands as spacers, by the means of co-adsorption of different thiols or using unsymmetrical sulphide adsorption.[42,51,55] Another way is increasing the lateral intermolecular distance between azobenzene units in the monolayer employing thiol ligands with integrated bulky groups, those with multiple surface "anchors", or by adsorbing UV-irradiated ligand molecules.[56]

Physisorbed on mica surface, azobenzene containing ligands without headgroups still formed monolayers stabilized by lateral van der Waals interactions between molecules. In contrast to the chemisorbed monolayers, physisorbed azobenzene monolayers completely isomerized in response to light irradiation without "dilution". Sufficient conformational freedom was attributed to the possible molecular diffusion in the absence of covalent bonds to the substrate.[57]

Cooperative isomerization occurred in the densely packed SAMs of covalently bound azobenzene ligands with additional aromatic rings, when the short axes of azobenzene units were arranged parallel to each other due to improved stacking interactions. In this case, the energetically favourable stacking interactions between azobenzene units in the monolayer are achieved as soon as the neighbouring azobenzenes are in the same conformation. Switching of one molecule creates a free volume for the switching of the neighbouring one. As a result, azobenzene ligands in SAM switch cooperatively in a domino-like way. Therefore, isomerization in the monolayers had an increased yield with respect to that in solution.[42,58]

Photoisomerization of azobenzene containing sulfonate surfactants was studied in mixed Langmuir-Blodgett monolayers. The free volume of azobenzene moiety was controlled by the degree of the monolayer "dilution" by alkyl chains. It was found that the azobenzene unit requires a minimum free cross-sectional molecular area of approximately 0.5 nm^2 for its sufficient trans-cis photoisomerization.[59] Ten years later Klajn[42] reviewed photoswitching of azobenzene containing thiols in self-assembled monolayers on metal surfaces. The reported critical value of molecular surface area was ~ 0.40 nm^2 for ligands attached to planar substrates. Surface area requirements are lower for azobenzenes attached to nanoparticle surface.

Surface curvature crucially influences the conformational freedom and therefore the photoresponse of azobenzene-containing SAMs. For azobenzenes attached to nanoparticles, their free volume increases with surface curvature, *i. e.* the decrease in nanoparticle diameter.[42,51,60] Non-diluted chemically bound azobenzene containing monolayers photoisomerized on nanoparticle surfaces as long as the nanoparticle diameter was small enough. To allow isomerization on larger particles, the strategies to decrease azobenzene density in the monolayer might be required similar to the SAMs on planar surfaces.[42,61,62,51,55]

Recently, the photoresponse of azobenzene functionalized thiol with alkyl spacer 11-(4-(phenyldiazenyl)phenoxy)undecane-1-thiol (Az11) was investigated on planar gold and gold nanoparticles of 2.5 – 12 nm in diameter.[51] The monolayer on planar surface essentially did not show photoswitching. Dilution of the planar monolayer with an alkyl thiol enabled its photoisomerization. On gold nanoparticles Az11 photoisomerized as effective as in solution even without dilution. Azobenzene surface coverage could be increased via increasing mole fraction of Az11 for planar SAM or via increasing the diameter of gold nanoparticles. In both cases the π-π* absorption band of azobenzenes blue-shifted more prominently with the increase in azobenzene density, originating from the improved stacking interactions. In planar mixed SAMs, blue light induced almost complete back cis-trans isomerization, whereas the photostationary state in blue light in solution contained a substantial amount of cis-isomers. This indicated a cooperative switching of relatively simple azobenzene ligands, mediated by the energetically favourable lateral interactions between trans-isomers in SAMs.

1.1.4. Isomerization of azobenzene radicals

Azobenzene molecules can attach or withdraw an electron, forming azobenzene anion or cation radicals.

In the electrochemical reduction of azobenzenes, two one-electron steps have been observed. In dimethylformamide solutions,[63] the product of the first electron transfer was a stable anion radical. Azobenzene radical anions participated in a slow chemical reaction, which nature was not investigated. The second reversible one-electron transfer resulted in completely reduced dianion radicals, followed by their fast chemical reaction, probably a protonation step. Protonated species oxidized to the initial azobenzene compound.

In spectrophotometrical investigations by Neta and Levanon,[64] the radical anions produced by direct one-electron reduction of cis- and trans- azobenzene have been studied in various media. The rate of this reaction of radical anion formation was determined for both cis- and trans-azobenzene in solution. All the kinetic and spectral parameters were identical for anion radicals produced from cis- and trans-isomers. Both cis- and trans- anion radicals oxidized into trans-isomers. These findings led to the conclusion that in solution at room temperature cis-azobenzene radical anion converts very rapidly to the trans-radical anion. Conversion in the opposite direction was not detected. Trans- radical anion was found to rapidly catch a proton in solution to produce the neutral species.

Laviron and Mugnier[65] in 1978 studied the stability of the anion radical formed by electrochemical reduction of cis-azobenzene in dimethylformamide with tetra-n-butylammonium perchlorate as supporting electrolyte. The experimental polarograms did not differ for cis- and trans-azobenzene, the observed two electron-transfer waves indicated the formation of anion and dianion radicals. Pure trans-azobenzene was obtained after the re-oxidation in air. It was shown that the cis-azobenzene radical anion (obtained in the first electron-transfer step) isomerized rapidly to the trans-azobenzene anion, which itself further reacted to form the neutral trans-isomer. One proposed mechanism of cis-trans isomerization of radical anion was the inversion on the nitrogen atoms. The second proposed mechanism was the rotation around azo bond obtaining single bond character due to the unpaired electron on one of the nitrogen atoms. The rate constant of the electron transfer was found to be smaller for cis-azobenzene than for trans-isomer.

The fast isomerization of neutral cis-azobenzenes to trans-azobenzenes occurred also when a small amount of the solution of trans-azobenzene anion radicals, prepared electrochemically, was added to the cis-azobenzene solution. Authors suggested that in this reaction a trans- radical anion (T^-) transports an electron to a cis-azobenzene (C), forming a neutral trans-isomer (T) and a cis- radical anion (C^-), which rapidly isomerizes into a trans- radical anion and continues the reaction:

$$T^- + C \rightarrow T + C^- \rightarrow T + T^-$$

The electron-transfer pathway of azobenzene isomerization suggested by Laviron and Mugnier[65] has been confirmed in 2017.[66] Spectroelectrochemical studies revealed a mechanistic model of the accelerated cis-trans isomerization of azobenzene radical anion compared to the neutral species. In all studied azobenzene derivatives, rapid cis-trans isomerization occurred in a similar electrocatalytic fashion upon reduction to the radical anion. It was shown experimentally that smaller potentials are necessary for the electrochemical reduction of the cis-isomer than of the trans-isomer. Calculations showed almost no difference in electron affinity between the two isomers. Thermal cis-trans isomerization of the radical anion was accelerated compared to neutral molecules due to a chain of electron transfers from the trans- radical anion to the neutral cis-isomer. A substoichiometric amount of reduced species, *i. e.* “injected” electrons, was able to rapidly isomerize the entire solution of cis-azobenzene, similar to catalytic reactions. The underlying electrocatalytic mechanism of the cis-trans isomerization of azobenzene solution was that suggested by Laviron and Mugnier.[65] As soon as the cis-azobenzene radical anion (C^-) forms by the reduction of neutral cis-isomer, it rapidly thermally isomerizes to the trans- radical anion, which transfers an electron to another neutral cis-isomer and the cycle repeats:

$$C + C + C^- \rightarrow C + (C + T^-) \rightarrow C + C^- + T \rightarrow (C + T^-) + T \rightarrow C^- + T + T \rightarrow T^- + T + T$$

Further, catalytic cis-trans isomerization of azobenzene was induced by the addition of iridium complex to UV-irradiated azobenzene solution (predominantly cis- photostationary state) and subsequent irradiation with UV light. The iridium complex is a photoelectron transfer agent, UV light enabled electron transfer from photoexcited iridium complexes to cis-azobenzenes, initiating electrocatalytic cycle of cis-radical anion. The percentage of trans-isomer in the UV-photostationary state increased with the iridium-to-azobenzene ratio up to a certain saturation. The latter was explained by the competition between two reactions resulting in the formation of neutral trans-isomer: (i) the electron propagation from trans-radical anion to neutral cis-isomer, $T^- + C \rightarrow T + T^-$, and (ii) electron withdrawal from trans-radical anion and transfer back to oxidized iridium complex, acting against the cycle.

The electrocatalytic cycle of azobenzene cis-trans isomerization in solution is independent on the substituents and apparently on the origin of the first electron injection.

1.2.Optical properties of metal nanoparticles

Metal nanostructures possess unique optical properties, including strong light absorption/scattering at a particular wavelength and consequently bright colours of colloidal solutions of metal nanoparticles,[67] strong electromagnetic field enhancement for surface-enhanced Raman spectroscopy (SERS),[68] waveguiding beyond diffraction limit,[69] imaging capabilities,[70] ultrasensitivity to biological and chemical binding and thus vast technological applications.[71,72,73,74,75]

The physical origin of the peculiar optical effects of metal films and nanoparticles is surface plasmon resonance (SPR). Surface plasmon resonance is a particular light-matter interaction, occurred in noble metals, materials with negative real and small positive imaginary dielectric constant.

1.2.1. Surface plasmon resonance

Surface plasmon resonance (SPR) is the coherent oscillation of the surface conduction electrons excited by the interacting electromagnetic field. Upon interaction with incident light, thin metal films can yield propagating plasmons, also called surface plasmon polaritons (SPPs). Surface plasmon polaritons are electromagnetic waves coupled to the surface electron plasma of a conductor (metal) at a dielectric interface. They propagate along the surface of the metal-dielectric interface for distances up to hundreds of microns, and decay in the z-direction with the exponential decay length on the order of 200 nm.[73]

Localized surface plasmon resonance (LSPR) takes place when light interacts with noble-metal particles much smaller than the wavelength of incident light in the surrounding medium (**Figure 1.5**). In contrast to SPPs, localized surface plasmons are non-propagating excitations of the conduction electrons. In this case, a plasmon oscillates locally around the nanoparticle with a LSPR frequency, which is determined by nanoparticle size, shape, material, and local dielectric properties of the medium. The electron cloud displacement is coherent to the oscillating electromagnetic field. The collective oscillation of free electrons represents the dipolar plasmon mode, or dipole particle plasmon resonance. In fact, multipole LSPR excitations can occur. For instance, quadrupole mode would correspond to the displacement of a half of the conduction electrons parallel to the incident field, while the second half of the electrons moves antiparallel to the field.[76]

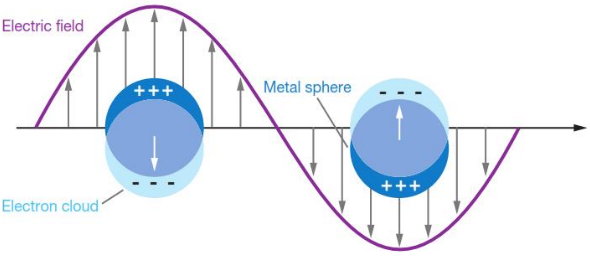

Figure 1.5. Schematic of localized surface plasmon oscillation for a spherical particle. The figure is the replica from Ref. 73.

1.2.2. Theoretical treatment of localized surface plasmons

Theoretical consideration of surface plasmons has been developed and widely reported in journal articles, reviews and books.[67,76,77,78,79,80]

Mie [81] was a pioneer to analytically solve Maxwell's equation for the absorption and scattering of light by spherical particles. According to Mie theory, extinction coefficient of particles interacting with electromagnetic field is a sum of all electromagnetic multipole oscillations.

When the particle size a is much smaller than the wavelength of incident light λ, the phase of the oscillating electromagnetic field is almost constant over the particle volume, so that the electric field of light can be considered static around the nanoparticle (**Figure 1.5**). This quasi-static approximation ($a << \lambda$) allows solving simplified Maxwell's equations for a particle in the electrostatic field. With this limit, Mie theory assumes only the dipole term contribution (dipole approximation), so that extinction spectra of particles can be calculated.

Briefly, the extinction spectrum of metal spheres of radius a interacting with light of wavelength λ ($a << \lambda$) can be calculated as follows:[73]

$$E(\lambda) = \frac{24\pi^2 N a^3 \varepsilon_m^{3/2}}{\lambda \ln(10)} \frac{\varepsilon_{im}(\lambda)}{(\varepsilon_r(\lambda) + \chi\varepsilon_m)^2 + \varepsilon_{im}(\lambda)^2} \tag{1.1}$$

Here ε_m is the dielectric constant of the surrounding medium, $\varepsilon_r(\lambda)$ and $\varepsilon_{im}(\lambda)$ are the real and imaginary parts of the particle material dielectric function $\varepsilon(\lambda) = \varepsilon_r(\lambda) + i\,\varepsilon_{im}(\lambda)$. If ε_{im} is small, the plasmon resonance condition is fulfilled when $\varepsilon_r(\lambda) = -\chi\,\varepsilon_m$. The value of the shape factor χ can be solved analytically for spheres ($\chi = 2$) and spheroids and must be numerically calculated for other geometries. For silver and gold nanoparticles, plasmon resonance condition is met in the visible spectral range, causing red color of colloidal gold and yellow color of colloidal silver.

1.2.3. Size effects

Surface plasmon resonance wavelength is highly dependent on the nanoparticle material, size, shape, as well as the dielectric constant of the surrounding medium.[67,76,77,79,82,83]

In the quasi-static regime (mean diameter d < 25 nm for gold nanoparticles) material dielectric function is considered size dependent. The corresponding size-response in the plasmon absorption spectra is referred to as intrinsic size effects. It is well established that for small spherical particles plasmon absorption bandwidth decreases with increasing particle size. Size dependence of the plasmon peak position is not pronounced.[67]

For larger particles, dipole approximation becomes not applicable as the electromagnetic field becomes non-uniform across the particle. Higher multipole oscillations, especially the quadrupole term,[76,80,84] become important. Plasmon resonances of higher multipolar order appear in the extinction spectra besides the usual dipolar resonance, and the higher-order terms determine extrinsic size effects. Electromagnetic retardation effects,[67] possible radiative damping[85,86] from spontaneous radiation emitted by the dipole, and the excitation of multipole plasmon modes[77] lead to the increase in plasmon bandwidth and shifts of plasmon absorption maximum toward longer wavelengths with increasing particle size. For instance, Sönnichsen *et. al.*[85] detected polaritonic red-shifts and increased radiation damping of the plasmon band in light scattering spectra of gold and silver clusters with mean diameters larger than 20 nm.

El-Sayed *et. al.*[83] reviewed size effects on the plasmon band in the optical absorption spectra of spherical gold nanoparticles in water. Plasmon absorption maxima of gold nanoparticles were found at 517 – 521 nm for gold nanoparticles with mean diameter of 9 – 22 nm, and 533 and 575 nm for particles with diameters d = 48 nm and d = 99 nm respectively (**Figure 1.6**). Calculated[79,80] plasmon resonance wavelengths of gold nanoparticles of different size and shape were in good agreement with experimental results. For nanospheres, calculated size dependence of plasmon wavelength followed a linear trend. Increase in the diameter of spherical gold nanoparticles from 20 to 80 nm resulted in the red shift of plasmon peak position from 520 to 550 nm. Scattering contribution into extinction spectra increased with increasing particle diameter, but remained negligible for nanospheres with d < 40 nm.[80]

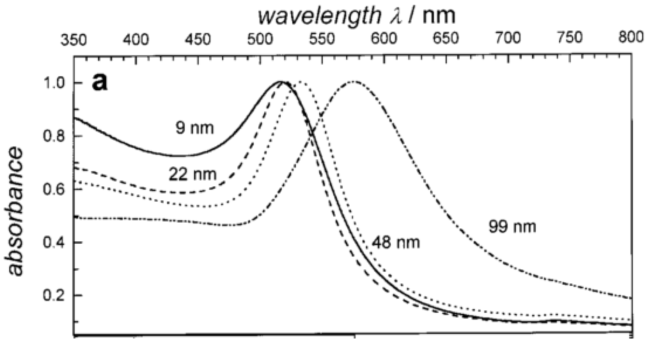

Figure 1.6. UV-Vis absorption spectra of spherical gold nanoparticles in water. Diameter of the particles increased from 9 to 99 nm, causing the plasmonic absorption maximum red-shift with increasing size. From Ref. 83.

1.2.4. **Shape effect**

In contrast to metal spherical particles with a single dipolar resonance, two or more plasmon modes differing by oscillation directions occur in particles of non-spherical shape. For instance, three plasmon resonance peaks have been detected in the recorded UV-Vis and polarization-averaged calculated extinction spectra of silver triangular prisms in water,[76] corresponding to the dipole and quadrupole in-plane, and quadrupole out-of-plane oscillations. The fourth broad out-of-plane dipole resonance peak was predicted by theory, but not resolved in the measurements.

Spheroidal particles with three distinct axes have three plasmon resonance bands. Plasmon resonance condition is fulfilled when $\varepsilon_r(\lambda) = -\chi\,\varepsilon_m$ (see Equation (1.1)). The shape factor χ for spheroids can be calculated via the geometrical factors G_i along each of three axes as follows:

$$\chi_i = \frac{1 - G_i}{G_i} \qquad (1.2a)$$

Oblate and prolate spheroids exhibit two surface plasmon resonances, corresponding to the extinction maxima of incident electric fields polarized along the major (long) and minor (short) axis. As a particle becomes more oblate/prolate, the plasmon band associated with the major axis red-shifts, and the one associated with the minor axis blue-shifts.

Rod-shaped particles can be approximated as prolate spheroids with spherical symmetry along the long axis (A). In this case, two short axes (B, C) are identical. One can introduce the aspect ratio R as the ratio of the longer to shorter axis, and the eccentricity of the spheroid e:

$$R = A/B$$

$$e = \sqrt{1 - \frac{1}{R^2}}$$

The corresponding geometrical factors $G_B = G_C$ can be found via the geometrical factor G_A:

$$G_A = \frac{1-e^2}{e^2}\left[\frac{1}{2e}\ln\left(\frac{1+e}{1-e}\right) - 1\right] \tag{1.2b}$$

$$G_B = G_c = \frac{1-G_A}{2}$$

Two types of electron oscillations are possible in gold nanorods: along and perpendicular to the long axis of the rods. These plasmonic oscillations occur in the optical absorption spectra as two bands, similar to prolate spheroids. The transverse mode (perpendicular to the long axis, along the radius) shows a resonance near the plasmon absorption band of spherical particles with the same radius, usually around 520 nm for gold particles. The longitudinal mode (along the long axis) is far red-shifted to around 800 nm for gold nanorods with aspect ratio 4.1.[83] Aspect ratio is the length-to-diameter ratio for cylindrical rods.

Longitudinal plasmon resonance position of nanorods is sensitive to particle size (volume) and strongly depends on the aspect ratio. Calculations suggested the longitudinal plasmon resonance position to follow a non-linear trend. With increasing nanorod volume twofold at a fixed aspect ratio of 3.9, the red shift of around 50 nm was predicted.[80]

With increasing aspect ratio, longitudinal plasmon peak readily shifted towards longer wavelengths following a linear dependence, predicted numerically and observed experimentally in the optical extinction spectra of gold nanorods synthesized by an electrochemical method in the presence of organic surfactants.[83] Increasing the aspect ratio by one unit induced a pronounced red shift of longitudinal plasmon peak of roughly 100 nm. At the same time, the transverse plasmon maximum was found to blue-shift by only several nanometers.

Scattering contribution to the total extinction of nanorods is not affected by aspect ratio at a fixed volume, but increases rapidly with the nanorod volume at a fixed aspect ratio.[80]

1.2.5. Effect of dielectric environment

Mie theory predicts a shift of the plasmon resonance extinction band induced by the refractive index of the solvent. With increasing dielectric constant of the medium ε_m, plasmon absorption is enhanced, the bandwidth increases and the LSPR peak position red-shifts.[67] A possible explanation of the plasmon band broadening is chemical interface damping.[87] Adsorbed molecules offer additional resonance states and therefore can dampen electron oscillations as soon as surface plasmon energy matches the new resonance state.

The optical changes associated with the transfer of 16-nm gold nanoparticles into organic solvents with different refractive indices n ($\varepsilon_m = n^2$) are investigated in Ref. 82. The authors observed around 25-nm red shift of plasmon wavelength with changing refractive indices between n = 1.376 and n = 1.602.

The sensitivity of the plasmon band position to the medium dielectric constant, *i. e.* refractive index, is the main principle of LSPR sensing. The adsorption of ligand molecules onto nanoparticle surface alters the refractive index of local dielectric environment and causes a plasmon wavelength shift, which is measured. For instance, authors in Ref. 88 suggested a method for specific biomolecular sensing based on light scattering spectroscopy of single gold nanoparticles, employing the shift in plasmon resonance upon protein binding.

The LSPR sensing is based on the following relationship between the changes in the local environment and the observed shift in the LSPR wavelength $\Delta\lambda_{max}$:[73]

$$\Delta\lambda_{max} = m\Delta n\left(1 - e^{-2d/l}\right) \tag{1.3}$$

Here m is the refractive index sensitivity of nanoparticles, Δn – change in refractive index due to molecular adsorption, d – adsorbate layer thickness, l – characteristic decay length of the electromagnetic field. Therefore, to increase nanoparticle response, (i) m can be increased, or (ii) d/l can be optimized. It requires tuning of nanoparticle size, shape and composition, as well as occurrence of sharp features on the surface.

The medium-related shift of plasmon peak position is especially pronounced in the longitudinal mode of nanorods. El-Sayed *et. al.*[83] offer the following approximation for the linear red-shift of longitudinal plasmon maximum of nanorods with aspect ratio *R*:

$$\lambda_{max} = (33.34R - 46.31)\varepsilon_m + 472.31 \tag{1.4}$$

Employing the advantages of the SPR theory, Amendola and Meneghetti [89] presented a method for the estimation of the average size of gold nanoparticles from their experimental UV-Vis absorption spectra. The authors exploited the Mie model for spheres and the Gans model for spheroids to fit the recorded absorption spectra, taking into account possible nanoparticle shape distribution. The method has been tested on gold nanoparticles with different surface chemistry under 25 nm in diameter in water and other solvents. Plasmon maximum was detected at different wavelengths for aqueous suspensions of gold nanoparticles with the same size but decorated with different ligands.

1.2.6. **Interparticle gap**

Surface plasmon resonance is also extremely sensitive to the distance between nanoparticles. In particle aggregates, electron oscillations of closely situated individual nanoparticles couple with each other. This results in collective electron oscillations of the electromagnetically coupled system. In the optical properties, collective plasmon modes appears as additional extinction bands at longer wavelengths than the plasmon maximum of individual dispersed nanoparticles.[67,84,90]

For instance, the results on salt-induced aggregation of nanoparticles were reported in Ref. 78, 79. The addition of counterions inhibits electrostatic repulsion between nanoparticles. Aggregation of spherical gold nanoparticles of 13 nm in diameter into larger random, presumably non-spherical objects, was induced by successive addition of 6.0 M NaCl to nanoparticle suspension.[92] The recorded UV-Vis extinction spectra showed broadening of the gold plasmon peak originally located at $\lambda_{max} \approx 520$ nm, its red-shift, and increase in the extinction at $\lambda = 600 - 800$ nm.

The relationship between the morphology of the aggregates, plasmon resonance, and electromagnetic enhancement in gold nanoparticle dimers and trimers was addressed in Ref. 93. Spherical monodisperse gold particles (roughly 100 nm in diameter) were assembled into different aggregation states from monomers to octamers. The aggregates were tagged with organic Raman-active molecules and encapsulated in a SiO_2 shell (roughly 50-nm thick), forming plasmonic SERS nanoantennas. Since the SiO_2 shell guaranteed constant dielectric environment among the nanoantennas, the observed 300-nm distribution of their LSPR maxima was assigned to the structural heterogeneity of nanoparticle assemblies varied by the number of particles and aggregate shape. For instance, LSPR spectrum of an L-shaped trimer nanoantenna was found to consist of three peaks, corresponding to dipolar and multipolar plasmon resonances. The studies showed, however, that not only the amount of constituents and shape of the gold aggregates influence their LSPR condition. Individual gold particle dimers exhibited different plasmonic properties despite having essentially same structures (particle and shell size, shape), implying a crucial role of interparticle gap width in the LSPR phenomenon. Nanoantennas with coalescent or being in subnanometer proximity gold particles showed the best electromagnetic enhancement for SERS.

Three groups of Schatz, El-Sayed, Aussenegg [84,94,95] reported the dependency of plasmon maximum position on the spacing in nanoparticle pairs. For the light polarized parallel to the long particle pair axis, significant red shifts of the surface plasmon band occurred with narrowing the interparticle gap, originating from plasmonic coupling. At the same time, resonant wavelength corresponding to light with the orthogonal polarization blue-shifted.[95]

Near-field coupling between closely spaced metal nanoparticles allows plasmon propagation along the ordered nanoparticle array, so that the latter can serve as plasmon waveguide. Maier, Kik and Atwater [96] determined collective plasmon resonance frequencies of lithographically prepared one-dimensional nanoparticle chains of 3, 5, 7, 80 spherical gold nanoparticles with 50 nm in diameter and an interparticle spacing of 75 nm on glass slides. Both finite-difference time-domain (FDTD) simulations [97] and far-field extinction spectra of gold nanoparticle chains showed two extinction bands corresponding to longitudinal (along the chain axis) and transverse (perpendicular to the chain axis) collective plasmon-polariton modes. The peak positions of the longitudinal and transverse extinction bands were shifted relative to the single-particle LSPR band due to near-field coupling. The splitting between the two collective modes increased with chain length and saturated at the length of seven particles.

1.2.7. **Nanoparticle composition**

Optical properties of metal alloy nanoparticles can be tuned by varying their composition, morphology (segregation pattern), shape and size.[98] According to Ferrando *et. al.*,[99] four main types of mixing/segregation patterns can occur for nanoalloys: (i) core−shell segregated structure, with possible mixing in the intermediate volume; (ii) subcluster segregated structure is in principle possible; (iii) ordered or random mixed structure; (iv) multishell layered or onion-like structure. The term "alloyed" nanoparticles used in literature is usually referred to random mixed alloy morphology. The factors determining the segregation and atomic ordering in bimetallic nanoalloys include the strength of interatomic bonds, surface energies of bulk elements, relative atomic sizes, electron transfer, strength of binding to surface ligands or support, specific electronic/magnetic effects, *e.g.* electronic shell structure, preparation method and, importantly, experimental conditions. Atoms with the strongest homonuclear bonds, smaller atoms and elements with higher surface energy tend to segregate to the nanoparticle core. Electron transfer from less to more electronegative elements favours mixing. In supported alloys, the element that stronger binds to the support may be pulled out toward the surface. In general, the geometric or electronic structure of free alloy nanoparticles differs from that of the corresponding surface-supported clusters due to the substrate influence. Free non-supported metal nanoparticles are in the focus of this work.

The properties of the elements relevant for this work are listed in **Table 1.1**.

Table 1.1. Elemental properties of palladium, silver and gold: atomic radii, cohesive energy (ε_{coh}), average surface energy (E_{surf}), Pauling electronegativity, and electron work function of (111) metal surface. From Ref. 99,100.

	Pd	Ag	Au
atomic radius (Å)	1.375	1.445	1.44
ε_{coh} (eV)	−3.89	−2.95	−3.81
E_{surf} (meVÅ^{-2})	131	78.0	96.8
electronegativity	2.2	1.9	2.4
Work function (eV)	5.6	4.74	5.31

Gold-silver alloy nanoparticles

Optical properties of gold-silver alloy particles are widely studied.[98] Their plasmonic band can be varied by the content of gold and silver in the alloy.

In the case of spherical solid particles, core-shell structures exhibit two plasmon absorption bands at the wavelengths close to the SPR wavelengths of the corresponding monometallic spherical particles. The intensity of each band is proportional to the metal fraction.

In contrast to the core-shell structures, gold-silver alloy particles exhibit a single plasmonic maximum at the wavelength between the plasmon resonances of pure gold and pure silver. The position of the LSPR maximum is determined by the ratio between the mole fractions of gold and silver, independently on the preparation method.[91,92,93,104,105,106,107] With the increase in gold fraction, the LSPR maximum of alloy nanoparticles shifts to the longer wavelengths, toward the position of the gold nanoparticle LSPR, following a linear trend. The color of alloy nanoparticle suspensions changes correspondingly from yellow to red. The single plasmon peak in extinction spectra of gold-silver nanoparticles is considered as evidence of random alloy structure formation.[108]

The gold-silver alloy particles, alike the pure gold and silver nanoparticles, have face centered cubic structures. Since gold is more electronegative than silver, electron transfer from silver to gold atoms is expected in bimetallic structures.[99]

According to the thermodynamic considerations (**Table 1.1**) and calculations by Ferrando *et. al.*,[99] core enrichment of Au and Ag segregation to shell is favoured for gold-silver alloy particles. This is in agreement with many experimental studies of gold-silver alloy particles synthesized chemically.[109] For instance, recently near-spherical gold-silver alloy nanoparticles were chemically synthesized by a combination of the coreduction of gold and silver salts in solution and the seeded growth approach using small gold seed nanoparticles.[106] The color of alloy nanoparticle suspensions changed from red to yellow with increasing silver content, consistent with the position of the single plasmonic absorption peak. Energy-dispersive X-ray spectroscopy in TEM revealed inhomogeneous alloy composition with silver-rich surface and gold-rich core. Silver molar fraction linearly depended on the radial position. However, the authors explained the silver-rich surface by the galvanic replacement during particle growth. This work demonstrates that plasmon band in absorption spectra cannot track the segregation of one metal to the surface and in general local distribution of elements in the volume of a nanoparticle with statistically random alloy structure.

Alloy nanoparticles can be prepared using a plenty of techniques.[99] One of the effective methods is laser ablation in liquids.[110] In the recent study,[111] the mixtures of laser ablated gold and silver colloids with different volume ratios were further irradiated with the focused laser beam. The resulting alloy particles were found to be almost spherical with the average diameter about 20 nm. Plasmon band of nanoalloy particles appeared in between the SPR maxima of pure silver (415 nm) and pure gold (520 nm), depending on the molar fraction of gold. Corresponding gradual color changes from light yellow to light pink occurred. (**Figure 1.7**) Non-linear optical properties of gold-silver alloy nanoparticles were found to depend on the composition due to the tunable SPR position. The morphology of such alloy particles prepared by laser ablation was not investigated.

Palladium nanoparticles

Extinction spectra of palladium particles show a slope in visible range and a plasmon peak in UV range. For instance, 22-nm diameter particles prepared non-chemically and immobilized on fused silica exhibited absorption peak at 220 – 247 nm at environment refractive indices 1.25 – 1.5 respectively.[112]

Recently reported calculated extinction spectra[113] of spherical palladium nanoparticles from 40 to 90 nm in diameter in water possessed a single plasmon absorption peak. The position of the plasmonic maximum was predicted to red-shift with increasing nanoparticle size, from 200 nm for 40-nm particles to 450 nm for 90-nm particles. Only a slope and no peak at $\lambda > 200$ nm was predicted for palladium nanoparticles with diameters smaller than 40 nm. For particle diameters larger than 90 nm, additional plasmonic modes were predicted in the spectra.

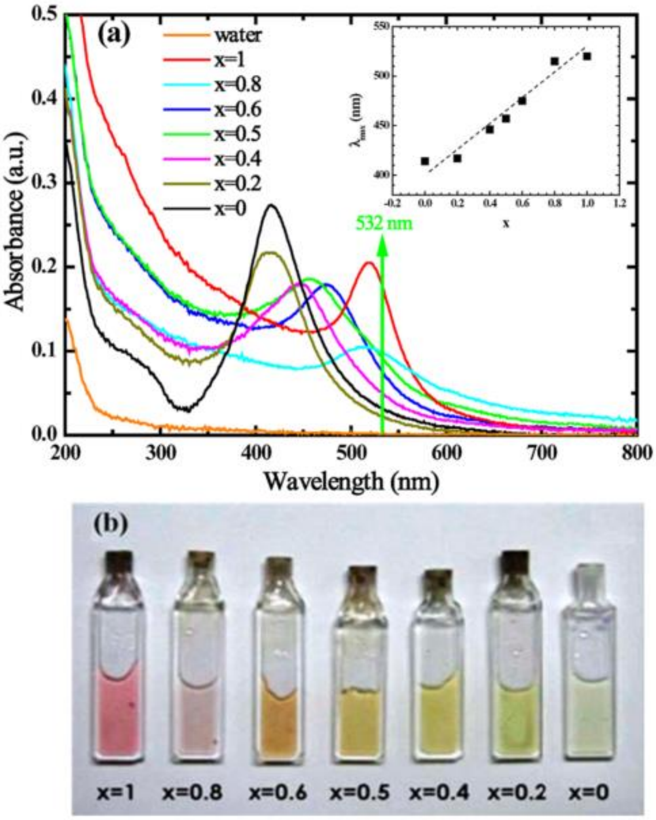

Figure 1.7. Absorption spectra (a) and suspension photographs (b) of aqueous colloids of spherical gold-silver alloy nanoparticles with different gold molar fraction x. From Ref. 111.

Gold-palladium alloy nanoparticles

Based on **Table 1.1** and simple thermodynamic considerations, gold-enriched surface is expected in gold-palladium alloys. The simulations of small bimetallic clusters in Ref. 114 predicted the coexistence of core-shell, alloy and eutectic-like structures in the samples prepared by the same method. The morphology with palladium core and gold shell was enthalpically the most favourable at ambient temperatures. The homogeneous (random) alloy morphology had a less negative enthalpy of formation than for the core-shell morphology, but the highest entropy. Eutecticlike structures were favourable in the case of one-component enriched composition. Coupled with the effect of structural incoherency, the core-shell structure with gold shell and palladium core was energetically more favorable. However, the configuration energies of different structures did not differ much. Experimental studies of anticipated alloy particles often revealed Pd-core/Au-shell and inverted core-shell structures along with random alloy bimetallic structures, as well as alloys with gold- or palladium-rich surface and surface with mixed monometallic regions, depending on the composition and preparation technique.[98,99,108]

Turkevich[115] reported in 1985 that the optical spectra of the gold-platinum alloy nanoparticles are not an additive superposition of the spectra of pure gold and platinum. The plasmon peak of gold was absent until the amount of gold reached 75 weight percent, when the gold LSPR peak appeared as a shoulder. The similar effect of gold LSPR damping occurs in gold-palladium alloy nanoparticles in comparison with physical mixtures of monometallic nanoparticles with the same percentage.

For alloy gold-palladium particles capped with poly(N-vinyl-2-pyrrolidone),[116] prepared by coreduction of gold and palladium ions in solution, plasmon peak of gold became apparent starting from 60 % of gold and grew with the amount of gold, whereas for physical mixtures of monometallic suspensions gold plasmon peak was visible already at 20 % of gold. Based on the observed changes in plasmonic properties, authors suggested palladium-rich surface and gold-rich core of the alloy nanoparticles with ≤ 40 % of gold. This has been confirmed by other methods.

The same trends occurred for gold-palladium alloy nanoparticles encapsulated in dendrimer.[117] Gold plasmon peak was not detectable in the extinction spectra of gold-palladium alloy nanoparticles, but visible in the monometallic mixtures.

In fact, similar drop of intensity of gold LSPR absorption peak occurred experimentally[118] and was predicted by calculations[119] for Au-core/Pd-shell particles. For the inverted Pd-core/Au-shell structure, gold LSPR band intensity increased with gold content.

Therefore, it is not possible to reveal the core-shell morphology of gold-palladium bimetallic particles using UV-Vis absorption spectroscopy, unlike gold-silver nanoparticles. However, when gold plasmon peak is suppressed in a bimetallic gold-palladium nanoparticle, it might indicate bimetallic particle formation, probably with the palladium-rich surface.[108]

1.3.Nanoparticle aggregation

1.3.1. Aggregation regimes in solution

Two universal, independent from the chemical properties, and determined by short-range interparticle interactions, regimes of irreversible colloidal aggregation have been introduced in 1985.[120] Small amounts of pyridine were stepwise added to aqueous colloid of citrate-stabilized gold nanoparticles with 15 nm in diameter. This led to aggregation due to the displacement of charged ions from gold surface by neutral pyridine molecules. Initial aggregation rate increased with the amount of pyridine added. The slow aggregation regime occurred at low concentration of pyridine added and was labeled reaction-limited colloidal aggregation (RLCA). At these conditions, there was a substantial repulsive force between particles to overcome. Therefore, aggregation was limited by the time needed for two particles to overcome the repulsion by thermal activation. Rapid aggregation occurred at sufficient pyridine amount was referred to as diffusion-limited colloidal aggregation (DLCA), because the repulsive barrier between particles was negligible and aggregation rate was essentially limited by diffusion.

Universality in the two aggregation regimes has been supported by comparing chemically different aqueous colloids of gold, silica and polystyrene latex by the means of static and dynamic light scattering and computer simulations.[121, 122, 123] Citrate-stabilized 15-nm gold particles were coagulated by pyridine. Silica particles of diameter d = 7 nm initially possessed negative surface charge due to OH- or SiO- groups, and their aggregation via electrostatic charge screening was induced by NaCl addition at pH ≥ 11. Polystyrene latex particles with d = 38 nm stabilized by carboxylic acid were treated with HCl and NaCl to implement DLCA and RLCA regimes respectively. The behaviour of the aggregation kinetics and the properties of the resulting clusters (in terms of mass distribution and structure anisotropy) were identical for all three colloidal systems. RLCA aggregates were found to be more compact, while DLCA aggregates appeared to be more open and loose.

1.3.2. Plasmonic properties of nanoparticle aggregates

Taylor *et al.* [124] mediated aggregation of 20-nm gold nanoparticles using cucurbit[5]uril (CB[5]) and observed the plasmonic peak evolution in the recorded time-resolved extinction spectra. Due to its shape and rigidity, CB[5] is capable of binding gold particles with the precise spacing of 0.9 nm, allowing for the distinct plasmonic modes. DLCA regime was fulfilled at higher amounts of CB[5], due to higher probability of nanoparticle coagulation. One could see rapid decrease and broadening of gold nanoparticle LSPR band at 525 nm, along with the appearance of the second broad peak at 650 nm and its growth and red shift to 690 nm over time. At lower CB[5] concentrations, aggregation was reaction-limited, with similar but significantly slower changes in the extinction spectra (**Figure 1.8**). TEM micrographs, obtained in parallel to the recording UV-Vis spectra, showed compact slowly growing RLCA clusters, whereas open chain-like aggregates were growing during DLCA, resulting in micrometer-sized networks. In fact, two plasmon modes arising from different structural specimens within aggregates were revealed in the broad secondary plasmon band ($\lambda > 600$ nm). The plasmon mode at 590 nm was assigned to the longitudinal plasmon resonance of nanoparticle dimers, it remained at its initial position over time. The broad resonance mode at 650 nm was identified as the coupled longitudinal mode of embedded nanoparticle chains. This mode red-shifted over time owing to the chain growth, *i. e.* increasing number of particles, until a saturation in interparticle coupling was achieved (690 nm). The third mode near the individual gold particle resonance at 525 nm was assumed to be the transverse plasmon mode of the nanochains within aggregates. Much smaller spectral red shifts in RLCA regime are explained by the lack of the optical nanochain response in compact RLCA structures, as opposed to open networks resulting from DLCA.

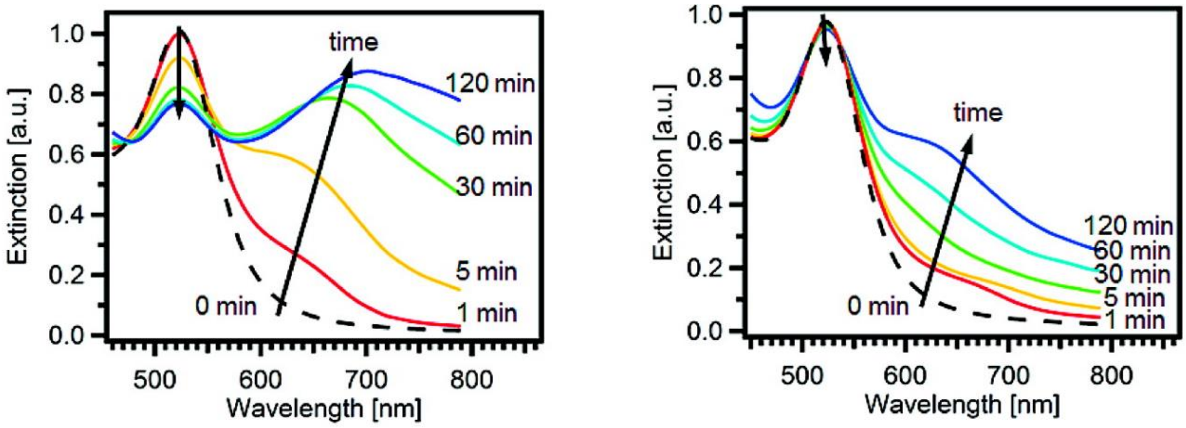

Figure 1.8. Changes in the extinction spectra of gold nanoparticles upon diffusion-limited (left) and reaction-limited (right) aggregation induced by cucurbit[5]uril. The figure is the replica from Ref. 124.

Esteban *et. al.* [125] numerically studied optical response of self-assembled gold clusters of moderate compactness, consistent with the case of DLCA. The aggregates consisted of a large number of strongly interacting spherical gold nanoparticles of the same size (10 – 40 nm in diameter) separated by fixed 0.9-nm gaps in water. The optical behaviour of a large three-dimensional aggregate of unknown structure was interpreted as a composition of collective plasmon modes of individual distorted one-dimensional chains within the aggregate. Calculated absorption spectra were in good agreement with experimental extinction spectra for the aggregates of spherical particles of the same size and with the same gap width. Three modes were distinguished for complex three-dimensional 40-nm particle aggregates in unpolarized light: (i) a peak near the plasmon resonance of a single particle, $\lambda \approx 540$ nm, (ii) plasmon mode at long wavelengths $\lambda \approx 800$ nm, corresponding to the long chain excitations, and (iii) short chain mode at $\lambda \approx 700$ nm, corresponding to the plasmonic excitations of dimer-like short chains at the periphery of the aggregate. Two modes were visible for 20-nm particle aggregates: at $\lambda \approx 540$ nm and $\lambda \approx 650$ nm. Authors suppose the broadening of the spectrum when the interparticle gap and particles' size vary within an aggregate, so that the long chain modes might be hard to register.

Self-assembled nanoparticle chains are promising structures for plasmonic waveguiding. For instance, post-treatment of plasmonic nanochains with femtosecond laser radiation led to threading the chains into strings with plasmon resonance in the NIR spectral region.[126]

1.3.3. Surfactant-mediated nanoparticle aggregation

Aggregation of 13-nm citrate-stabilized gold nanoparticle into chains was induced by the addition of the conventional surfactant cetyltrimethylammonium bromide (CTAB) to nanoparticle aqueous colloid.[127] Extinction spectra were recorded over time for different CTAB concentrations, accompanied by TEM micrographs. One sustained narrow plasmon band at 520 nm was found for monodisperse nanoparticles at low and high CTAB amounts, when the CTAB molecules negligibly or extensively displaced citrate ions on gold surface. At high concentrations, CTAB bilayers were expected to stabilize gold particles. Large aggregates of CTAB-modified particles rapidly precipitated from solutions at certain CTAB concentrations. Short nanoparticle chains were found at the intermediate surfactant concentrations, exhibiting coupled plasmon modes in the UV-Vis-NIR absorption spectra along with the transverse mode near $\lambda = 520$ nm. These longitudinal chain modes appeared at different wavelengths $\lambda > 600$ nm depending on CTAB concentration and red-shifted with time. Surfactant-mediated self-assembly of gold particles into chains was explained by electric dipole formation upon partial displacement of citrate surface layer by CTAB at intermediate surfactant concentrations, when the residual surface charge distribution turns anisotropic. Such suggestion was also published earlier for the aggregation of gold nanoparticles into short chains mediated by mercaptoethyl alcohol.[128]

Muto *et. al.* [129] investigated laser ablated spherical gold nanoparticles of 11-nm diameter in aqueous solutions of several surfactants. Laser ablation used to prepare nanoparticle colloid in water allowed to avoid additional stabilizing agents, because the as-prepared particles were stable through their negative surface charge in water (pH 7). Gold nanoparticles were mixed with cetyltrimethylammonium bromide (CTAB, C_{16}TAB), sodium dodecyl sulfate (SDS), as well as with a series of CTAB-like surfactants: cetyltrimethyl ammonium chloride (CTAC, C_{16}TAC), tetramethyl ammonium bromide (C_1TAB), octyltrimethyl ammonium bromide

(C_8TAB), and dodecyltrimethyl ammonium bromide (C_{12}TAB). In SDS solutions above critical micelle concentration, gold particles were likely stabilized by the micelles of negatively charged DS^- ions. Addition of CTAB-like and CTAC surfactants at different concentrations to gold nanoparticles induced their irreversible aggregation. UV-Vis absorption spectra recorded after precipitation showed a single plasmon peak of gold nanoparticles at 520 nm. Absorption intensity sharply decreased down to zero and began to increase again with increasing concentration of cationic CTAB-like surfactants. At the same time, ς-potential of gold particles in water measured right after mixing increased from -30 mV without surfactant to 0 mV when the particles aggregated, and became positive at higher surfactant concentrations. Absorption spectrum recorded 15 min after mixing gold particles with CTAB at the concentration, at which particles aggregated (confirmed by TEM), exhibited the second plasmon mode at 650 nm. Electrostatic interaction between cationic surfactants and gold nanoparticles was suggested to drive particle aggregation: CTA^+ ions attached to the particle surface pointing inward and neutralized the particle surface charge until all negative charge sites had been screened and particles aggregated at certain threshold surfactant concentrations. Stabilization of particles in concentrated solutions of cationic surfactant was explained by the positive charge of CTA^+ groups pointing outward in the surfactant bilayer on the gold particle surface. Based on the CTAB concentration inducing all-particle aggregation, the authors of the Ref. 129 estimated 3.3-6.6 % of negatively charged atoms on the surface of 11-nm laser ablated gold nanoparticles. Total precipitation of particles in CTAC solution was detected in the same concentration range as CTAB, implying no impact of counteranion on the gold-surfactant interaction in diluted surfactant solutions. Increasing hydrophobic tail length in CTAB-like surfactants led to the precipitation in nanoparticle suspensions at lower surfactant concentrations.

1.3.4. Light-induced aggregation of nanoparticles

Colloidal stability of nanoparticles is determined by van-der-Waals and electrostatic interactions in suspension. Irreversible aggregation of 11-nm gold nanoparticles in organic solvents was induced by irradiation with mercury lamp with and without optical filters.[78, 117] The particles were prepared in the absence of surfactants or other stabilizing agents. Their plasmon absorption band was positioned at 523 nm in 2-propanol. Additional plasmon band arised gradually and red-shifted to 830 nm with irradiation time, following the formation of aggregates. At the same time, suspension colour changed from wine red to blue. After sufficient time the aggregates precipitated and were not capable to re-disperse. The authors separated particle *coalescence* occurred upon irradiation with UV light, and particle *coagulation* induced by irradiation with visible light. The suggested cause of the visible-light induced coagulation was the excitation of surface plasmon oscillations and consequent particle charge neutralization or van-der-Waals attractive forces between plasmon dipoles.[91] Furthermore, the coagulation was found to proceed in the diffusion-limited fashion, starting with one-dimensional aggregate formation (chains) in the beginning of the illumination and ending in fractal clusters with chain-like segments.

Metal nanoparticles, functionalized with the monolayers of azobenzene thiol ligands and rendered by this means photosensitive, aggregate in nonpolar solvents as soon as trans-cis photoisomerization of azobenzene groups takes place. The aggregation of such photosensitive nanoparticles is driven by a combination of solvophobic interactions and attractive dipole–dipole interactions between cis-azobenzenes in the ligands on different nanoparticles. For instance, increase in the dipole moment due to azobenzene ligand trans-cis isomerization in UV light, weakens the interaction between nanoparticle shell and nonpolar toluene, what leads to the destabilization of the suspended nanoparticles. Additional dipole-dipole interactions between azobenzene cis-isomers make interparticle interactions comparable with thermal energy and therefore induce nanoparticles aggregation. At the same time, in polar solvents nanoparticles coated with azobenzene monolayer remain stable in UV light through the higher dipole moment of cis-isomers, and aggregate upon cis-trans transition. Depending on the strength of solvophobic and dipolar coupling effects, which in the same solvent depend on the substitution pattern of azobenzene in the monolayer shell, nanoparticles can assemble reversibly or irreversibly when exposed to UV or visible light.[42,62,131,132]

Reversible nanoaggregation of gold nanoparticles decorated with differently substituted thiolated azobenzenes was induced by exposure to UV or blue light in a nonpolar solvent.[133] Dodecylamine-capped gold NPs of approximately 5.5 and 2.5 nm in diameter were functionalized with a parent azobenzene-terminated alkanethiol and derivative thiolated 4-(dimethylamino)azobenzene, respectively. Absorption bands of the latter alkanethiol were found around 50 nm red-shifted relatively to the parental compound. In contrast to the parental azobenzene, irradiation of the “red-shifted” azobenzene with blue light induced its trans-cis isomerization with 12 % of trans-isomers in the blue-photostationary state. Subsequent exposure to near-UV light enabled its back cis-trans isomerization resulting in around 48 % of trans-isomers. Alternatively, thermal cis-trans relaxation was accelerated by heating at 45°C.

Gold nanoparticles decorated with different azobenzene thiols aggregated after irradiation of their toluene/hexane colloids with light at different wavelengths. Nanoparticles functionalized with the parental azobenzene thiol aggregated in response to UV light, and re-dispersed in blue light.[134] Opposite to this behaviour, nanoparticles functionalized with the “red-shifted” azobenzene self-assembled into metastable aggregates after exposure to blue light, when azobenzene compound was in predominantly cis- conformation. UV light, as well as thermal treatment, caused the aggregates to disassemble.

In a mixture of 2.5-nm and 5.5-nm nanoparticles each decorated with a different azobenzene ligand,[133] selective self-assembly of one type of nanoparticle occurred depending on the wavelength of the incident light. Exposure to blue light induced the trans-cis isomerization of the “red-shifted” azobenzene and therefore aggregation of the 2.5-nm particles decorated with this compound. Following irradiation with UV light simultaneously caused trans-cis isomerization of the parental azobenzene and back cis-trans isomerization of the red-shifted azobenzene. This allowed self-assembly of 5.5-nm particles decorated with the parental compound and at the same time disassembly of the aggregates of 2.5-nm particles. Blue light in the next irradiation cycle restored the aggregates of the smaller particles and re-dispersed the larger particles. Nanoparticles functionalized with mixed monolayers of both azobenzenes, with approximately 31 % of the “red-shifted” compound, aggregated in toluene/hexane solution in response to either UV or blue light, but disassembled after heating, when both azobenzenes returned into trans-conformation.

Light-controlled reversible aggregation of azobenzene-functionalized nanoparticles in a nonpolar environment has found an application for creating self-erasing images.[61] Gold and silver nanoparticles of roughly 5 nm in diameter were coated with mixed self-assembled monolayers of dodecylamine and photoswitchable azobenzene-terminated thiol 4-(11-mercaptoundecanoxy)azobenzene (MUAzo), and embedded in thin organogel films. Azobenzene groups of MUAzo ligands isomerized into cis-conformation once irradiated with UV light. Photoisomerization in UV light caused increase in dipole moment from 1 Debye for the trans-isomer to 5 Debye for the cis-isomer and thus governed attractive dipole-dipole interactions between the particles. At certain surface coverage of MUAzo the attractive forces were just so to cause reversible nanoparticle aggregation. Visible light induced back cis-trans isomerization of azobenzene containing ligands, which occurred also spontaneously via thermal relaxation and could be accelerated by heating. Irradiation with visible light and heating (50°C) weakened the coupling between nanoparticles and led to the rapid disassembly of their aggregates. Reversible nanoparticle aggregation was associated by colour changes from red to pale blue for gold, and from yellow to violet for silver nanoparticles. In the absence of UV light, plasmon absorption peaks of gold and silver nanoparticles in gels were found at 525 nm and 420 nm, respectively. These plasmon wavelengths were near plasmon peak positions of free nanoparticles in toluene. Painting multi-colour images with UV light was possible due to red-shifting of the plasmon resonance bands upon nanoparticle aggregation. The images in the dark self-erased after a week due to thermal cis-trans relaxation of azobenzene and the corresponding disassembly of particle aggregates. Visible light and heating erased the images in a few seconds, so that the films could be re-written.

Recently, alternative light-induced reversible aggregation of non-photosensitive gold nanoparticles was implemented via photocontrol over pH of the medium.[135] The gold nanoparticles of 2.5, 5.5, 11 nm in diameter were functionalized with pH-sensitive monolayers of 11-mercaptoundecanoic acid (MUA). The photoresponsive medium comprised spiropyran solution, which pH was modulated with blue light. Changing the acidity of the medium affected the colloidal stability of nanoparticles in methanol and caused their reversible self-assembly into aggregates. In the dark, gold nanoparticles were in aggregated state forming a black precipitate. The solution had yellow colour originating from the medium. In blue light MUA-coated nanoparticles were fully re-dispersed due to the ligand protonation and thus obtaining positive surface charge. The light-irradiated solution had red colour due to strong plasmon absorption band of dispersed nanoparticles. Gold nanoparticles readily aggregated once the blue light source was off. The colour change between red and yellow was used to create self-erasing images in thin films of crosslinked poly(ethylene glycol) (PEG) gels by their local exposure to blue light through a mask.

Similar approach was reported later for light-controlled, reversible assembly of gold nanoparticles in aqueous solution of a photoacid.[136] Gold nanoparticles of 5.8 and 10 nm in diameter were functionalized with 6-mercaptohexanoic acid. The pH of the medium decreased upon irradiation with blue light, causing formation of metastable nanoparticle aggregates. In the dark, with the pH increase, rapid spontaneous disassembly of the aggregates occurred.

1.4. Catalytic properties of metal nanoparticles

Metal nanoparticles are successfully employed in catalysis for a variety of reactions.[137] Even chemically inert gold exhibit catalytic properties when in form of nanoparticles.[138] In fact, Parravano's group reported on catalytic properties of metal nanoparticles in the 1970s (Ref. 72 and references therein). However, the discovery by Haruta *et. al.*[139] of metal oxide-supported gold nanoparticles as highly active catalysts has started the era of nanoparticle catalysis. Gold nanoparticles are widely used in oxidation-reduction reactions, *e.g.* carbon monoxide and alcohol oxidation, hydrogenation of various compounds, carbon-carbon coupling, water splitting, organic synthesis and other miscellaneous reactions.[140,141,142,143]

In this work, catalytic properties of nanoparticles depending on their composition will be addressed. Therefore, this section attempts to give a brief overview on how nanoparticle properties influence their catalytic activity in various chemical reactions, and which physico-chemical processes are behind the nanoparticle catalysis.

The reduction of 4-nitrophenol by sodium borohydride in the presence of metal nanoparticles has been used frequently to study catalytic properties of nanoparticles in aqueous solution.[144] This reaction is well-studied and proceeds in water at ambient conditions. The study of the reduction of 4-nitrophenol by El-Sayed *et al.*[145] stated that nanoparticle catalysis has heterogeneous mechanism, *i. e.* reactions proceed at the nanoparticle surface. For that, plasmonic properties of gold spherical particles, hollow spheres, and cubical nanocages of roughly 40 nm size have been employed, namely the shift of their surface plasmon band position upon changes in the local dielectric environment during the reaction.

1.4.1. Electron transfer

The believed physical origin of the catalytic activity of metal nanoparticles is electron transfer between nanoparticle surface and reactants. In 2014, Studer and Curran[146] suggested to generally consider the electron as the catalyst in the majority of catalytic reactions proceeding as cascades with radical and radical ion intermediates. In redox reaction catalysis, metal nanoparticles can accommodate electrons,[147,148] and electron transport from the oxidation site to the reduction site takes place on nanoparticle surface. Reducing agent injects electrons into nanoparticles, which can be discharged to an electron acceptor. In photocatalysis, free radicals formed in a colloidal solution by irradiation diffuse to the particles and transfer electrons to them.[147]

In the reduction of hexacyanoferrate (III) ions by borohydride ions in aqueous solution catalysed by gold particles, the metal nanoparticles can accept electrons from borohydride and serve as an electron storage. In the second step, ferricyanide ions diffuse to the nanoparticle surface and are reduced by excess surface electrons. The reaction kinetics is second-order.[144,149]

The reduction of 4-nitrophenol is also an electron-transfer reaction which proceeds with the first-order kinetics as follows.[144,145] Borohydride (BH) ions react with the surface of the nanoparticles resulting in the oxidized form of $NaBH_4$ on the surface and the hydrogen gas around it. Then, 4-nitrophenol molecules are adsorbed on the surface of the nanoparticles. 4-nitrophenol becomes reduced to the nitrosophenol and then quickly converts to 4-

hydroxylaminophenol. In the second, rate-determining step, the latter compound is reduced to the final product 4-aminophenol. All intermediates adsorb onto active sites on the nanoparticle surface to react, with an adsorption/desorption equilibrium in all steps.[150]

1.4.2. **Nanoparticle size and shape**

Many studies demonstrated that the catalytic properties of nanoparticles depend on their size and shape.[151,152] For instance, Lin *et. al.*[153] studied size effect of gold nanoparticles for the catalytic reduction of 4-nitrophenol. The size of the particles ranged from 1.7 to 8.2 nm. The highest reaction rate was observed for the intermediate 3.4-nm particles. CTAB-stabilized gold nanoparticles with mean sizes from 3.5 to 56 nm diameter were tested for the catalytic reduction of 4-nitrophenol.[154] The total concentration of gold (in terms of atoms) was kept constant. The particles with the intermediate 13-nm size appeared to be the most effective. Zeng *et al.*[155] compared the catalytic properties of gold cubic nanocages, hollow cubic nanoboxes, and solid particles of approximately 50 nm size using the reduction of 4-nitrophenol as well. The concentrations of particles were the same. The nanocages were found to be catalytically more active than the nanoboxes and nanoparticles. The authors explained it by higher particle surface area (surface-to-volume ratio) of nanocages and by the size effect due to ultrathin walls of the nanocages.

Nanoparticles with different shapes were used to catalyse the reaction between hexacyanoferrate (III) ions and thiosulfate ions.[156] Tetrahedral, cubic, and "near spherical" platinum nanoparticles of 5 – 7 nm size were capped with a polymer. In the reaction, thiosulfate ions bound to the platinum nanoparticle surface and then reacted with hexacyanoferrate(III) ions to form final products. The tetrahedral particles were found to be the most efficient, rationalized by the highest fraction of chemically unsaturated (low-coordinated) surface atoms on corners and edges. The same conclusion that atoms on the corners and edges of nanoparticles are the active catalyst sites was made for gold nanoparticles.[157] Indeed, unsaturated surface atoms more likely participate in electron transfer. To the point, plasmon oscillations are also enhanced on the corners of nanoparticles.[158]

Therefore, there are two main factors of effective nanoparticle catalysts: (i) surface area, or surface-to-volume ratio, in the context of the number of available surface sites; and (ii) surface roughness, with respect to the number of active unsaturated atoms on surface. There are also other effects, such as nanoparticle aggregation and oxidation state (regarding the available surface sites), surface potential, crystallographic facets ((111) facets have sharper corners and edges than (100) and therefore are more favorable in catalysis), and the energy of the Fermi level.[108] Catalytic activity cannot be attributed to a single metal property, but a combination of factors influencing the interaction of reactants with active metal atoms on nanoparticle surface.

1.4.3. **Nanoparticle capping**

Catalytically active nanoparticles are often stabilized by thiolate ligands,[159] surfactants,[154] polyelectrolytes,[160] to assure their colloidal stability on the purpose of reusability and maximal surface area, and allow for the study of catalytic properties of individual nanoparticles.

Gold, silver and platinum nanoparticles of approximately 1.5 – 3 nm in diameter were immobilized in spherical cationic polyelectrolyte brushes grafted to a polystyrene core.[161,162] The catalytic activity of different metal nanoparticles was compared towards the reduction of 4-nitrophenol. Since the catalytic reactions take place on the surface of the particles, rate constants normalized to the particle surface area have been compared. Gold nanoparticles were found to be less active than platinum particles immobilized in the same carrier system.[162] Among different metal nanoparticles prepared with similar carriers, silver nanoparticles appeared the least active, palladium nanoparticles – the most active, Pd > Pt > Au > Ag.[161] The reason of this phenomenon was not investigated.

In another study,[163] the catalytic activity of metal-microgel composite particles have been probed by the oxidation of alcohols to the corresponding aldehydes or ketones at room temperature in water using air as oxidant. Gold, ruthenium, and platinum nanoparticles (d_{Au} = 4.8 nm, d_{Rh} = 4.5 nm, d_{Pt} = 2.8 nm) were embedded into cross-linked PNIPA microgel network. Gold nanoparticles showed higher catalytic activities than Pt or Rh, in contrast to the results in Ref. 161.

Capping ligands can reduce nanoparticle catalytic activity due to the screening of the active surface sites and changing nanoparticle surface properties upon binding.[108,164,165,166,167] The catalytic activity of nanoparticles in the reduction of 4-nitrophenol could be tuned by the swelling and shrinking of the thermoresponsive poly(Nisopropylacrylamide) (PNIPA) microgels in core-shell[168] and yolk-shell structures.[169] In yolk-shell structures, the temperature-mediated volume transition of the PNIPA shell between swollen (15 °C) and collapsed (50 °C) state induced 10-nm red shift of the surface plasmon absorption maximum of gold nanoparticles in the cores with temperature increase, apparently due to the changes in the local refractive index.[170] Recently, catalytic activity of gold nanoparticles towards the reduction of 4-nitrophenol was controlled by light using the photoresponsive peptide capping with integrated azobenzene unit, probably due to light-controlled changes in the active surface area of nanoparticles.[171]

1.4.4. **Nanoparticle composition**

The nanoparticles used in this work were not capped with stabilizing ligands. Silver nanoparticles are well-known to oxidize and aggregate rather fast in the absence of proper stabilization. Gold particles perform a better colloidal stability and resistance to oxidation, and therefore are usually more favoured as catalysts than silver nanoparticles.

Catalytic properties of laser ablated gold nanoparticles were studied using the reduction of 4-nitrophenol.[172] Laser ablated particles have “bare” surface, because they are not capped with stabilizers or ligands. The mean size of nanoparticles was around 7 nm. However, accounting for the lognormal size distribution of laser-ablated particles (there is a fraction of big particles), the mass-weighted arithmetic mean of 11 nm was used to calculate total nanoparticle surface and compare ligand-free nanoparticles with other systems. The ligand-free gold particles showed higher or similar kinetic constants (*i. e.* better catalytic activity) in comparison with carried nanoparticles (polymer brushes, micelles, core-shell microgel, graphene oxide support). However, gold particles immobilized in spherical polymer brushes showed higher kinetic constants than ligand-free particles, due to lower adsorption of 4-nitrophenol onto "bare" gold surface. This was attributed to the negative ς-potential of laser-ablated gold nanoparticles and thus electrostatic repulsion between the negatively charged 4-nitrophenol molecules and nanoparticle surface.

Recently, catalytic properties of bare porous palladium nanostructures were studied using the reduction of 4-nitrophenol.[173] The structures were synthesized chemically and purified by decantation to remove stabilizers. Catalytic performance was higher for the structures with higher surface area.

Noble metal alloy nanoparticles are effective catalysts for a wide range of dehydrogenation, hydrogenation, and selective oxidation reactions of organic molecules.[174] Catalytic behaviour of alloy nanoparticles depends on their shape and size, surface structure, composition, and segregation pattern, which strongly depend on the preparation technique.[108]

Catalytic properties of nanoalloys are usually enhanced in comparison with pure metal or *e.g.* bimetallic core-shell structures due to synergistic effects.[175] For example, catalytic activity for the hydrogenation of 1,3-cyclooctadiene[116] and allyl alcohol[117] was higher for gold-palladium alloy nanoparticles than for the corresponding physical monometallic mixtures, increasing with the palladium content in the alloy. For 1,3-cyclooctadiene,[116] catalytic activity of pure gold particles was negligible, the alloys with 80 % of palladium showed the best performance.

The synergistic catalytic effect is the mutual influence of different components and/or active sites in the catalyst. Among four kinds of possible synergistic catalytic effects in nanocomposite catalysts, the activation of one component by another dominates, typically due to a charge transfer between the components.[176] However, the synergistic effects are not yet fully understood.

Gold-silver alloy nanoparticles

In the reaction of low-temperature oxidation of carbon monoxide, silver was catalytically inactive, gold particles showed low activity, while gold-silver alloy nanoparticles exhibited high catalytic performance, improving with the increasing gold content.[177]

Catalytic activity for the reduction of 4-nitrophenol of 4-nm alloy gold-silver particles stabilized by poly(amidoamine) dendrimers was found to enhance proportionally to the fraction of gold in the particles.[178] Apparently, in those works, the number of gold atoms on the particle surface increased with the gold content, and silver atoms amplified their activity.

Haigh *et. al.*[179] correlated catalytic activity of hollow gold-silver alloy nanoparticles, synthesized chemically, with their segregation pattern. In a coupling reaction to form propargylamine, pure gold nanoparticles showed slightly better catalytic activity than silver particles. Alloying significantly improved the catalytic performance with the peak at 18 atom % Au. EDX mapping and tomography revealed particle morphology changes with the composition. Gold-rich surface occurred below 25 % Au, alloy structure without surface segregation existed between 25 % and 35 % of gold, silver segregated to surface starting from 50 % of gold. At the intermediate composition, 35 % < Au < 50 %, non-segregated alloy structures coexisted with particles with silver-rich surface. In fact, the coexistence between mixed and surface-segregated structures occurred also on the border around 20 % of Au.

Authors attributed the high catalytic performance at 18 % Au to the increased surface electron density of particles with alloy or gold-rich surface due to electron transfer from silver to gold (electronegativity effect). Increasing gold fraction did not improve catalytic activity because of morphology changes to silver-rich surface, although propargylamine yield was still slightly higher than for pure metal particles.

Gold-palladium alloy nanoparticles

Gold-palladium nanoalloys have been widely used as catalysts.[99,108] For instance, Hutchings *et. al.* reported on the direct synthesis of hydrogen peroxide from hydrogen and oxygen catalyzed by gold-palladium nanoalloy on TiO_2 in water at ambient conditions.[180]

Depending on the reaction, gold or palladium surface atoms have been identified as active sites, charge transfer between gold and palladium is mentioned in the majority of the studies.

In the reaction of N_2O decomposition,[181] the contiguous Pd atoms were better active sites than Au atoms, pure palladium nanoparticles showed higher activity compared to pure gold. Gold-palladium alloy nanoparticles of ~ 2 nm size on a mesoporous support showed lower catalytic activity than pure Pd in this reaction, because the surface Pd atoms became isolated by gold atoms gradually at increasing gold fraction.

In aerobic oxidation of benzyl alcohol,[182] gold surface atoms were suggested to be the active sites. Catalytic properties of gold-palladium random alloy nanocubes of less than 2 nm size and stabilized by poly(N-vinylpyrrolidone) were studied. Pure palladium particles showed negligible activity, pure gold – moderate activity. The alloy particles showed enhanced activity increasing with gold fraction due to the increasing number of surface active sites up to a certain percentage, after which alloy catalytic activity decreased to the level of pure gold. The enhanced activity of alloy particles was explained by the electron transfer from palladium to gold, which in turn activated molecular oxygen on gold surface and promoted the alcohol oxidation.

Visible light irradiation enhanced catalytic activity of gold–palladium random alloy nanoparticles, less than 10-nm sized and supported on ZrO_2, for oxidant-free dehydrogenation of aromatic alcohols to the corresponding aldehydes at ambient temperatures.[183] Both under light illumination and in the dark, catalytic activity of alloys was enhanced in comparison with monometallic catalysts and determined by the alloy composition. The most effective was the Au:Pd molar ratio 1:1.86, equal to 65 % Pd. Authors believed that palladium surface atoms were the active sites. The enhanced catalytic activity was explained by the following several factors related to alloying. Firstly, electron redistribution from Au to Pd led to the electron-rich Pd sites and thus increased surface charge heterogeneity on the alloy nanoparticle surface. This enhanced the interaction between the alcohol molecules and the nanoparticle surface. The electron transfer from Au to Pd varied with the composition and reached the maximum at Au:Pd molar ratio 1:1.86. Secondly, the electron transfer to the adsorbed benzyl alcohol molecules causing their transformation was easier from the higher Fermi level of the alloy nanoparticles compared to that of pure Pd. The photocatalytic efficiency of the alloy nanoparticles strongly correlated with the electron transfer. In the photocatalytic effect, light-induced energetic conduction electrons of gold (LSPR effect) had even better ability to migrate to the Pd sites on the surface. The Fermi level of the alloy NPs increased under light irradiation. This further increased the possibility of electron transfer from the alloy NPs to the reactant molecules. The strong interaction with the surface facilitated the transfer of the photoexcited electrons of the nanoparticles to the adsorbed alcohol molecules. The authors in the proposed mechanism rely on the electron transfer from gold to palladium, which contradicts the difference in elemental electronegativities. However, the electronegativity values of gold and palladium do not differ much (**Table 1.1**).

The reduction of 4-nitrophenol to 4-aminophenol by sodium borohydride has been used to study the catalytic activity of gold–palladium nanoalloy particles immobilized on cationic spherical polyelectrolyte brushes. The particles of 1 – 3 nm size were synthesized chemically in solution by the reduction of salts. Catalytic activity was studied as a function of composition of the nanoalloys.[184] For comparison of different samples, the apparent reaction rates have been normalized to the surface area of the nanoparticles per volume unit. Nanoalloys showed significantly enhanced catalytic performance in comparison with pure metals, AuPd > Au > Pd. Catalytic efficiency of nanoalloy particles increased with the amount of gold. Gold-palladium alloy nanoparticles with the highest amount of gold (75 molar % Au and 25 molar % Pd) exhibited the highest catalytic activity. DFT calculations showed the decrease in the density of states close to Fermi level with the increase in Au content. The gold-palladium alloy nanoparticles appeared as facetted particles with face-centered cubic (fcc) structure. Structural analysis[185] of the gold-palladium alloy nanoparticles with 75 % Au showed a structure close to a random alloy. In the particles with less gold, slight enrichment of palladium at the surface and gold in the core occurred. Palladium surface atoms were found partially oxidized, indicated by the Pd^{2+} species besides metallic Pd. The catalytic active sites were suggested to consist of small groups of contiguous Pd atoms at the surface defects. It was concluded that the palladium surface atoms with non-metallic character (Pd^{2+}) decreased the catalytic activity, what explained the low activity of pure palladium nanoparticles. The better catalytic activity of the gold-palladium alloy nanoparticles with 75 % of gold was explained by electronic effects and the large number of surface defects due to atomic rearrangement at the surface upon alloying.[186]

In the trichloroethene hydrodechlorination catalysis,[118] gold nanoparticles were inactive, while palladium nanoparticles showed moderate activity. Chemically unsaturated Pd atoms, located at surface defects, were supposed to be the active sites. Palladium-coated gold particles (core-shell morphology) showed enhanced catalytic performance increasing with the gold content. The highest catalytic activity occurred for particles with a palladium submonolayer on the surface (1.9 weight % Pd), probably with palladium islands on the surface. At Pd amount sufficient for the monolayer formation, nanoparticle catalytic activity dropped down, and further decreased to the level of pure palladium particles with the increasing palladium content (number of palladium surface layers). The intensity of the gold SPR band decreased with the increase in palladium coverage.

1.5. Accelerated cis-trans isomerization of azobenzenes

Azobenzene derivatives are used in catalysis as reactants and as promoters. For instance, azobenzenes can undergo a complexation with metals resulting in azobenzene metallocycle formation. Palladium-catalyzed reactions and complexations involving azobenzenes are of particular interest in literature.[187]

The majority of studies involving azobenzene photoswitches and catalytic nanoparticles relate to photocontrollable nanoaggregation of particles upon azobenzene photoisomerization. In one of the examples,[188] 5.5-nm gold nanoparticles were covered with a self-assembled monolayer of azobenzene-terminated alkane thiol "diluted" by a conventional surfactant. The catalytic activity was studied in the hydrosilylation reaction with the formation of 4-methoxybenzyloxy-diphenylsilane, and was found to correlate with the light-tunable nanoparticle aggregation state. Particles in toluene aggregated in UV light and redispersed in visible light, reversibly switching their catalytic activity off and on, apparently via varying the nanoparticle surface area.

Upon binding of azobenzene containing molecules to metallic substrates, the molecule–substrate electronic coupling shortens the lifetime of molecular excited states and thus affects the switching properties of the surface-bound azobenzenes up to quenching, depending on the interaction strength, which is distant-dependent. Tetra-*tert*-butyl-azobenzene (TBA) aflat adsorbed on Au (111) surface can undergo photo- and thermal isomerization. The bulky *tert*-butyl groups were expected to enable photoinduced and thermally activated reversible trans-cis switching due to spatially decoupling the azobenzene unit from the metallic substrate. Indeed, cis-trans switching occurred, but electronic coupling between azobenzene units and gold surface remained sufficiently strong, presumably *via* the N = N bonding or the lone pairs of the nitrogen.[52] The following indirect mechanism of the photoinduced azobenzene switching on gold substrate has been revealed: unlike in solution (direct molecular photoexcitation), not the photoswitch but metal absorbs light energy. Upon light absorption, charge carriers (hot electrons and holes) can be generated in metal substrate. Substrate-mediated charge transfer between gold and azobenzene would lead to the formation of an ionic transition state and subsequent isomerization and back charge transfer to the substrate. Authors suggest that light with photon energies more than 2.2 eV generates hot holes in the *d*-band of gold rather than hot electrons. This is assumed to be a two-step process: (i) electron-hole pairs are formed in the gold d-band, (ii) the holes rapidly relax to the top of the *d*-band, becoming "hot". Therefore, a hole driven photoisomerization is assumed at the gold surface, where holes participate in the charge transfer to the TBA molecule, thus transient azobenzene cation forms and isomerizes. It was mentioned that such hole transfer should not occur on silver surface. The energy barrier for thermal cis-trans isomerization of gold surface-bound TBA was found to be reduced by the factor of four in comparison with free molecules in solution, implying faster isomerization. The reaction was sterically strongly hindered in the adsorbed state.

1.5.1. Thermal cis-trans isomerization of azobenzene monolayers on gold nanoparticle surface

Nanoparticles have recently been found to catalyse cis-trans isomerization of azobenzene containing compounds. In fact, these new studies emerged during the work on this thesis and therefore not so many relevant publications are available at the moment. The studies are mentioned in the chronological order.

An early report on nanoparticle-enhanced azobenzene isomerization is Ref. 60, where trans-cis photoisomerization and cis-trans thermal isomerization of azobenzene containing alkanethiol, self-assembled into a monolayer on 2-nm gold particles, occurred at least two and three times faster than in solution, respectively. Although the authors did not discuss the mechanism of this phenomenon, it might be due to the steric confinement and cooperativity effects in self-assembled monolayers. Apparently, nanoparticle surface curvature allowed photoisomerization. At the same time, one can expect sterically confined monolayers on the facets of the small particles. Isomerization might have started on the edges, where azobenzenes had enough spatial freedom, following by cooperative and therefore accelerated switching of the densely packed monolayers. Similar mechanism was described in Ref. 51.

Azobenzene photoisomerization was investigated in a confined environment within gold nanoparticle aggregates.[189] Dialkylsulfide with incorporated azobenzene (4-butyl-4'-(11-dodecylthioundecyloxy)-azobenzene) chemisorbed on 33-nm citrate-stabilized gold nanoparticles with plasmon resonance at 530 nm in the extinction spectra. The alkyl branch served for the dilution of the formed SAM to assure its photoactivity. Stabilizing citrate ions were displaced upon the ligand adsorption. Therefore, the addition of azobenzene ligand induced gold nanoparticle aggregation in water-ethanol mixture, manifested by the appearance of surface plasmon coupling band at around 780 nm in the UV-Vis spectra. SERS spectrum indicated trans- azobenzene isomers in the aggregates of functionalized nanoparticles. The aggregates were then exposed to UV light, and trans-cis isomerization of azobenzene ligands took place. The resulting further red shift of surface plasmon coupling band to 830 nm, and the increase in SERS intensity, revealed nanoparticle nearing, explained by increased dipole-dipole interactions between adsorbed azobenzene ligands on their surfaces. However, trans-cis isomerization of confined azobenzene molecules in the aggregates occurred less effective than in solution, consistent with steric hindrance effects. Thermal back isomerization from cis- to trans-state was found to proceed 15 times faster in the nanoparticle aggregates than in dichloromethane solution. This was rationalized by the registered by SERS weakening of the N=N bond of cis-isomers due to their interactions with neighbouring gold nanoparticles in the aggregates, and the thus facilitated rotation mechanism of cis-trans isomerization.

In fact, two factors may cause accelerated azobenzene switching on metal nanoparticle surfaces: confined environment and electron transfer. In the earlier works above,[60,189] it is impossible to distinguish between them. In Ref. 189 azo bond weakening was not assigned to the electron transfer.

1.5.2. **Thermal cis-trans isomerization of azobenzenes in solution in the presence of gold nanoparticles**

In 2013 Hallett-Tapley *et al.*[190] first reported on gold-enhanced thermal isomerization of azobenzenes not attached to gold nanoparticle surface and hypothesized an electron-transfer mechanism of cis-trans isomerization. Since this is apparently the only external work at least hypothesizing the mechanism of the fast thermal isomerization in the presence of gold nanoparticles, it deserves specification.

Spherical gold nanoparticles of around 12 nm in diameter have been prepared photochemically and post-treated with laser ablation to improve their size and shape distribution. The particles resulting from the photochemical synthesis were ''pseudo-naked'' without organic stabilizers, with negatively charged chloride ions on surface. Nanoparticles slightly aggregated within 3 days after preparation and that's why they were filtered shortly before use.

A small amount of gold colloid added to UV-irradiated azobenzene aqueous solutions triggered their fast spontaneous cis-trans isomerization in the dark, detected by absorption spectra. In the absence of gold nanoparticles, azobenzene isomerization was not detected on the same timescale of 30 minutes. Because of low concentration of gold, plasmon peak was not visible in the spectra. In fact, azobenzene aqueous solutions contained a low amount of acetonitrile, because concentrated acetonitrile solutions were diluted with water. Isomerization rates were calculated from the exponential fit of the absorption at the maximum wavelength of trans-isomers as a function of time, applying a first-order kinetic model. Contribution of the residual cis-isomer was subtracted from absorption spectra prior to data analysis.

Experiments with higher concentrations of gold nanoparticles revealed their colloidal stability during experiments. Isomerization rate nonlinearly increased with gold concentration. Assuming higher binding affinity to gold for trans-isomers, due to the larger dipole moment of cis-isomers and their better solubility in water, the non-linear trend was rationalized by the binding competition between reactants (cis-isomers) and products (trans-isomers) for active surface sites.

Nanoparticles from different batches showed different catalytic activities, attributed to different physico-chemical properties, such as surface chemistry and number of active sites. This implied that the interaction with gold surface actively contributes into the azobenzene isomerization mechanism. Authors mentioned that gold nanoparticles likely act as electron storage, similar to the catalysis of redox reactions.

Para-substitution of the azobenzene unit appeared to impact the rate of the enhanced cis–trans thermal isomerization. Symmetrically substituted dichloro- and dimethylazobenzene isomerized around 2 times slower than parental unsubstituted molecules, while unsymmetrical substitution (4-methoxyazobenzene) led to up to 4.5 times higher isomerization rates. Such activity row is unexpected in the context of electronic substitution effects, but was correlated with dipole moment consideration: methoxyazobenzene has the strongest dipole moment and shows the fastest isomerization.

The authors speculated that the isomerization mechanism might be the electron transfer between azobenzene moieties and gold surfaces, facilitated in the case of more polar molecules due to their stronger binding to nanoparticle surfaces. According to the proposed scheme, the electron transfer from a cis-azobenzene unit to a gold surface would result in a cis-azobenzene cation radical formation with the weakened N=N bond ($N\text{-}N^{\cdot +}$ with one electron pair and an electron-hole pair, instead of N::N). In such intermediate state rotation around the N-N bond is promoted, and trans-azobenzene cation is formed. More polar molecules more likely remain near the gold surface, and electron transfer from gold to trans-azobenzene cation happens, filling the hole on N-N bond. As a result, neutral trans-azobenzene forms. However, no evidence for this hypothesis was given.

It is intriguing that the hypothesized by Hallett-Tapley *et. al.*[190] electron transfer from azobenzene to gold surface can be interpreted as hole transfer from gold surface to azobenzene group, which was suggested by Wolf and Tegeder[52] to be the mechanism behind the photoisomerization of azobenzene adsorbed on gold surface. In both studies, isomerization in a charged cationic state is proposed.

Haag *et. al.*[191] investigated photoswitches on planar gold surfaces and gold nanoparticles. Bulkiness of host-guest ligands assured effective photoswitching of incorporated azobenzene units from trans- to cis- conformation in UV light. Photoswitching on gold surfaces occurred as fast as in solution. Thermal isomerization rates were calculated from first-order exponential fits of absorption maximum (at 360 nm), and half-lives of azobenzene cis-isomers have been compared in different systems. Free azobenzene containing ligands isomerized slowly in aqueous solution. Thermal isomerization rate significantly increased for the host-guest complex in water, explained by reduced solvophobic effects. Water stabilized free cis-isomers, but the interaction was weakened by the inclusion of the azobenzene containing "guests" into "hosts". Thermal isomerization was further accelerated by around 15 times on gold nanoparticle surface. On planar gold surfaces, isomerization rates were similar to the values in solution despite another interface (air). Authors mentioned two mechanisms of the catalysis of azobenzene thermal isomerization on gold nanoparticles without preference and discussion: the electron transfer hypothesized by Hallett-Tapley *et. al.*[190] and enhanced dissipation of electron-hole pairs due to plasmon resonance of gold nanoparticles. Notably, in this work, host-guest chemistry makes the direct proximity of the azobenzene group to gold surface improbable.

Simoncelli and Aramendia[192] in 2015 reported on the accelerated kinetics of the thermal cis-trans isomerization of a number of para-substituted azobenzenes in gold nanoparticle colloids, extending the earlier findings of Hallett-Tapley and co-authors. Gold nanoparticles were synthesized photochemically and coated with silica shell. Initial particles were "semi-naked" and highly monodisperse with a diameter of around 15 nm, silica shell thickness varied from around 2.7 to 15 nm.

A small amount of azobenzene acetonitrile solution was added to gold nanoparticles in water or water-acetonitrile mixture (acetonitrile:water 5:1). The thermal isomerization kinetics after UV irradiation was detected in azobenzene solutions with and without gold particles using absorption spectroscopy. The kinetics followed the first order, isomerization rates were determined from monoexponential fit of trans- absorption maximum intensity as a function of time. The highest acceleration factor was found for unsubstituted azobenzene and methoxyazobenzene in gold aqueous colloids, in fact reproducing the results of Hallett-Tapley *et. al.* Symmetrically substituted dimethyl-, dichloro-, and diethoxyazobenzenes showed intermediate isomerization rates in gold water-acetonitrile colloids. Nitro-substituted azobenzenes (electron-acceptor group) had the lowest acceleration factors in water-acetonitrile mixture.

Authors relied on the rotation mechanism with N=N bond weakening revealed earlier by Yoon and Yoon[189] without specific proposals. As mentioned earlier by Hallett-Tapley *et. al.*, substitution effects cannot explain the higher thermal isomerization rate of methoxyazobenzene compared to symmetrically substituted molecules. Authors discussed the influence of acetonitrile presence in the solvent, which in this work was apparently higher than in the report by Hallett-Tapley *et. al.* Acetonitrile can adsorb to gold surface and thus compete with azobenzene molecules for gold surface adsorption sites, what in turn can decrease the thermal isomerization acceleration factor in water-acetonitrile mixture compared to water.

The decrease in the acceleration factor upon NO_2-substitution was explained in a similar way by a competition between NO_2 groups and azo-moieties for gold surface sites. Further, pH in gold colloid is acidic in the work of Hallett-Tapley and slightly acidic in the work of Simoncelli and Aramendia due to preparation method. The effect of pH was examined in the absence of gold nanoparticles, to exclude the increase in isomerization rate resulting from pH decrease in azobenzene solution upon gold addition. For 4-nitro-4′-dimethylaminoazobenzene, 4-(4′-nitrophenylazo)phenol and 4-[4-(dimethylamino)phenylazo]benzoic acid N-succinimidyl ester the catalytic performance of gold nanoparticles was masked by pH changes.

Experiments with different concentrations of gold showed that the kinetic rate depends on azobenzene/gold molar ratio and particularly on the proportion of azobenzene molecules associated with gold surface.

Citrate-stabilized 15-nm gold nanoparticles were functionalized with polyvinylpyrrolidone, selectively binding to (100) facets. Such polymer-functionalized particles exhibited worse catalytic performance than non-functionalized particles. Authors suggested that (100) facets are the catalytic active sites.

Gold nanoparticles with thin silica shell had even lower activity than polymer-coated particles, compared in ethanolic solutions. This further supported the surface nature of the gold-mediated catalysis. With thick silica shell, two-order kinetics occurred, rationalized by diffusion of azobenzene molecules through silica shell to reach the active gold surface. The estimated diffusion coefficient of azobenzene in porous silica was significantly smaller than in water and increased with silica thickness.

When Hallett-Tapley and co-authors published their results on the ability of gold nanoparticles to accelerate thermal cis-trans isomerization of small azobenzene derivatives, I was already investigating on the thermal cis-trans isomerization of azobenzene containing surfactants enhanced by gold nanoparticles. These experimental results, partially reported in Ref. 193, developed into a part of the current thesis and will be discussed in the corresponding chapters.

2. Objectives

The topic of this thesis stems from the research attempt of our group to introduce plasmonic and photoswitching properties to negatively charged polymer brushes. The recipe is loading them with the complexes between plasmonic nanoparticles and photosensitive azobenzene surfactants. The relationship between the properties of nanoparticle-surfactant systems, nature of nanoparticles, surfactant structures, and experimental conditions, appeared to be complex and required an independent study. Further modification of polymer brushes and DNA molecules in solution with the explored nanoparticle-surfactant complexes has been successfully performed, but the obtained results are beyond the scope of this thesis.

The main objective of my work was the study of the complexes between plasmonic nanoparticles and photosensitive azobenzene containing cationic surfactants in aqueous environments.

For that, characterization of the optical properties and surface potential of plasmonic nanoparticles of different sizes, shapes and compositions was required, which became the first objective.

The second objective was the formation and investigation of the complexes between trans-isomers of azobenzene containing surfactants and plasmonic nanoparticles. This included (i) finding the conditions for complex formation in water, (ii) characterization of physical properties of the complexes, particularly plasmon resonance wavelength, (iii) revealing the constitution of the complexes between spherical gold nanoparticles and azobenzene containing surfactant self-assembled at different conditions.

The important third objective of my work was the investigation of the azobenzene trans-cis photoinduced isomerization in complexes with plasmonic nanoparticles, and the influence of light irradiation on their physical properties. Light response of the complexes between azobenzene containing surfactant and gold, silver, and silicon spherical nanoparticles was studied.

The fourth objective was to study the interaction between cis-isomers of azobenzene containing surfactants and spherical metal nanoparticles. For that, thermal cis-trans isomerization of a series of azobenzene compounds differing by chemical composition, particularly the structure of their charged groups and tail lengths, was to be explored in the dark in the presence of gold, silver, palladium, silicon, and alloy gold-silver and gold-palladium spherical nanoparticles.

Finally, reversible changes in surface plasmon resonance wavelength of gold nanorods in complexes with azobenzene containing surfactants of different length were to be studied upon their trans-cis photoswitching.

3. Materials and methods

3.1.Azobenzene containing compounds

Azobenzene containing trimethyl- and triethylammoniumbromide surfactants with varied number (*n*) of CH_2-groups in the spacer between azobenzene unit and cationic head, and azobenzene containing polyamines with varied number of amine groups in the head, were synthesized following the procedures, reported in Ref. 194, 195 with slight modifications by Dr. Nino Lomadze at the University of Potsdam. Azobenzene containing peptidomimetic (Azo-PM) was synthesized in the group of Prof. Dr. Laura Hartmann in Max-Planck Institute of Colloids and Surfaces in Potsdam as described in Ref. 196. The chemical structures of studied azobenzenes are shown in **Figure 3.1**. The substances were dissolved in water (MilliQ) to prepare solutions. 4-Nitroazobenzene was purchased from "Sigma Aldrich" and dissolved in methanol. All compounds were stored in the dark at room temperature.

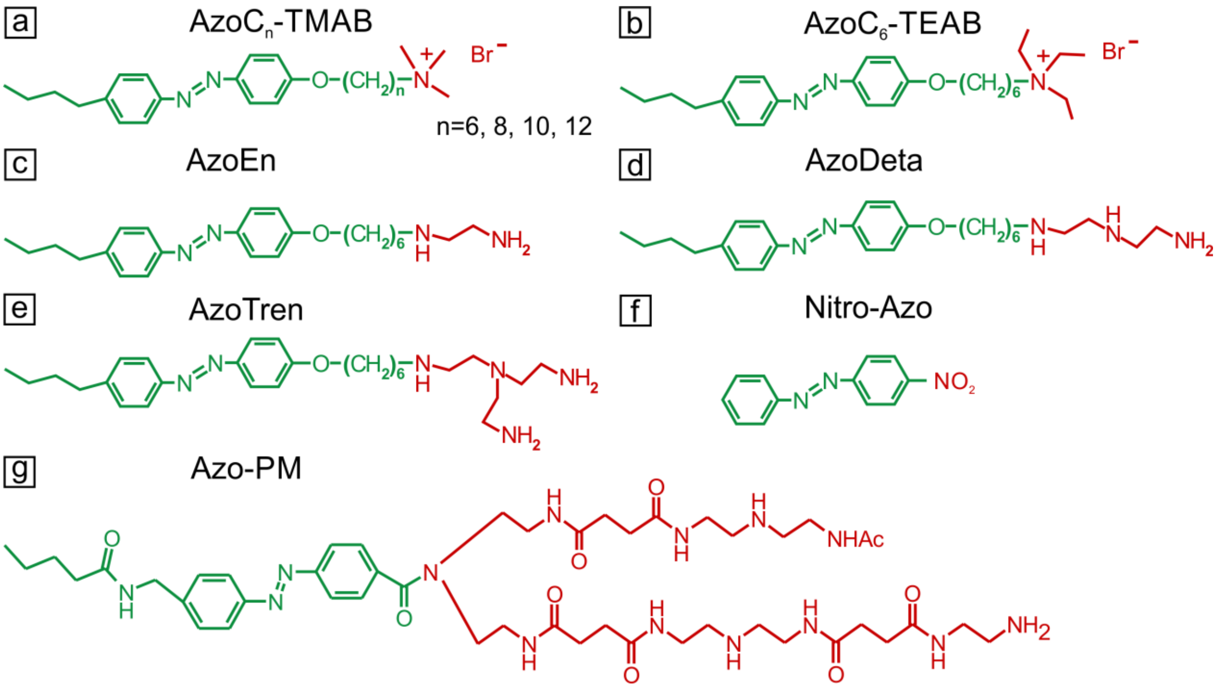

Figure 3.1. Chemical structures and short names of azobenzene containing compounds: (a) trimetylammoniumbromide surfactants with *n* CH_2- groups in the spacer between the azobenzene unit and the cationic head (red); (b) triethylammoniumbromide surfactant with 6 CH_2- groups in the spacer; (c e) polyamines with different number of amine groups in the head and the same tail containing 6 CH_2- groups in the spacer; (f) 4-nitroazobenzene; (g) azobenzene containing peptidomimetic.

Azobenzene surfactants with structure (a) in **Figure 3.1** were in the center of the present study. The short names $AzoC_n$ were used for them (n = 6, 8, 10, 12). The working horse was the surfactant $AzoC_6$ with trimetylammonium head and 6 CH_2- groups in the spacer between the positively charged head and azobenzene moiety in the hydrophobic tail.

Initial azobenzene solutions were diluted to appropriate concentrations. Critical micelle concentration (CMC) of azobenzene containing surfactants was determined earlier in our group.[5,20] For instance, for $AzoC_6$ surfactant in water CMC is 0.5 mM at room temperature. In the current study, working concentrations of azobenzenes did not exceed their CMC. Concentrated solutions of azobenzene containing ammoniumbromide surfactants had basic pH up to pH = 9.2, while the solutions diluted to working concentrations exhibited slightly basic $pH \approx 7.5 \pm 0.3$. Azobenzene containing polyamine surfactants acquire positive charge depending on the pH of the medium. This effect will be highlighted later in the corresponding chapter. In concentrated stock solutions of azobenzene containing polyamines, pH was set to $pH \approx 5.0$ by adding HCl, in order to assure the protonation of amine groups. Under working conditions, pH of diluted azobenzene polyamine solutions was almost neutral ($pH \approx 6.5 \pm 0.2$).

Based on absorption spectra analysis,[5] 88 % of $AzoC_6$ cis-isomers and 67 % of trans-isomers occur in solution in photostationary states after exposure to UV and blue light sources, respectively. The long lifetime of $AzoC_6$ cis-isomer in water $\tau_0 = 62$ hours[193] allows for its controlled photoisomerization. Extinction properties and cis-trans thermal relaxation kinetics of other ammoniumbromide surfactants and azobenzene containing polyamines (**Figure 3.1**. **a – e**) are similar to those of $AzoC_6$, due to the same ring substitution pattern of the azobenzene unit. Stored in the dark, solutions of azobenzenes contain molecules in trans-conformation, although a small amount of cis-isomers is present in the dark photostationary state too due to thermodynamic equilibrium. Solutions of all studied azobenzenes have yellow color.

3.2.Laser-ablated nanoparticles

Aqueous colloidal solutions of gold, silver, palladium, silicon, as well as alloy gold-silver and gold-palladium spherical nanoparticles were prepared in the group of Prof. Dr. Andrei Kabashin (Aix Marseille University, France) by Dr. Yuri Ryabchikov and Dr. Ksenia Maximova using the methods of femtosecond laser ablation in aqueous solution[197,198], and in some cases fragmentation[199,200,201] in order to obtain a more homogeneous size distribution of nanoparticles. Silver nanoparticles (AgNP) were represented by two batches, produced by Dr. Ryabchikov in Aix Marseille University (France) and by Dr. Kucherik in Vladimir State University (Russia) following a similar procedure of laser ablation in aqueous media. Briefly, in the method of laser ablation a target is irradiated in liquid environment with a focused laser beam. Nanoclusters are released into liquid, forming nanoparticle colloid.

To prepare gold nanoparticles (AuNP) of 10 and 25 nm in diameter, a gold disk was placed on the bottom of a glass vessel with deionized water and ablated with focused Yb:KGW femtosecond laser (Amplitude Systems [Pessac, France], 1025 nm, 480 fs, 500 mJ, 1–5 kHz). Resulting aqueous nanoparticle colloids had dark red color. Gold nanoparticles with two different sizes were studied, but 10-nm diameter gold nanoparticles were the main object of the study. The chemical analysis reported in the Ref. 202 showed partial oxidation of gold nanoparticles prepared by laser ablation, with 88.7 % Au^0, 6.6 % Au^+, and 4.7 % Au^{3+}. The following hydroxylation of nanoparticle oxidized surface leads to obtaining strong negative charge:

$$\text{Au-O-Au} + \text{OH}^- \rightarrow \text{Au-OH} + \text{Au-O}^-$$

The -OH groups were found to be in equilibrium with -O$^-$, with their ratio depending on the pH value of the environment. Under the used experimental conditions (pH>6) gold nanoparticle surface is expected to consist of Au-O$^-$ groups. This results in the high stability of the bare nanoparticle colloids.

Similar to gold nanoparticles, silver nanoparticle (AgNP) colloids were prepared by direct 800-nm wavelength femtosecond laser ablation of a cleansed solid-state silver target in deionized water with preliminary argon bubbling. Palladium nanoparticles (PdNP) were prepared following a similar protocol. Resulting AgNP colloids obtained yellow color, PdNP colloids exhibited grey color.

To prepare metal alloy nanoparticles, laser ablated gold nanoparticle colloid was mixed with silver or palladium nanoparticle colloids at 1:1 volume ratio. Concentrations of the mixed colloids were as follows: 60 mg/ml AgNP, 130 mg/ml PdNP, 100 mg/ml AuNP. The Au-Ag and Au-Pd nanoparticle mixtures were exposed to a femtosecond laser beam for fragmentation for 1 hour in the atmosphere of He or Ar passed through suspensions. Aqueous colloids of alloy gold-silver (AuAgNP) and gold-palladium (AuPdNP) nanoparticles had orange and brown colors, respectively.

Silicon nanoparticles (SiNP) were prepared by the method of femtosecond laser fragmentation of silicon powder dispersed in deionized water. Before exposure to the laser beam, suspension was sonicated for 30 minutes. Colloids were prepared following three different protocols: at ambient conditions with stirring during the fragmentation process (SiNP), and without stirring with simultaneous argon (two batches: SiNP-Ar, SiNP-Ar II) or helium (SiNP-He) bubbling to attenuate particle surface oxidation. Resulting colloids had orange reddish color. Precipitation formed in SiNP, SiNP-He and SiNP-ArII colloids and they were filtered through a 100-nm filter.

Nanoparticle aqueous suspensions were stored in the dark at 4 °C. Molar concentrations of gold, silver and silicon nanoparticles were calculated by dividing mass concentration by element atomic weight.

The properties of different nanoparticles will be discussed in details in the corresponding chapters below.

3.3. Gold nanorods

Gold nanorods have been fabricated using a seeded growth method by Qianling Cui in the group of Prof. Bargheer at the University of Potsdam, following the procedure in Ref. 203 with modifications. Gold nanorods AuNR-CTAB were stabilized with the shell of CTAB surfactant. AuNR-Si1, AuNR-Si2, AuNR-Si3 represent three batches of gold nanorods capped with a thin layer of porous silica.

3.4. Methods

Experiments were carried out at room temperature in yellow light in order to avoid uncontrollable photoisomerization of azobenzenes.

Before preparation of complexes with azobenzenes, colloids were sonicated for 10 – 30 min to destroy possible aggregates.

Unless specified in the text, the complexes between nanoparticles and azobenzene-containing surfactant trans- isomers (Chapter 4, 5) have been prepared in yellow light by mixing aqueous surfactant solutions and nanoparticle suspensions at certain concentrations. Complexes were equilibrated for 30 min at room temperature before measurements.

To study nanoparticle catalytical properties (Chapter 6, 7), a droplet of non-diluted nanoparticle aqueous suspension was added into a quartz cuvette filled with UV-irradiated azobenzene solution of certain concentration, the components were mixed remaining in UV light. UV-Vis absorption spectra of the surfactant-nanoparticle mixture were recorded immediately at room temperature in dark without equilibration. The time tolerance up to 5 s is possible, due to manually placing the cuvette into spectrophotometer.

Cis-trans photoisomerization of azobenzenes was triggered using UV lamp VL-4.L (Vilber Lourmat, Marne-la-Valle´e, France) with 365 nm wavelength and blue-light lamp LED Spot Luxeon Royal Blue, P453E-PR09 (Conrad Electronic, Hirschau, Germany) with 453 nm wavelength. Exposure for 10 minutes is sufficient to reach equilibrium photostationary state.

Absorption spectra were recorded using a Cary 5000 UV-vis-NIR spectrophotometer (Varian Inc., Palo Alto, CA) in quartz cuvettes with optical pathways of 1, 2, 5, and 10 mm. If not specified in the text, optical pathway was 10 mm. Data fitting was implemented in OriginPro 8.1G software. In one experiment in Chapter 8 (specified in the text) absorption spectra were recorded using UV-Vis spectrophotometer Lambda 16 (Perkin Elmer).

The ζ-potential and dynamic light scattering (DLS) studies were performed with a Zetasizer Nano ZS system (Malvern Instruments Ltd., Malvern, U.K.) at a scattering angle of 173°. Incident light from a He-Ne laser has the wavelength 633 nm.

Electron micrographs were collected using transmission electron microscopes (TEM) JEM-1011, JEM-2011, JEM-2100, JEM-3010 (JEOL Ltd., Tokyo, Japan) and Ultra Plus scanning electron microscope (SEM) (Carl Zeiss, Oberkochen, Germany). TEMs were operated by Dr. Claudia Prietzel, Dr. Yuriy Ryabchikov, Dr. Ksenia Maximova, Dr. Zdravko Kochovski in collaborating groups at the University of Potsdam, Aix Marseille University, and Humboldt University in Berlin. Scanning electron microscope (SEM) was operated by Dr. Alexey Kopyshev in our group. TEM JEM-2011 (JEOL Ltd., Tokyo, Japan) equipped with Energy Dispersive X-ray spectroscopy was operated by Dr. Yuriy Ryabchikov at Aix Marseille University to determine chemical composition of alloy gold-palladium nanoparticles.

To prepare the TEM samples, a droplet of freshly prepared aqueous nanoparticle or nanoparticle-surfactant suspension was placed on a carbon-coated copper grid and dried at ambient conditions.

Cryo-EM was performed with a TEM JEM-2100 (JEOL Ltd., Tokyo, Japan) operated at 200 keV (LaB6 cathode) by Dr. Zdravko Kochovski at Humboldt University in Berlin. To prepare the samples, a droplet of freshly prepared gold nanoparticle-surfactant aqueous suspension was pipetted on a glow-discharged Lacey Carbon Copper Grid (Plano GmbH, Wetzlar, Germany) and plunge frozen into liquid ethane with an FEI Vitrobot Mark IV (FEI, Eindhoven, Netherlands).

Calculation of nanoparticle size distribution was performed by the means of Image J software. TEM micrographs of spherical nanoparticles partially have been processed by the author. TEM analysis of gold nanorods has been fully done by the author.

Centrifugation was performed at room temperature, using centrifuge ROTOFIX 32 A (Hettich Zentrifugen, Germany) with the swing-out rotor Nr. 1619 at 4000 revolutions per minute (relative centrifugal force RCF = 2701).

Photographs were processed in Adobe Photoshop and Corel Draw software without colour modifications.

4. Interaction of gold nanoparticles with azobenzene containing surfactants in trans-conformation

This chapter describes the complexes between laser ablated gold nanoparticles of 10 and 25 nm diameter and azobenzene containing cationic surfactant AzoC$_6$. The results for 10-nm particles were partly published in Ref. 204.

4.1.Azobenzene containing surfactant

Chemical structure of the AzoC$_6$ surfactant is shown in the experimental part (**Figure 3.1a**). In **Figure 4.1** one can see absorption spectra of aqueous solution of azobenzene containing surfactant AzoC$_6$ in cis- and trans-conformation. Surfactant in trans-state has the characteristic absorption peak at λ = 353 nm. This peak results from π-π* transitions of the azobenzene unit and blue-shifts towards 315 nm upon trans-cis isomerization. In cis-conformation one more peak appears at λ = 437 nm with respect to n-π* transitions in azobenzene unit. The third absorption peak in UV range is related to the absorption of the π-conjugated benzene rings and therefore does not shift significantly upon isomerization, remaining at about 240 nm for both isomers.

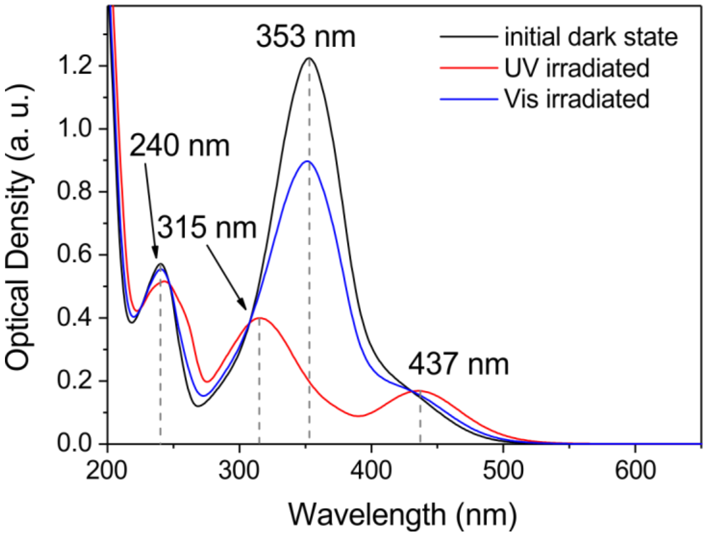

Figure 4.1. Absorption spectra of azobenzene containing trimethylammoniumbromide suractant AzoC$_6$.in dark state, after UV irradiation and subsequent blue light irradiation. In dark state (black curve) surfactant molecules are in predominantly trans-conformation, UV light irradiation (red curve) induces isomerization into predominantly cis-conformation, subsequent irradiation with blue light (blue curve) initiates re-isomerization into trans-conformation. C_{Azo} = 0.055 mM.

4.2.Properties of gold nanoparticles

Absorption spectra of gold nanoparticles, their TEM micrograph and size distribution are shown in **Figure 4.2 and Figure 4.3**. Mean diameters of the solid spherical gold particles are d = 9 ± 3 nm and d = 25 ± 5 nm.

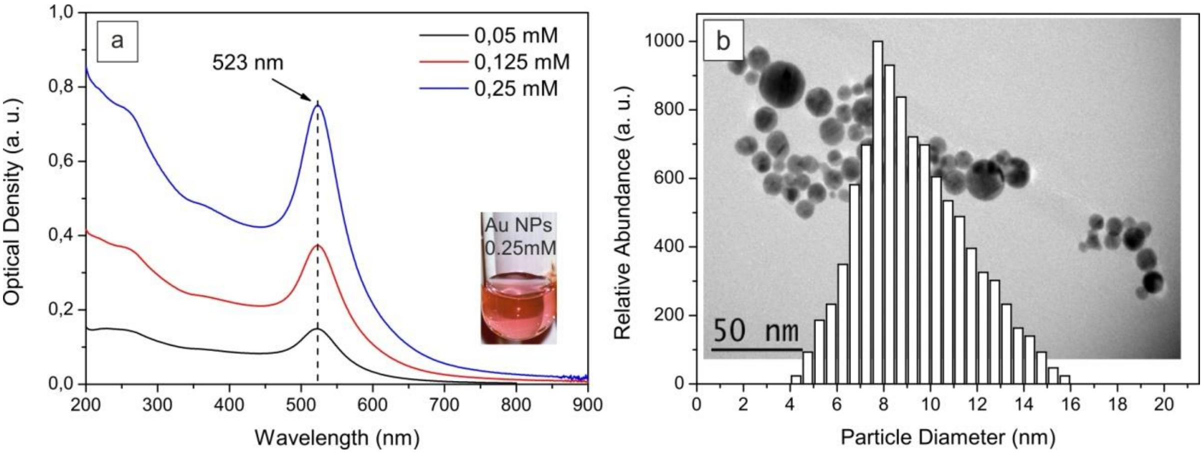

Figure 4.2. (a) UV-Vis absorption spectra of 10-nm laser ablated gold nanoparticles at three different molar concentrations (listed in the legend). The inset shows the photo of gold nanoparticle colloid at the molar concentration $C_{Au} = 0.25$mM, demonstrating its pink color. (b) Size distribution of the 10-nm gold nanoparticles with a TEM micrograph placed to the background.

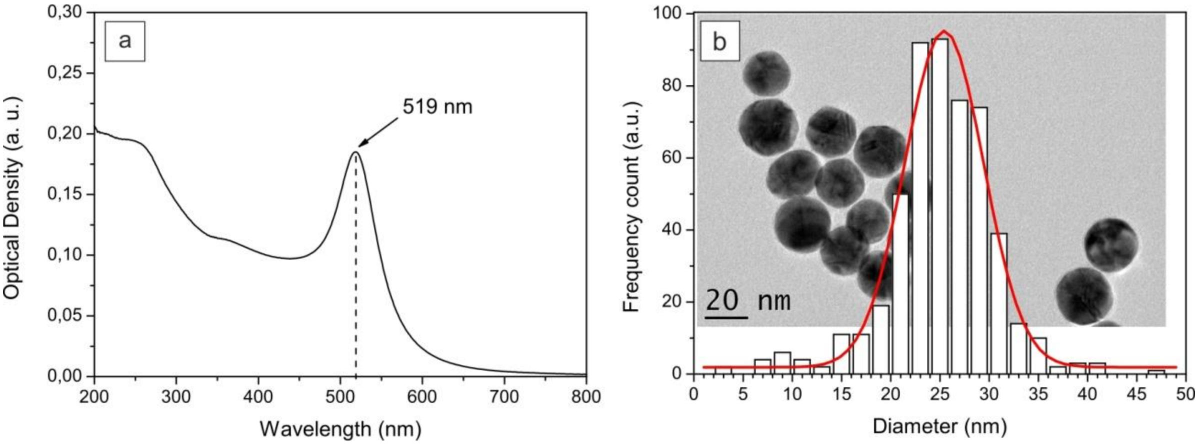

Figure 4.3. (a) UV-Vis absorption spectrum of laser ablated 25-nm gold nanoparticles in water at $C_{Au} = 0.06$ mM . (b) TEM micrograph of the 25-nm gold nanoparticles, with the superimposed histogram of the size distribution of the particles.

Gold nanoparticles with 10-nm diameter have plasmon absorption peak at $\lambda = 523$ nm. Gold aqueous colloid has pink color. The unexpected plasmon peak position at 519 nm for 25-nm particles can be explained by the lognormal size distribution, with the more pronounced fraction of bigger particles in 10-nm particle colloid. By recording absorption spectra of gold nanoparticles at different molar concentrations (**Figure 4.2a and Figure 4.4a**) one can determine their extinction coefficient. In **Figure 4.4a** the spectra correspond to another batch of 10-nm gold particles, with TEM mean diameter $d = 10 \pm 2$ nm. From the slope of the linear fit of the absorption maximum versus gold molar concentration (**Figure 4.4b**), extinction coefficient of 10-nm gold nanoparticles is around 3000 l·mol^{-}1·cm^{-1}. ζ-potential of 10-nm gold nanoparticles in water is around -30 mV.

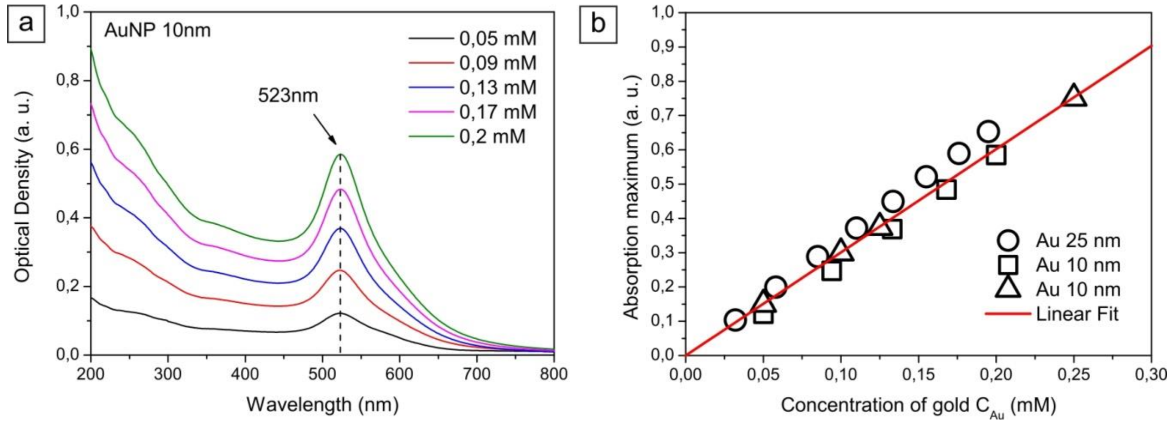

Figure 4.4. (a) UV-Vis absorption spectra of laser ablated gold nanoparticles with mean diameter of 10 nm in water at different molar concentrations of gold atoms, listed in the legend. Optical path is 1 cm. (b) Optical density in UV-Vis absorption maximum of gold nanoparticles versus gold molar concentration. Symbols show values for 25-nm gold particles and two batches of 10-nm gold particles. Red line represents the linear fit.

It is well known that plasmon wavelength is sensitive to the distance between nanoparticles. The distance between the charged particles can be controlled by tuning their electrostatic repulsion, for instance, via the addition of a simple salt to a nanoparticle colloid. **Figure 4.5a** shows absorption spectra of 10-nm gold nanoparticles in water and in sodium chloride aqueous solution at two different molar concentrations, *i. e.* in different ionic strengths. In this case nanoparticle Debye length λ_D (the thickness of the electrical double layer around a nanoparticle) can be estimated as follows:[205]

$$\lambda_D = 0.304/\sqrt{[NaCl]}$$

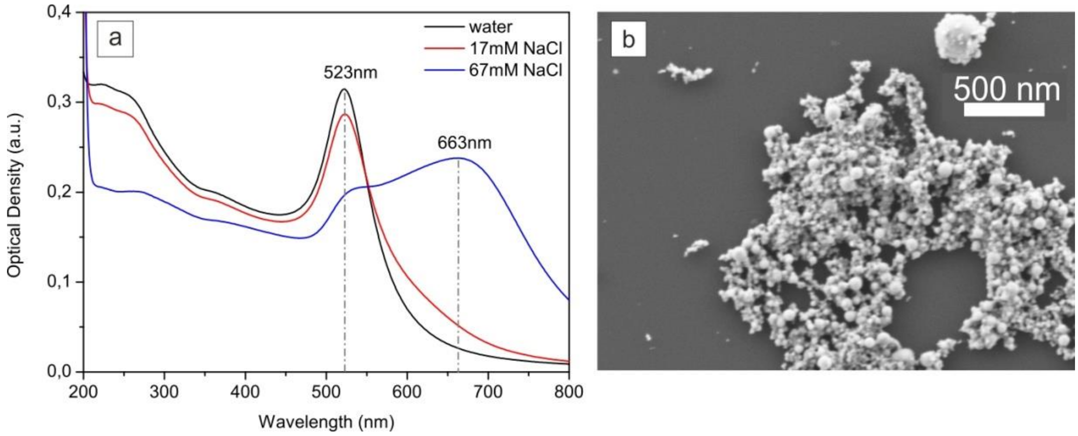

Figure 4.5. (a) UV-Vis absorption spectra of 10-nm gold nanoparticles at $C_{Au} = 0.2$ mM in different ionic strengths, listed in the legend. (b) SEM micrograph of the aggregated 10-nm gold nanoparticles in 67 mM NaCl.

In 17 mM NaCl (red curve in **Figure 4.5a**) the intensity of the peak at 523 nm slightly decreases and a second absorption peak at $\lambda > 600$ nm appears. Counterions of salt inhibit electrostatic repulsion between nanoparticles, but nanoparticle surface charge is not neutralized, $\lambda_D = 2.33$ nm. When the Debye length is twice shorter, $\lambda_D = 1.17$ nm in 67 mM NaCl (blue curve), the plasmon peak initially located at 523 nm red-shifts, its intensity significantly decreases, and the second absorption peak located at 663 nm becomes main absorption maximum. The broad second absorption peak originates from the collective oscillations of electrons in nanoparticle aggregates. Indeed, ζ -potential of the particles in 67 mM NaCl turns zero, suspension is unstable, and electron microscopy (**Figure 4.5b**) shows big aggregates.

4.3.Molar ratio σ.

To characterize the complexes between the gold particles and photosensitive surfactant we introduce a molar ratio σ as the amount of the photosensitive surfactant molecules in relation to one gold atom on the surface of a nanoparticle. Eventually, the molar ratio σ reflects charge properties of the complexes between gold nanoparticles and azobenzene containing cationic surfactant.

Scheme 4.1 displays the assumptions made in the σ determination. A spherical gold nanoparticle of radius R is composed by homogeneously distributed N spherical gold atoms of diameter $d_{Au} \approx 0.28$ nm (covalent atomic radius of gold is around 0.14 nm). Negatively charged surface of a nanoparticle is represented by a spherical layer of thickness $dR = d_{Au}$ containing dN^-negatively charged gold atoms. Assuming that every gold atom on a surface carries negative charge -1, and every molecule of azobenzene containing cationic surfactant carries charge +1, molar ratio σ is the charge ratio between the surfactant and gold particles. The introduced molar ratio σ does not take into account crystalline structure of nanoparticles, lattice constant and the percentage of oxidized gold atoms on the surface of nanoparticles which are responsible for the negative charge of the particles in surfactant solution. Nevertheless, the size distribution of nanoparticles must be the main contribution to inaccuracy in σ.

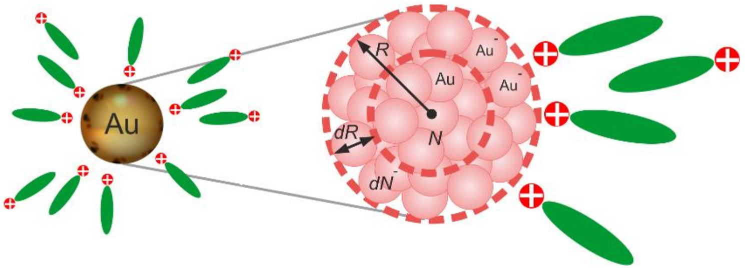

Scheme 4.1. Individual gold nanoparticle in complex with azobenzene containing cationic surfactant.

According to the definition, σ value should be calculated as the ratio between the amount of azobenzene containing cationic surfactant $v(Azo)$ and the amount of surface gold atoms $v(Au^-)$. In the same volume one can turn to the use of molar concentrations of the components in a mixture $C(Azo)$ and $C(Au^-)$:

$$\sigma = \frac{v(Azo)}{v(Au^-)} = \frac{C(Azo)}{C(Au^-)}$$

The concentration of surface gold atoms $C(Au^-)$ can be determined via molar concentration of gold $C(Au)$ and the volume fraction of gold atoms on the surface of a nanoparticle dN^-/N:

$$C(Au^{-}) = C(Au) \cdot \frac{dN^{-}}{N}$$

Amount of atoms in a nanoparticle *N* depends on the size of the nanoparticle, $N \sim R^3$ (R – nanoparticle radius). For instance, *N* can be determined as follows:

$$N = \tfrac{4}{3}\pi R^3 \rho N_A / M \sim R^3 \ ,$$

where $\rho = 19.32$ g/cm^3 is density of gold, $M = 197$ g/mol – molar mass of gold, $N_A = 6.02 \cdot 10^{23}$ mol^{-1}– Avogadro's number.

The amount of atoms within the spherical layer of thickness dR is $dN \sim 3R^2 dR$, and therefore the amount of gold atoms on nanoparticle surface is

$$dN^{-} = \frac{4\pi R^2 \rho N_A d_{Au}}{M} \sim 3R^2 \cdot d_{Au}$$

Finally,

$$\sigma = \frac{C(Azo)}{C(Au)} \cdot \frac{R}{3d_{Au}} \tag{4.1}$$

For 10-nm gold particles $\sigma = \frac{C(Azo)}{C(Au)} \cdot 5.95$, for 25-nm gold particles $\sigma = \frac{C(Azo)}{C(Au)} \cdot 14.88$.

4.4.Gold-surfactant complexes

To prepare the complexes, gold nanoparticle aqueous colloids were mixed with aqueous solution of azobenzene containing surfactant AzoC$_6$, varying concentrations of the components. Absorption bands of azobenzene containing surfactants do not overlap gold plasmon peak, allowing for tracking the spectral changes in the plasmon peak of gold nanoparticles.

Absorption spectra were recorded for several sample lines, differing in concentration of gold nanoparticles $C_{Au} = 0.05\ \ 1$ mM. In every sample line concentration of gold nanoparticles was kept constant, the concentration of the azobenzene containing surfactant AzoC$_6$ was varied. **Figure 4.6** shows the absorption spectra of the gold-surfactant sample line with 10-nm gold nanoparticles at $C_{Au} = 0.2$ mM.

With the increase in surfactant concentration, reversible bathochromic shift in the position of gold nanoparticle surface plasmon peak occurs. The intensity of the peak at 353 nm – characteristic absorption peak of surfactant trans-isomer – increases due to the increase of surfactant concentration. At extremely low concentrations of azobenzene surfactant ($\sigma = 0.002$, black curve in **Figure 4.6**) no changes in spectral properties were detected in comparison to the pure gold nanoparticles in water, single gold plasmon peak was located at 523 nm. At higher surfactant concentrations, this peak red-shifted to 527 nm after gold-surfactant complexes are formed (the process takes 30 min, **Figure 4.7**) due to the change in the refractive index of the medium near the gold particle. At $0.002 < \sigma \leq 0.5$ (magenta, blue and green curves in **Figure 4.6**) the second absorption peak at $\lambda > 600$ nm was observed, along with the decrease in the intensity of the plasmon peak at 527 nm. At $\sigma = 0.15$ (blue curve in **Figure 4.6**) the second plasmon peak located at $\lambda = 700$ nm became the main absorption maximum. However, at σ = 0.5 (green curve in **Figure 4.6**) the additional plasmon peak position reverted to a shorter wavelength and the intensity of the peak at 527 nm significantly increased. At even higher surfactant concentrations the second absorption peak disappeared, a single gold plasmon peak was located at 527 nm (σ = 1.6, red curve in **Figure 4.6**).

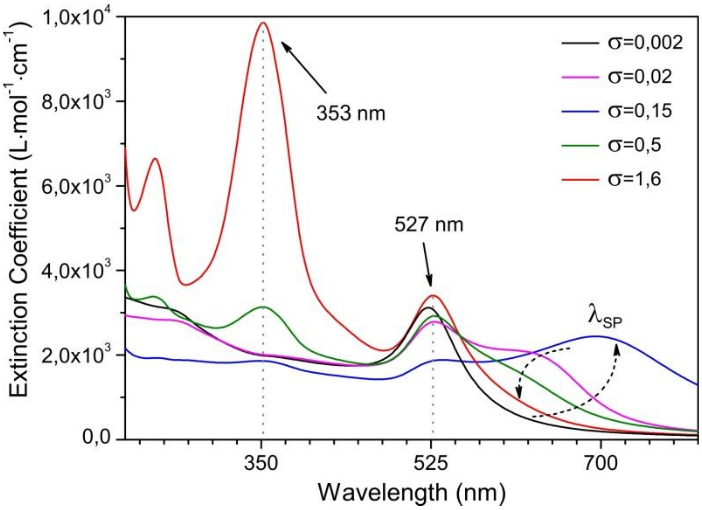

Figure 4.6. UV-Vis absorption spectra of 10-nm gold nanoparticles mixed with azobenzene containing surfactant AzoC$_6$ at different concentrations, σ values are listed in the legend.

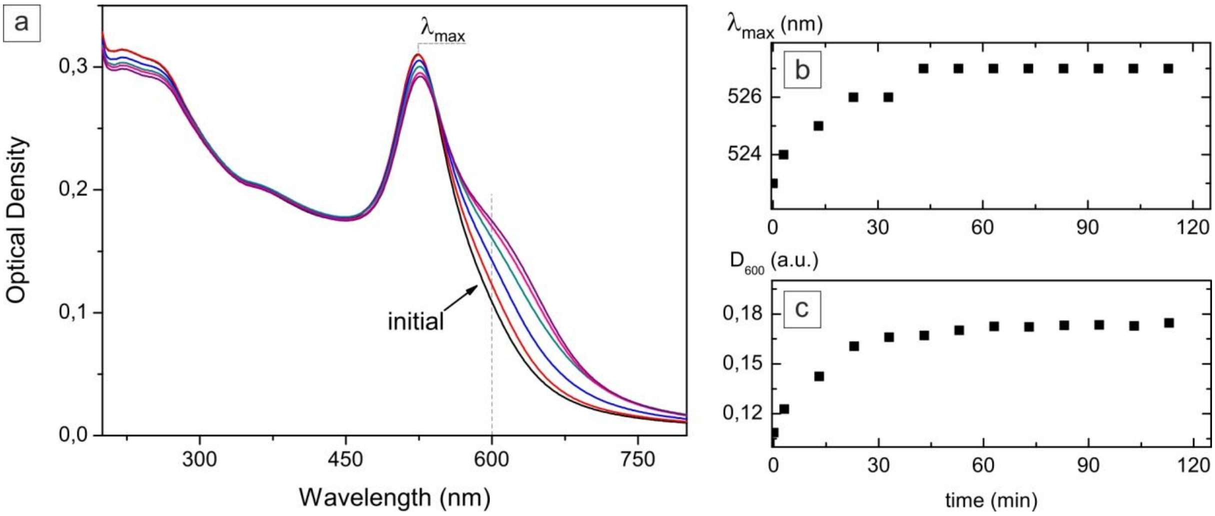

Figure 4.7. Time-dependent absorption spectra of 10-nm gold nanoparticles interacting with azobenzene containing surfactant AzoC$_6$ in trans-conformation at σ = 0.01: periodically recorded UV-Vis absorption spectra (a), time dependence of gold plasmon wavelength (b) and optical density at 600 nm (c). Plasmon peak position is red-shifting from 523 to 527 nm, second absorption peak gradually appears and levels off after 30 minutes.

Changes in plasmonic spectral properties were similar in sample lines with other concentrations of 10-nm and 25-nm gold particles, using AzoC$_6$, AzoTren and Azo-PM surfactants. The results for AzoTren and Azo-PM essentially reproduced those for AzoC$_6$. That's why the comprehensive study of AzoC$_6$ surfactant-mediated nanoaggregation of gold particles is included into the thesis.

4.5.Phase diagram

The red shift of the absorption peak of 10-nm gold nanoparticles in complex with azobenzene surfactant AzoC$_6$ in several sample lines is shown in **Figure 4.8a** as a function of σ. The detected spectral changes are consistent with the changes in the ζ-potential of the gold-surfactant complexes (**Figure 4.8b**) and the color of the nanoparticle suspensions (**Figure 4.8c**).

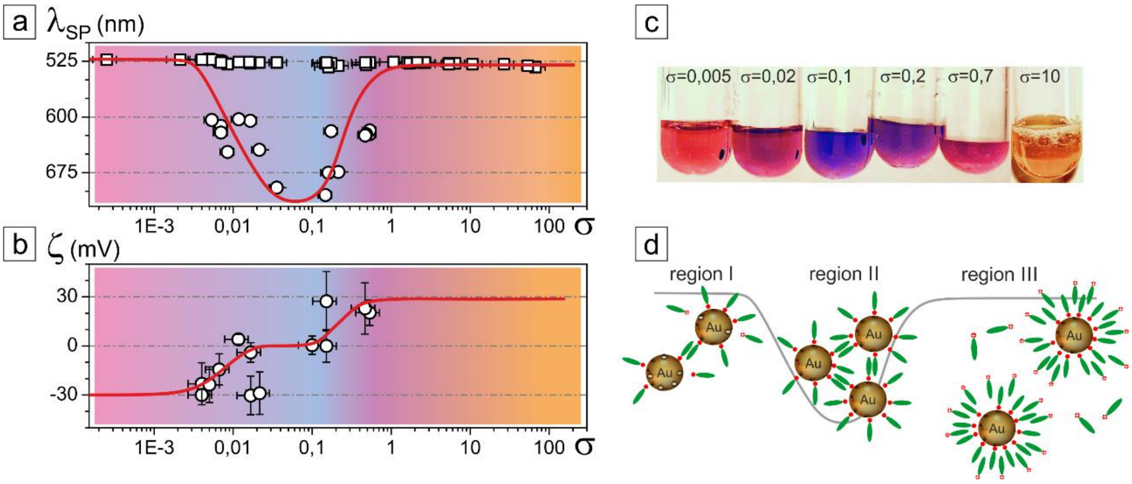

Figure 4.8. (a) Position of the UV-Vis absorption peak of 10-nm gold nanoparticles in complex with azobenzene containing surfactant AzoC$_6$ as a function of σ. The evolution of the gold nanoparticle plasmon peak (initially located at $\lambda = 523$ nm) is shown by open squares. Open circles represent the position of the second absorption peak, occurred at $0.01 \leq \sigma \leq 0.5$ (region II). Red curve serves a visual guideline for the reader. Background shows the drawn color change in the gold-surfactant suspensions. (b) Corresponding changes in the ζ-potential of gold –surfactant complexes with σ. (c) Photo of the six suspensions of 10-nm gold nanoparticles and azobenzene containing surfactant AzoC$_6$, demonstrating the real color change with the value of σ. (d) Schematic representation of speculated configurations of the gold–surfactant complexes in different regions. Positively charged surfactant heads are shown green, azobenzene containing tails are shown red.

Physical properties of the complexes between gold nanoparticles and azobenzene surfactant can be accommodated within three regions depending on σ value (**Figure 4.8**). In region I, at $\sigma<0.01$, no significant spectral changes were observed (single plasmon peak was located at 523 – 527 nm), ζ-potential of the gold-surfactant complexes remained negative, as it would for pure gold nanoparticles, and color of the gold-surfactant suspensions did not differ from the pink color of gold nanoparticles aqueous colloid without surfactant. In region II, at $0.01 \leq \sigma \leq 0.5$, the properties of the gold-surfactant complexes dramatically changed. A second absorption peak was present in the spectra, its position shifted with σ, color of the suspensions changed between violet and blue, and ζ-potential of the complexes turned zero (detected on the borders with large error, because the wavelength of the red laser used as the light source in the light scattering experiment matched the absorption band of the complexes). In region III, at $\sigma > 0.5$, a single plasmon peak was located at 527 nm, and the color of the suspensions had a pink tone similar to region I, while the ζ-potential of the complexes became positive. At very high values of σ gold-surfactant suspensions had orange color, apparently due to pink color of gold-surfactant complexes mingled with the yellow color of highly concentrated surfactant solution.

One can speculate about electrostatic nature of the interaction between azobenzene containing cationic surfactants and negatively charged laser ablated gold nanoparticles. Assuming that 10 % of the gold nanoparticle surface atoms carry negative charge[202], a complete neutralization of the surface charge of gold-surfactant complexes is fulfilled at σ ≈ 0.1. Indeed, in this range of σ values zero ζ-potential (**Figure 4.8b**) implies the neutral surface charge of the gold-surfactant complexes and their colloidal instability. Gold-surfactant suspensions from region II precipitated in around 30 minutes after recording spectra.

In fact, the spectral changes detected in the region II of gold-surfactant complexes are similar to those upon gold particle charge neutralization by counterions of salt without added surfactant (**Figure 4.5**). The broad second plasmon peak in long-wavelength region indicates aggregation in diffusion-limited manner, in agreement with rapid color change. However, the mechanism of gold-surfactant complexes aggregation is driven not only by the inhibited electrostatic repulsion, and likely involves dipole-dipole interactions between surfactant molecules.

Figure 4.8d schematically shows possible configurations of the gold–surfactant complexes in different regions. In region I, surface charge of gold nanoparticles is screened, but remains negative (**Figure 4.8b**), as only few surfactant molecules attached to nanoparticle surface by their cationic heads. In region II surfactant concentration is sufficient to form a shell around the nanoparticles. At σ ≈ 0.1 (assumed complete surface charge neutralization) a monolayer of surfactant molecules is formed on a nanoparticle surface, with surfactant hydrophobic tails exposed to the aqueous medium. Thus rendered hydrophobic, surfactant-decorated gold nanoparticles aggregate in water. In region III of high σ surfactant molecules form a bilayer on nanoparticle surface via dipole-dipole interactions between azobenzene containing surfactant tails. In this configuration cationic groups of surfactant point outwards, providing gold-surfactant complexes with the positive charge. Blue shift in the position of the π-π* absorption maximum of azobenzene surfactant typical for H-aggregates was not detected in the spectra in **Figure 4.6**. On the one hand, the fraction of possibly aggregated azobenzene molecules is only around 10 % for σ = 1.5 and thus not detectable. On the other hand, the absence of blue shift might indicate the absence of H-aggregates due to loose packing in the double layer shell. The following simple calculation supports the proposed configurations of the complexes.

The total amount of gold atoms on a 10-nm gold nanoparticle surface $dN^{-} \approx 5200$. Assuming 10 % of negatively charged gold atoms on the surface of a nanoparticle, and full charge neutralization by cationic surfactant molecules, σ = 0.1 corresponds to a monolayer of around 520 surfactant molecules on the spherical surface of a 10-nm particle. For 10-nm gold particles, surface area $S_{Au} \approx 314$ nm^2, yielding surface area $S_{Azo} \approx 0.6$ nm^2 available for one surfactant molecule in the monolayer. In fact, this surface area may accommodate azobenzene unit adsorbed to nanoparticle surface. Yet, a fully adsorbed surfactant molecule in elongated trans-conformation might require up to 1.5 nm^2. One simple alkyl azobenzene thiol molecule occupies around 0.187 nm^2 in monolayer on gold surface.[50] Therefore, cross-sectional area of azobenzene surfactant molecule can be roughly estimated as 0.2 nm^2 for the current qualitative calculation. At σ = 0.5 available surface area per molecule $S_{Azo} \approx 0.12$ nm^2, which is not enough for molecules to attach to the surface. However, this value is in a very good agreement with the double-layer formation: surface area per molecule would be doubled, $S_{Azo} \approx 0.24$ nm^2, enough to form densely packed layer attached to the surface.

Azobenzene-decorated gold nanoparticles from region III have been successfully employed to functionalize polymer brushes and DNA strands (**Figure 4.9**). These results are beyond the scope of this thesis, but will be reported in the nearest future.

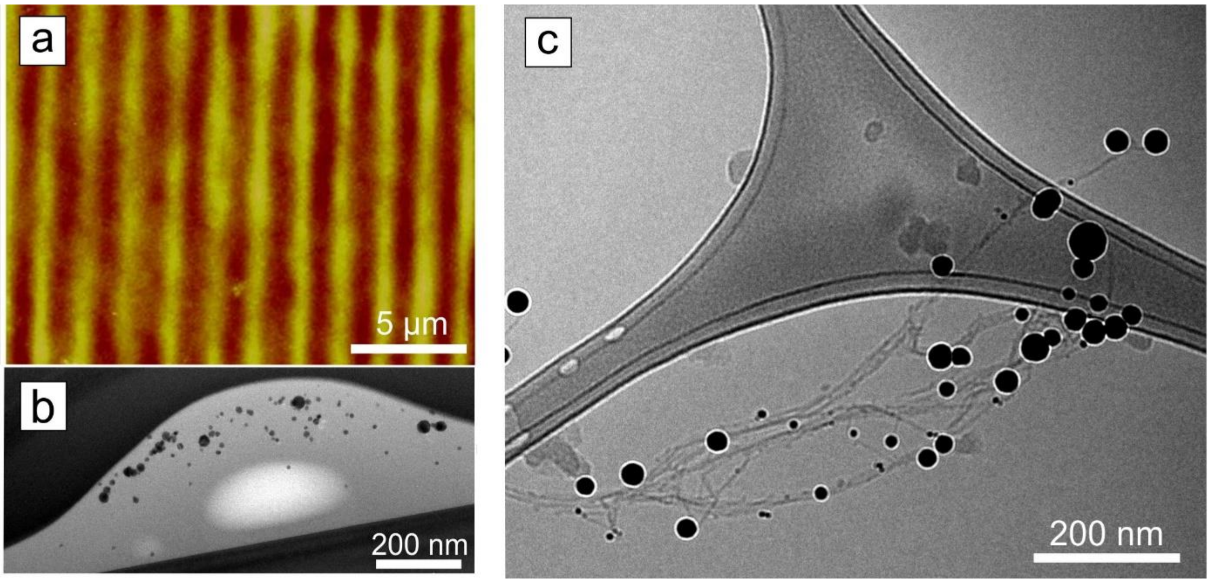

Figure 4.9. Applications of the investigated complexes between gold nanoparticles and azobenzene containing surfactants. Left: two polymethacrylic acid brushes loaded with AzoC$_6$-decorated gold nanoparticles after surface relief grating inscription. (a) AFM micrograph of surface topography, and (b) TEM micrograph of a thin cross-sectional cut.[a] (c) Cryo-TEM micrograph of gold nanoparticles attached to strands of linearized plasmid DNA via azobenzene containing cationic polyamine AzoTren in aqueous solution.

4.6.Constitution of gold-surfactant complexes

TEM micrographs of dried gold-surfactant suspensions at different values of σ for 10-nm (**Figure 4.10**) and 25-nm gold nanoparticles (**Figure 4.11**) support the results above.

---

[a] Data of Dr. Markus Wollgarten at Helmholtz Zentrum Berlin of Materials and Energy

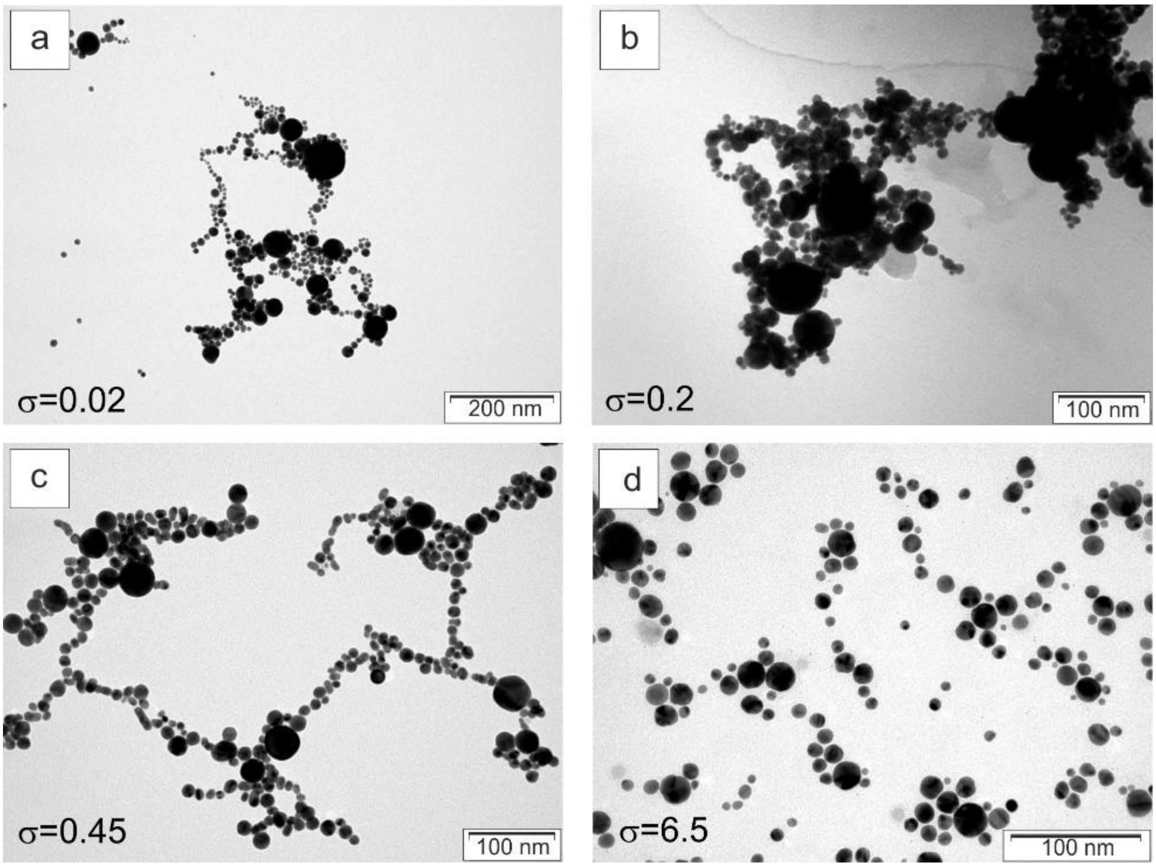

Figure 4.10. TEM micrographs of dried suspensions of 10-nm gold nanoparticles in complexes with azobenzene containing surfactant AzoC$_6$ at $\sigma = 0.02$ (a); $\sigma = 0.2$ (b); $\sigma = 0.45$ (c); $\sigma = 6.5$ (d).

In region I (**Figure 4.11a, b**) and region III (**Figure 4.10d and Figure 4.11f**) TEM reveals ensembles of individual particles. Being less electron dense than gold, surfactant looks grey in TEM micrographs. In region I (**Figure 4.11a, b**) individual gold nanoparticles were detected partly surrounded with surfactant shell. Consequently, one can speculate about the selective formation of gold-surfactant complexes, rather than simultaneous coverage of nanoparticle surface with surfactant, when dipolar interactions cause surfactant molecules cooperatively attach to some nanoparticles, while the rest of the particles remains “bare”. With the increase of surfactant concentration all nanoparticles obtain surfactant shell. In the micrographs at high values of σ from region III (**Figure 4.11f**), individual gold nanoparticles (stabilized by surfactant) were found among the surfactant spherical micelles.

The micrographs in region II (**Figure 4.10b and Figure 4.11d**) display densely packed gold nanoparticle aggregates with chain-like segments, indicating diffusion-limited aggregation. In fact, DLCA aggregates are expected to be loose. The observed compactness of the aggregates can be rationalized by the drying effect. Indeed, **Figure 4.12** shows the results of cryo- electron microscopy (cryo-EM) of a gold-surfactant suspension from region II ($\sigma = 0.3$). In contrast to the compact aggregates observed in dried suspensions, in solution one can see several-micrometer big loose dendrimer-like agglomerates adhered to a carbon fiber (**Figure 4.12a**). The micrograph with higher magnification (**Figure 4.12b**) shows that the aggregates consist of long gold nanoparticle chains. These microscopy findings are consistent with the absorption spectra showing coupling chain plasmon mode.

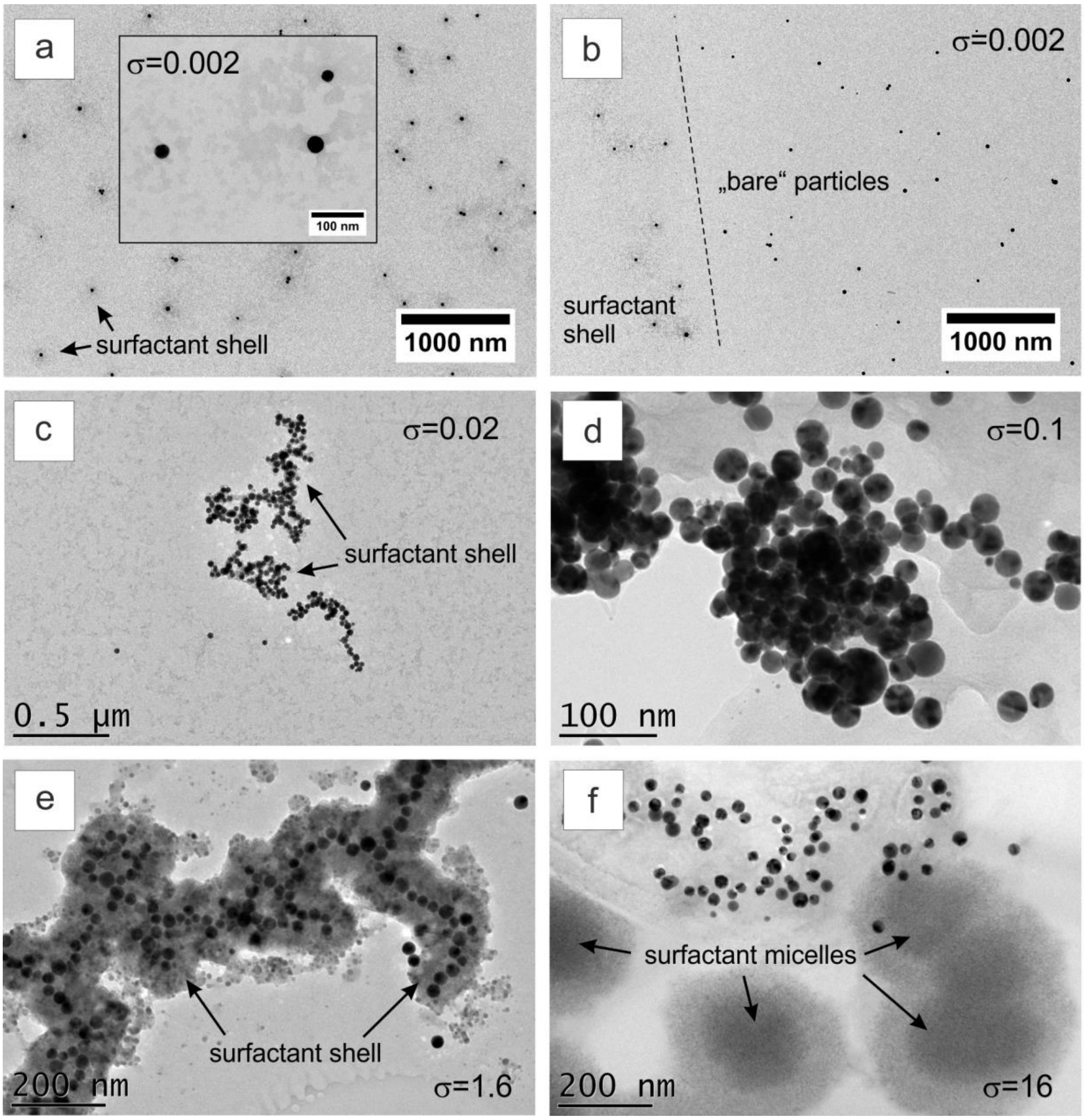

Figure 4.11. TEM micrographs of dried suspensions of 25-nm gold nanoparticles in complexes with azobenzene containing surfactant AzoC$_6$ at σ = 0.002 (a, b); σ = 0.02 (c); σ = 0.1 (d); σ = 1.6 (e); σ = 16 (f). The inset in (a) shows a zoomed in micrograph of three gold particles. The dashed line in (b) represents a borderline between the area with surfactant-covered particles (in the left) and "bare" particles (in the right).

The smaller chain-like nanoparticle assemblies were detected along with individual particles near the borders of region II (**Figure 4.10a, c and Figure 4.11c**) and at σ = 1.6 (**Figure 4.11e**). This supports the hypothesis about the aggregation of nanoparticles, covered with the azobenzene surfactant monolayer: as soon as some particles get covered with the monolayer, they rapidly coagulate into chains, probably driven by attractive dipolar interactions between surfactant tails in the diffusion-limited aggregation regime. The formation of such particle aggregates might be also due to a drying effect. However, the chain plasmon mode was also detected in the UV-Vis absorption spectra at $\sigma = 0.02$. Probably, at $\sigma = 1.6$ the volume fraction of individual particles dominated over the coagulated particles, that's why the chain mode was suppressed in the spectra. The coexistence of nanochains and individual particles explains the broad width of the region II: in fact, all nanoparticles are rendered hydrophobic at local $\sigma \approx 0.1$. In the center of region II likely all particles are covered with the azobenzene surfactant monolayer, whereas in the intermediate σ range the amount of monolayer-decorated particles is smaller, and therefore they form smaller aggregates.

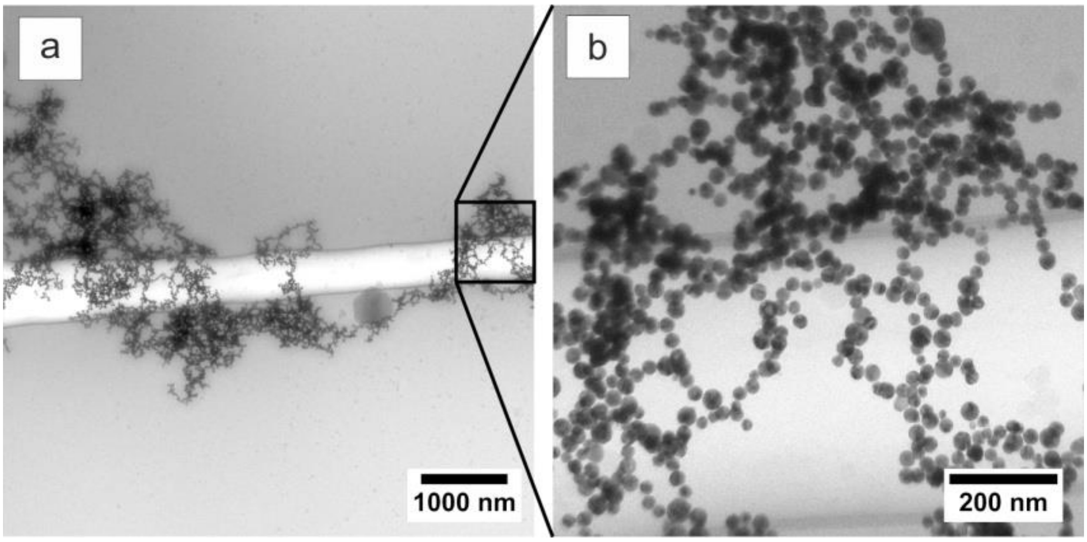

Figure 4.12. Cryo-EM micrographs of 25-nm gold nanoparticles in complex with azobenzene containing surfactant $AzoC_6$ from region II.

TEM results support the suggested mechanism of gold nanoparticle – surfactant complex formation, showing a shell of azobenzene containing surfactant around gold nanoparticles and particle aggregates in region II. Next section highlights the presence of nanochains in the intermediate regions.

4.7.Nanoaggregation in gold-surfactant suspensions

The complexes between gold nanoparticles and azobenzene containing surfactants can be prepared also by successively adding small volumes of one component to another (titration). Such preparation procedure, in contrast to the described above systems of mixed components, allows gradually varying σ values and therefore the examination of the particular qualities of gold-surfactant complexes, such as the reversibility of complex formation.

In the first way of complex preparation, droplets of surfactant ($AzoC_6$) aqueous solution of a certain concentration were step-by-step added to a relatively big volume of aqueous colloid of gold nanoparticles. In the first step, surfactant was added to the pure gold nanoparticles in water. In the second and further steps, surfactant was added to a gold-surfactant colloid resulting from the preceding step. After each step the concentration of gold particles slightly decreased, while the concentration of surfactant increased, *i. e.* the value of σ increased. Absorption spectra were recorded after each step. The spectra recorded for 10-nm gold nanoparticles with step-by-step added azobenzene containing surfactant AzoC$_6$ are shown in **Figure 4.13a**. Since the concentration of gold changed in the experiment, the spectra are represented in terms of gold extinction coefficient. The results of two experiments with initial concentration of gold C_{Au} = 0.08 mM are combined in one plot.

In the second way of complex preparation, droplets of gold aqueous colloid were step-by-step added to a system of gold particles preliminary mixed with surfactant at very high σ. The concentration of gold particles being added was the same as in the initially mixed gold-surfactant suspension. Therefore, the concentration of gold particles did not change, while the concentration of surfactant decreased after each step, *i. e.* the value of σ decreased. **Figure 4.13b** shows the absorption spectra of 25-nm gold nanoparticles mixed with azobenzene containing surfactant AzoC$_6$ at extremely high concentration (region III) upon the subsequent addition of gold nanoparticles. The spectra were recorded in the quartz cuvette with 5 mm optical path length.

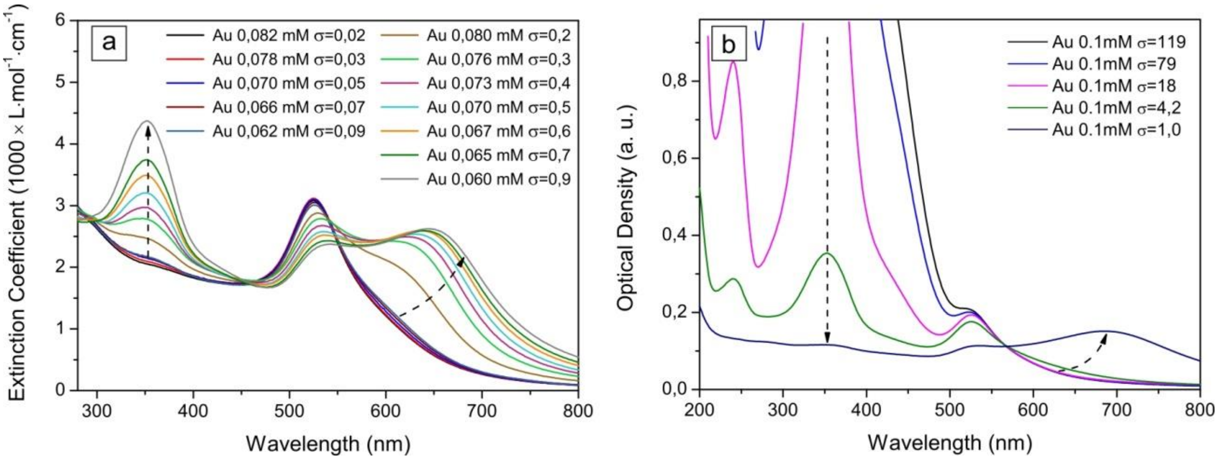

Figure 4.13. UV-Vis absorption spectra of (a) 10-nm gold nanoparticles with step-by-step added azobenzene containing surfactant AzoC$_6$ (way 1); (b) 25-nm gold nanoparticles mixed with azobenzene containing surfactant AzoC$_6$ with step-by-step added gold nanoparticles (way 2). Concentrations of gold particles and corresponding values of σ are listed in the legends.

With the increase of the σ value up to σ = 0.9 by step-by-step adding surfactant (way 1, **Figure 4.13a**), gold nanoparticle plasmon peak initially located at 523 nm slightly red-shifted and its intensity decreased, along with the growth of the second absorption peak. The position of the second plasmon peak shifted roughly from 600 nm up to 650 nm, its intensity gradually increased. Similar changes were observed with the decrease of σ values up to σ = 1 via step-by-step adding gold nanoparticles to a gold-surfactant suspension (way 2, **Figure 4.13b**). The position of the second absorption peak shifted up to 700 nm in this case.

In the experiments with 10-nm gold particles the range of σ covered all three regions in the phase diagram in **Figure 4.8** (not all the spectra are shown in **Figure 4.13a**). The observed spectral changes were irreversible: the second absorption peak remained the main absorption maximum even upon achieving region III (σ>0.5, orange, olive and grey curves in **Figure 4.13a**). **Figure 4.14** demonstrates the comparison between the phase diagrams with the successive increase of σ in the 10-nm gold-surfactant systems (way 1, **Figure 4.13a**) and for the systems initially mixed at different σ (**Figure 4.8a**). The two diagrams do not overlap. The possible explanation could be different aggregation regimes (RLCA and DLCA). Adding small amounts of surfactant realizes reaction-limited aggregation at every step at $\sigma<0.1$, which is consisitent with the shape of the spectra. Further addition of surfactant induces the transition into diffusion-limited regime. At the same time, immediate addition of sufficiently high surfactant concentration corresponds to diffusion-limited aggregation with more pronounced spectral changes.

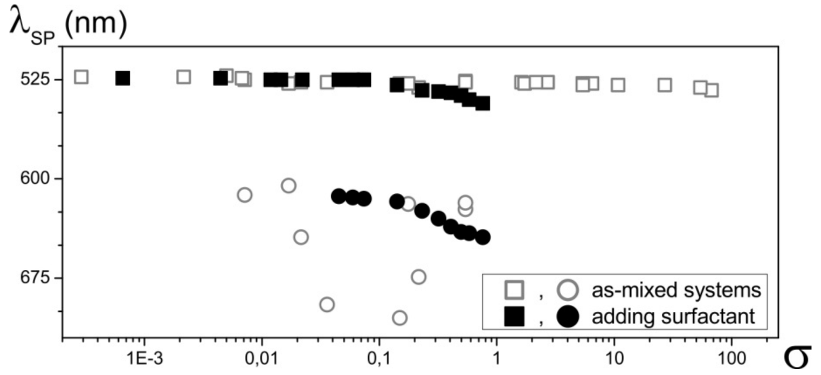

Figure 4.14. Position of the UV-Vis absorption peak as a function of σ for the complexes between 10-nm gold nanoparticles and azobenzene containing surfactant $AzoC_6$, prepared by mixing components at different concentrations (open symbols) and by step-by-step adding surfactant to gold nanoparticles (closed symbols). Squares show the position of the gold nanoparticle plasmon peak initially located at $\lambda = 523$ nm. Circles show the position of the second absorption peak, arising at certain values of σ.

The comparison between the two ways of step-by-step preparation of the 25-nm gold nanoparticle-surfactant complexes is shown in **Figure 4.15**.

Black open symbols in **Figure 4.15.a** show the red shift of gold plasmon peak position upon adding surfactant to 25-nm gold nanoparticles (way 1), therefore increasing the molar ratio σ from $\sigma = 0$ to $\sigma = 10$ (from region I to region III). The final gold-surfactant suspension prepared in this way is labeled as "#10". Similar to the case of 10-nm gold nanoparticles (**Figure 4.13a and Figure 4.14**), once appeared in the spectra in region II, the second absorption peak remained present even in region III, its position red-shifted with every step of σ increase. The color of the gold-surfactant suspensions changed accordingly from pink (region I) to violet and blue (region II) and further to green-yellow (system "#10" in **Figure 4.15b**).

The second way of gold-surfactant complex preparation, with decreasing σ values by adding gold particles, is shown with red closed symbols in **Figure 4.15a**. Gold nanoparticles of 25 nm in diameter were mixed with azobenzene surfactant at extremely high value of σ ($\sigma = 119$, system "B"). Concentration of gold nanoparticles in the suspension was $C_{Au} = 0.1$ mM. Gold nanoparticle aqueous colloid ($C_{Au} = 0.1$mM) was then step-by-step added to the suspension, leading to $\sigma = 79$ (system "B1"), $\sigma = 18$ (system "B2"), $\sigma = 4$ (system "B3") and $\sigma = 1$ (system "B4") (corresponding absorption spectra were shown in **Figure 4.13b**). Further decrease of σ was not performed due to the lack of gold nanoparticle colloid. As $\sigma = 4$ was achieved, changes in plasmon spectral properties were registered, when the second absorption peak at $\lambda = 650$-

700 nm has appeared. The color of the suspensions at σ>4 was orange, at σ = 4 it changed to violet, and at σ = 1 it became blue (systems "B"-"B4" in the left in **Figure 4.15b**). The suspensions with a single plasmon peak in the absorption spectra ("B2") and with the pronounced red shift, *i. e.* the second absorption peak ("B3"), were diluted with water, and the spectral properties were monitored (red open symbols in **Figure 4.15a**). The spectra and color of the gold-surfactant suspensions did not change even after several dilutions. That means, the properties of the nanoparticle-surfactant complexes are determined only by the value of σ which was not changed by the dilutions.

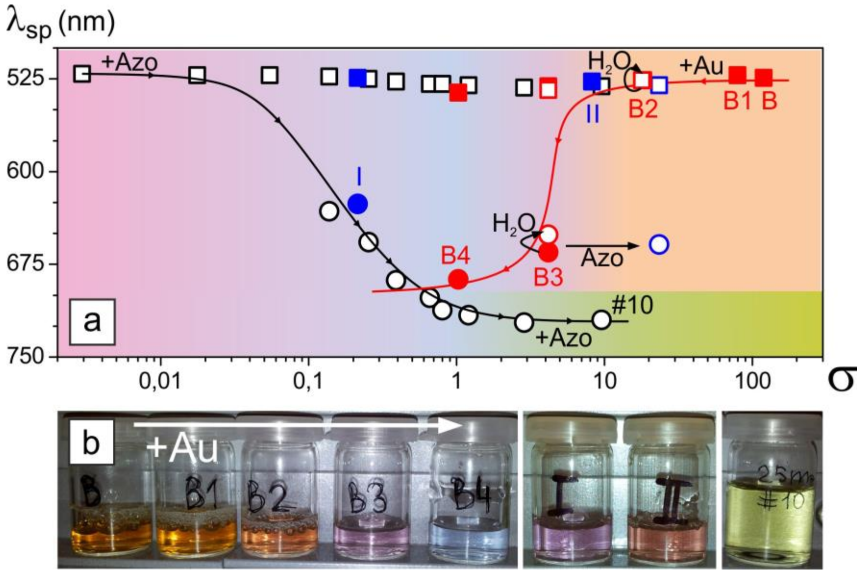

Figure 4.15. (a) Position of the UV-Vis absorption peak of as a function of σ for the complexes between 25-nm gold nanoparticles and azobenzene containing surfactant AzoC$_6$, prepared with step-by-step varying σ values: by successive adding surfactant to gold nanoparticles (way 1, black open symbols) and by adding gold nanoparticles to a gold-surfactant system (way 2, red closed symbols). Squares show the position of the gold nanoparticle plasmon peak initially located at λ = 521 nm, circles - the position of the second absorption peak, observed at certain σ. Blue closed symbols represent the two systems, prepared by initially mixing gold particles with surfactant at different values of σ (labeled "I" and "II"). Red and blue open symbols show the results of manipulations with the systems labeled "B2" and "B3". Background shows the drawn color change in the gold-surfactant suspensions. (b) Photos of the suspensions of 25-nm gold nanoparticles and azobenzene containing surfactant AzoC$_6$. From left to right: change in the color of the suspensions with decreasing the value of σ via adding gold nanoparticles (systems "B"-"B4"); the color of the two gold-surfactant suspensions, prepared by initially mixing components at different concentrations ("I" and "II"); the color of the resulting gold-surfactant system, prepared by adding surfactant to gold nanoparticles ("#10"). The labels of the suspensions are also shown in the plot of λ_{SP} (σ) in a) next to the corresponding data points.

For comparison, the gold-surfactant suspensions, initially mixed at σ = 0.2 and σ = 8 (systems "I" and "II" respectively) exhibited the spectral changes, similar to those in the step-by-step prepared systems. In region III (system "II") a single plasmon peak was observed at λ = 527 nm, while in region II (system "I") the second absorption peak was registered at

$\lambda = 626$ nm (**Figure 4.15a**). The color of the suspension “I” was violet, the color of the suspension “II” was peach (between pink and orange) (**Figure 4.15b**).

The changes in σ provide the phase transitions between the regions only in one direction – into region II. One can shift a gold-surfactant system into region II via the increase of σ in region I and the decrease of σ in region III. Manipulating σ in a gold-surfactant system in region II does not lead to the back transitions. Adding surfactant to the gold-surfactant suspension labeled “B3” (increasing σ) did not result in the disappearance of the second absorption peak (it remained at $\lambda \approx 660$ nm, blue open symbols in **Figure 4.15a**) and did not change the color of the suspension to orange.

Spectral changes observed for both ways of complex preparation (adding surfactant or adding gold particles) indicate particle aggregation starting from certain values of σ. If compare the two systems with similar high values of σ from region III, prepared in different ways, one can clearly see the dramatic difference in gold-surfactant properties. For instance, the system “II” with $\sigma = 8$ (initially mixed) has pink-orange color and single gold plasmon peak in the absorption spectra, indicating individual nanoparticles, whereas in the system “#10” with $\sigma = 10$ (prepared by adding surfactant) one can see blue precipitation in the bottom of the glass with the yellowish liquid phase (**Figure 4.15b**).

This shows that once the conditions for particle aggregation get fulfilled, the gold-surfactant complexes get “stuck” in region II. The gold particles (covered with hydrophobic trans-surfactant shell) aggregate in water into DLCA nanochains irreversibly, as the complexes from region II are sensitive to varying neither concentrations of the components (dilution) nor σ values. Replacing water with less polar solvents (ethanol, dimethylsulfoxide, chloroform) was also helpless to redisperse gold particles. As mentioned above, surface area $S_{Azo} \approx 0.6$ nm^2 is available for one surfactant molecule at $\sigma = 0.1$. This value is above the critical value of required molecular surface area for azobenzene isomerization by rotation mechanism on planar surfaces, what implies effective photoswitching of azobenzene containing surfactant on gold nanoparticle surface. Yet, UV irradiation of the aggregates in water did not have impact on their aggregation state. This might be attributed to the solvophobic effect, when the changes in dipole moment upon azobenzene trans-cis photoisomerization were insufficient in polar water environment. Also, approaching instead of dissociacion of the particles in aggregates upon trans-cis azobenzene isomerization have been reported earlier.[189]

Thereby, particle aggregates with negligible volume fraction might co-exist with individual particles even in region I or region III near the boundaries of region II. The volume fraction of the particle aggregates becomes detectable in the region II. TEM micrographs, showing both individual and aggregated gold nanoparticles (for instance, **Figure 4.10a**), support this suggestion. When the volume fraction of the aggregated particles is comparable with or dominates the fraction of the individual particles (the middle of the region II), gold-surfactant suspensions obtain violet or blue color respectively. Indeed, violet suspensions can be a superposition of blue phase of aggregates and pink phase of individual particles, similar to the green-yellow system “#10”, having blue precipitation and yellow liquid phase (likely extensional surfactant).

The following experiment was implemented in order to reveal the aggregates in region III. Gold nanoparticles of 25 nm in diameter (absorption spectrum and size distribution in **Figure 4.3**) were mixed with azobenzene surfactant AzoC$_6$ at five different concentrations. The resulting suspensions had $C_{Au} = 0.1$mM and five different values of σ, covering all three regions of phase diagram. The UV-Vis absorption spectra of the prepared colloids are shown in **Figure 4.16.**

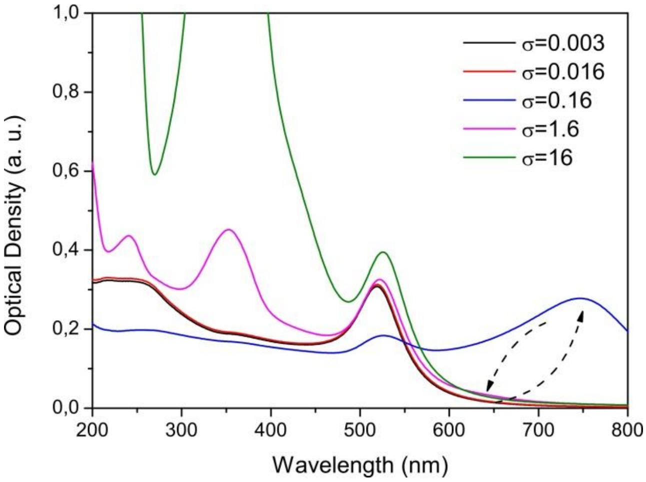

Figure 4.16. UV-Vis absorption spectra of 25-nm gold nanoparticles mixed with azobenzene containing surfactant AzoC$_6$ at different concentrations, σ values are listed in the legend.

All gold-surfactant suspensions were then centrifuged for 15 minutes, forcing the precipitate to the bottom of the tubes. The precipitate compressed into a solid state in two out of five suspensions, with σ = 0.16 (region II) and σ = 1.6 (region III). In the other three suspensions (σ = 0.003, σ = 0.016 and σ = 16) gold nanoparticles partly sedimented and quickly redispersed, precipitation did not occur.

Figure 4.17 shows the absorption spectra of suspensions at σ = 0.16 and σ = 1.6 before and after centrifugation. As prepared, suspensions had blue and pink color respectively. Their absorption spectra were typical for the systems from region II (absorption maximum at λ ≈ 750 nm, violet curve) and region III (single plasmon peak at λ = 522 nm, black curve). After centrifugation, the supernatant (above liquid) was poured off, and the precipitate was suspended in water to the initial volume. Sonication of the precipitant for 20 minutes resulted in a blue suspension in the case of σ = 1.6, precipitation from σ = 0.16 did not redisperse. Absorption spectra of supernatant and precipitant were recorded. In the case of σ = 0.16 UV-Vis absorption of the supernatant was not detectable (magenta curve), indicating that all gold-surfactant aggregates precipitated. Absorption spectrum of the supernatant for σ = 1.6 (red curve) did not differ from the the spectrum of the as-prepared system (black curve), except for lower intensity. At the same time, absorption spectrum of the precipitate (blue curve) demonstrated two plasmon peaks with the plasmon mode at λ ≈ 750 nm, similar to the spectra of gold-surfactant suspensions in the center of region II.

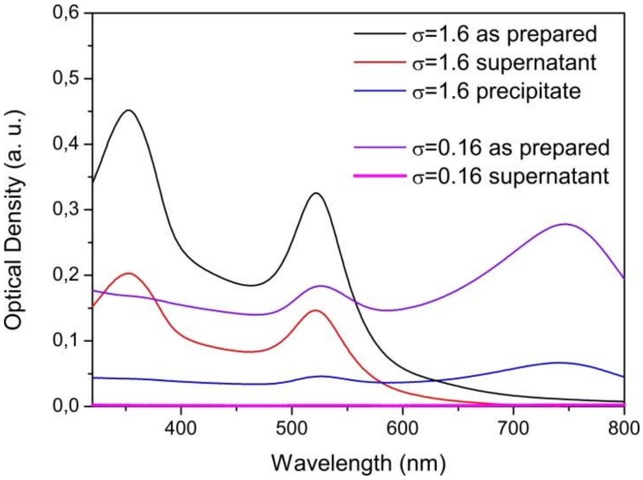

Figure 4.17. UV-Vis absorption spectra of gold-surfactant complexes at σ = 1.6 and σ = 0.16 as prepared (black and violet curves) and after decantation (red, blue and magenta curves).

Thus, the precipitate formed in region III consisted of chain-like aggregates of gold particles, covered with surfactant molecules. Due to the volume fraction of the aggregated phase was negligible at σ = 1.6, the absorption peak at λ ≈ 750 nm was not detectable before centrifugation, and a single plasmon peak of individual gold nanoparticles, stabilized with a surfactant shell (in liquid phase), was observed in the absorption spectrum of the suspension. Therefore, one can conclude that the aggregates of gold particles form as soon as the conditions of particle charge neutralization and surface coverage with surfactant are locally fulfilled. The volume fraction of gold particles in aggregated state (in fact, particle nanochains) depends on the value of σ. Near the borders of region II, in region I the fraction of particle aggregates might coexist with individual negatively charged particles (not fully covered with surfactant), in region III – with positively charged particles (stabilized with double layer of surfactant). The aggregation of the particles in complex with azobenzene surfactant in water is irreversible and can be governed by varying the molar ratio between azobenzene surfactant and gold nanoparticles.

5. Light-induced aggregation of nanoparticles

Azobenzene containing surfactants are photosensitive, as their conformation can be triggered between trans- and cis- by illumination with certain wavelengths. For the surfactants used in this work, UV light induces the transition of the molecules from trans- to cis-state. Laser ablated gold, silver and silicon nanoparticles were mixed with the azobenzene containing surfactant AzoC$_6$, and absorption spectra of the suspensions were recorded. In three different nanoparticle-surfactant systems, the observed UV-light induced spectral changes were similar.

5.1.Gold nanoparticles

The pronounced influence of UV light on the complexes between gold nanoparticles and photosensitive surfactants was detected in a certain range of σ values. **Figure 5.1a** demonstrates absorption spectra of the 10-nm gold-surfactant suspension at σ=0.45 (border between regions II and III of phase diagram in **Figure 4.8**) before and after UV illumination. After exposure of the quartz cuvette with the suspension to UV light for 5 minutes (blue curve in **Figure 5.1a**), the intensity of the surfactant absorption band decreased, and the second plasmon absorption peak appeared at $\lambda \approx 680$ nm. The color of the suspension changed from pink to lila and blue. The observed changes indicated gold nanoparticle aggregation. TEM micrographs of this dried suspension (**Figure 5.1b**) showed nanoparticle-surfactant aggregates, similar to **Figure 4.10b**.

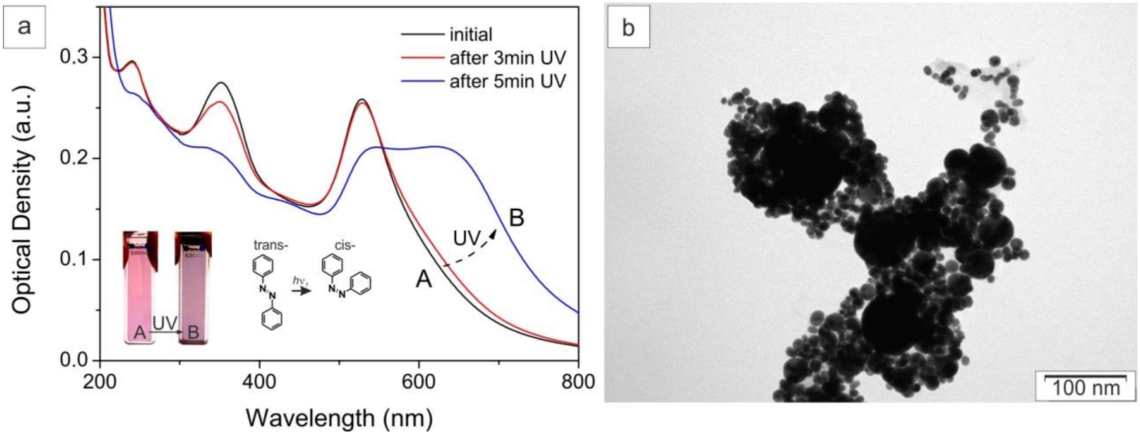

Figure 5.1. (a) UV-Vis absorption spectra of the complex between 10-nm gold nanoparticles and azobenezene containing surfactant AzoC$_6$ at σ = 0.45 as prepared (black curve) and illuminated with UV light for 3 min (red curve) and for 5 min (blue curve). The inset shows changes in the color of the gold-surfactant suspension during UV irradiation and the scheme of the UV light-induced trans-cis isomerization of the azobenzene unit of surfactant. (b) TEM micrograph of the dried UV-irradiated gold-surfactant suspension prepared at σ = 0.45.

The physical properties of the UV-irradiated suspension correspond to the region II of phase diagram, although before irradiation they matched the region III. Thus, UV irradiation induced the phase transition from region III to region II. Such transition was achieved in the previous chapter by decreasing σ value in gold-surfactant suspensions with non-irradiated predominantly trans-surfactant via step-by-step addition of gold nanoparticles into a system from region III (**Figure 4.13b**, red line in **Figure 4.15a**). The use of photosensitive surfactant allows the phase shift to be governed by UV light, not altering the total concentration of surfactant.

However, UV irradiation changes the concentration of cis- and trans- isomers of surfactant. There is 88 % of cis-isomers and 12 % of trans-isomers in UV irradiated surfactant solution. That means, after irradiation $\sigma_{UV}^{trans} = 0.12\sigma$ and $\sigma_{UV}^{cis} = 0.88\sigma$. Due to higher hydrophilicity of azobenzene surfactant in cis-conformation, one can assume that the trans-isomers adsorb to gold nanoparticle surfaces more readily than cis-isomers. **Scheme 5.1** illustrates the phase shift of the nanoparticle−surfactant complex during UV irradiation. Although the absolute σ value $\sigma_{abs} = 0.45$, after irradiation $\sigma_{UV} = \sigma_{UV}^{trans} = 0.05$, which corresponds to the region II of phase diagram for trans-isomers (see **Figure 4.8**). Irradiation destabilizes the surfactant shell around nanoparticles, as the trans-cis isomerized molecules leave the suggested surfactant double layer for the medium (aqueous solution of surfactant cis-isomers).

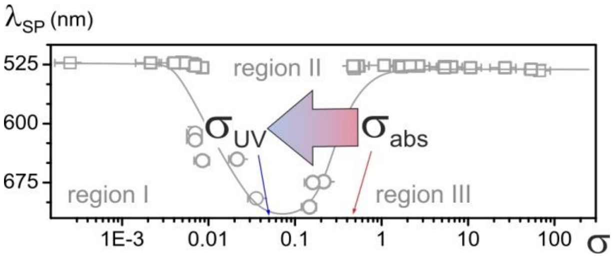

Scheme 5.1. UV-induced phase transitions in the complexes between gold nanoparticles and azobenzene surfactants: absolute value of σ_{abs} on the borderline between regions II and III of the phase diagram, and the $\sigma_{UV} = 0.12\sigma_{abs}$ corresponding to region II after UV irradiation of a complex with σ_{abs}. The background reproduces the phase diagram from Figure 4.8a.

UV irradiation of complexes in region III with $\sigma_{abs} > 5$, *i. e.* at $\sigma_{UV} > 0.6$, did not initiate the red-shift in the position of the gold plasmon absorption peak. The ζ-potential remained positive after UV irradiation. The properties of the systems with $\sigma_{abs}>5$ exposed to UV light match the region III, because the concentration of surfactant molecules in trans-conformation is sufficient to retain double layers around gold nanoparticles ($\sigma_{UV} > 0.6$). UV irradiation of the complexes in region I ($\sigma < 0.01$) influenced neither their absorption spectra nor their surface ζ-potentials.

Subsequent illumination with blue light of the gold-surfactant systems UV-shifted to region II, induced back cis-trans isomerization of surfactant, but did not result in the back phase transition to region III. The aggregates formed after UV exposure, were not redispersed into individual particles in visible light. This can be explained in a way similar to the step-by-step increasing σ value by adding surfactant (**Figure 4.13a**, black line in **Figure 4.15a**). Irradiation with visible light increased the concentration of surfactant trans-isomers, $\sigma_{Vis} = 0.67\sigma_{abs}$. However, the increase of σ in a system from region II did not provide the transition to region III.

Centrifugation of the UV-irradiated gold-surfactant suspensions validated the proposed mechanism of the light impact.

Figure 5.2 shows the results of the centrifugation of the UV-irradiated suspension at $\sigma_{abs} = 0.45$. Absorption spectrum of the supernatant (black curve in **Figure 5.2a**) shows only the absorption peak at λ = 353 nm of azobenzene surfactant in trans-conformation[b]. The gold plasmon peak was not detected in the absorption spectrum of supernatant, indicating that all gold-surfactant aggregates precipitated after centrifugation. The precipitate was suspended in water and in dimethylsulfoxide (DMSO). DMSO was chosen in the attempt of reducing solvophobic effects, probably hindering the reversible nanoparticle aggregation. The absorption spectrum of the precipitate in DMSO (red curve in **Figure 5.2a**) shows gold plasmon absorption at roughly 670 nm, as well as the weak absorption peak of surfactant at 353 nm. Such optical properties imply that all gold-surfactant complexes coagulated after exposure to UV light, likely into nanochains. The TEM micrograph of the dried precipitate aqueous suspension (**Figure 5.2b**) displays particle aggregates. Compared to the dried suspension before centrifugation (**Figure 4.10b**), the aggregates involve significantly less small particles, revealing big gold clusters of (100 ± 20) nm in diameter.

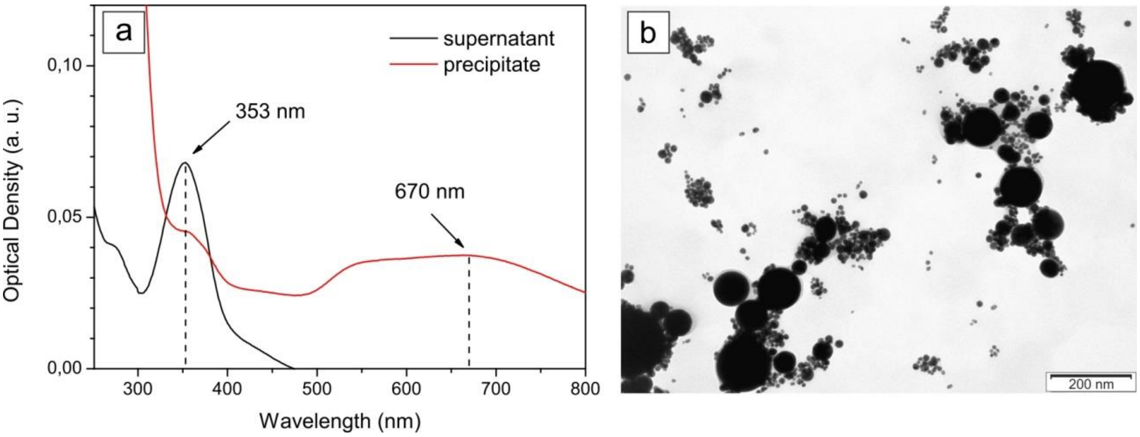

Figure 5.2. (a) UV-Vis absorption spectra of UV-illuminated 10-nm gold-surfactant suspension at $\sigma_{abs} = 0.45$ after decantation: supernatant (black curve) and precipitate in DMSO (red curve). (b) TEM micrograph of the dried suspension of the precipitate in water.

Figure 5.3 demonstrates similar results for the centrifugation of the UV-irradiated gold-surfactant suspension at $\sigma_{abs} = 1.6$ prepared with 25-nm gold nanoparticles. In the experiment the precipitate was suspended in water, its absorption spectrum is shown in **Figure 5.3b** (blue curve). The suspension had light blue color, and the observed spectral properties indicate aggregated state of gold particles. The absorption spectrum of the supernatant was similar to that of the stabilized gold-surfactant suspensions from region III. These results indicate that UV irradiation destabilized surfactant shell around only a part of gold particles in the suspension, making them aggregate, while the rest of the gold-surfactant complexes remained colloidally intact.

---

[b] Centrifugation was performed after spontaneous relaxation of azobenzene surfactant into predominantly trans-conformation, occurred within 15 minutes.

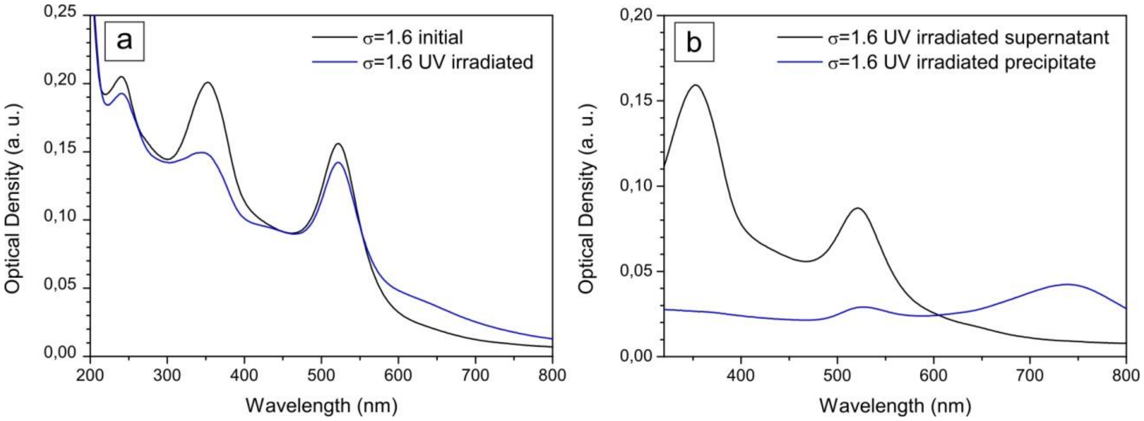

Figure 5.3. UV-Vis absorption spectra of 25-nm gold nanoparticles in complex with azobenzene containing surfactant $AzoC_6$ at $\sigma = 1.6$ as prepared and after UV irradiation (a) and the subsequent centrifugation (b). The spectra were recorded in the quartz cuvette with 5 mm optical path length.

5.2.Silver nanoparticles

Absorption spectrum of silver nanoparticle aqueous colloid[c] is shown in **Figure 5.4a**. Silver nanoparticles in water possess plasmon absorption peak at $\lambda = 406$ nm, with the corresponding yellow color of the nanoparticle suspension (the inset in **Figure 5.4a**). The absorption bands of silver nanoparticles and azobenzene surfactant overlap, which constrains the spectral data interpretation. However, the absorption peak of silver nanoparticles interfere mainly with the absorption peak of the surfactant in cis-state (437 nm), whereas the absorption of surfactant trans-isomers at 353 nm can be recognized not essentially altered.

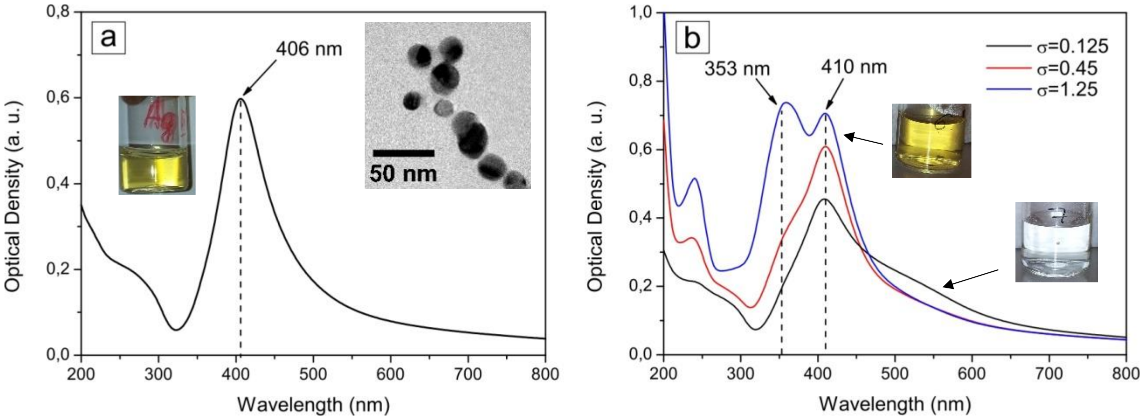

Figure 5.4. UV-Vis absorption spectra and color of silver nanoparticles at $C_{Ag} = 0.35$ mM: (a) in water; (b) mixed with azobenzene containing surfactant $AzoC_6$ at three values of σ, listed in the legend. The insets show TEM micrograph of silver nanoparticles (a) and photographs of nanoparticle suspension colors with and without surfactant.

---

[c] prepared at Vladimir State University (Russia)

The concentration of silver nanoparticles from this batch[d] was estimated via the extinction coefficient of silver particles ε ≈ 1740 $M^{-1}cm^{-1}$, which was calculated from the absorption maximum over the concentration of similar laser ablated silver particles from another batch[e], with plasmon peak at λ = 406 nm too (their properties are described in details in Section 7.2). The diameter of the silver nanoparticles measured by DLS $d = 33.5 \pm 7.3$ nm is in a good agreement with TEM micrographs (the inset in **Figure 5.4a**). The measured surface ζ-potential was around -33 mV, implying negative surface charge of silver nanoparticles.

To characterize complex formation between silver nanoparticles and azobenzene surfactants, the same model as for gold particles (Section 4.3) has been applied. For the 30-nm silver nanoparticles, assuming $d_{Ag} = 0.16$ nm, the number of surfactant molecules interacting with silver surface atoms is:

$$\sigma = \frac{C(Azo)}{C(Ag)} \cdot \frac{R}{3d_{Ag}} = \frac{C(Azo)}{C(Ag)} \cdot 15.625$$

Figure 5.4b shows the absorption spectra of silver nanoparticle colloid mixed with azobenzene surfactant in the dark photostationary state (trans-conformation) at different concentrations. The sample line was prepared with the molar concentration of silver $C_{Ag} = 0.35$ mM. The increase of surfactant concentration, *i. e.* values of σ, caused an increase in intensity of absorption peaks at 240 nm and 353 nm. Plasmon peak of silver, initially located at λ = 406 nm, slightly red-shifted to λ = 410 nm in the presence of surfactant, due to the changes in dielectric properties of the medium around silver nanoparticles. At σ = 0.45 (red curve in **Figure 5.4b**) and σ = 1.25 (blue curve) no other changes in plasmon absorption peak of silver occurred. Yellow color of the suspensions (the top inset) is anticipated as a superposition of yellow surfactant solution and yellow silver nanoparticle colloid. At σ = 0.125 (black curve) the second absorption peak appeared at λ ≈ 550 nm, and the silver-surfactant suspension had light blue color (the inset at the bottom right).

UV irradiation of silver-surfactant complexes induced the red shift of silver plasmon peak position up to λ = 630 nm at σ = 0.45 (**Figure 5.5a**). The corresponding color change from yellow to blueish green occured (the inset in **Figure 5.5a**). At higher σ = 1.25, irradiation with UV light and subsequently with visible light triggers surfactant photoisomerization, without impact on the silver plasmonic peak and yellow color of silver-surfactant complexes (**Figure 5.5b**).

---

[d] prepared at Vladimir State University, Russia

[e] prepared at Aix Marseille University, France

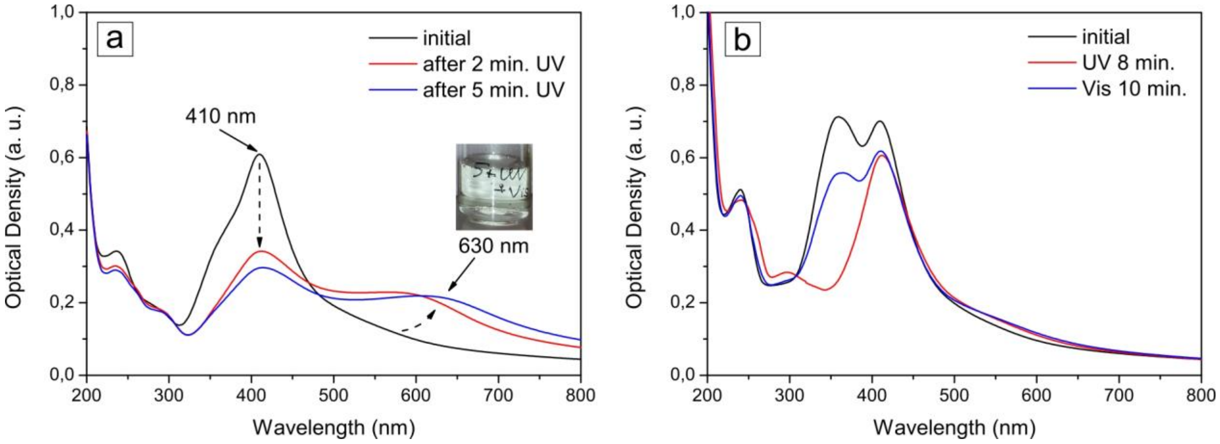

Figure 5.5. UV-Vis absorption spectra of silver-surfactant complexes at σ = 0.45 (a) and σ = 1.25 (b) as prepared and exposed to UV and blue (Vis) irradiation. The inset in (a) shows the color of silver-surfactant complexes after irradiation.

5.3.Silicon nanoparticles

Silicon nanoparticles were prepared at Aix-Marseille University by laser ablation without (SiNP), and with simultaneous blowdown with He (SiNP-He), and Ar (SiNP-Ar, SiNP-Ar II) in order to attenuate particle surface oxidation. All particles had negative ζ-potential around -40 mV. Particle diameters are around 50 nm for SiNP-Ar and SiNP-He, and around 100 nm for SiNP, as measured by DLS. TEM micrographs of the particles were not available. Concentration of silicon particles in prepared colloids is roughly 2.85 mM, as estimated at Aix-Marseille University. Unfortunately, this value is inaccurate due to the silicon nanoparticle preparation process.

Assuming silicon atomic size d_{Si} = 0.2352 nm, for 50-nm silicon nanoparticles one can calculate the molar ratio σ as follows:

$$\sigma = \frac{C(Azo)}{C(Si)} \cdot \frac{R}{3d_{Si}} = \frac{C(Azo)}{C(Si)} \cdot 35.4$$

Figure 5.6a shows absorption spectra of silicon nanoparticles. Silicon nanoparticles SiNP-Ar possess the most apparent absorption peak at λ = 481 nm and the most reddish color (in the inset), probably due to the thinnest layer of silicon oxide on particle surface[f]. The recorded absoption maximum is the evidence of successful preparation of silicon colloid.[206] The orange color of other silicon colloids is shown in **Figure 5.7a**. Silicon absorption peak position did not change once particles were mixed with azobenzene containing surfactant at σ ≈ 1.9 (black curve in **Figure 5.6b**), but red-shifted upon UV irradiation of silicon nanoparticle-surfactant complexes (red curve). Suspension color changed to cold pink (the inset in **Figure 5.6b**). Over time UV-irradiated silicon-surfactant complexes precipitated on the glass walls (**Figure 5.7b**).

---

[f] Data of Dr. Ryabchikov from Aix-Marseille University

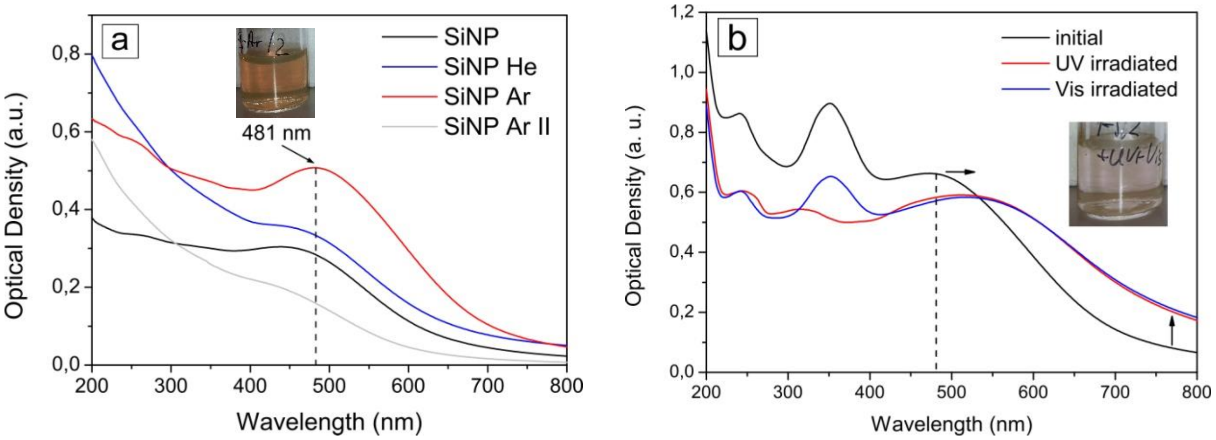

Figure 5.6. (a) UV-Vis absorption spectra and color (the inset) of silicon nanoparticle aqueous colloids, prepared at different conditions. (b) Absorption spectra of silicon nanoparticles prepared in Ar environment (SiNP Ar), mixed with azobenzene containing surfactant AzoC$_6$ at $\sigma \approx 1.9$, as prepared (black curve) and after illumination with UV (red curve) and visible light (blue curve).

Figure 5.7. (a) The color of three silicon nanoparticle aqueous suspensions prepared by laser ablation (from left to right) without gas (SiNP), with He (SiNP He), and with Ar blowdown (SiNP Ar II). (b) Precipitated UV-exposed silicon nanoparticles SiNP Ar decorated with azobenzene surfactant.

Applying the same model of nanoparticle-surfactant complexes, and taking into account inaccurate particle concentrations, sizes, as well as different surface properties, the results with silver and silicon nanoparticles mimic the results for the comprehensively investigated gold nanoparticle-surfactant complexes. Azobenzene surfactant trans- isomers are electrostatically attracted to nanoparticle surfaces, compensating particle charges and inducing particle nanoaggregation at certain conditions, and overcompensating particle charges via decorating the particles with surfactant double-layer shells at exceeding surfactant concentrations. UV irradiation of surfactant-decorated particles with overcompensated charges destabilizes the double-layered surfactant shells upon surfactant trans-cis photoisomerization. This in turn triggers particle nanoaggregation and enables the corresponding coupling plasmonic mode.

6. Cis-trans isomerization of azobenzene surfactants enhanced by gold nanoparticles

In the previous chapters, the nanoparticle-surfactant complexes were prepared via mixing colloid nanoparticle solutions with azobenzene containing surfactant in trans-conformation. In this chapter, gold nanoparticles were mixed with UV-irradiated azobenzene containing compounds, *i. e.* in predominantly cis-conformation.

6.1. Complexes between gold nanoparticles and azobenzene surfactants in cis- conformation

The complexes prepared between UV-irradiated azobenzene surfactant AzoC$_6$ and 10-nm gold nanoparticles were equilibrated for 30 minutes before recording their absorption spectra, similar to the complexes with non-irradiated surfactant. The spectra are shown in **Figure 6.1**. The prepared absolute values of σ covered region II of phase diagram and the beginning of region III. In the UV spectral range one can see the increase in surfactant absorption intensity due to its increasing concentration. Unexpectedly, the π-π* absorption band has maximum at 353 nm, indicating trans- conformation of azobenzene surfactant. This is clearly seen in **Figure 6.1b**. At the same time, similar to the previous study, one can see two gold plasmon peaks in region II (black, red, and blue curves in **Figure 6.1a**). With the increase in surfactant concentration, gold nanoparticle peak remains at 523 nm, while the second plasmon peak, initially found at around 625 nm, disappears. The changes in plasmon wavelength overlap the phase diagram for gold-surfactant complexes with non-irradiated (trans-) surfactant (**Figure 6.2**). These results indicate fast cis-trans isometization of azobenzene surfactant in the presence of gold nanoparticles, with essentially complete conversion to trans-isomer within 30 minutes.

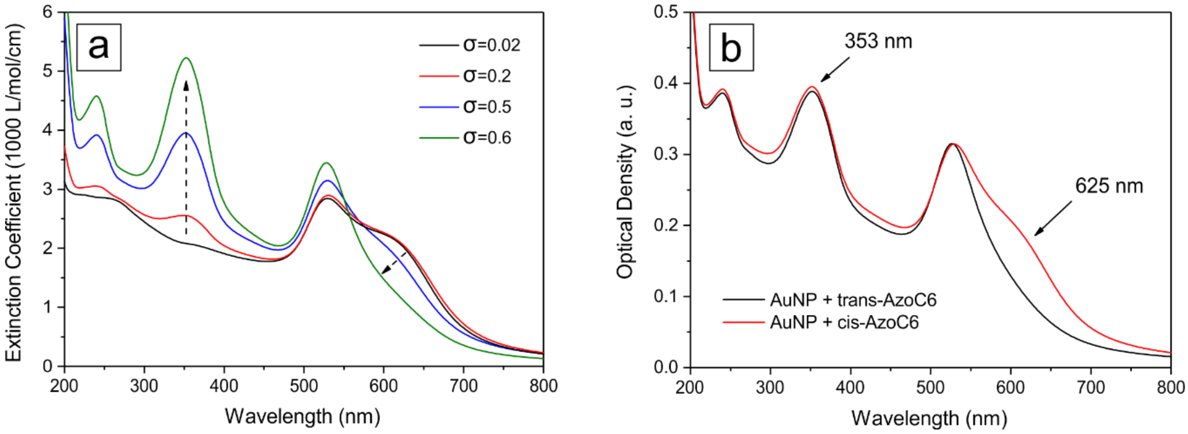

Figure 6.1. (a) Extinction coefficient of equilibrated complexes between 10-nm gold nanoparticles and preliminary UV-irradiated azobenzene surfactant AzoC$_6$ at different absolute values of σ (in the legend), $C_{Au} = 0.2$ mM. (b) UV-Vis absorption spectra of gold-surfactant complexes, prepared at $\sigma_{abs} = 0.5$ with non-irradiated (black line) and UV-irradiated (red line) azobenzene containing surfactant AzoC$_6$, $C_{Au} = 0.2$ mM, optical pathway 5 mm.

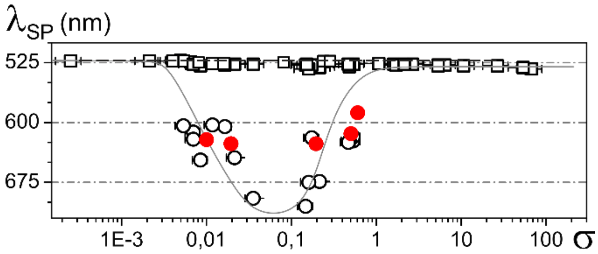

Figure 6.2. Second plasmon wavelength of gold-surfactant complexes prepared with UV-irradiated surfactant AzoC$_6$ (red circles) superimposed over the phase diagram for the complexes between 10-nm gold particles and non-irradiated AzoC$_6$ surfactant from Figure 4.8a.

The second plasmonic maximum appeared as a shoulder at $\lambda \approx 610$ nm in the spectrum of gold nanoparticles with UV-irradiated surfactant at $\sigma_{abs} = 0.5$ (red line in **Figure 6.1b**) can be attributed to nanoaggregation of gold particles decorated with trans-isomers of surfactant present in the UV photostationary state. Indeed, for UV-irradiated surfactant $\sigma_{trans} \approx 0.12\sigma \approx 0.06$, corresponding to region II of phase diagram, in contrast with $\sigma_{trans} \approx \sigma \approx 0.5$ (region III) for non-irradiated surfactant.

The second plasmon peak in region II was found to arise gradually with time (**Figure 6.3**). In this experiment, absorption spectra were recorded immediately after mixing UV-irradiated surfactant AzoC$_6$ with 10-nm gold nanoparticles without equilibration. The growth of the coupling plasmon mode might indicate aggregation of nanoparticles with time, apparently due to increase in the value of σ_{trans} upon fast cis-trans azobenzene conversion and thus shifting from region I to region II of phase diagram (see **Figure 4.8**).

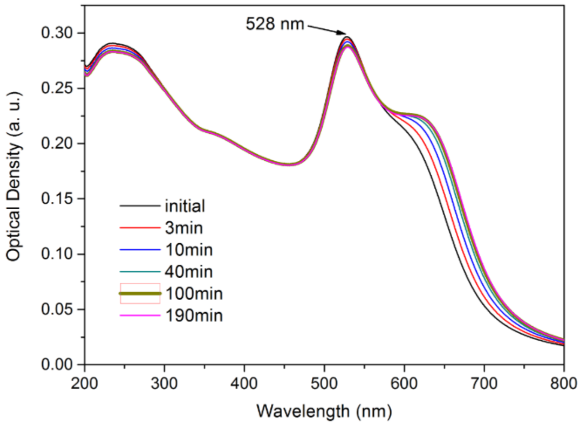

Figure 6.3. UV-Vis absorption spectra of a UV-irradiated solution of AzoC$_6$ surfactant containing 10-nm gold nanoparticles at $\sigma \approx 0.01$. The spectra were recorded as a function of time. For clarity, selected spectra are shown.

The low concentration of surfactant does not allow for the tracking of azobenzene absorption changes. This is done in the next sections for complexes from region III of phase diagram (**Figure 4.8.**).

6.2. Spontaneous cis-trans isomerization of azobenzene surfactants in the presence of gold nanoparticles

UV-irradiated azobenzene containing surfactants are capable of thermal relaxation in the dark from cis-state into trans-state. **Figure 6.4** demonstrates this process for the pure aqueous solution of azobenzene containing surfactant AzoC$_6$. Right after UV irradiation (purple curve, “initial UV irradiated”), one can see the characteristic absorption band of the azobenzene unit in cis-conformation ($\lambda_1 = 437$ nm, $\lambda_2 \approx 315$ nm). The spectrum recorded after 3 days (dark red curve, “after thermal relaxation”) has the absorption maximum at $\lambda_2 = 353$ nm, corresponding to the π-π* band of azobenzene surfactant in trans-conformation. Its intensity grew gradually with time, indicating the increase in the amount of azobenzene trans-isomers in solution. The third observed peak of benzene rings in the UV range ($\lambda_3 = 240$ nm) did not significantly change with time.

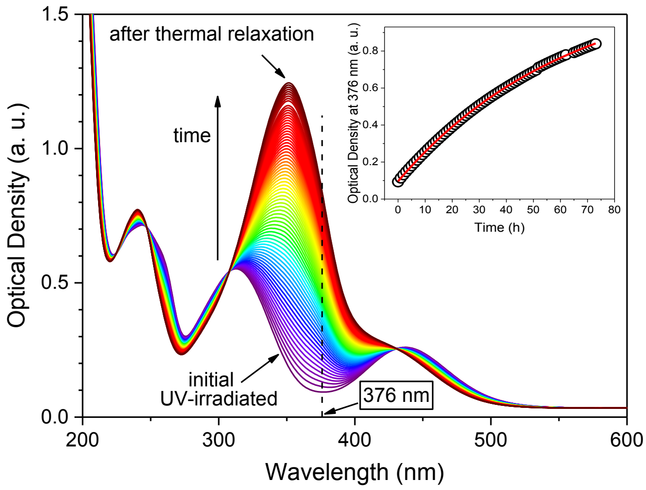

Figure 6.4. Time-dependent absorption spectra of UV-irradiated azobenzene containing cationic surfactant AzoC$_6$ in water. The inset shows optical density at 376 nm as a function of time, recorded experimentally (open circles) and exponentially fitted (red curve).

The time dependency of optical density at 376 nm (D_{376}), shown in the inset in **Figure 6.4**, allows to estimate the thermal relaxation time of azobenzene surfactant cis-isomers, by applying exponential fitting to $D_{376}(t)$. This is in agreement with literature reports on first-order kinetics of thermal cis-trans isomerization of azobenzenes. The wavelength $\lambda = 376$ nm (dashed line in the absorption spectra plot) was chosen due to low absorption of cis-isomers at this wavelength, so that substantially the absorption of trans-isomers can be tracked. Although this approach is not precise in the context of the amount of switched molecules, optical density $D_{376}(t)$ as a function of time is a convenient way to visualize changes in the azobenzene photostationary state without the need of additional data processing. From the spectra in **Figure 6.4**, the thermal relaxation time of cis-isomers of azobenzene containing surfactant AzoC$_6$ in water at room temperature is $\tau_0 = 62 \pm 1$ h. That means, thermodynamically complete cis-trans isomerization of the AzoC$_6$ surfactant in the dark in water requires around one week.

A droplet of 10-nm gold colloid was added to the solution of UV-irradiated azobenzene containing surfactant AzoC$_6$. **Figure 6.5** shows evolution of absorption spectra of the surfactant after mixing with gold nanoparticles.

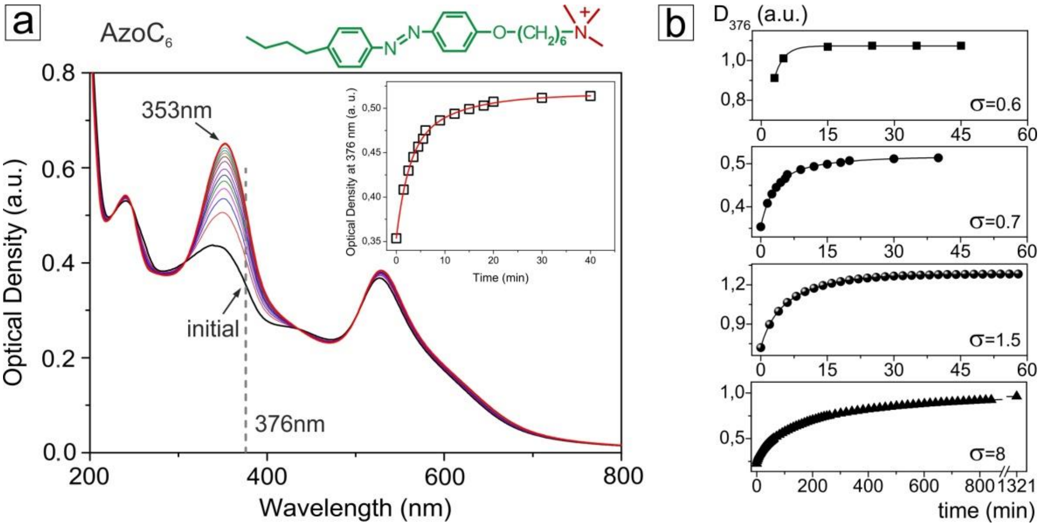

Figure 6.5. (a) Chemical structure of azobenzene containing cationic surfactant AzoC$_6$ (on the top) and its absorption spectra after exposure to UV light and mixing with 10-nm gold nanoparticles at $\sigma = 0.7$ (calculated with the total molar concentration of both isomers). The spectra show rapid isomerization of the surfactant from cis- (black curve, "initial") into trans-state. The inset shows optical density at 376 nm as a function of time, recorded experimentally (open squares) and exponentially fitted (red curve). (b) Optical density at 376 nm (D_{376}) over time for UV-irradiated AzoC$_6$ surfactant in the presence of 10-nm gold nanoparticles at different values of σ (in the legend), as registered (symbols) and exponentially fitted (curves). $C_{Au} \approx 0.2$ mM except for $\sigma = 8$ with $C_{Au} = 0.05$ mM.

In **Figure 6.5a** one can see time dependent absorption spectra of UV-irradiated AzoC$_6$ surfactant in cis-conformation mixed with gold nanoparticles at σ=0.7. Right after the mixing (black curve, "initial"), the characteristic absorption band of the azobenzene unit in cis-conformation can be seen in the spectrum ($\lambda_1 = 437$ nm, $\lambda_2 \approx 315$ nm) along with the peak of benzene rings in the UV range ($\lambda_3 = 240$ nm) and plasmon absorption peak of gold particles at $\lambda_{sp} = 527$ nm. The indistinct plasmon coupling mode $\lambda \approx 600$ nm can be perceived, yet it is negligible for the analysis of azobenzene cis-trans isomerization.

Over time the absorption band of the azobenzene surfactant at 300 nm < λ_2 < 400 nm gradually transformed into the absorption maximum at $\lambda_2 = 353$ nm, indicating azobenzene trans-conformation. The peak of benzene rings λ_3 and the gold plasmon peak did not change because they are independent from the azobenzene conformation. The invariance of plasmonic band means that gold nanoparticles remained colloidally stable during experiments.

The inset in **Figure 6.5a** shows the time dependency of optical density at 376 nm. One can clearly see the saturation after 30 minutes. After this time, the cis-trans isomerization of azobenzene surfactant in water in the presence of gold nanoparticles, via thermal relaxation in the dark, was essentially complete. Without gold nanoparticles, this process requires around a week (see **Figure 6.4**). Therefore, gold nanoparticles dramatically increase the rate of azobenzene thermal cis-trans isomerization in solution.

Figure 6.5b shows the results of similar experiments on cis-trans thermal isomerization of azobenzene containing surfactant AzoC$_6$ in the presence of gold nanoparticles at different σ values, all corresponding to the region III of the phase diagram in **Figure 4.8**. One can see that saturation in spectral changes occured after longer time in the systems with higher σ. For instance, saturation in the absorption spectra at σ = 8 (**Figure 6.6**) occured after a day, while in the system at σ = 1.5 cis-trans relaxation required less than an hour.

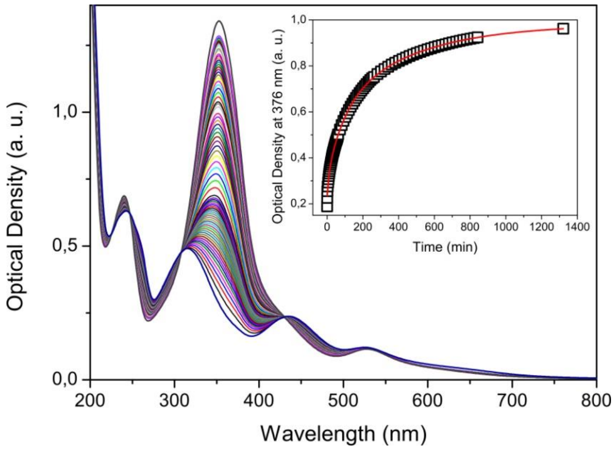

Figure 6.6. Evolution over time of absorption spectra of UV-irradiated azobenzene containing surfactant AzoC$_6$ in the presence of 10-nm gold nanoparticles at σ = 8. The inset shows time dependency of optical density at 376 nm.

In order to quantitatively describe the influence of gold nanoparticles on surfactant isomerization rates, we performed exponential fit of optical density at 376 nm as a function of time $D_{376}(t)$. Gold absorption does not change over time and therefore contributes into D_{376} only as a constant. A reliable fit of experimental points using monoexponential decay was achieved only in few cases. Hence, the multiexponential fit was used:

$$D_{376}(t) = D_0 + D_1 e^{-t/\tau_1} + D_2 e^{-t/\tau_2} + \cdots \qquad (6.1)$$

Usually biexponential representation was required to fit thermal relaxation kinetics in the presence of gold nanoparticles. From the exponential fitting, one can estimate the lifetime τ of cis-isomers of azobenzene containing surfactants in the presence of gold nanoparticles. The results for gold-surfactant systems at different values of σ are summarized in **Table 6.1**.

Table 6.1. Thermal lifetimes of cis-isomers of azobenzene containing surfactant AzoC$_6$ in the presence of gold nanoparticles at different σ values.

Lifetime, min	σ = 0.6	σ = 0.7	σ = 1.5	σ = 8	Average σ < 2
τ_1	2.1 ± 0.1	2.5 ± 0.4	2.4 ± 0.1	8.8 ± 0.6	2.3 ± 0.2
τ_2	-	10.7 ± 2.9	9.6 ± 0.1	94.2 ± 4.4	10.2 ± 1.5

τ_3	-	-	-	442 ± 21	

At $\sigma = 0.6$ kinetics had first-order fashion, the monoexponential fit was accurate and yielded the lifetime $\tau_1 \approx 2$ min. For gold-surfactant systems at $\sigma = 0.7$ and $\sigma = 1.5$ biexponential fitting was necessary, exhibiting short $\tau_1 \approx 2$ min and longer $\tau_2 \approx 10$ min. The monoexponential fit yielded $\tau_1 = 6.9 \pm 0.2$ min for $\sigma = 1.5$. At $\sigma = 8$ the short time around 2 minutes was not registered, and the triexponential fit resulted in the times around 9 minutes and significantly longer. As one can see from **Table 6.1**, the short time τ_1 occurs at $\sigma < 2$, with the mean values $\tau_1 = 2.3 \pm 0.2$ min and $\tau_2 = 10.2 \pm 0.8$ min. Compared with the isomerization in water without gold nanoparticles with the lifetime $\tau_0 \approx 62$ h, thermal isomerization of AzoC$_6$ surfactant is accelerated by three orders of magnitude in the presence of gold nanoparticles.

These results indicate that the interaction with gold nanoparticle surface is responsible for the acceleration of azobenzene thermal isomerization. Consequently, the fact that the fast mode $\tau_1 \approx 2$ min was not detected at $\sigma = 8$ is not surprising. There are more free azobenzene molecules in solution at higher σ value, so that the fraction of azobenzene surfactant molecules interacting with gold surfaces is lower. The overwhelming contribution of the slow relaxation of free surfactant molecules in solution suppresses the term of rapid isomerization in the overall absorption. Indeed, the longer relaxation times τ_2, τ_3 at $\sigma = 8$ are on the scale of the lifetime τ_0 in solution without gold nanoparticles.

Thus, the optimal concentrations to study the acceleration of thermal cis-trans isomerization of azobenzene surfactants appear to be $1 \leq \sigma \leq 2$ with sufficient gold concentration, so that azobenzene isomerization and gold colloidal stability can be tracked simultaneously, plasmon coupling mode is not detected in the absorption spectra, and the short lifetime of cis-isomers τ_1 can be revealed.

6.3. UV-irradiated complexes between gold nanoparticles and azobenzene surfactant in trans-conformation

Thermal cis-trans isomerization of azobenezene containing surfactant AzoC$_6$ has been investigated in complexes with 10-nm gold nanoparticles initially prepared with trans-isomers at $\sigma = 1.5$ (region III of phase diagram in **Figure 4.8**). As discussed in Chapter 4, at such conditions gold nanoparticles are decorated with a double layer of surfactant trans-isomers. In solution, azobenzene molecules are also in the trans- photostationary state. The suspension has been exposed to UV irradiation, followed by recording its time-dependent absorption spectra. The results are shown in **Figure 6.7a**. One can observe the acceleration of surfactant cis-trans isomerization in the dark. The plasmonic chain mode at $\lambda \approx 625$ nm appeared as a shoulder in the absorption spectra after UV irradiation, in agreement with Section 5.1. For comparison, the experiment was twice conducted with the complexes prepared with UV-irradiated surfactant after their fast thermal relaxation into the predominantly trans-state (resulting gold-surfactant complexes from the previous Section), when these complexes were re-exposed to UV light. **Figure 6.7b** shows the resulting optical densities over time $D_{376}(t)$.

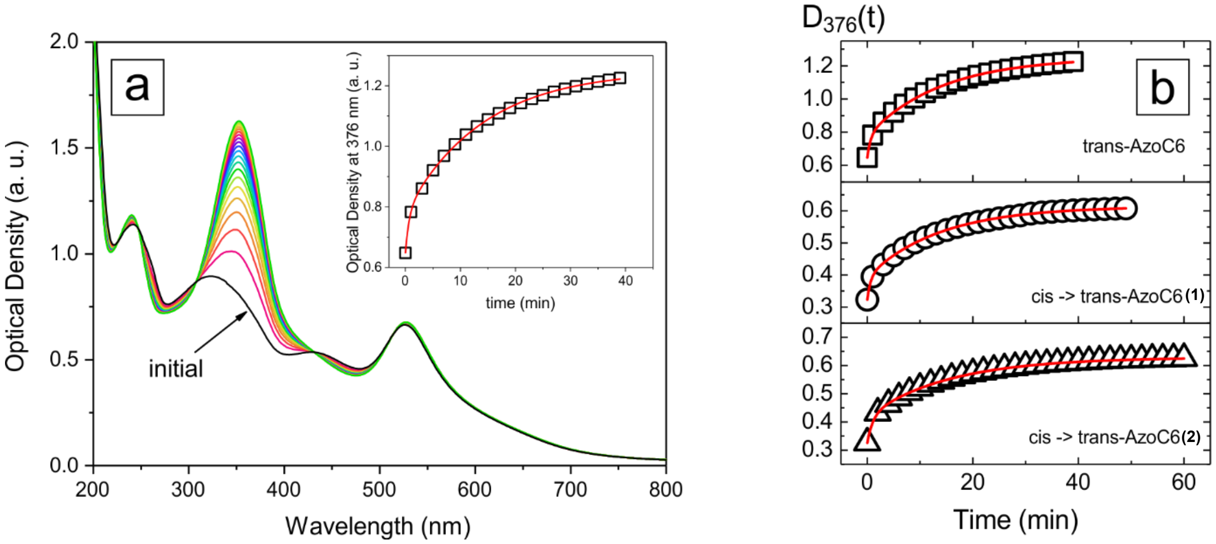

Figure 6.7. (a) UV-Vis absorption spectra of UV-irradiated complexes between 10-nm gold nanoparticles and azobenzene containing surfactant AzoC$_6$ prepared at σ = 1.5. The spectra were recorded over time. The inset demonstrates the evolution of optical density at 376 nm D$_{376}$(t) (symbols) and its biexponential fit (red line). (b) Optical densities at 376 nm as functions of time (symbols) and their biexponential fits (red lines) for UV-irradiated gold-surfactant complexes at σ = 1.5, prepared with surfactant trans-isomers (on the top, squares), and initially cis-isomers after their thermal relaxation to the trans-state (circles and triangles).

Biexponential fits of optical density D$_{376}$(t) were accurate and yielded two relaxation times, as summarized in **Table 6.2**. One can see that the thermal isomerization times are similar for the gold-surfactant complexes prepared with trans-isomers (non-irradiated surfactant) and cis-isomers (UV-irradiated surfactant) after their conversion into trans-state. Average times are $\tau_1 = 0.8 \pm 0.1$ min and $\tau_2 = 14.4 \pm 0.5$ min. This implies the similar configuration of the compared complexes, and thus the formation of surfactant double layers on gold nanoparticle surfaces upon the gold-enhanced cis-trans thermal isomerization of azobenzene surfactant. Trans-azobenzene surfactant molecules in the stabilizing double-layer shell on nanoparticle surface are capable of photoisomerization with the following destabilization of the shell (see Chapter 5). UV-produced surfactant cis-isomers rapidly isomerize back to trans-conformation on gold surfaces and probably fill in surfactant double layers. Indeed, nanoparticles did not aggregate during the thermal isomerization, indicated by the intact gold plasmon peak.

Table 6.2. Lifetimes of cis-isomers in UV-irradiated gold-surfactant complexes at σ = 1.5, prepared with non-irradiated surfactant AzoC$_6$ (trans-AzoC$_6$), and in the complexes prepared with UV-irradiated surfactant AzoC$_6$, re-irradiated with UV light after their thermal relaxation (cis → trans-AzoC$_6$).

Lifetime, min	trans-AzoC$_6$	cis → trans-AzoC$_6$ (1)	cis → trans-AzoC$_6$ (2)	Average
τ_1	0.7 ± 0.1	0.6 ± 0.1	1.1 ± 0.1	0.8 ± 0.1
τ_2	14.1 ± 0.4	13.7 ± 0.2	15.5 ± 0.2	14.4 ± 0.5

The revealed relaxation times are slightly different from those in the previous Section. The difference between the experiments is the following. In the previous Section, gold nanoparticle surface was initially "bare" (neglecting 12 % of trans-isomers in the UV-photostationary state), and the trans- surfactant shell was forming during surfactant cis-trans thermal isomerization. In this Section, trans- surfactant double-layer shells were formed on nanoparticle surfaces prior to UV irradiation, and thus the thermal cis-trans isomerization within the UV-destabilized surfactant shells was observed. That means, destabilization of surfactant double layer opens active surface sites on gold nanoparticles to switch azobenzene molecules from cis- to trans-conformation.

In the next Section, preformed trans-surfactant double-layer shells on gold nanoparticle surfaces were preserved.

6.4. Exchange of isomers of azobenzene surfactant on gold nanoparticle surface

In the following experiment, it has been tested whether cis- and trans- surfactant isomers can exchange on gold nanoparticle surface and compete for binding to active surface sites. Complexes between 10-nm gold nanoparticles and trans-azobenzene surfactant AzoC$_6$ prepared at $\sigma = 0.8$ (region III) were added to UV-irradiated AzoC$_6$ surfactant solution (cis-conformation) and its absorption spectra were recorded in the dark over time.

Absorption spectrum of prepared gold-surfactant complexes at $\sigma = 0.8$ is shown in **Figure 6.8a**. The prepared system has been three times diluted with water to record the spectrum. The spectrum looks typical for gold-surfactant complexes from region III of the phase diagram in **Figure 4.8** with trans-azobenzene absorption maximum at $\lambda = 353$ nm and gold plasmon peak at $\lambda = 527$ nm. To remind it to the reader, the constitution of gold-surfactant complexes in region III is schematically shown in the inset in **Figure 6.8a**, represented by a gold particle decorated with the surfactant bilayer. **Figure 6.8b** shows the spectra of UV-irradiated AzoC$_6$ surfactant mixed with gold-surfactant complexes with $\sigma = 0.8$ (solid lines). For comparison, the spectrum of cis-surfactant just mixed with "bare" gold nanoparticles form another experiment is shown as grey dash line. Addition of azobenzene trans-isomers from the gold-surfactant suspension decreased the percentage of cis-isomers in the UV-irradiated surfactant solution from roughly 88 % (without surfactant-decorated gold nanoparticles) to 72 % (with surfactant-decorated gold nanoparticles). This explains the pronounced increase in the intensity and the red shift of the surfactant π-π* peak registered immediately after mixing with surfactant-decorated nanoparticles compared to "bare" particles, when 88 % of cis- isomers remain after mixing.

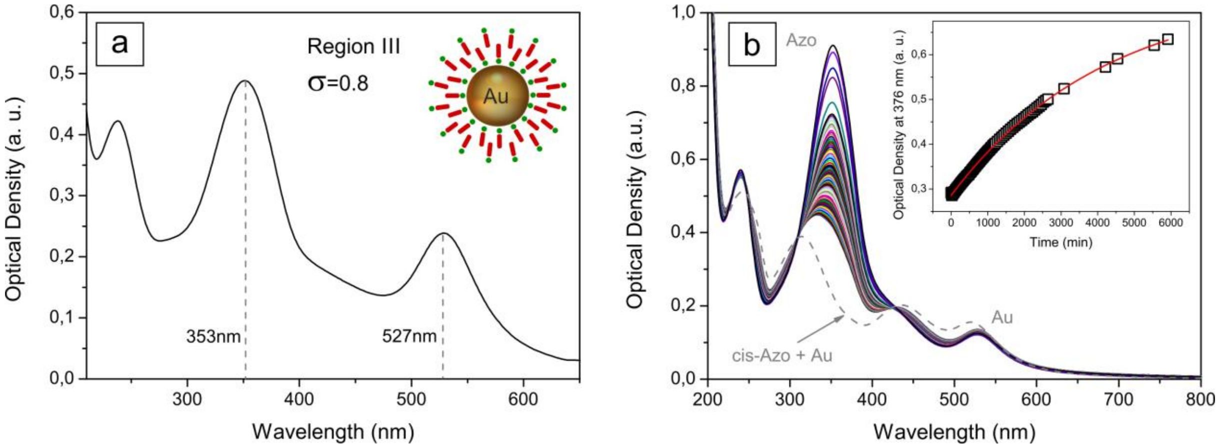

Figure 6.8. (a) Absorption spectrum of 10-nm gold nanoparticles mixed with azobenzene containing surfactant AzoC$_6$ at $\sigma = 0.8$. The inset shows a sketch of the prepared gold-surfactant complexes. (b) Evolution of absorption spectra of UV-irradiated azobenzene containing surfactant AzoC$_6$ after mixing with surfactant-decorated gold nanoparticles with $\sigma = 0.8$. The inset shows the time dependency of optical density at 376 nm, demonstrating a slow cis-trans isomerization rate. For comparison, the grey dashed line shows the initial spectrum of UV-irradiated AzoC$_6$ surfactant mixed with "bare" gold nanoparticles.

The slow kinetics of thermal isomerization of AzoC$_6$ followed the first-order trend (the inset in **Figure 6.8b**). Calculated from the monoexponential fit of $D_{376}(t)$, thermal relaxation time (lifetime) of cis- azobenzene surfactant AzoC$_6$ in the presence of trans-surfactant-decorated gold nanoparticles $\tau = 70.35 \pm 0.98$ h. This value is close to the relaxation time of the surfactant in water without gold nanoparticles, indicating that cis-molecules in solution do not exchange with trans-surfactants attached to gold surface. Furthermore, aggregation of nanoparticles did not occur. If cis-molecules would replace trans-isomers in the outer layer of surfactant shell, it would destabilize the double layer. Hypothetically, after the exchange with trans-isomers in the outer layer, cis-isomers could rapidly convert to trans-state in order to stabilize the system. For instance, such conversion could be attributed to the cooperativity effect in the densely packed double layer. However, the increase of the isomerization rate was not registered experimentally.

Therefore, (i) thermal cis-trans isomerization is enhanced by the interaction with gold nanoparticle surface; (ii) cis-isomers of surfactant unlikely exchange with trans-isomers attached to gold surface. In this experiment, the preliminarily formed surfactant double-layer shell blocked active sites on gold nanoparticle surface.

6.5. Influence of surfactant tail length

In order to better understand the phenomenon of the enhanced cis-trans isomerization of azobenzenes in the presence of gold nanoparticles, experiments have been conducted with azobenzene containing surfactants with fine tuned chemical structure. It might be worth it to mention that in further experiments another batch of 10-nm gold particles was used. Although their geometry, charge and optical properties do not differ (see Section 4.2), variation in surface chemistry might influence the interaction with azobenzenes. Yet, this was not the case. In this section, azobenzene containing surfactants differed in tail length by two -CH$_2$ groups. Similar to AzoC$_6$ surfactant, azobenzene containing surfactants AzoC$_8$, AzoC$_{10}$ and AzoC$_{12}$ were exposed to UV light and mixed with 10-nm gold nanoparticles. Absorption spectra of surfactants, periodically recorded in the dark in the presence of gold nanoparticles, demonstrated accelerated cis-trans isomerization of azobenzenes.

Figure 6.9a shows evolution of absorption spectra of UV-irradiated azobenzene containing surfactant AzoC$_8$ mixed with gold nanoparticles at $\sigma = 1.6$. Optical density at 376 nm *vs.* time is shown in the inset in **Figure 6.9a** and in **Figure 6.9b** (squares). **Figure 6.9b** demonstrates that the monoexponential fit (blue line) is not suitable for the quantitative analysis. The accurate biexponential fit (red line) provides the values of relaxation time for AzoC$_8$ $\tau_1 = 2.8 \pm 0.2$ min and $\tau_2 = 25 \pm 2$ min.

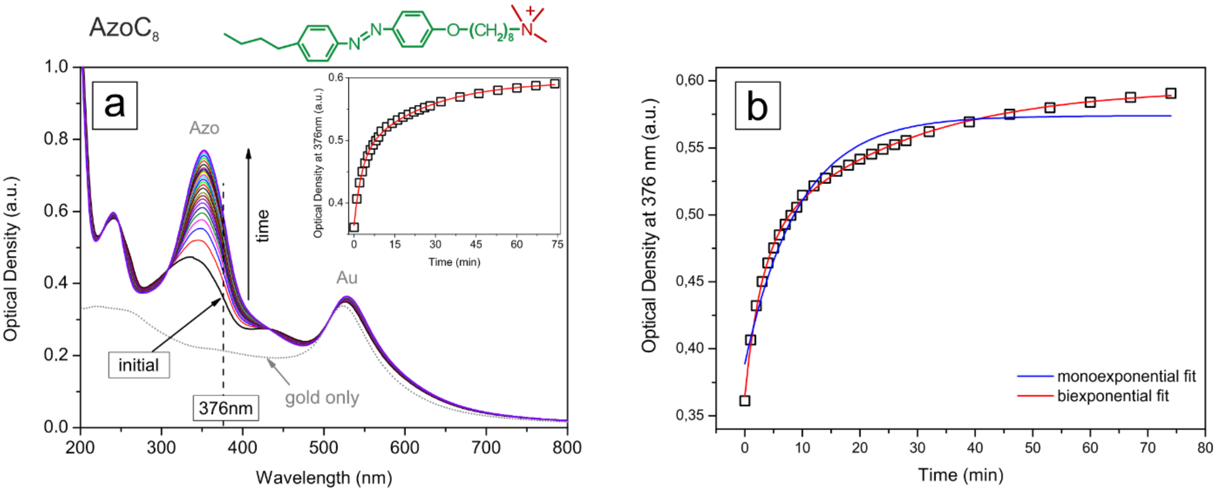

Figure 6.9. (a) Absorption spectra of UV-irradiated surfactant AzoC$_8$, recorded over time in the presence of 10-nm gold nanoparticles. C(AuNP) = 0.1mM, C(AzoC$_8$) = $2.8 \cdot 10^{-5}$M, $\sigma = 1.6$. Chemical structure of the surfactant is shown on top. The inset shows time dependency of optical density at 376 nm, recorded experimentally (open squares) and biexponentially fitted (red line). (b) The comparison of mono- (blue line) and biexponential fit (red line) of optical density at 376 nm *vs.* time (open squares) for cis-trans isomerization of UV-irradiated AzoC$_8$ surfactant in the presence of 10-nm gold nanoparticles.

Absorption spectra and evolution of optical density at 376 nm for UV-irradiated AzoC$_{10}$ and AzoC$_{12}$ surfactants in the presence of gold nanoparticles are shown in **Figure 6.10**.

One can notice that the π-π* absorption maximum of AzoC$_{12}$ does not shift toward $\lambda = 353$ nm. This is because π-π* maximum of AzoC$_{12}$ in trans-conformation is blue-shifted. **Figure 6.11a** shows absorption spectra of azobenzene containing surfactant AzoC$_{12}$ before and after exposure to UV light. Absorption maximum of its trans-isomer is located at $\lambda = 333$ nm. At the same time, absorption maximum at $\lambda = 353$ nm can be recognized, and the spectrum of the UV irradiated AzoC$_{12}$ surfactant has the same features as for AzoC$_6$ (red line in **Figure 6.11a**). Such blue shift of the absorption maximum indicates formation of H-aggregates and typically occurs for azobenzene surfactants at concentrations above CMC. Indeed, the used concentration $C_{Azo} = 0.03$ mM might already be above CMC for AzoC$_{12}$ surfactant, according to the trend in Ref. 5. However, it does not influence the analysis of the spectral evolution in the presence of gold nanoparticles, since optical density at 376 nm remains unaffected. **Figure 6.11b** demonstrates once more strikingly, that the surfactant thermal isomerization in the presence of gold nanoparticles required biexponential fitting.

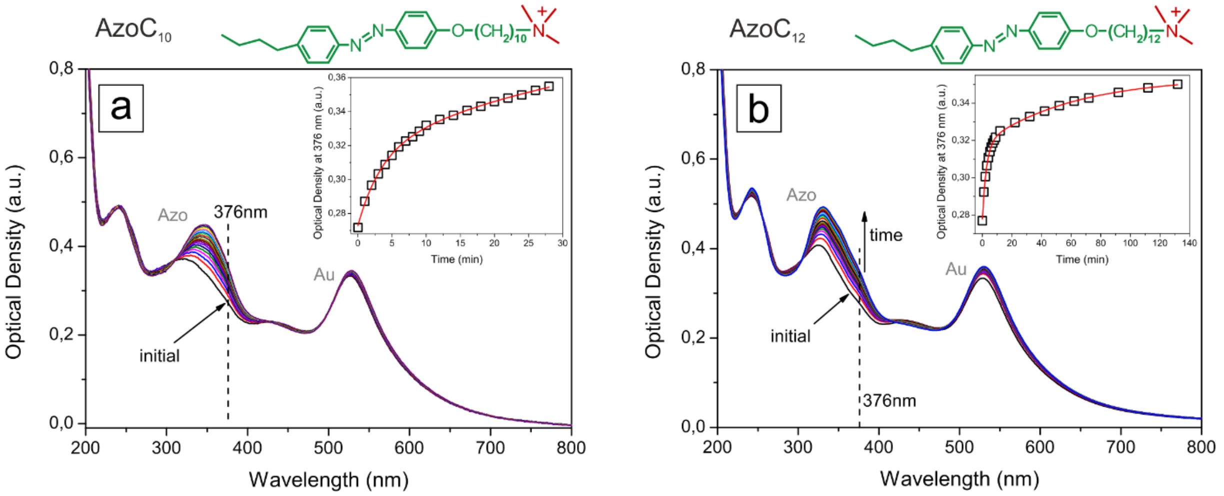

Figure 6.10. Absorption spectra of UV-irradiated azobenzene containing surfactants AzoC$_{10}$ (a) and AzoC$_{12}$ (b), recorded over time in the dark in the presence of 10-nm gold nanoparticles. Chemical structures of AzoC$_{10}$ and AzoC$_{12}$ surfactants are shown on the top in (a) and (b) respectively. The insets shows time dependency of optical density at 376 nm, measured experimentally (open squares) and exponentially fitted (red line). (a) $C_{Au} = 0.1$mM, $C(AzoC_{10}) = 2.2 \cdot 10^{-5}$ M, $\sigma = 1.3$ (b) $C_{Au} = 0.09$mM, $C(AzoC_{12}) = 2.75 \cdot 10^{-5}$ M, $\sigma = 1.8$.

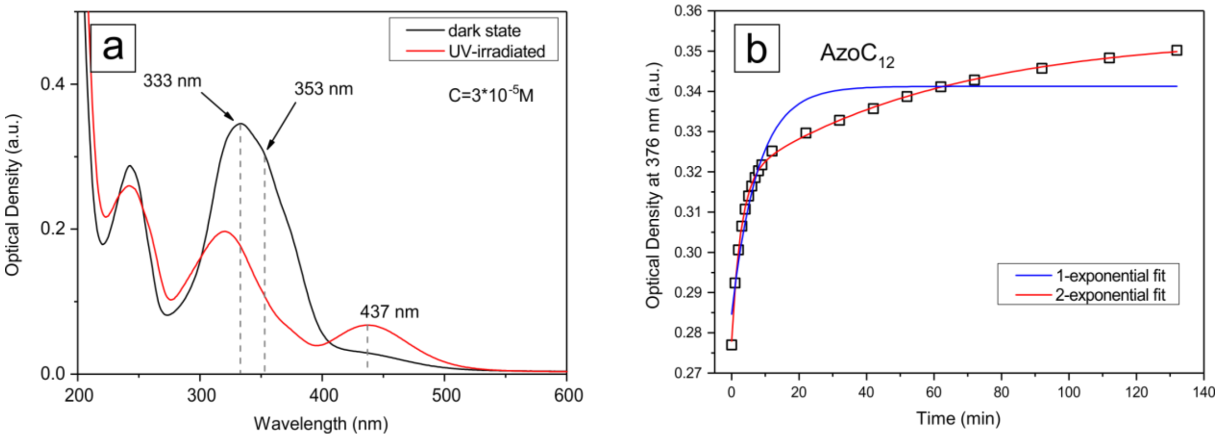

Figure 6.11. (a) Absorption spectra of azobenzene containing surfactant AzoC$_{12}$ before (black curve) and after UV-irradiation (red curve). $C_{Azo} = 0.03$ mM. (b) The comparison of mono- (blue line) and biexponential fit (red line) of optical density at $\lambda = 376$ nm *vs.* time (open squares) for cis-trans isomerization of UV-irradiated azobenzene containing surfactant AzoC$_{12}$ in the presence of 10-nm gold nanoparticles.

Table 6.3 lists relaxation times of cis-isomers in the dark in the presence of 10-nm gold nanoparticles for azobenzene containing surfactants with 6, 8, 10 and 12 CH$_2$ groups in the spacers between azobenzene units and cationic heads. One can see that the value of τ_1 (fast mode) is similar for all four surfactants, with the mean value $\tau_1^{av} = 2.8 \pm 0.3$ min. It indicates that the surfactant tail length does not influence the fast mode of cis-trans isomerization in the presence of gold nanoparticles, while the longer time τ_2 increases with the increasing distance between the cationic head and the azobenzene moiety.

Table 6.3. Lifetimes of cis-isomers of azobenzene surfactants differing in tail length in the presence of 10-nm gold nanoparticles.

Lifetime, min	AzoC$_6$ $0.5 < \sigma < 2$	AzoC$_8$ $\sigma = 1.6$	AzoC$_{10}$ $\sigma = 1.3$	AzoC$_{12}$ $\sigma = 1.8$	Average
τ_1	2.3 ± 0.2	2.8 ± 0.2	3.4 ± 0.5	2.7 ± 0.1	2.8 ± 0.3
τ_2	10.2 ± 0.8	25 ± 2	38 ± 29	61 ± 6	-

6.6.Influence of surfactant head structure

The following experiments tested the influence of surfactant head structure on its cis-trans isomerization in the presence of gold nanoparticles.

Azobenzene containing triethylammonium bromide (AzoC$_6$-TEAB) is structurally very similar to AzoC$_6$, despite that it has ethyl groups instead of methyl in the positively charged head. Absorption spectra of aqueous solutions of this surfactant (**Figure 6.12a**) are identical to those of AzoC$_6$. Kinetics of its cis-trans isomerization in water in dark without gold nanoparticles is shown in **Figure 6.12b**. Thermal relaxation time of AzoC6-TEAB without gold particles is found to be $\tau_0 = 77 \pm 3$h. This value is slightly larger than $\tau_0 = 62 \pm 1$h, occurred for azobenzene containing trimethylammonium bromide surfactants AzoC$_n$.

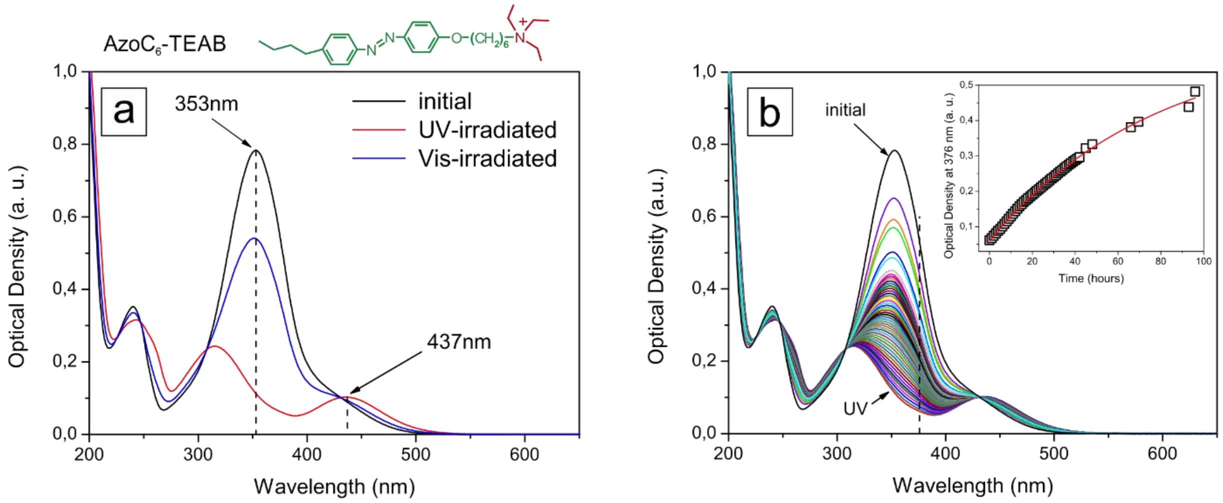

Figure 6.12. (a) Absorption spectra of AzoC$_6$-TEAB surfactant aqueous solution in the dark state (black), irradiated with UV light (red), and subsequently irradiated with blue light (blue). (b) Absorption spectra of UV-irradiated aqueous solution of AzoC$_6$-TEAB recorded over time during its thermal relaxation in the dark. Black curve shows the absorption spectrum before UV irradiation, in the initial dark state. The inset shows optical density at 376 nm as a function of time, as recorded (squares) and exponentially fitted (red curve). C(AzoC$_6$-TEAB) = $3 \cdot 10^{-5}$ M.

Figure 6.13. demonstrates rapid cis-trans isomerization of AzoC$_6$-TEAB in the presence of gold nanoparticles. Cis-trans relaxation times are estimated to be $\tau_1 = 1.3$ min and $\tau_2 = 5.2$ min, what is almost two times shorter than for AzoC$_6$. It indicates that the properties of the surfactant head are the most decisive factor for azobenzene isomerization on gold surface.

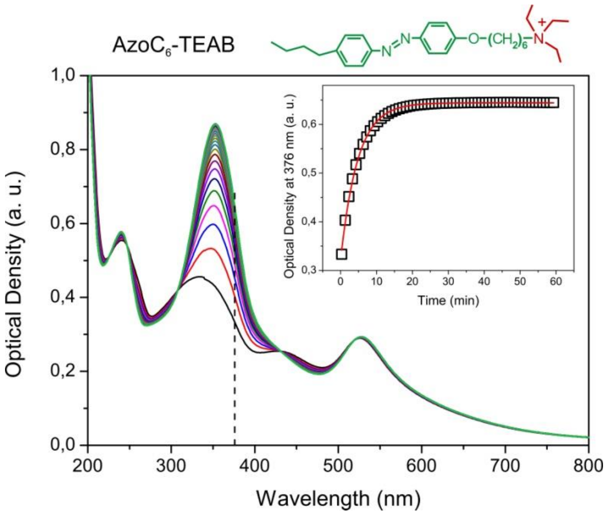

Figure 6.13. Evolution over time of absorption spectra of UV-irradiated surfactant AzoC$_6$-TEAB in water in the presence of 10-nm gold nanoparticles. Optical density at 376 nm *vs.* time in the inset demonstrates rapid cis-trans isomerization of surfactant. $C_{Azo} = 3 \cdot 10^{-5}$ M, $C_{Au} = 0.09$ mM, $\sigma = 2$.

When a cationic surfactant molecule interacts with the negatively charged gold particle surface, two processes are possible: (i) electrostatic attraction between the gold surface and the surfactant head, and their ionic binding, (ii) adsorption of the N=N bond to the gold surface and a charge transfer between them. In order to reveal the role of the electrostatic attraction between surfactant heads and gold particle surfaces, cis-trans thermal relaxation experiments were performed with 4-nitroazobenzene possessing negative charge in solution.

Figure 6.14 shows absorption spectra, chemical structure, and thermal isomerization kinetics of 4-nitroazobenzene (Nitro-Azo) alcohol solution. As one can see from **Figure 6.14a**, absorption band of Nitro-Azo is blue-shifted in comparison with AzoC$_n$ surfactants, with the main absorption maximum at $\lambda_{max} = 328$ nm. Therefore, due to a low absorption intensity at $\lambda = 376$ nm, the analysis of the cis-trans isomerization kinetics (**Figure 6.14b**) has been performed at $\lambda = 360$ nm. Thermal relaxation time of Nitro-Azo $\tau_0 \approx 345$ min.

Figure 6.15a shows cis-trans thermal relaxation of 4-nitroazobenzene in the presence of gold nanoparticles. Relaxation time of Nitro-Azo was found to be accelerated by gold particles, $\tau_1 \approx 3.5$ min. This gives evidence for the interaction of N=N bond of azobenzenes with the "bare" surfaces of laser ablated gold nanoparticles. The plasmonic band of gold changed due to changes in solvent properties upon mixing aqueous nanoparticle suspension with alcohol surfactant solution, as shown in **Figure 6.15b**. Concentrated gold aqueous colloid has been diluted with pure methanol, so that the solvent (water) has been replaced by alcohol. To be precise, end solvent was methanol-water mixture with around 90 % of methanol. The bathochromic shift in the gold plasmon peak position has been registered already in a minute after the solvent replacement. The color of the nanoparticle suspension turned purple (the inset in **Figure 6.15b**). Precipitation of gold nanoparticles did not occur and thus the changes in the gold plasmonic band did not influence the quantitative analysis of Nitro-Azo thermal isomerization.

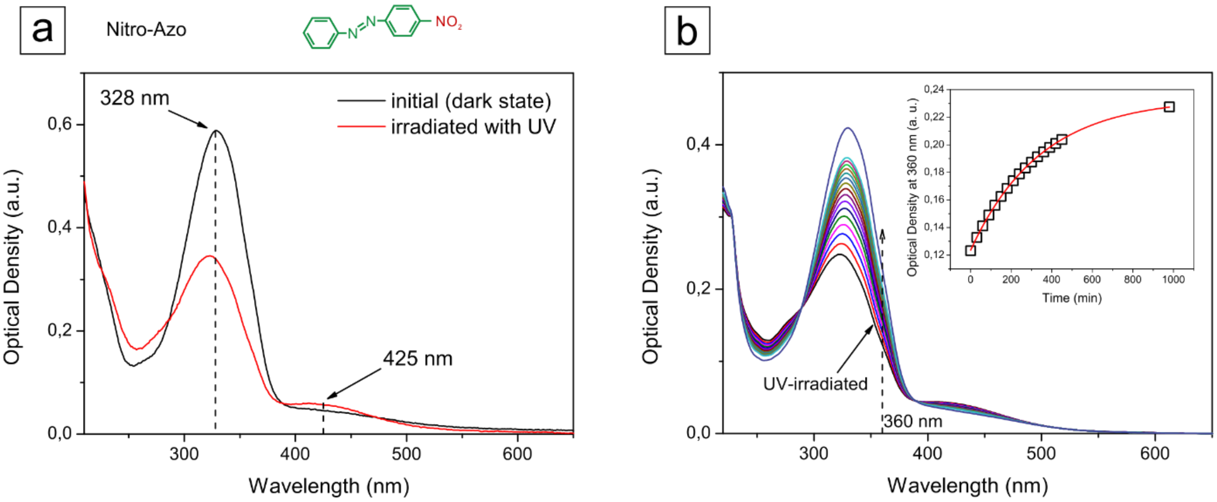

Figure 6.14. (a) Absorption spectra of 4-nitroazobenzene in methanol before (black) and after UV irradiation (red), C_{Azo} = 0.018 mM. The chemical structure of 4-nitroazobenzene is shown on the top. (b) Absorption spectra of UV-irradiated 4-nitroazobenzene in methanol, periodically recorded over time upon its thermal relaxation. The corresponding plot of optical density at 360 nm over time is shown in the inset.

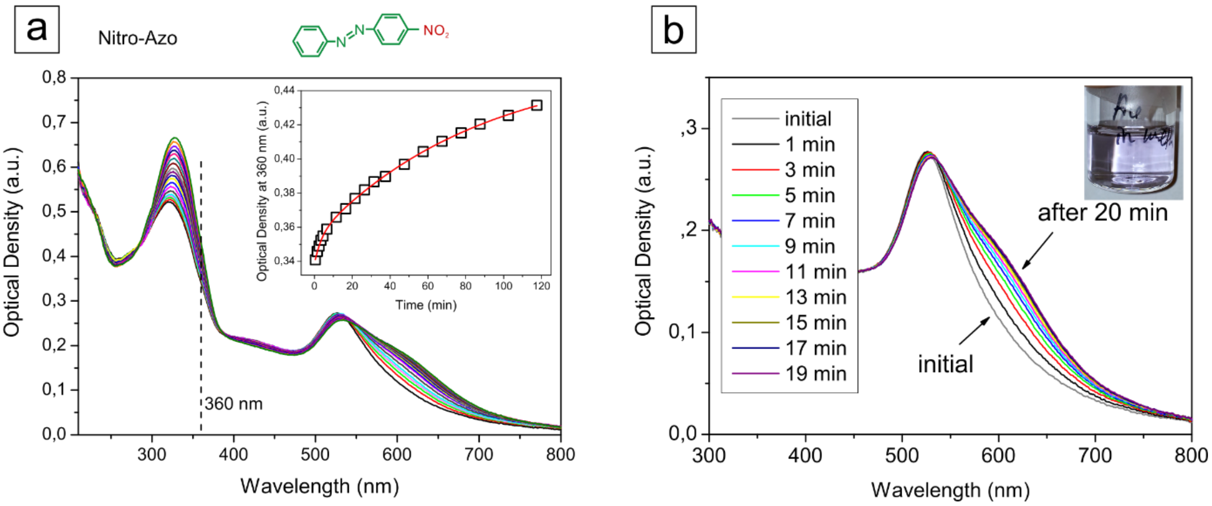

Figure 6.15. a) Absorption spectra of preliminarily UV-irradiated 4-nitroazobenzene in the presence of gold nanoparticles, recorded over time. $C_{Azo} = 1.7 \cdot 10^{-5}$ M, C_{Au} = 0.09 mM, σ = 1.1. The inset shows optical density at λ = 360 nm as a function of time. b) Evolution of absorption spectrum of gold nanoparticles in methanol, C_{Au} = 0.09 mM. The grey line ("initial") is the spectrum right after the water-to-alcohol solvent replacement. The inset demonstrates purple color of the gold nanoparticle alcohol suspension.

6.7. Influence of surfactant charge

The influence of charge properties of the surfactant head on its gold nanoparticle-enhanced thermal relaxation was studied using azobenzene containing di-, tri-, and tetra-amine surfactants (AzoEn, AzoDeta, AzoTren respectively). Positive charge of amino groups in the surfactant head can be tuned by pH. At working conditions pH was neutral, and the studied azobenzene containing polyamines acquired +1.5, +2 and +3 charges (**Table 6.4**).[20]

Table 6.4. pH values and surfactant charges in azobenzene surfactant solutions mixed with 10-nm gold nanoparticles.

Surfactant	$AzoC_6$	$AzoC_8$	$AzoC_{10}$	$AzoC_{12}$	AzoEn	AzoDeta	AzoTren
pH	7.0	7.0	7.05	7.1	7.1	7.0	6.7
Charge	+1	+1	+1	+1	+1.5	+2	+3

Absorption spectra and photoisomerization behaviour of azobenzene containing polyamines are similar to those of azobenzene containing trimethylammonium bromides $AzoC_n$ (**Figure 6.16**). The spectra in **Figure 6.16a,c** recorded for AzoEn, containing two amino groups, and AzoTren with four amino groups in the head, show absorption maxima of trans-isomers at 350 nm, 3-nm blue-shifted compared to $\lambda = 353$ nm for $AzoC_n$ and AzoDeta with three amino groups. The spectroscopic behaviour of the studied azobenzene containing polyamines is described in details in the PhD thesis of Selina Schimka.[g] The centers of the absorption maxima of azobenzene containing polyamines in trans-conformation are not relevant for the quantitative analysis of their cis-trans isomerization in the presence of gold nanoparticles.

The results on cis-trans isomerization of azobenzene containing polyamines in the dark in the presence of gold nanoparticles are shown in **Figure 6.17**. The calculated values of σ do not take into account surfactant charge, thus reflecting the number of surfactant molecules interacting with one gold surface atom, but not the surfactant-to-gold charge ratio. Relaxation times for AzoEn ($\tau_1 = 9.7$ min, $\tau_2 = 394$ min) and AzoDeta ($\tau_1 = 9.4$ min, $\tau_2 = 342$ min) are similar, what can be explained by similar charge of the head group (their tails do not differ). Relaxation of AzoTren takes longer with $\tau_1 = 137$ min. Apparently, relatively strong ionic binding between AzoTren heads and gold particles hinders the interaction between azo bonds in the surfactant tails and gold nanoparticle surfaces.

---

[g] in preparation in the group of Prof. Santer

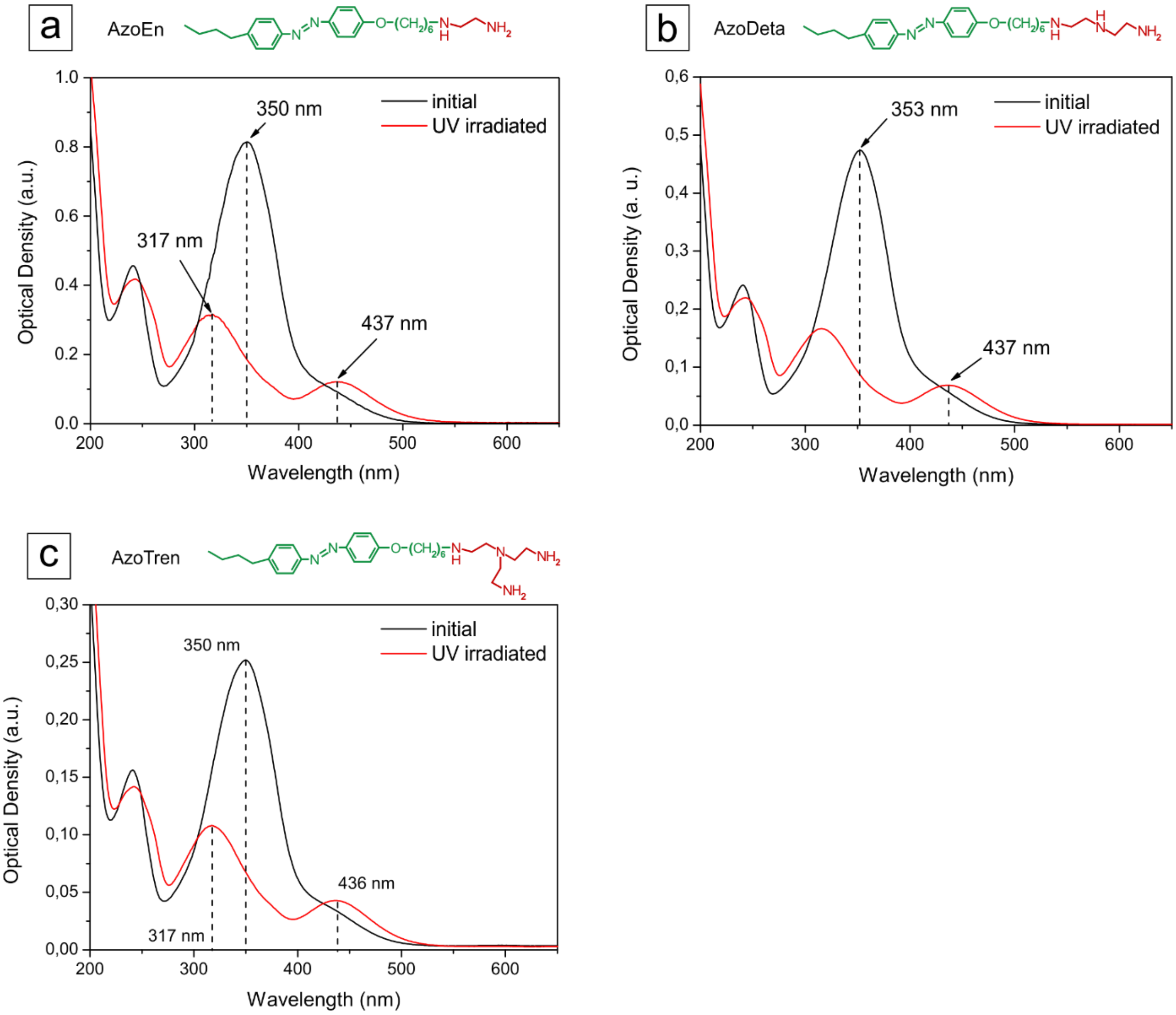

Figure 6.16. UV-Vis Absorption spectra of azobenzene containing polyamines AzoEn (a), AzoDeta (b) and AzoTren (c) before (black curves) and after UV irradiation (red curves). Chemical structures of surfactants are shown on the top. C(AzoEn) = 5×10^{-5} M, C(AzoDeta) = 2.3×10^{-5} M, C(AzoTren) = 2.5×10^{-5} M.

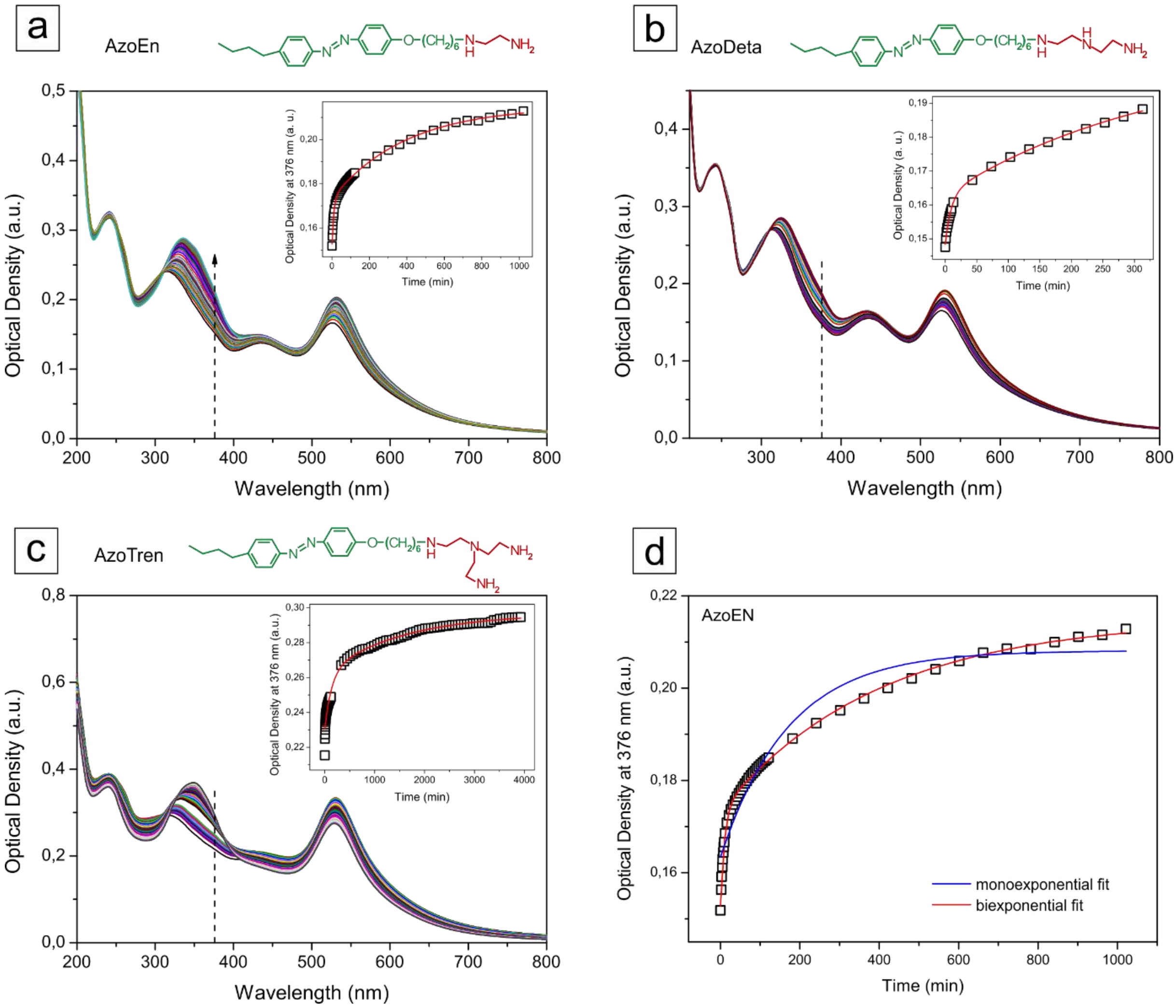

Figure 6.17. Time dependent absorption spectra of UV-irradiated azobenzene containing polyamine surfactants upon their thermal relaxation in the dark in the presence of 10-nm gold nanoparticles: (a) AzoEn, $C_{Azo} = 2.4 \times 10^{-5}$ M, $C_{Au} = 4.8 \times 10^{-5}$ M, $\sigma = 3$; (b) AzoDeta, $C_{Azo} = 2.2 \times 10^{-5}$ M, $C_{Au} = 4.8 \times 10^{-5}$ M, $\sigma = 2.5$; (c) AzoTren, $C_{Azo} = 1.9 \times 10^{-5}$ M, $C_{Au} = 8 \times 10^{-5}$ M, $\sigma = 1.4$. Chemical structures of surfactants are shown on the top, respectively. The insets show optical densities at $\lambda = 376$ nm over time, measured experimentally (open squares) and biexponentially fitted (red line). The difference between mono- and biexponentional fit is shown in (d) for AzoEn isomerization.

Azobenzene containing peptidomimetic surfactant (Azo-PM) has a bulky peptide-like cationic head (structure in **Figure 3.1g**). At working pH ≈ 7 it carries triple positive charge. Absorption spectra of Azo-PM surfactant in dark and UV- photostationary state are shown in **Figure 6.18a**. In dark state (black line), π-π* absorption maximum of the surfactant is located at $\lambda = 333$ nm. Isomerization behaviour of this surfactant is described in details in Ref. 196. Absorption spectra of UV-irradiated Azo-PM upon thermal relaxation in dark in the presence of gold nanoparticles are shown **Figure 6.18b**. Relaxation time $\tau_1 = 6$ min has been calculated from the exponential fit of time dependency of optical density at $\lambda = 360$ nm (the inset in **Figure 6.18b**), since $\lambda = 376$ nm is very close to isobestic point in absorption spectra. Although both surfactant carry the same +3 charge at working conditions, opposed to AzoTren, thermal relaxation of Azo-PM is sufficiently enhanced by gold nanoparticles.

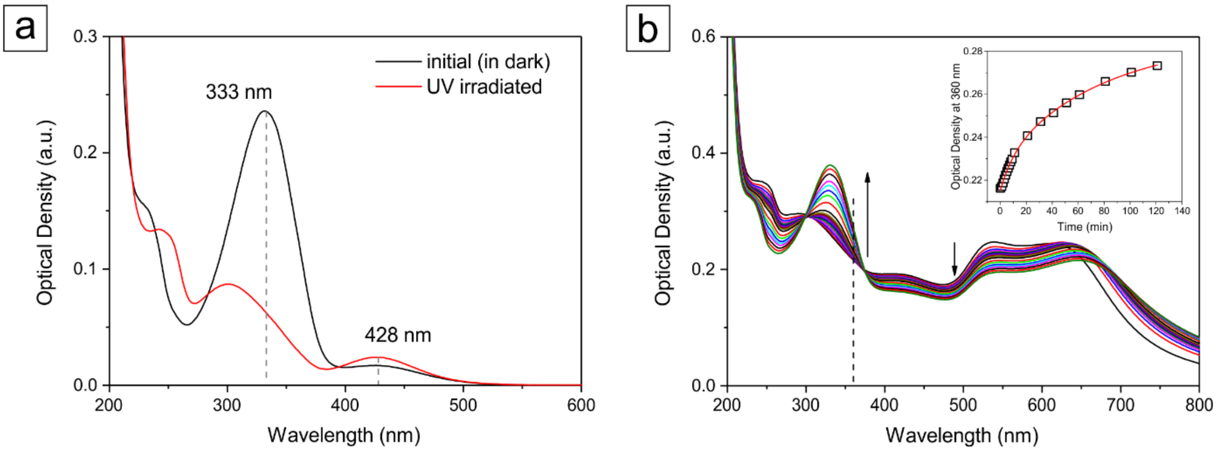

Figure 6.18. (a) Absorption spectra of azobenzene containing peptidomimetic in the initial dark state (black line) and exposed to UV irradiation (red line). $C_{Azo} = 2.2 \times 10^{-5}$ M. (b) Periodically recorded absorption spectra of UV-irradiated azobenzene containing peptidomimetic mixed with 10-nm gold nanoparticles. The inset shows optical density at $\lambda = 360$ nm over time, experimentally measured (open squares) and exponentially fitted (red line). $C_{Azo} = 2 \times 10^{-5}$ M, $C_{Au} = 0.09$ mM, $\sigma = 1.3$.

6.8.Summary

Thermal relaxation times of azobenzene containing surfactants in the presence of gold nanoparticles are summarized in **Table 6.5**. In all cases, gold particles drastically accelerated surfactant thermal relaxation in the dark, although the structures of the surfactants differ significantly (**Figure 3.1**). Indeed, surfactants AzoC$_6$, AzoC$_8$, AzoC$_{10}$, AzoC$_{12}$ differ by the number of CH$_2$ groups in the spacer between azobenzene unit and cationic trimethylammonium head. Surfactants AzoC$_6$, AzoC$_6$-TEAB, AzoEn, AzoDeta, AzoTren have the same azobenzene containing tail with 6 CH$_2$ groups in the spacer and differ by head groups. For AzoC$_6$, mean values for $0.5 < \sigma < 2$ are shown.

Our results, in agreement with literature reports, demonstrate that the origin of azobenzene fast isomerization in the presence of gold nanoparticles is the interaction of their azobenzene groups with the gold surface, and thus the azobenzene-to-gold ratio is decisive for the correct comparison. The molar ratio σ reflects the ratio between azobenzene molecules and surface gold atoms. The values of σ were similar in all experiments, $1 < \sigma < 2$, *i. e.* the fraction of azobenzenes interacting with gold surface was similar for different compounds. Values of σ do not account for surfactant charge. For surfactants with charge $z > 1$, σ can be recalculated by multiplying the values by charge, to give the information about the azobenzene-to-gold charge ratio.

Lifetimes of AzoC$_n$, AzoEn, AzoDeta, AzoTren cis-isomers in solution without nanoparticles $\tau_0 = 62$ h were determined by Dr. Nino Lomadze by recording absorption spectra of UV-irradiated solutions in pure water at pH 7 over time. Two relaxation times $\tau_0 = 18$ h and $\tau_0 = 270$ h in solution of Azo-PM without nanoparticles were reported in Ref. 196. All the other numbers in **Table 6.5** were determined in the experiments above. One can notice that the inaccuracy in the lifetimes and acceleration factors is around 10 %.

Table 6.5. Acceleration of cis-trans isomerization of different azobenzene compounds in the presence of gold nanoparticles: concentration of gold in the experiment C_{Au}, surfactant-to-gold ratio σ, surfactant charge z, lifetime of cis-isomers in solution without gold τ_0, the two lifetimes in the presence of 10-nm gold nanoparticles τ_1 and τ_2, acceleration factor τ_0/τ_1.

Surfactant	C_{Au}, mM	σ	z	τ_0, h	τ_1, min	τ_2, min	τ_0/τ_1
AzoC$_6$-TMAB (AzoC$_6$)	0.2	$0.5 < \sigma < 2$	+1	62 ± 1	2.3 ± 0.2	10.2 ± 0.8	1620 ± 140
AzoC$_8$	0.1	1.6	+1	62 ± 1	2.8 ± 0.2	25 ± 2	1330 ± 100
AzoC$_{10}$	0.1	1.3	+1	62 ± 1	3.4 ± 0.5	38 ± 29	1100 ± 160
AzoC$_{12}$	0.09	1.8	+1	62 ± 1	2.7 ± 0.1	61 ± 6	1380 ± 60
AzoC$_6$-TEAB	0.09	2	+1	77 ± 3	1.3 ± 0.1	5.2 ± 0.1	3550 ± 310
Nitro-Azo	0.09	1.1	-1	5.8 ± 0.1	3.5 ± 0.5	87 ± 5	99 ± 14
AzoEn	0.05	3	+1.5	62 ± 1	9.7 ± 0.5	394 ± 16	384 ± 21
AzoDeta	0.05	2.5	+2	62 ± 1	9.4 ± 0.8	342 ± 65	396 ± 34
AzoTren	0.08	1.4	+3	62 ± 1	137 ± 14	1600 ± 270	27 ± 3
Azo-PM	0.09	1.3	+3	18 ± 2 270 ± 18	6.0 ± 1.0	81 ± 8	180 ± 36 2700 ± 490

The following observations can be made:

(i) cis-trans thermal isomerization of studied azobenzene containing surfactants is up to 3600 times accelerated by gold nanoparticles;

(ii) the biexponential fashion of azobenzene thermal isomerization in the presence of gold nanoparticles implies two first-order reactions;

(iii) the fast mode $\tau_1 < 10$ min occurred independently on surfactant structure, except for AzoTren;

(iv) the slow mode $\tau_2 > 10$ min is affected by the distance between surfactant charged head and azobenzene moiety in the tail;

(v) not taking into account AzoTren, acceleration factor for 4-nitroazobenzene (Nitro-Azo) was the smallest among studied compounds because of its shortest lifetime without gold nanoparticles τ_0 attributed to the electron-acceptor substitution.

The common mechanism for azobenzenes to interact with the gold surface is adsorption by azobenzene unit. Apparently, this is the reaction proceeding with the shorter time τ_1. Indeed, the fast mode is not influenced by surfactant tail structure: values of τ_1 are very close for all AzoC$_n$ surfactants. There are three more electron-donating CH_2 groups in the positively charged head of AzoC$_6$-TEAB. Probably this facilitates the interaction of AzoC$_6$-TEAB with gold nanoparticle surface via azobenzene unit compared to AzoC$_6$. The acceleration factor for AzoC$_6$-TEAB is the highest. Similar to AzoC$_n$ surfactants, but a slightly longer time $\tau_1 \approx 3.5$ min occurred in Nitro-Azo, probably due to its negative molecular charge and thus electrostatic repulsion from gold nanoparticles inhibiting azo bond adsorption.

The isomerization times of AzoEn and AzoDeta do not differ within error bars. Indeed, their tails are the same, and head groups possess almost the same charge properties. Chemisorption strength plays an important role in catalysis. Azobenzene containing polyamines carry stronger positive charges than surfactants AzoC$_n$ and thus their ionic binding to negatively charged gold surfaces should occur more readily, which can interfere with the interaction via azobenzene units. Indeed, the lifetime $\tau_1 \approx 9.5$ min for AzoEn and AzoDeta, and for AzoTren the fast relaxation mode does not occur at all. In fact, $\tau_1 \approx 9.5$ min might be related to $\sigma > 2$ for these polyamines, coupled with stronger ionic interaction than for AzoC$_6$, so that the fast mode is suppressed similar to AzoC$_6$ isomerization at $\sigma = 8$. Indeed, accounting for surfactant charge, the values of σ in azobenzene containing polyamines would be $\sigma_+ > 4.5$, *i. e.* the amount of trans-isomers in UV-irradiated azobenzene solutions $\sigma_+^{trans} > 0.45$, corresponding to primary trans- double layer formation. In this case, adsorption of azobenzene unit onto gold surface is difficult, and the registered relaxation time around 9.5 min would actually correspond to the slow mode τ_2, very close to $\tau_2 \approx 10$ min of AzoC$_6$ having the same tail structure.

Nevertheless, for AzoTren, the amount of azobenzene units (N=N bonds) able to interact with gold surface was essentially the same as for other compounds. The absence of the fast mode in this case highlights the importance of (competing) ionic interaction, influenced by surfactant head properties. Strong ionic binding restricts the mobility of the AzoTren molecules on gold surface, which in turn decreases the probability of interaction via azo bond. Acceleration of thermal isomerization rate of AzoTren might be explained by cooperative switching of the self-assembled cis- AzoTren monolayer on nanoparticle surface rather than the interaction via azo bond. In Azo-PM, azobenzene moiety is not separated from the charged head by a spacer, and +3 positive charge is distributed along three sites in the bulky peptidomimetic head. Therefore, its ionic binding can drive the adsorption of azobenzene unit, opposite to AzoTren with rather concentrated positive charge. Lifetime $\tau_1 \approx 6$ min of Azo-PM is different from other surfactants, which is to be expected because of different azobenzene substitution pattern and possible steric confinement.

The times $\tau_2 > 1$ h can be attributed to the slow isomerization of free azobenzene molecules which are not attached to gold nanoparticle surface. These molecules in solution cannot interact with gold via azo bond once all the surface sites are occupied by the double-layered shell around gold nanoparticles (Section 6.4), therefore they isomerize on the same timescale as without nanoparticles. The fact that τ_2 are shorter than τ_0 may be attributed to the different from pure water surrounding matrix possessing local "distortions" in thermodynamic balance, e.g. micelle-like surfactant structures on gold nanoparticle surfaces.

6.9.Possible mechanism

In catalysis, activity of gold nanoparticles is usually attributed to an electron transfer between metal and adsorbed reactant molecules. When a cis-azobenzene molecule acts as a reactant, electron exchange between gold and N=N bond in the azobenzene unit is expected. Both possible gold-mediated azobenzene isomerization pathways are schematically shown in **Figure 6.19**. Electron attachment to or withdrawal from cis-azobenzene moiety results in the formation of charged cis-azobenzene radical, which is capable of rapid cis-trans isomerization. Indeed, an electrocatalytic rapid cis-trans isomerization of anion radical has been experimentally observed in solution (Section 1.1.4).[65,66] In the joint project with the theoretical group of Prof. Saalfrank,[193] we predicted the formation of azobenzene (di-)cation radical when the azobenzene containing cationic surfactant AzoC$_6$ contacts the gold nanoparticle surface, considering the interaction of gold with the surfactant N=N bond.

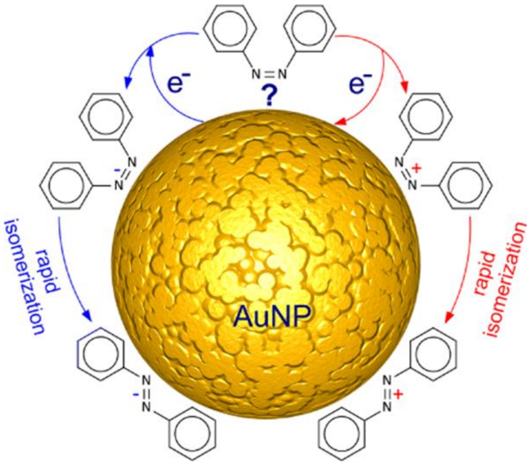

Figure 6.19. Two possible pathways of azobenzene isomerization on gold nanoparticle surface: the cis-azobenzene anion formation in the left (blue), and the cis-azobenzene cation formation in the right (red). The Figure is the replica from Ref. 193.

6.9.1. Theoretical calculations

The reported density functional theory (DFT) calculations[193] became the first attempt to verify the proposed mechanism of fast thermal isomerization of azobenzenes in the presence of gold particles via an electron transfer between gold surface and azo group. The row of the theoretically investigated azobenzenes included (i) parental unsubstituted azobenzene, (ii) unsymmetrically para-substituted azobenzenes with electron-donor substituents (CH3, OCH3, NH2; 4-methylazobenzene, 4-methoxyazobenzene, 4-aminoazobenzene, respectively), (iii) azobenzenes with electron-aceptor substituents in para-position (CF3, NO2; 4-trifluoromethylazobenzene, 4-nitroazobenzene), (iv) cationic azobenzene containing trimethylammonium bromide surfactant, where the azobenzene moiety is para-substituted with a butyl chain on the one side, and on the other side with an alkoxy spacer with a hexyl carbon chain between azobenzene unit and cationic head. The initial, reference state of compounds (i)-(iii) was neutral. Addition and removal of an electron to molecules (i)-(iii) results in anion and cation radical formation, respectively. Azobenzene containing surfactant (iv) is cationic in its reference state in solution. Therefore, adoption of an electron makes its molecule neutral, while withdrawal of an electron from a cationic molecule results in its dicationic radical.

The isolated molecules of azobenzene derivatives were computationally studied under ideal gas conditions at the ambient temperature of 298.15 K and the pressure of 1 atm. At first, molecular geometries in cis- and trans- conformation were optimized to correspond to minima of potential energy surface. Then, optimized transition states for cis-trans transformation were found. The trans-isomer has the lowest energy (most favourable), and the transition state has the highest energy. Subtracting the energy of the cis-isomer from the energy of the transition state yielded the energy barriers for cis-to-trans isomerization. By the means of DFT, electronic energy barriers were calculated. Using Eyring's transition state theory, the isomerization rates of azobenzene cis-trans thermal isomerization were calculated from the values of the activation Gibbs free energy.

The activation energies and thermal cis-trans isomerization rates were calculated for neutral azobenzene molecules (i)-(iii) (reference state) and their anion and cation radicals in gas phase. For the azobenzene containing surfactant (iv), a cation was the reference state. The calculations under ideal gas conditions did not account for the influence of solution or metal surface in the context of steric hindrance and thus altered energies and structures, as well as interaction of charged radicals with other charged and/or neutral molecules. Thermal isomerization rates for the reference states were in good agreement with experimental data, especially for the azobenzene containing surfactant. Indeed, isomerization rate of AzoC$_6$ surfactant in gas phase without nanoparticles $k = 1.6 \cdot 10^{-5}\ s^{-1}$ corresponds to relaxation time $\tau = 1/k = 17$ h, which is only 3.7 times smaller than the experimental value $\tau_0 = 62$ h in solution.

The energy barriers and isomerization rates obtained upon electron addition/removal have been compared with those for the reference state. It was shown that the activation barrier of thermal cis-trans isomerization decreases in both charged radicals (neutral molecule and dication radical for azobenzene surfactant) in comparison with the reference state. Therefore, the calculated thermal cis-trans isomerization rate was drastically increased for the charged species compared to neutral molecules, in agreement with previous studies.

Activation energies of cation species were lower than those of anion azobenzene radicals (and neutral surfactant). Thus, the reduction of energy barrier in cis-trans thermal isomerization was more pronounced upon electron withdrawal, implying faster thermal isomerization of cis-cation radical compared to anion. For unsubstituted azobenzene (i), compared to the neutral molecule, activation energy barriers of the anion and cation radicals were 4 and 7 times smaller, respectively. Consequently, the calculated thermal isomerization rates of charged species were 10^{13} (anion) and 10^{15} (cation) times higher than for the neutral azobenzene molecule. For azobenzene containing surfactant (iv), isomerization rate of neutral molecule was 10^{14} times higher than that of reference cationic state, the isomerization of dication radical was 10^{15} times accelerated.

Further, the substitution effect was discussed. For neutral and anion species, electron-acceptor substituents (iii) reduced the energy barrier, *i. e.* increased thermal isomerization rate, in comparison with unsubstituted azobenzene, whereas electron-donor substituents (ii) did not lead to significant changes in activation energy. Particularly, compared to unsubstituted azobenzene, isomerization rate of 4-nitroazobenzene (electron-acceptor NO_2-group) was 10^3 times higher in neutral state and 10^2 times in anionic state. For cation radicals, a pronounced substitution effect did not occur.

Acceleration of cis-trans thermal isomerization of azobenzenes upon electron transfer to or from a molecule was considered in terms of the highest occupied molecular orbital (HOMO) and the lowest unoccupied molecular orbital (LUMO) of neutral unsubstituted azobenzene in cis-conformation. Upon electron attachment, the electron is expected to settle in the LUMO of the neutral cis-isomer, followed by weakening and elongation of the N=N bond. Upon electron withdrawal, the electron is expected to leave the HOMO, with a slight shortening of the N=N bond. The calculations revealed rotation mechanism in cis-trans isomerization of radical anions. For cations, both inversion and rotation mechanisms could be possible. The registered by SERS weakening of the N=N bond by the trans-cis azobenzene isomerization in UV-irradiated gold nanoparticle aggregates in Ref. 189 might imply the electron transfer from gold nanoparticles to cis- azobenzene moieties and thus accelerated thermal relaxation of anion radical via rotation mechanism. However, precise structure of these azobenzene molecules on gold nanoparticles was not calculated.

In the attempt to highlight the direction of electron transfer between azo bond and gold surface, first energies of anion and cation cis-azobenzene radical formation in gas phase have been compared via the calculation of relaxed electron affinities and ionization potentials. That means that the geometries of cation and anion radicals have been optimized. Energies of azobenzene anion radicals E_- were lower than the energies of neutral molecules E_0, opposed to cation radicals with higher energies E_+, $E_- < E_0 < E_+$. To calculate electron affinity EA, the energy of cis- anion radical in optimized geometry (with minimal energy) E_- was subtracted from the energy of the optimized neutral cis- isomer E_0: $EA = E_0 - E_-$.To calculate ionization potential IP, the energy of the optimized neutral cis- isomer E_0 was subtracted from the energy of optimized cationic radical in cis-conformation E_+, $IP = E_+ - E_0$. Thus calculated for isolated molecules (i)-(iii) in gas phase, electron affinities were smaller than ionization potentials and, importantly, positive: $0 < EA < IP$. That means, the energy costs of cis- anion radical formation $\Delta E_- = E_- - E_0 = -EA$ were negative, opposed to the energy costs of cis- cation radical formation $\Delta E_+ = E_+ - E_0 = IP$. Therefore, in the gas phase, obtaining an electron by a free neutral cis-isomer was found to be energetically favourable, in contrast with electron withdrawal from cis-azobenzene.

Finally, the energies of cis- azobenzene ion formation in the presence of gold surface were estimated similar to the gas phase, by subtracting the energy of a neutral isomer E_0^{surf} from the energy of its charged radical E_+^{surf} or E_-^{surf}:

$\Delta E_+^{surf} = E_+^{surf} - E_0^{surf}$

$\Delta E_-^{surf} = E_-^{surf} - E_0^{surf}$.

Both cation and anion radicals were considered because of uncertainty in the direction of the electron transfer between gold and azobenzenes. Molecular geometries on a metal surface were assumed to not differ from the free gas phase, neglecting surface-induced distortions. (For the illustration of the geometries, please see Ref. 193.) Chemical interaction with the surface, as well as surface charge and probable ionic bonding were not taken into account either. The metal surface was assumed neutral. The contribution of the metal surface into ion formation energies was regarded by the work function of the surface Φ and the negative image charge term $\Delta_{im} = - 1/(4z)$, which is inversely proportional to the distance *z* between an ion and image plane (surface). The energy of an anion formation near metal surface was therefore the sum of energy of cis- anion radical formation in the gas phase $\Delta E_- = -EA$, the energy of electron withdrawal from metal surface, *i. e.* surface work function, and the image charge term:

$\Delta E_-^{surf} = -EA + \Phi + \Delta_{im}$.

The energy of a cation formation near metal surface consisted of the cation formation energy in the gas phase $\Delta E_+ = IP$, image charge term, and the energy of electron attachment by metal surface represented by negative work function:

$\Delta E_+^{surf} = IP - \Phi + \Delta_{im}$.

The ion formation energies were calculated using work function of planar (111) gold $\Phi = 5.31$ eV and reported in literature vertical distance between Au (111) planar surface and azo group $z = 2.4$ Å ($\Delta_{im} = - 1.5$ eV). Increasing the distance between the azobenzene unit and metal surface would increase both ion formation energies.

Calculated values of cation formation energies $\Delta E_+^{surf} \approx 0$ eV for azobenzenes (i), (ii) were lower than anion formation energies $\Delta E_-^{surf} \approx 3$ eV, indicating that near gold surface electron withdrawal from cis-azobenzenes is energetically favourable, oppositely to the ideal gas conditions. The difference between the energies of cation and anion formation was less pronounced for the azobenzene derivatives with electron-acceptor substituents (iii) ($\Delta E_+^{surf} > 0.4$ eV, $\Delta E_-^{surf} < 3$ eV) compared to the unsubstituted molecule (i) ($\Delta E_-^{surf} = 3.09$ eV, $\Delta E_+^{surf} = 0.15$ eV) and electron-donor substituted azobenzene (ii) ($\Delta E_-^{surf} \geq 3.1$ eV, $\Delta E_+^{surf} \leq 0$ eV). The negative values of energy of cis-isomer cation formation ΔE_+^{surf} for azobenzenes having electron-donor substituents (ii) mean possible spontaneous formation of cis-isomer cation radical of these azobenzenes on gold surface.

The performed DFT calculations corroborate the hypothesis of Hallett-Tapley *et. al.*[190] about azobenzene thermal cis-trans isomerization via a cation formation near gold surface, and elucidate the experimentally registered highly accelerated thermal isomerization of 4-methoxyazobenzene in the presence of gold nanoparticles in comparison with solution without nanoparticles.

6.9.2. Discussion

Based on the computational results, we believe that the fast mode $\tau_1 \approx 3$ min, detected in thermal cis-trans isomerization of azobenzene containing cationic surfactants in the presence of gold nanoparticles, corresponds to the pathway via the electron transfer from the adsorbed azobenzene unit to the gold surface, followed by the azobenzene cis-trans isomerization in the dication radical form (for surfactants with +1 charged heads).

Now, let's discuss the possible mechanism of slow mode $\tau_2 > 10$ min. When cis-isomers of cationic azobenzene surfactants interact with gold particles via azo bond, they readily switch into the trans-state. Cis- and trans-isomers have to compete for gold surface sites. The number of the available surface sites can gradually decrease due to ionic binding of trans-isomers. Trans-isomers can decorate gold nanoparticles with the double-layer stabilizing shell. Indeed, gold nanoparticles did not aggregate during the experiments.

Since τ_2 likely increases with the distance between surfactant head and azobenzene unit, one can expect that the relaxation time $\tau_2 > 10$ min corresponds to the thermal cis-trans isomerization of the surfactant molecules, not adsorbed to gold surfaces with their N=N bonds. Probably, these molecules isomerize to form the outer layer of the stabilizing shell, while the trans- inner layer facing gold surface is formed via electron transfer between gold and azobenzene units. Qualitative thoughts about a possible pathway are discussed in the following paragraphs.

Relaxation times $\tau_2 > 10$ min could characterize the isomerization of the cis- molecules due to steric confinement in the energetically favourable nanoparticle-stabilizing shell. Dipole-dipole interactions between azobenzene containing tails of surfactant molecules in the inner (facing gold) and the outer (facing medium) layer of the shell reduce their spatial freedom and cooperative switching effects can take place. Then, AzoC$_n$ molecules with longer tails would have more spatial freedom and therefore isomerize into trans-conformation slower, in agreement with experimental results. In this situation, it is unclear why nanoparticles do not aggregate upon formation of the monolayer of surfactant molecules. Perhaps, newly formed trans-isomers on the gold surface do not necessarily ionically bind to gold, but can couple with already surface-attached trans-species via dipolar interactions, and thus build the double layer shell pair by pair. After the surfactant double-layer shell is formed, it is unclear why the rest of the solution isomerizes faster than without gold particles ($\tau_3 \approx \tau_0$ was not detected in AzoC$_n$ at $\sigma < 2$).

Alternatively, the electrocatalytic switching of a surfactant matrix around gold nanoparticles could explain the relatively high isomerization rate of azobenzene molecules that are not in direct contact with the gold surface. This is the case of τ_2 in AzoC$_n$, UV-irradiated gold-surfactant complexes, and probably τ_1 in AzoEn and AzoDeta.

In terms of reaction kinetics, electron-mediated azobenzene isomerization on gold surface can be treated as a catalytic redox reaction including (i) oxidation of cis-azobenzene on gold surface, (ii) cis-trans isomerization of azobenzene radical, (iii) reduction of trans-azobenzene radical. These three reactions are consecutive and assumed to have different reaction rates. The corresponding rate equation in chemistry includes three exponential terms, similar to the Equation (6.1) chosen for the fitting of time-dependent absorption data. The picosecond rate of the isomerization step is beyond our experimental limit and thus only the two relatively slow redox reactions can be taken into account. The fast mode with the time τ_1, dependent on the gold-surfactant binding, is apparently characteristic for the oxidation reaction. Therefore, the mode τ_2 is to be the parameter of the reduction reaction.

In the computationally predicted pathway of electron withdrawal from adsorbed azo bond on gold surface and AzoC$_n$ dication formation, the catalytic redox cascade can be imagined as follows. Cis- azobenzene dication radicals isomerize to trans-conformation and ionically attach to gold. Trans- azobenzene dication radical (T^+) can be reduced by an electron (a) accommodated in gold or (b) from a proximate cis-azobenzene in solution. In this step, T^+ transports positive charge to the cis-azobenzene unit (C) in the vicinity. The positive charge carrier can be (a) a hole or (b) a proton in solution, depending on the pathway. Next formed cis-azobenzene radical dication isomerizes into trans-dication and gets reduced to the cationic trans-isomer. Schematically: $\text{Au-T}^+ + \text{C} \rightarrow \text{Au-T} + \text{C}^+ \rightarrow \text{Au-T} + \text{T}^+$ (**Scheme 6.1**). Thus, nanoparticles in solution are all the time protected from aggregation, first by cation radicals, then by the formed double-layer shell. The way (a) of reduction by an electron from gold surface is more likely distance-dependent because of transport of electron from gold to azo bond along the ionically attached elongated dication radical of trans-azobenzene. Indeed, the image charge term in DFT calculations would increase with the length of the spacer between surfactant charged group and azobenzene unit, increasing energy costs of electron transfer and thereof the reaction time.

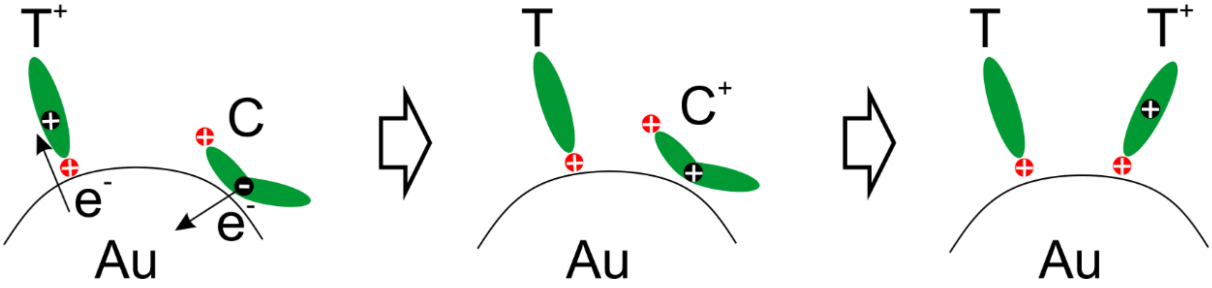

Scheme 6.1. The proposed electrocatalytic mechanism of cis-trans isomerization of azobenzene surfactants in the presence of gold nanoparticles.

To be systematic, there's no experimental evidence of azobenzene dication radical formation, and calculations predict that both directions of electron transfer would lead to the rapid thermal relaxation of azobenzene cis-isomers. Thus, a mechanism explaining the registered acceleration of cis-trans isomerization rate via azobenzene anion formation should be discussed too. This mechanism may be the electron injection from gold nanoparticles to azobenzene solution, probably also by another pathway than via adsorbed azo bond. Indeed, in Ref. 191 azobenzene thermal isomerization was enhanced, although direct interaction of azobenzene moieties with gold surface was unlikely. Assuming the electron transfer from gold to adsorbed cis-azobenzene N=N bond, "zwitterionic" species of AzoC$_n$ surfactants are expected to form, with positively charged head and negative charge on the azobenzene tail. These species with neutral total charge would be able to rapidly cis-trans isomerize too.[193] Cis- AzoC$_n$ zwitterions (C^-) would likely have a compact geometry. Hypothetically, they could initiate the electron-driven catalytic cycle in solution as described in Ref. 65,66 in Section 1.1.4: $\text{C} + \text{C}^- \rightarrow \text{C} + \text{T}^- \rightarrow \text{C}^- + \text{T} \rightarrow \text{T}^- + \text{T}$. Without primary ionic binding of cis-isomers via surfactant charged heads, final cationic trans-isomers (T) would ionically bind to gold nanoparticle surfaces and the reaction would proceed slower with time due to decreasing active surface area. In the case of ionic binding of cis-isomers, $AzoC_n$ zwitterions C^- attached to gold surface would rapidly isomerize to T^-, and the same electron-driven isomerization cascade would be possible. In this case, electron transfer from T^- attached to gold toward C in solution would occur, *e.g.* via protons, and thus isomerized free molecules would form the outer layer of surfactant shell.

Our results demonstrate that thermal cis-trans isomerization of azobenzene containing compounds is tremendously accelerated on gold nanoparticle surface. We believe that the underlying mechanism is electron withdrawal from azobenzene moiety to gold surface, followed by the facilitated cis-trans isomerization of azobenzene in its (di-) cationic state, and suggest to consider the kinetics of the gold-enhanced azobenzene isomerization similar to catalytic redox reactions. Yet, the proposed electrocatalytic mechanism remains a trustworthy speculation. Other methods, which are sensitive to azobenzene molecular structure, *e.g.* vibrational spectroscopy, as well as to the nanoparticle charge state, may elucidate the detailed mechanism behind the catalytic cis-trans isomerization of azobenzenes in the dark in the presence of gold nanoparticles in the future. Also, one could try to disable, *e.g.* by varying the structure of azobenzene compounds, or by co-adsorbing electron donors/acceptors on nanoparticle surface, one of the redox steps and investigate the charge state of gold nanoparticles via their plasmon resonance to experimentally probe the direction of the electron transfer.

7. Cis-trans isomerization of azobenzene containing surfactant in the presence of nanoparticles of different materials

In this chapter, the influence of nanoparticle material on cis-trans isomerization of azobenzene surfactants is tested and compared with gold nanoparticles.

After exposure to UV light, aqueous solution of azobenzene containing trimethylammonium bromide surfactant AzoC$_6$ was mixed with nanoparticle suspensions and its thermal relaxation in dark was tracked by periodically recording absorption spectra.

For all materials in this chapter, nanoparticle absorption band overlapped absorption band of AzoC$_6$. Therefore, to detect the changes in azobenzene surfactant absorption, the spectra of surfactant-nanoparticle suspensions were recorded versus pure nanoparticle suspension diluted to the same concentration. The concentrations of the nanoparticles were unknown except for silver nanoparticles, that's why it was impossible to perform quantitative analysis in the context of nanoparticle surface area and the ratio between azobenzene surfactant molecules and particle surface atoms σ.

7.1.Palladium and gold-palladium alloy nanoparticles

Figure 7.1 shows absorption spectra and TEM micrographs of 13-nm palladium (PdNP) and 8-nm alloy gold-palladium nanoparticles (AuPdNP). Diameter of the particles was estimated from the TEM micrographs. Particles of both materials had negative surface charged according to the measured ς-potential around -30 mV. To record the absorption spectra (**Figure 7.1a**), stock nanoparticle aqueous suspensions of concentration C_0 were 13.5 times diluted with water ($C_{NP} = 0.074C_0$). One can see a weak gold plasmon absorption peak at $\lambda = 523$ nm in the absorption spectrum of gold-palladium nanoparticles (red curve). The inset in **Figure 7.1a** demonstrates brown color of AuPdNP aqueous suspensions. Gold-palladium alloying has been proofed by TEM, thus the core-shell morphology has been excluded. Along with small alloy AuPd nanoparticles, bigger pure gold and pure palladium nanoparticles have been detected in the TEM micrographs of dried suspension of gold-palladium alloy nanoparticles (**Figure 7.1c**),[h] probably as non-ablated rest particles. According to the preparation procedure, the expected alloy composition Au:Pd is 30:70 mol %. EDX data revealed 27.5 % Au and 72.5 % Pd in alloy gold-palladium nanoparticles (see **Figure Appendix-13.1**). The obtained spectroscopy and TEM results indicate random alloy morphology of gold-palladium nanoparticles, probably with palladium-enriched surface. The weak gold-plasmon peak in the absorption spectra might stem from the non-ablated gold nanoparticles in the suspension.

---

[h] Based on the integrated Energy Dispersive X-ray spectroscopy (data of Dr. Ryabchikov)

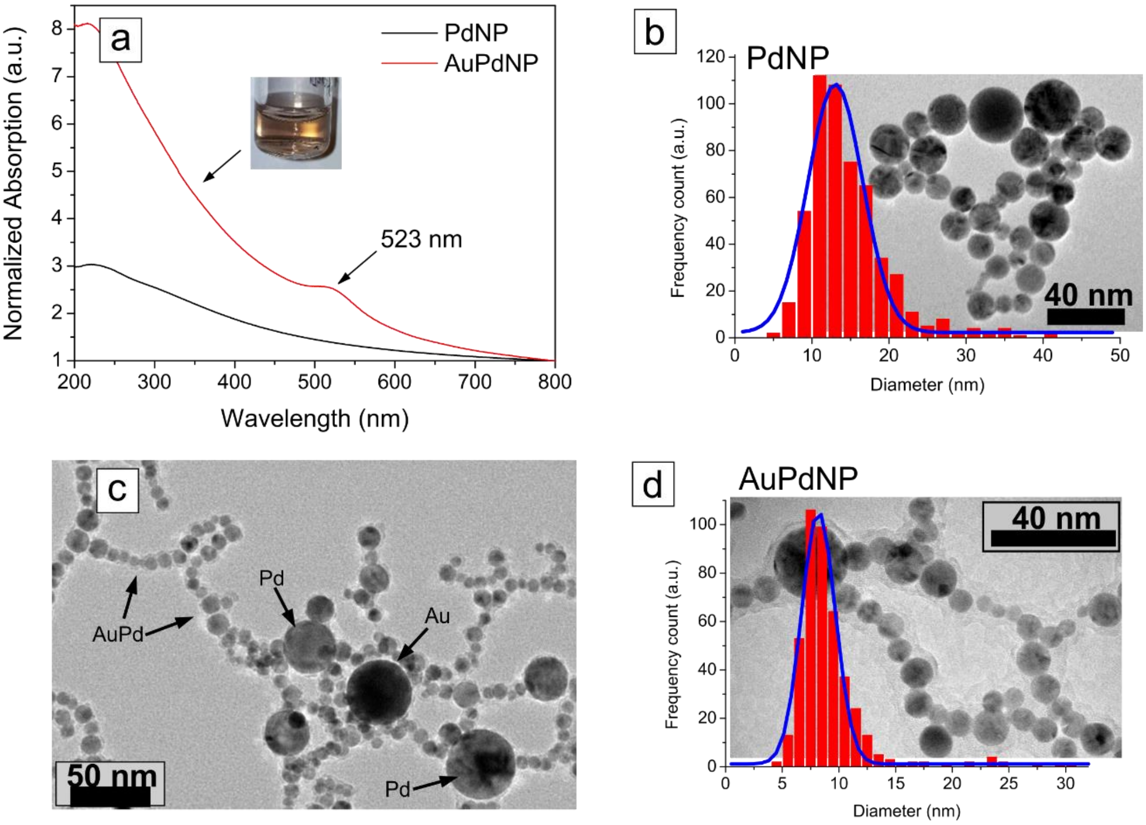

Figure 7.1. Properties of palladium and alloy gold-palladium nanoparticles. (a) Normalized absorption spectra of palladium (black line, PdNP) and alloy gold-palladium (red line, AuPdNP) nanoparticles. The inset in shows a photograph of a diluted suspension of gold-palladium alloy nanoparticles. (b) TEM micrograph and superimposed size distribution diagram of palladium nanoparticles. (c, d) TEM micrographs and size distribution diagram of alloy gold-palladium nanoparticles.

The results on azobenzene containing surfactant thermal relaxation in the presence of palladium nanoparticles are shown in **Figure 7.2a**. Absorption spectra of palladium-surfactant suspension were recorded versus palladium nanoparticles without surfactant. Concentration of nanoparticles in both suspensions was $C_{NP} = 0.074C_0$, $C_{Azo} = 2.3 \times 10^{-5}$ M in palladium-surfactant sample. Palladium nanoparticles in water aggregated after around 10 hours, while the palladium-surfactant sample remained intact. This implies that surfactant molecules stabilized palladium nanoparticles via the double layer formation on surface. In order to continue the experiment, the reference nanoparticle sample has been replaced with a freshly diluted palladium colloid. In the last five spectra recorded after 25 hours, optical density was normalized to the isobestic points of the spectra within the first 10 hours. The corresponding non-normalized spectra are shown in **Figure Appendix-13.2**. Cis-trans isomerization of azobenzene containing surfactant in the presence of alloy gold-palladium particles is shown in **Figure 7.2b**. The spectra were recorded versus pure AuPd nanoparticle colloid, which remained stable during the entire experiment. $C_{NP} = 0.108C_0$, in AuPd-surfactant sample $C_{Azo} = 2.5 \times 10^{-5}$ M. The estimated thermal relaxation times of azobenzene containing surfactant are $\tau_1 = 23.2 \pm 1.3$ h in the presence of palladium nanoparticles, and $\tau_1 = 3.5 \pm 0.1$ h in the presence of gold-palladium alloy nanoparticles. Here and below monoexponential fitting of optical density $D_{376}(t)$ has been applied, because the monoexponential fits were accurate, and biexponnetial fitting did not yield different times. Yet, the plot of $D_{376}(t)$ in the inset in **Figure 7.2b** for alloy gold palladium nanoparticles visually suggests a biexponential fitting.

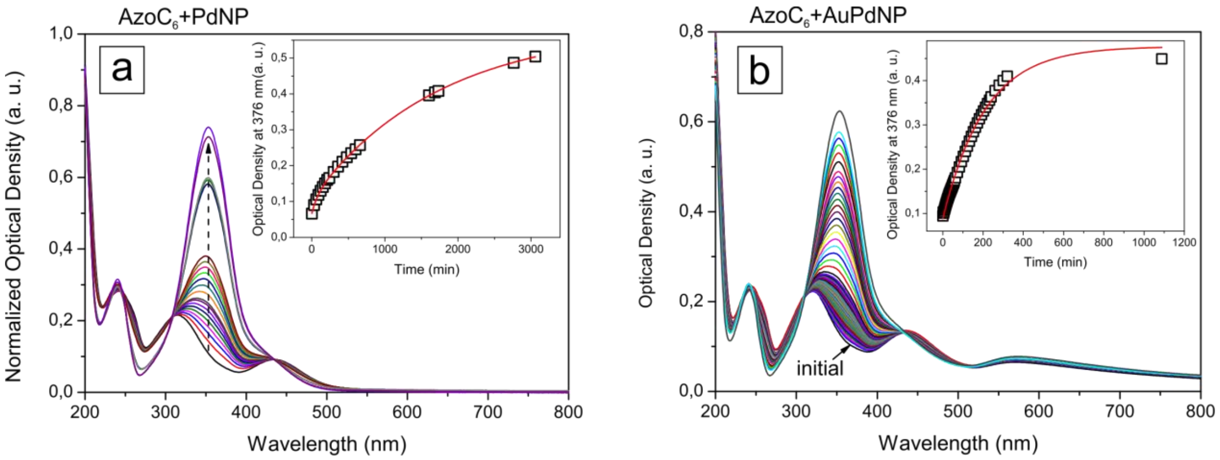

Figure 7.2. Absorption spectra over time of UV irradiated azobenzene containing surfactant $AzoC_6$ in the presence of palladium (a) and alloy gold-palladium nanoparticles (b). The insets show (normalized) optical density at 376 nm over time (squares) and its exponential fit (red line).

7.2.Silver and gold-silver alloy nanoparticles

Laser ablated silver nanoparticles[i] had the mean diameter d = (12.1 ± 0.2) nm determined from TEM micrographs, and ς-potential around -30 mV. Pronounced plasmonic absorption maximum of silver is to be seen at $\lambda = 406$ nm (**Figure 7.3**).

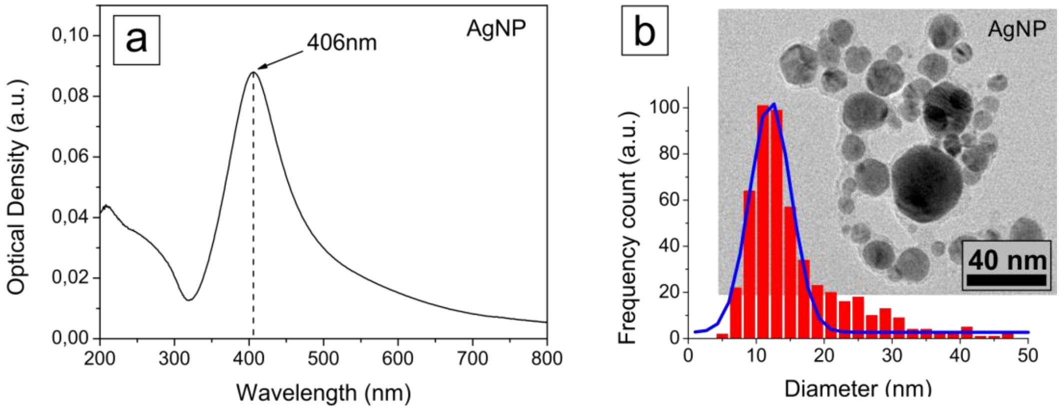

Figure 7.3. Absorption spectrum (a), TEM micrograph with superimposed size distribution histogram (b) of laser ablated silver nanoparticles. $C_{Ag} = 0.05$ mM.

Absorption spectra of azobenzene surfactant $AzoC_6$ mixed with silver nanoparticles, periodically recorded during surfactant thermal cis-trans relaxation in the dark, are shown in **Figure 7.4**. The reference silver nanoparticle suspension without surfactant, as well as the

---

[i] prepared at Aix-Marseille University

silver-surfactant suspension, remained stable throughout the whole measurement (**Figure Appendix-13.3**). The seeming decrease in optical density at around 440 nm results from the "subtraction" of silver nanoparticle spectra from silver-surfactant spectra. Saturation in spectra occurred after around a week, indicating slow azobenzene relaxation rate, $\tau_1 = 78.3 \pm 1.5$ h.

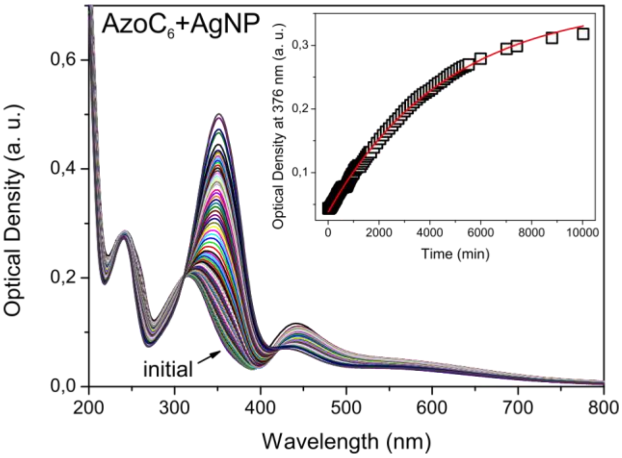

Figure 7.4. Absorption spectra over time of UV irradiated azobenzene containing surfactant AzoC$_6$ in the presence of silver nanoparticles. The inset shows time dependency of optical density at $\lambda = 376$ nm as recorded (squares) and exponentially fitted (red line). $\sigma = 4$, $C_{Azo} = 0.025$mM, $C_{Ag} = 0.075$ mM.

Similar results were obtained for silver nanoparticles prepared at Vladimir State University in Russia, described above in Section 5.2. **Figure 7.5a** shows absorption spectra of UV-irradiated surfactant AzoC$_6$ mixed with silver nanoparticles from this batch, recorded versus reference silver colloid of the same concentration $C_{Ag} = 0.35$ mM. Monoexponential fitting of optical density $D_{376}(t)$ resulted in the slow thermal relaxation time $\tau_1 = 64.8 \pm 2.2$ h. This value is equal within error bars to the relaxation time of AzoC$_6$ aqueous solution without nanoparticles. The suspensions of silver nanoparticles in pure water (reference) and containing UV-irradiated surfactant were colloidally stable during the experiment. The changes in spectral range $\lambda > 400$ nm are due to slight nanoaggregation of silver nanoparticles upon addition of surfactant, similar to gold nanoparticles (Section 6.1). Indeed, $\sigma_{UV} = 0.15$, corresponding to the region II of phase diagram in **Figure 4.8**. **Figure 7.5b** shows absorption spectra recorded versus air, tracking the changes in plasmonic properties over time. These spectra were partly reconstructed from the recorded versus silver nanoparticles via addition of reference silver nanoparticle spectra. Along with cis-trans isomerization of surfactant, one can see that plasmonic coupling mode appeared at around 580 nm within 30 minutes after mixing and after that did not change during one week of measurements. The first two spectra (initial and after 2 minutes, black and grey curve, respectively) were excluded from data analysis to estimate thermal relaxation time.

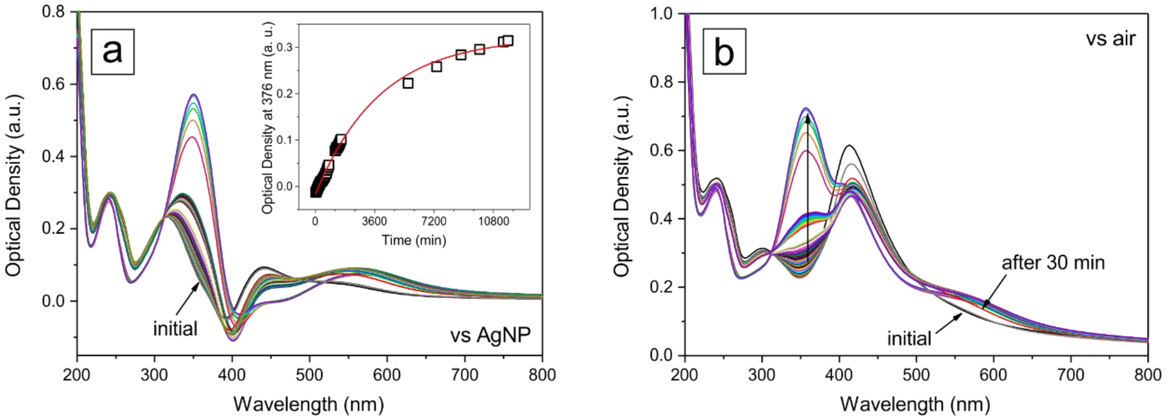

Figure 7.5. (a) Absorption spectra of UV irradiated azobenzene containing surfactant AzoC$_6$ in the presence of silver nanoparticles at $\sigma = 1.25$, $C_{Ag} = 0.35$ mM, $C_{Azo} = 0.028$mM. The spectra were recorded over time versus reference silver nanoparticles in water. The inset shows optical density at 376 nm as a function of time (squares) and its monoexponential fit (red line). (b) The same time-dependent absorption spectra recorded versus air.

Alloy gold-silver nanoparticles have been prepared in two batches with helium (AuAgNP He) and argon (AuAg Ar) bubbling during irradiation by femtosecond laser. TEM micrographs, size distribution histograms and absorption spectra of the nanoparticles are shown in **Figure 7.6**. To record the absorption spectra, both initial nanoparticle suspensions were diluted with water to $C_{NP} = 0.074\ C_0$. Diameter of the particles was found to be d = (11.0 ± 0.1) nm for AuAg He and d = (8.9 ± 0.1) nm for AuAg Ar. Determined ς-potentials were $\varsigma = (-31.3 \pm 12.8)$ mV for AuAg He particles and $\varsigma = (-23.3 \pm 5.9)$ mV of AuAg Ar particles.

Plasmonic absorption maximum of AuAg He nanoparticles was detected at $\lambda_{SP} = 472$ nm (black curve in **Figure 7.6a**). The sharp single plasmonic maximum indicates random alloy morphology. According to the preparation procedure, approximately 1:1 Au:Ag ratio is expected in the alloy, with 48 molar % of gold. It is known that the position of plasmon absorption peak of gold-silver alloy nanoparticles is determined by their composition. The LSPR wavelength occurred near the mean value of plasmonic wavelengths of gold and silver nanoparticles (464.5 nm), indicating nearly equal proportions of gold and silver in the alloy. Indeed, 50:50 % Au:Ag alloy nanoparticles in Ref. 83, 89 possessed plasmonic absorption peak at $\lambda_{SP} = 472$ nm. In Ref. 111 $\lambda_{SP} = 472$ nm corresponded to alloy particles with 60:40 % Au:Ag composition. Ref. 179 suggested silver segregation to the nanoparticle surface at ≥ 50 % Au in the alloy composition. Therefore, random alloy morphology with silver-segregated surface is to be expected in alloy gold-silver nanoparticles AuAg He.

Alloy nanoparticles AuAg Ar exhibited two absorption maxima at $\lambda_{SP} = 480$ nm and $\lambda = 550$ nm (red curve in **Figure 7.6a**). The second plasmonic maximum may indicate (a) core-shell morphology, and (b) nanoparticle aggregation. Indeed, rather small ς-potential $\varsigma \approx -20$ mV implies suspicious stability of AuAg Ar colloid. Both situations are not desirable in quantitative analysis of azobenzene cis-trans isomerization. That's why these particles were not further investigated.

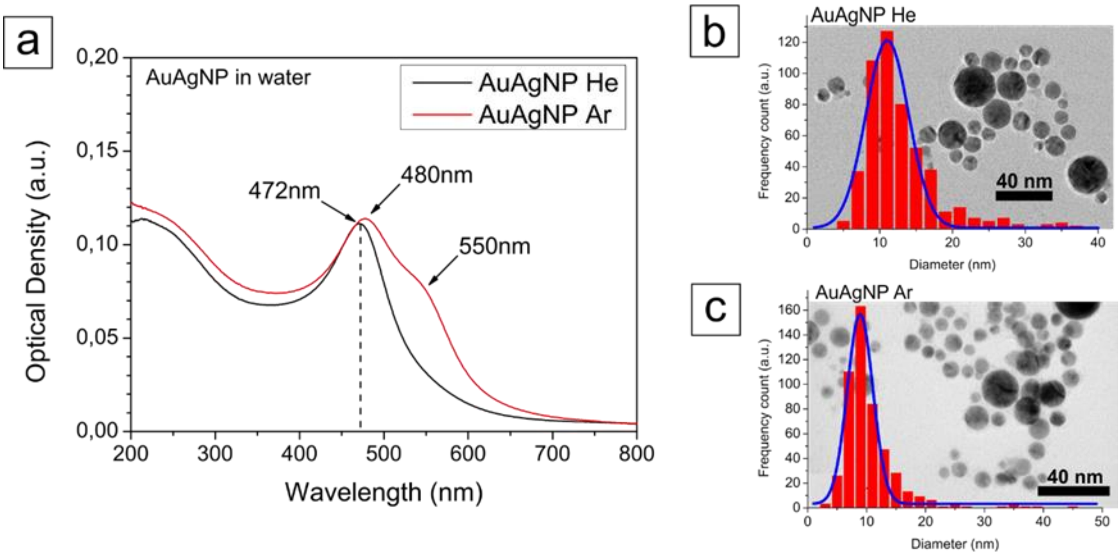

Figure 7.6. (a) Absorption spectra of gold-silver alloy nanoparticles from two batches, prepared in the environment of He (black curve) and in the environment of Ar (red curve). (b, c) TEM micrographs and size distribution of gold-silver alloy nanoparticles, prepared in He (b) and Ar (c) environment.

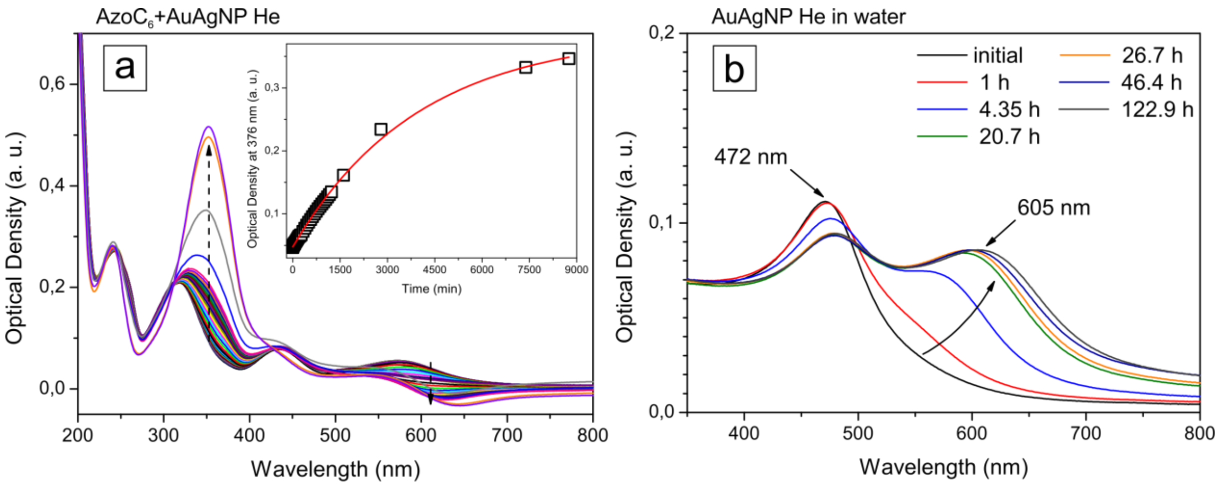

Figure 7.7. (a) Absorption spectra over time of UV irradiated azobenzene containing surfactant $AzoC_6$ in the presence of alloy gold-silver nanoparticles AuAg He, recorded versus AuAg He suspension. The inset shows time dependency of optical density at 376 nm (squares) and its exponential fit (red line). (b) Absorption spectra over time of the reference alloy gold-silver nanoparticles in water.

Cis-trans thermal relaxation of $AzoC_6$ surfactant was examined in the presence of alloy gold-silver nanoparticles AuAg He. The corresponding absorption spectra are shown in **Figure 7.7**. The spectra in **Figure 7.7a** were recorded against pure AuAg He aqueous suspension. $C_{NP} = 0.074\ C_0$ in both suspensions, $C_{Azo} = 2.6 \times 10^{-5}$ M in AuAg-surfactant sample. The observed decrease in optical density in visible range in **Figure 7.7a** is attributed to the aggregation process in the reference AuAg He suspension, manifested by the absorption spectra in **Figure 7.7b**. One can see how optical properties of gold-silver alloy nanoparticles change with time. Already after an hour (red curve), coupling plasmonic mode appears in the spectrum, indicating nanoparticle aggregation. However, spectral changes in the reference AuAg He sample occurred outside the surfactant absorption band, and therefore did not significantly affect quantitative estimation of its thermal relaxation rate. The resulting relaxation time $\tau_1 = 66.1 \pm 1.3$ h is close to the value in pure water without nanoparticles.

Absorption spectra of azobenzene containing surfactant with AuAg He nanoparticles recorded versus air are shown in **Figure 7.8**. One can see the increase in optical density in the UV range due to cis-trans surfactant isomerization and the evidence for the colloidal stability of alloy gold-silver nanoparticles mixed with cis-azobenzene surfactant.

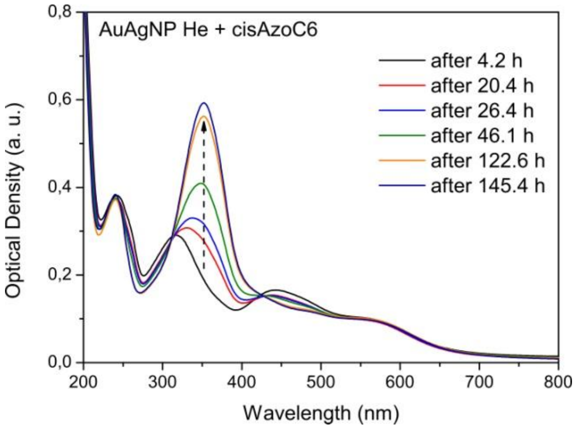

Figure 7.8. Time-dependent absorption spectra of UV irradiated azobenzene containing surfactant AzoC$_6$ in the presence gold-silver alloy nanoparticles AuAg He recorded versus air.

7.3.Silicon nanoparticles

The properties of laser ablated silicon nanoparticles have been described in Section 5.3. For these experiments silicon nanoparticles prepared in argon environment (SiNP Ar and SiNP Ar II) have been chosen. Their absorption spectra were shown in **Figure 5.6**.

Figure 7.9a and Figure Appendix-13.4 show thermal relaxation of azobenzene containing surfactant AzoC$_6$ mixed with silicon nanoparticles SiNP Ar. Absorption spectra were recorded versus air (**Figure 7.9a**) and reference silicon nanoparticles in water (**Figure Appendix-13.4**). In **Figure 7.9** one can see (i) the second absorption peak of silicon nanoparticles at $\lambda \approx 550$ nm, and (ii) continuous lowering of the entire spectrum with time. The first indicates that silicon nanoparticles mixed with cis- azobenzene surfactant aggregated fast (within 8 minutes, black curve). The second can be related to a slow precipitation process. Reference silicon nanoparticles in pure water were colloidally stable (**Figure 7.9b**).

Nanoaggregation of silicon nanoparticles during surfactant cis-trans isomerization supports the proposed formation of the surfactant monolayer on nanoparticle surface. The amount of trans-isomers in solution increases with time. Once formed, trans-azobenzenes attach to silicon particles. As soon as the monolayer is formed, particles aggregate. This situation corresponds to moving from region I to region II of phase diagram in **Figure 4.8**.

Absorption spectra of UV-irradiated azobenzene surfactant mixed with silicon nanoparticles SiNP Ar II, recorded versus air and reference particle colloid, reproduce the results for SiNP Ar (**Figure Appendix-13.5**).

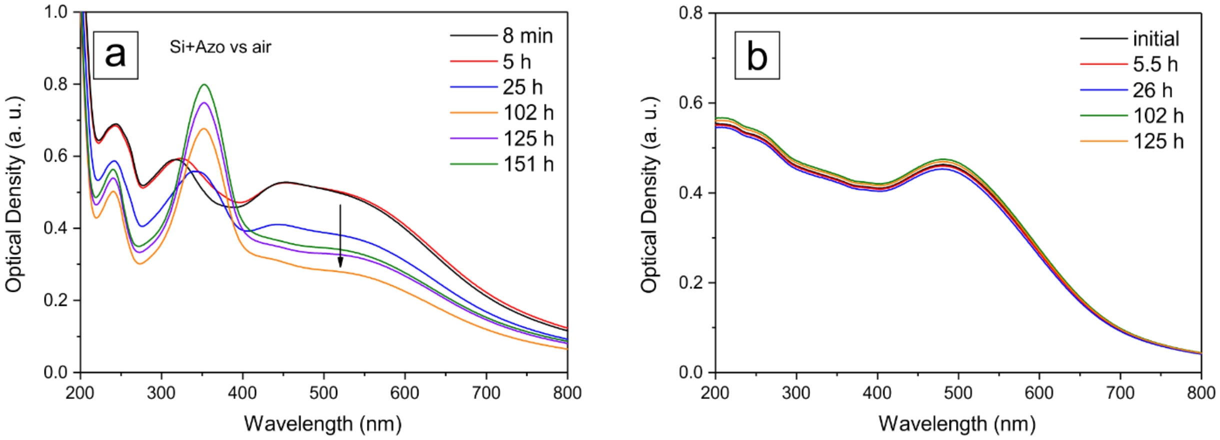

Figure 7.9. Periodically recorded absorption spectra of (a) UV-irradiated azobenzene containing surfactant AzoC$_6$ mixed with silicon nanoparticles; (b) reference silicon nanoparticles in water.

Aggregation and precipitation in silicon-surfactant suspension hindered the quantitative analysis of azobenzene surfactant absorption kinetics (**Figure Appendix-13.4 and Figure Appendix-13.5**). Nevertheless, qualitatively, experiments did not reveal acceleration in cis-trans isomerization of azobenzene containing surfactant in the presence of silicon nanoparticles.

7.4.Summary

For each material, time dependencies of optical density at 376 nm were exponentially fitted to estimate cis-trans thermal relaxation rates of azobenzene surfactant AzoC$_6$ in the presence of nanoparticles τ_1, similar to the previous chapter. Monoexponential fits were accurate. Acceleration factor was calculated relatively to the lifetime of cis-isomer of AzoC$_6$ surfactant in water without nanoparticles $\tau_0 = 62 \pm 1$ h. The properties of different nanoparticles and their impact on cis-trans thermal isomerization rates of azobenzene containing surfactant AzoC$_6$ are summarized in **Table 7.1**.

Gold nanoparticles showed catalytic character, accelerating thermal isomerization of azobenzene containing surfactant AzoC$_6$ by more than 1500 times due to electron transfer between gold and azo bond, as described in the previous chapter. The time $\tau_{1} = 2.3 \pm 0.2$ min is the average time registered at $0.5 < \sigma < 2$ and calculated from biexponential fitting of $D_{376}(t)$. To be accurate in comparison, relaxation time resulting from monoexponential fitting $\tau_{1} = 6.9 \pm 0.2$ min should be used to calculate the acceleration factor. However, this does not change the conclusion, since thus calculated acceleration factor of 539 would remain the highest among the studied nanoparticle materials.

Silver, alloy gold-silver, and silicon nanoparticles did not accelerate thermal cis-trans isomerization of azobnezene surfactant AzoC$_6$. Acceleration factor 1 for silicon nanoparticles was estimated qualitatively due to particle aggregation.

Table 7.1. Properties of nanoparticles of different materials: LSPR wavelength (λ_{SP}), average nanoparticle size according to TEM (d_{TEM}) and DLS (d_{DLS}), nanoparticle surface ς-potential (ς), lifetime of cis-isomer of azobenzene containing surfactant AzoC$_6$ in the presence of the nanoparticles τ_1, and acceleration factor of surfactant thermal cis-trans isomerization in the presence of the nanoparticles τ_0/τ_1.

Material	λ_{SP}, nm	d_{TEM}, nm	d_{DLS}, nm	ς, mV	τ_1, min	τ_0/τ_1
Au	523	9 ± 3	10.6 ± 2.7	-30 ± 10	2.3 ± 0.2	1617 ± 143
Pd	-	13.0 ± 0.2	20.6 ± 3.2	-30 ± 5	1393 ± 80	2.7 ± 0.2
AuPd	523	8.2 ± 0.05	15.5 ± 3.6	-34 ± 11	210 ± 8	17.7 ± 0.7
Ag[j]	406	12.1 ± 0.2	17.7 ± 2.6	-31 ± 8	4695 ± 92	0.79 ± 0.02
Ag[k]	406	-	33.5 ± 7.3	-33 ± 6	3889 ± 133	0.96 ± 0.04
AuAg He	472	11.0 ± 0.1	-	-31 ± 13	3968 ± 78	0.94 ± 0.02
AuAg Ar	480, 550	8.9 ± 0.1	21.9 ± 4.3	-23 ± 6	-	-
Si Ar	-	-	54.2 ± 8.4	-43 ± 9	3720	1
Si He	-	-	52.8 ± 8.3	-42 ± 8	-	-
Si	-	-	122.9 ± 39.1	-41 ± 9	-	-

7.5.Discussion

In this discussion we follow the results of the computational study discussed in Section 6.9.1, which shows that the electron transfer from azobenzene molecules to metal nanoparticle surfaces is the reason for drastically enhanced cis-trans thermal isomerization of azobenezenes in the presence of nanoparticles. According to theoretical calculations, energy costs of electron withdrawal and attachment from/to cis- azobenzene near metal surface ΔE_+^{surf} and ΔE_-^{surf}, respectively, can be found as follows:

$\Delta E_-^{surf} = -EA + \Phi + \Delta_{im}$

$\Delta E_+^{surf} = IP - \Phi + \Delta_{im}$

Here, EA and IP are electron affinity and ionization potential of azobenzene in gas phase, Δ_{im} is the image charge term. Surface work function Φ plays a crucial role in the comparison of nanoparticles made of different materials. Decrease in work function Φ would decrease ΔE_-^{surf} and increase ΔE_+^{surf}, making the (di-) cation formation of azobenzene cis-isomer on the metal

---

[j] Prepared at Aix-Marseille University (France)

[k] Prepared at Vladimir State University (Russia)

surface less energetically favourable. Increase in the work function Φ would make cis-azobenzene (di-) cation formation more energetically favorable. The influence of the surface work function on formation energies of charged cis-azobenzene radicals is demonstrated in **Table 7.2** in a plain manner. The values of electron affinity and ionization potential of azobenzene in gas phase, and the image charge term were taken from Ref. 193. One can see that at the lower surface work function, both ways of electron transfer are energetically unfavorable.

Table 7.2 Influence of surface work function on the energies of cation and anion radical formation for unsubstituted azobenzene in cis-conformation near planar (111) palladium, gold, and silver surface, based on DFT calculations.[193]

	$\Phi_{Pd} = 5.6$ eV	$\Phi_{Au} = 5.31$ eV	$\Phi_{Ag} = 4.74$ eV
ΔE_{-}^{surf}, eV	3.38	3.09	2.52
ΔE_{+}^{surf}, eV	-0.14	0.15	0.72

Therefore, according to this simple consideration of energy difference for electron withdrawal from the azobenzene moiety on the metal surface, formation of dication radicals of azobenzene surfactant cis-isomers is expected to be more energetically favorable on palladium surface and less energetically favorable on silver surface compared to gold. In turn, in comparison with gold nanoparticles, higher acceleration factor is to be expected in the presence of palladium nanoparticles and lower acceleration factor – in the presence of silver nanoparticles.

Experimental results for silver nanoparticles are in agreement with theoretical predictions. Indeed, silver nanoparticles from two different batches did not enhance thermal isomerization of azobenzene containing surfactant, acceleration factor $\tau_0/\tau_1 \approx 1$ for these particles. Additionally, silver nanoparticles are known to oxidize more readily in comparison with gold. The oxide layer on the surface of silver nanoparticles may further inhibit electron transfer between metallic silver surface atoms and azobenzene units and following cis-trans isomerization of the latter. Similar results for gold-silver alloy nanoparticles ($\tau_0/\tau_1 \approx 1$) indicate silver segregation on their surfaces.

Work function of (111) silicon surface $\Phi_{Si} = 4.83$ eV $< \Phi_{Au} = 5.31$ eV for a wide range of dopings.[207] That means, experimental results for silicon nanoparticles are in agreement with theoretical predictions too. Moreover, silicon nanoparticles likely have surface silicon oxide layers, explaining their more negative surface ς-potential in comparison with other nanoparticles. Surface oxide layers can prevent the electron transfer between surfactant azobenzene units and silicon surfaces.

However, simple calculations cannot explain the results for palladium nanoparticles, which enhanced azobenzene cis-trans isomerization only by 2.7 times. This implies that the electron transfer between palladium surfaces and azobenzene units was not detectable or did not occur. For instance, it is possible that the cis-trans azobenzene isomerization proceeds faster in the presence of palladium nanoparticles than in pure solution because of cooperative switching of azobenzene surfactant bilayers formed on palladium nanoparticle facets. Chemisorption strength between azobenzene unit and metal surface can also play an important role.

In fact, it is possible that the surface work function of palladium nanoparticles is smaller than the work function of gold nanoparticles, so that the $AzoC_6$ dication radical formation is not so straightforward on palladium nanoparticle surface. Indeed, the work function of metal nanoparticles is usually different from that of bulk metals and depends on many factors. For instance, it is known to be inversely proportional to nanoparticle size,[208] can depend on nanoparticle charge state[209] and aggregation state.[210] Functionalization of gold and silver surfaces with akanethiol monolayers was reported to tune their work functions.[211] That means, the nanoparticle work function may dynamically change during our experiments because of adsorption of surfactant and possible electron transfer. Also, the crystalline structure of the nanoparticles should be controlled, because lower values of work function have been reported for polycrystalline specimens compared to (111) surface. [212] For instance, for polycrystalline palladium $\Phi_{Pd} = 5.12$ eV $< \Phi_{Au} = 5.31$ eV.

Furthermore, in the performed DFT calculations, the metal nanoparticle surface was assumed infinitely conductive. At the same time, surface charge of metal nanoparticles may contribute into energy costs of azobenzene cation radical formation on nanoparticle surface. Indeed, an electron travelling from azo bond to a negatively charged metal surface has to overcome electrostatic repulsion, *i. e.* additional energy is required for cation formation. In this situation accounting for the surface potential, introduction of an additional energy barrier term would decrease ΔE_-^{surf} and increase ΔE_+^{surf}, so that the proposed cation formation of azobenzene cis-isomer on charged nanoparticle surface would become less energetically favourable compared to the neutral surface.

Finally, the catalytic performance of gold-palladium alloy nanoparticles in thermal isomerization of azobenzene surfactant (acceleration factor $\tau_0/\tau_1 \approx 18$) was better in comparison with monometallic palladium nanoparticles, but significantly lower than for pure gold nanoparticles, Pd<AuPd<Au, what indicates the absence of synergestic effects in this case. Therefore, gold atoms are the surface active sites, participating in the electron transfer with azobenzene moieties. Apparently the amount of surface gold atoms decreased upon alloying with palladium as compared with pure gold, thus decreasing the amount of electron transfers per time unit and, in turn, acceleration factor in the reaction of thermal cis-trans isomerization of azobenezene. It is possible that the enhancement of azobenzene thermal relaxation is attributed to specific physical properties of gold, for instance plasmonic response, electronic configuration and d-band structure.

A more detailed theoretical and experimental study is required to fully describe the mechanism of enhanced azobenzene cis-trans isomerization in the presence of metal nanoparticles.

Experimentally, nanoparticle surface structure, segregation pattern, and electronic properties should be addressed. Investigation of isomerization rates of azobenzene surfactants of different structures in the presence of silver, palladium and alloy nanoparticles may help to reveal the chemisorption effect. A future study employing alloy gold-silver and gold-palladium nanoparticles with deviation in gold molar fraction would be helpful to verify the conclusion about gold catalytic active sites.

In theoretical calculations, some more sophisticated models may be helpful, accounting for the mutual influence of nanoparticle surface and azobenzene molecules. For instance, steric effects on azobenzene geometry on the metal surface, surface charge, electrical conductivity and work function alteration due to charge transfer and dipole adsorption can be improved in future computational studies.

8. Complexes between azobenzene containing surfactants and gold nanorods

This chapter explores the complexes between gold nanorods and azobenzene containing surfactants differing in the spacer length between azobenzene group and charged head group (see **Figure 3.1a**). Complexes were prepared using non-irradiated surfactants and subsequently exposed to UV and blue light. The corresponding reversible changes in the position of longitudinal plasmonic mode of nanorods were tracked using UV-Vis absorption spectroscopy. The concentration of gold nanorods was unknown, allowing only qualitative analysis in the context of molar ratio between nanorods and surfactant.

8.1. Properties of gold nanorods

Initially four batches of gold nanorods have been prepared: AuNR-CTAB, AuNR-Si1, AuNR-Si2, AuNR-Si3 (**Scheme 8.1**). Gold nanorods AuNR-CTAB are stabilized with cetyltrimethylammoiniumbromide (CTAB) surfactant. It is known that CTAB surfactant forms a bilayer on gold surface, with cationic head groups in the inner layer pointing to the gold surface and in the outer layer – pointing to the solution [213] Gold nanorods AuNR-Si1, AuNR-Si2, AuNR-Si3 are decorated with a thin layer of porous silica. Surface ς-potential of silica-coated gold nanorods AuNR-Si1 was around +15mV, indicating the presence of a surfactant layer on surface. The surfactant has likely remained in solution after the preparation of gold nanorods. The registered value of ς-potential is in agreement with literature reports on positive ς-potential of CTAB-stabilized gold nanorods.[214]

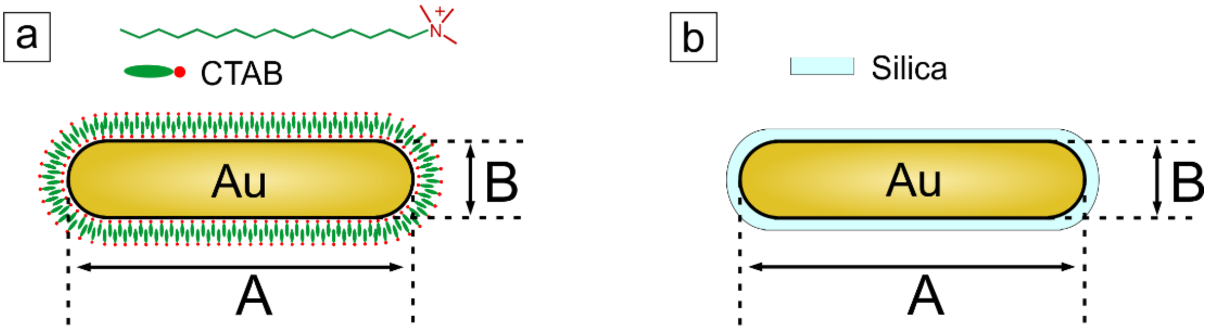

Scheme 8.1. Schematic of gold nanorods: (a) CTAB-stabilized gold nanorods AuNR-CTAB; (b) silica-coated gold nanorods AuNR-Si1, AuNR-Si2, AuNR-Si3.

Gold nanorods AuNR-AzoC6 have been prepared from AuNR-CTAB by surfactant replacement. Gold nanorods AuNR-CTAB were centrifuged and thus forced to the bottom of the tube. The decantant (above liquid) was replaced with the aqueous solution of azobenzene containing surfactant $AzoC_6$ ($C_{Azo} = 1$ mM). The process has been repeated several times in order to remove CTAB surfactant and other compounds remaining in solution after the synthesis procedure. The resulting AuNR-AzoC6 are supposed to be stabilized with a double layer of $AzoC_6$ instead of CTAB surfactant.

Figure 8.1 and Figure 8.2 show SEM and TEM micrographs of dried suspensions of the investigated gold nanorods. Dimensions of gold nanorods determined by TEM are listed in **Table 8.1**. The dimensions of gold nanorods are slightly different, but do not differ within the error bars. The all-mean aspect ratio of gold nanorods R = 3.8 ± 1.2. The silica shell was not detectable in TEM (**Figure 8.2**) and therefore it is to be less than 5 nm thin. In TEM and SEM micrographs (**Figure 8.1 and Figure 8.2**), one can see aggregates of gold nanorods densely packed side-by-side. Although it is not precise due to possible artefacts in TEM images, the distance between gold nanorods in such aggregates (column H in **Table 8.1**) appeared to be larger for the silica-covered nanorods AuNR-Si1, AuNR-Si2, as compared with the CTAB-stabilized AuNR-CTAB, implying a nanometer-thin coating.

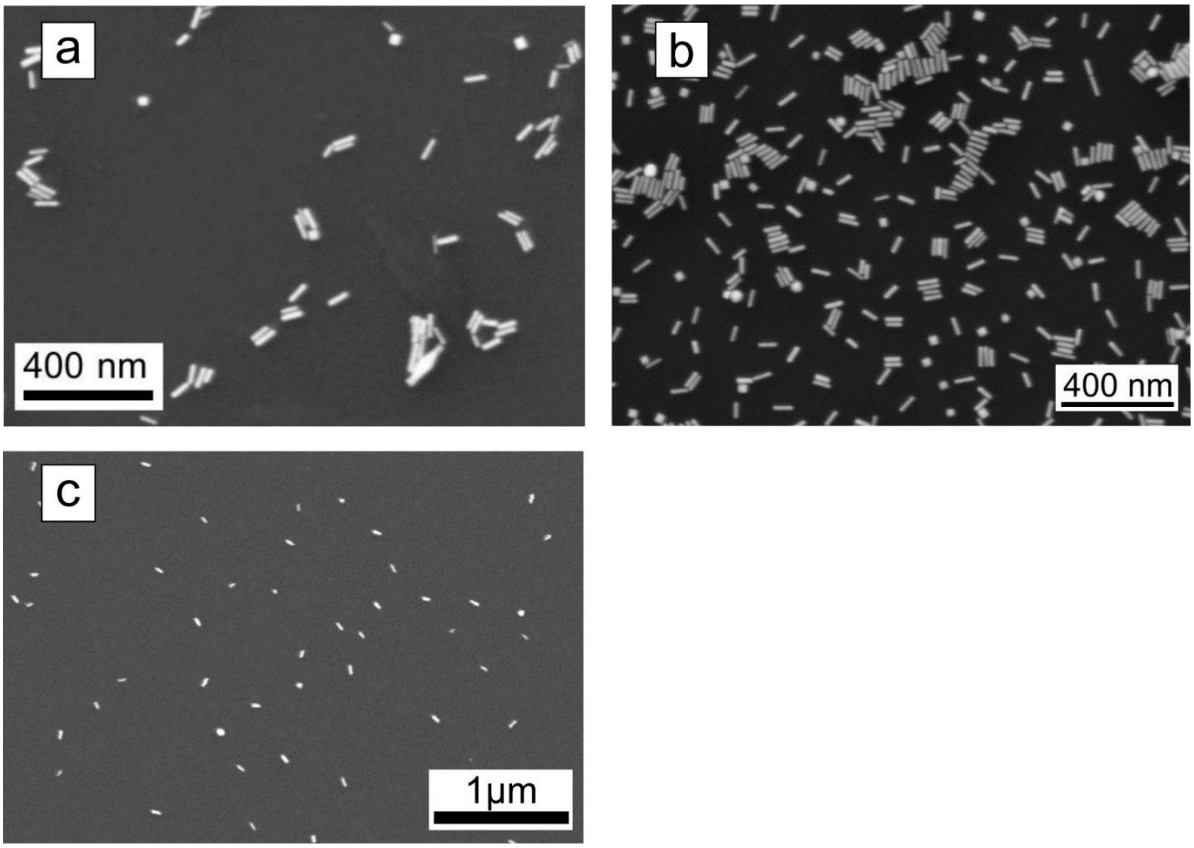

Figure 8.1. SEM micrographs of gold nanorods AuNR-CTAB (a), AuNR-AzoC6 (b), and AuNR-Si1 (c).

Table 8.1. Properties of the studied gold nanorods: length A, diameter B, aspect ratio R = A / B, minimal distance within aggregates H, and position of longitudinal plasmonic peak λ_{SP}.

Batch	A, nm	B, nm	R	H, nm	λ_{SP}, nm
AuNR-CTAB	65.4 ± 13.2	17.8 ± 4.6	3.9 ± 1.2	0.35 ± 0.11	837 ± 1
AuNR-C6	-	-	-	-	812 ± 1
AuNR-Si1	57.5 ± 14.6	19.1 ± 5.7	3.1 ± 0.8	1.21 ± 0.56	789 ± 4
AuNR-Si2	62.3 ± 12.7	17.9 ± 5.4	3.8 ± 1.1	1.36 ± 0.91	808 ± 2
AuNR-Si3	64.6 ± 13.6	16.3 ± 5.1	4.2 ± 1.1	-	820 ± 4

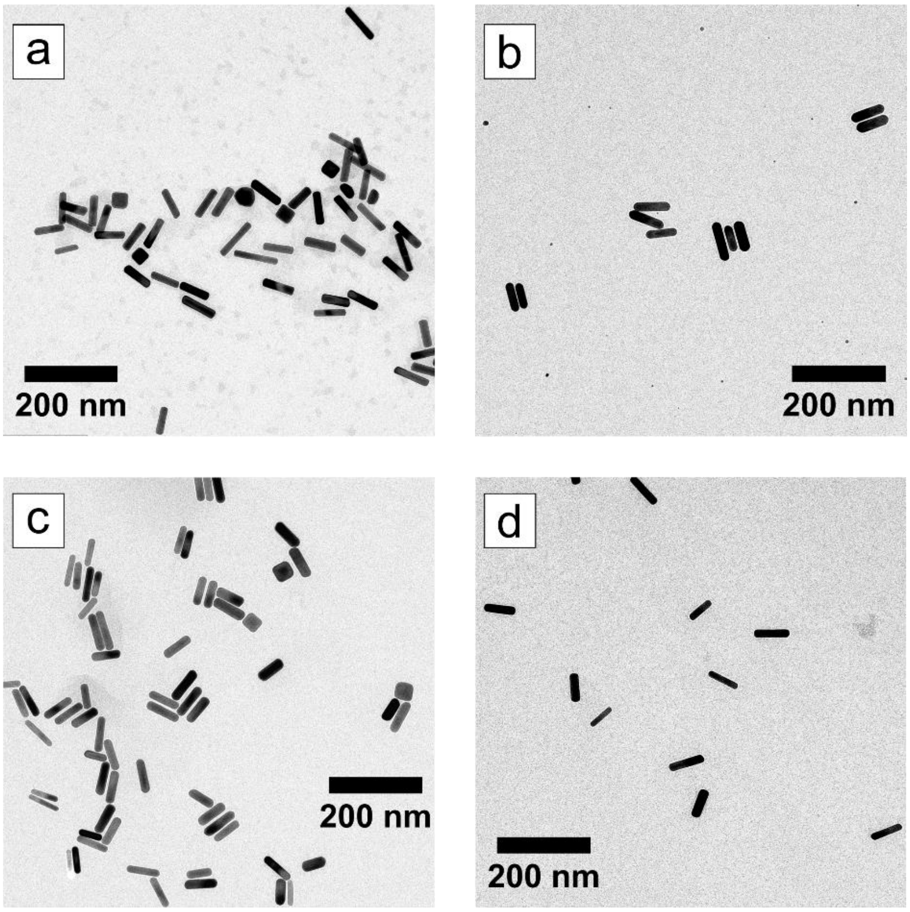

Figure 8.2. TEM micrographs of dried suspensions of gold nanorods: (a) AuNR-CTAB, (b) AuNR-Si1, (c) AuNR-Si2, (d) AuNR-Si3.

Absorption spectra of gold nanorods are shown in **Figure 8.3a**. One can see a transverse plasmon mode at $\lambda \approx 510$ nm and the pronounced longitudinal plasmonic maximum at $\lambda_{SP} \approx 800$ nm. Spectra have been normalized to the longitudinal plasmon maximum to facilitate their comparison. One can see that the longitudinal peak position depends on the nanorod sample. In fact, the longitudinal peak of nanorods from the same batch could occur at slightly different wavelengths in different experiments, probably due to the effects of dilution and aggregation state. The mean values of longitudinal peak position and standard deviations are listed in **Table 8.1** and demonstrated in **Figure 8.3b**. In the text below, longitudinal plasmonic peak position will be discussed and referred to as LSPR wavelength.

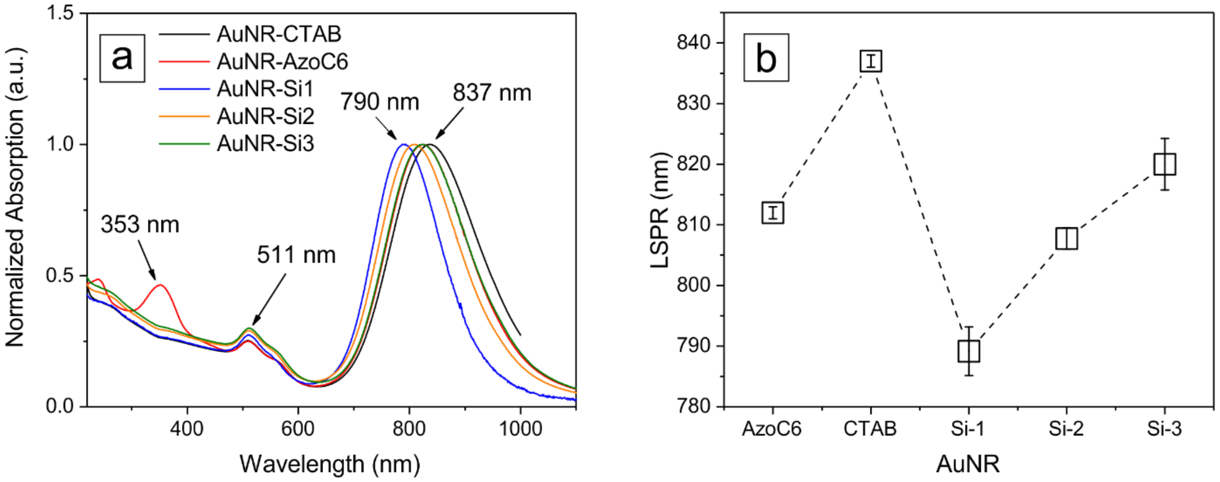

Figure 8.3. Normalized absorption spectra (a) and position of longitudinal plasmon maximum (b) of gold nanorods. The abscissas in (b) correspond to the batches of gold nanorods.

The difference in the position of longitudinal plasmon mode for different nanorods can be caused by (i) the difference in local dielectric environment, for instance due to the different thickness of silica shell, and (ii) by aspect ratio. The aspect ratio did not differ within error bars and is expected to cause up to 100-nanometer difference between LSPR wavelengths of AuNR-Si1 and AuNR-Si3 with similar silica dielectric environments.[83,215] Experimentally only ~30-nm difference in λ_{SP} was registered. Therefore, the effect of aspect ratio was assumed to be not decisive, but accompanied by the effect of the medium dielectric properties. Indeed, thin silica coating (< 10 nm thick) usually causes the longitudinal plasmon peak of gold nanorods to red-shift by several tenths of nanometer.[214,215]

The longitudinal LSPR mode of AuNR-CTAB occurs at the longest wavelength. Therefore, from the experiment we can expect higher dielectric constant of CTAB stabilizing shell than of silica capping.

One can see the π-π* absorption peak of trans-isomer of $AzoC_6$ surfactant at $\lambda = 353$ nm in the absorption spectrum of gold nanorods AuNR-AzoC6 (red line in **Figure 8.3a**). The transverse plasmon mode of AuNR-AzoC6 does not differ from AuNR-CTAB, while longitudinal plasmon maximum of AuNR-AzoC6 is blue-shifted relative to AuNR-CTAB. Apparently, removal of extensive stabilizing agents to prepare AuNR-AzoC6 changed the dielectric environment. The longitudinal peak occurred at shorter wavelengths in AuNR-AzoC6 samples with less surfactant in solution (tracked by its absorption maximum). **Table 8.1** contains the value registered in the sample with the lowest amount of $AzoC_6$.

Aggregation of gold nanorods can be induced by electrostatical screening via salt addition (**Figure 8.4a**), or by UV irradiation once the nanorods are stabilized with azobenzene containing surfactant (**Figure 8.4b**). In the case of sodium chloride addition, calculated Debye length is $\lambda_D \approx 7.47$ nm for 1.66 mM NaCl and $\lambda_D \approx 5.29$ nm for 3.31 mM NaCl.[205] These values show that the electrical double layer of gold nanorods is strongly suppressed by stabilizing agents, counterions and unknown supporting electrolytes in solution, since rather low concentration of sodium chloride induced gold nanorod aggregation. In **Figure 8.4b**, changes in the surfactant absorption maximum in the UV range (353 nm) indicate reversible isomerization of $AzoC_6$ surfactant. Estimated via extinction coefficient concentration of surfactant $C_{Azo} \approx 0.002$ mM. Gold nanorods AuNR-AzoC6 aggregated upon UV-induced trans-cis photoswitching (red curve), apparently due to UV-induced destabilization of stabilizing surfactant bilayer on gold nanorod surface.

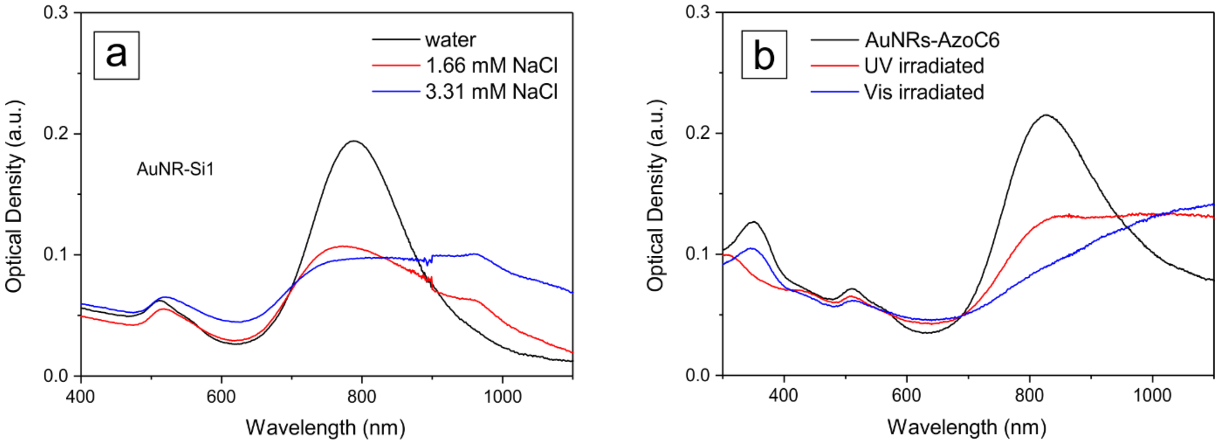

Figure 8.4. (a) Absorption spectra of gold nanorods AuNR-Si1 in water (black curve) and with added sodium chloride (see legend). (b) Absorption spectra of gold nanorods AuNR-AzoC6 as prepared (black curve) and exposed to UV (red curve) and subsequently visible irradiation (blue curve).

8.2. Complexes between gold nanorods and azobenzene containing surfactant

8.2.1. Successive addition of azobenzene surfactant

In the first series of experiments, small amounts of azobenzene containing surfactant have been successively added to aqueous suspensions of gold nanorods. The recorded absorption spectra show bathochromic shift in longitudinal plasmonic peak of gold nanorods upon addition of surfactant, likely due to the changes in the dielectric environment. **Figure 8.5a** shows the example of the absorption spectra of gold nanorods AuNR-Si1 recorded upon step-by-step addition of azobenzene containing surfactant $AzoC_6$. A slight decrease in the intensity of the gold nanorod longitudinal peak was registered, attributed to the dilution of nanorods during the titration process. **Figure 8.5b** shows absorption spectra of AuNR-AzoC6 with added surfactant $AzoC_6$. In the UV spectral range, the intensity of absorption maxima of surfactant increases because of increase in surfactant concentration. At the same time, transverse mode of gold nanorods remains intact, while the longitudinal mode red-shifts.

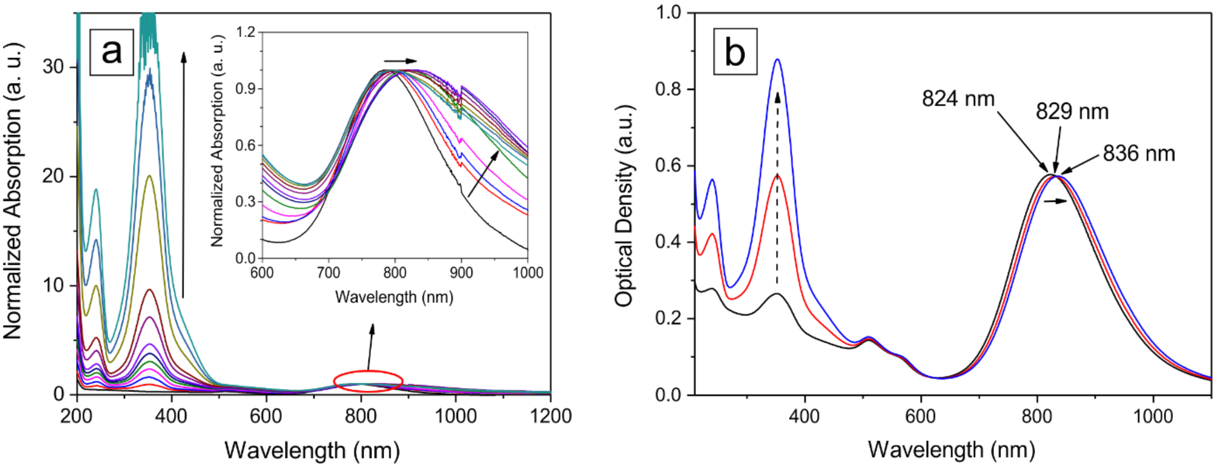

Figure 8.5. (a) Normalized UV-Vis-NIR absorption spectra of gold nanorods AuNR-Si1 at increasing concentration of azobenzene containing surfactant AzoC$_6$ up to $C_{Azo} = 0.2$ mM. Spectra were normalized to the longitudinal plasmonic maximum of gold nanorods, shown in the inset at higher magnification. C(AuNR-Si1) = 0.03 C_0 (b) UV-Vis absorption spectra of gold nanorods AuNR-AzoC6 at increasing concentration of azobenzene containing surfactant AzoC$_6$ from $C_{Azo} = 0.003$ mM to $C_{Azo} = 0.016$ mM. C(AuNR-AzoC6) = 0.2 C_0.

Figure 8.6 summarizes the red shift in the position of longitudinal plasmonic absorption peak of different gold nanorods upon successive addition of azobenzene surfactant AzoC$_6$, relative to the initial peak position in gold nanorods without surfactant. One can see that LSPR wavelength of gold nanorods does not shift within error bars at surfactant concentrations $C_{Azo} < 0.004$ mM. At higher surfactant concentrations, red shifts up to 45 nm were registered. For AuNR-Si1 (blue circles) at $C_{Azo} = 0.02$mM the behaviour of LSPR wavelength as a function of C_{Azo} changed: blue shift in the spectral peak position occurred at further increase of C_{Azo}. This might indicate plasmon coupling in nanorod-surfactant complexes in titrated suspensions, as discussed in more details below.

One can also notice that the slope of the red shift increase at $C_{Azo} \geq 0.01$ mM is the highest in AuNR-Si1 compared to other nanorod batches. This may be due to a higher surfactant-to-nanorod ratio. Indeed, gold nanorods AuNR-Si1 were the most diluted with C(AuNR-Si1) = 0.03 C_0. These results show that the molar ratio between gold nanorods and azobenzene containing surfactant may be important for their interaction, possibly due to formation of ionically bound surfactant bilayer.

With respect to the observed bathochromic shift of gold nanorod LSPR wavelength upon mixing with azobenzene containing surfactant, a border in surfactant concentrations can be distinguished: $C_{Azo} < 0.003$ mM with no red shift within error bars; and $C_{Azo} \geq 0.003$mM with up to 45-nm red shift in LSPR wavelength. Thus. the working concentrations of surfactant in the experiments with gold nanorods were $C_{Azo} > 0.003$mM to assure the LSPR red shift. In the text below, surfactant concentrations from three ranges will be considered and referred to as *low* ($C_{Azo} \approx 0.004$ mM, up to 5 nm shift in λ_{SP}), *intermediate* ($C_{Azo} \approx 0.02$ mM, maximal red shift in λ_{SP} of AuNR-Si1), and *high* ($C_{Azo} \geq 0.1$ mM, moderate λ_{SP} shift in AuNR-Si1).

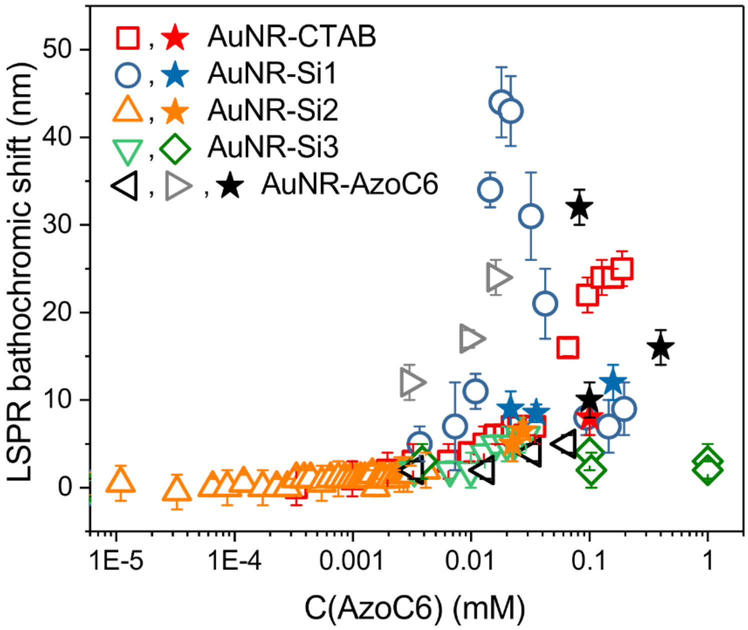

Figure 8.6 Red shift of longitudinal plasmonic maximum of gold nanorods as a function of added AzoC$_6$ surfactant concentration. Open symbols show titration experiments, when small volumes of surfactant were step-by-step added to gold nanorod suspensions. Solid stars correspond to surfactant-nanorod complexes initially prepared at certain surfactant concentrations. Concentrations of gold nanorods were the following: C(AuNR-CTAB) = 0.1 C$_0$; C(AuNR-Si1) = 0.03 C$_0$; C(AuNR-Si2) = 0.1 C$_0$; C(AuNR-Si3) = 0.04 C$_0$ (green rhombi), C(AuNR-Si3) = 0.1 C$_0$ (green tiangles); C(AuNR-AzoC6) = 0.2 C$_0$ (grey triangles), C(AuNR-AzoC6) = 0.9 C$_0$ (black triangles, black stars).

8.2.2. Complexes prepared by mixing components at certain concentrations

Compared with surfactant-nanorod suspensions prepared by titration (open symbols in **Figure 8.6**), the complexes prepared by mixing components at certain surfactant concentrations (stars in **Figure 8.6**) possess a less pronounced red-shift of longitudinal LSPR wavelength at similar surfactant concentrations. This can be seen on the examples of AuNR-CTAB at high $C_{Azo} = 0.1$ mM, and AuNR-Si1 at intermediate $C_{Azo} = 0.02$ mM (red and blue stars *vs.* open symbols).

Table 8.2 illustrates the spectroscopically registed red shift in longitudinal LSPR mode of gold nanorods in complexes with azobenzene containing surfactants. The complexes were prepared at low $C_{Azo} = 0.004$ mM, intermediate $C_{Azo} = 0.025 \pm 0.005$ mM, and high $C_{Azo} = 0.15 \pm 0.05$ mM, gold nanorods were diluted to $C = 0.1\ C_0$ and $C \approx 0.035\ C_0$, mentioned in the Table. Although the initial longitudinal LSPR wavelength of gold nanorods was slightly different in different experiments, the relative LSPR shift upon mixing with surfactant was similar at similar conditions. Thus, here and below, mean values are shown. Two sources of inaccuracy have been taken into account: (i) machinery inaccuracy of spectrometer, cautiously assumed to be 1 nm, (ii) mean standart deviation. Unfortunately, a detailed study of the LSPR shift as a function of C_{Azo} in the initially prepared nanorod-surfactant complexes was difficult due to limited volumes of gold nanorod suspensions. Yet, one can see that in the initially mixed systems the LSPR red shift is more prominent at higher surfactant concentrations.

Table 8.2 Influence of surfactant concentration C_{Azo} on the bathochromic shift in longitudinal plasmonic peak position in absorption spectra of the complexes between gold nanorods and azobenzene containing surfactant $AzoC_6$.

	C_{Azo} = 0.004 mM	C_{Azo} = 0.025 mM	C_{Azo} = 0.15 mM
AuNR-CTAB, C = 0.1 C_0	-	-	8.0 ± 2.4
AuNR-Si1, C = 0.03 C_0	5.0 ± 2.8 nm	8.8 ± 2.1	12 ± 2.8
AuNR-Si2, C = 0.1 C_0	-	5.5 ± 1.8	-
AuNR-Si3, C = 0.04C_0	3.0 ± 2.2	-	-

These results emphasize the influence of C_{Azo} on the observed plasmonic response. Two interpretations are possible here. On the one hand, azobenzene surfactant shell around gold nanorods can be gradually filled up and become denser at higher C_{Azo}, increasing the dielectric constant of local effective medium around gold nanorods. On the other hand, the thickness of the dense surfactant shell decorating gold nanorods *d* can increase with C_{Azo}, so that it better matches the electromagnetic decay length *l* of gold nanorods, and the LSPR red shift becomes more pronounced according to the Equation (1.3) in Section 1.2.5, which is:

$$\Delta\lambda_{max} = m\Delta n\left(1 - e^{-2d/l}\right)$$

The qualitative calculations below explain the latter effect. In Ref. 216 decay length of CTAB-coated gold nanorods was studied as a function of particle dimensions. For nanorods with similar size, decay length $l \approx 27$ nm. In this simple estimation, we neglect the thin silica capping. Assuming the thickness of $AzoC_6$ surfactant bilayer as $d = 3$ nm, $d/l = 0.1$ and $\Delta\lambda_{max} = 0.2\ m\Delta n$ (m – refractive index sensitivity of gold nanorods, Δn is the difference in the refractive index due to ligand, *i. e.* surfactant, adsorption). Upon surfactant multilayer formation, *e.g.* $d = 12$ nm, $d/l = 0.44$, $\Delta\lambda_{max} = 0.6\ m\Delta n$.

Figure 8.7a shows the comparison of the absorption spectra of nanorod-surfactant complexes at the same C(AuNR) and high surfactant concentration $C_{Azo} = 0.2$ mM, prepared by step-by-step increasing surfactant concentration ("titrated", black curve) and initially prepared at high C_{Azo} ("initially mixed", red curve). Relatively to the initially mixed system, the plasmonic peak in the titrated suspension is blue-shifted and broadened with a mode in the near-IR range, resembling the shape of the longitudinal peak of in **Figure 8.4a** for gold nanorods with screened electrostatic repulsion. This indicates possible aggregation of nanorods upon addition of small surfactant portions, *i. e.* at low C_{Azo} , so that step-by-step increasing surfactant concentration promotes nanoaggregation. Indeed, titrated suspension of AuNR-Si2 with $C_{Azo} = 0.004$ mM aggregated next day after preparation (**Figure 8.7b**). The suspension was stored in the dark at 4°C overnight, what might have preserved its colloidal stability. Next day thermal diffusion due to temperature increase, as well as mechanical stimulation upon filling the cuvett before recording absorption spectra, could have triggered rapid diffusion-limited aggregation of gold nanorods. The registered 62-nm hypsochromic shift of longitudinal peak position and simultaneous bathochromic shift of transverse plasmonic mode of gold nanorods indicated side-to-side nanorod assembling in the beginning of aggregation process.[217] Long-wavelength plasmonic mode gradually arised in the near-IR spectral region, apparently as a result of further random aggregation of nanorod-surfactant complexes, similar to **Figure 8.4**.

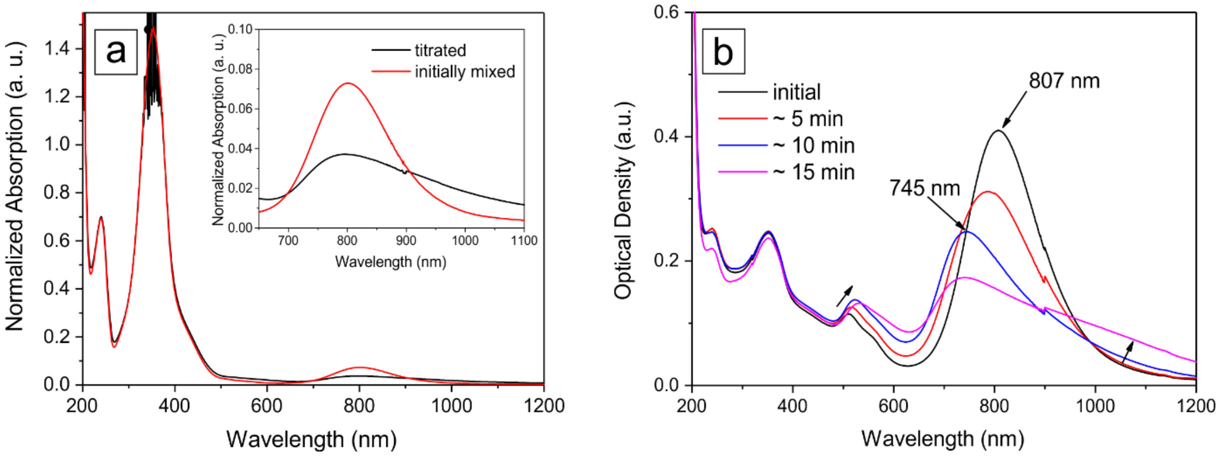

Figure 8.7. (a) Normalized absorption spectra of complexes between AuNR-Si1 and azobenzene containing surfactant $AzoC_6$ prepared by titration (black curve) and initially mixed (red curve). Spectra were normalized to the surfactant absorption maximum. $C(AuNR) = 0.03\ C_0$, $C_{Azo} = 0.2$ mM. (b) UV-Vis-NIR absorption spectra of gold nanorods AuNR-Si2 with successively added azobenzene containing surfactant $AzoC_6$ at $C(AuNR) = 0.1\ C_0$, $C_{Azo} = 0.004$ mM. Spectra were recorded next day after complex preparation.

Therefore, the 45-nm LSPR red shift upon titration of AuNR-Si1 in **Figure 8.6** may be caused by self-assembling of gold nanorods at low surfactant concentrations. Since the transverse nanorod plasmonic mode did not change during the titration experiments, perhaps the nanorod aggregation process begins with end-to-end nanorod assembling (LSPR red shift at $C_{Azo} < 0.02$ mM), and proceeds with side-to-side assembling of gold nanorods (blue shift at $C_{Azo} > 0.02$ mM).[217] Addition of a portion of surfactant in titration increases the occurrence of aggregates, to some extent reproducing the results in Section 4.7 for spherical gold nanoparticles.

Based on these results, it is worth mentioning that the complexes between gold nanorods and azobenzene containing surfactants are to be prepared by mixing components at initially high enough surfactant concentration $C_{Azo} > 0.004$ mM. Indeed, **Figure 8.8** demonstrates that in contrast with titrated suspensions, nanorod-surfactant complexes initially prepared at $C_{Azo} = 0.02$ mM remained colloidally stable, with only a slight blue shift of LSPR wavelength on the timescale of several days.

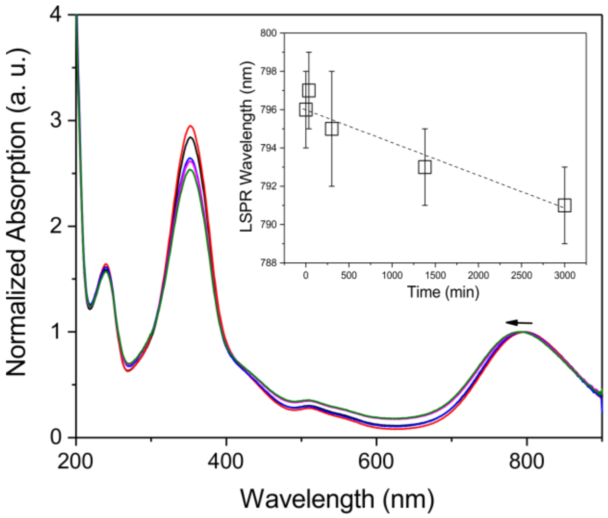

Figure 8.8. Normalized absorption spectra of AuNR-Si1 mixed with $AzoC_6$ at $C(AuNR) = 0.03C_0$, $C_{Azo} = 0.02mM$, recorded over time. Spectra were normalized to gold nanorod longitudinal plasmonic maximum. The inset shows the longitudinal peak position as a function of time. The dashed line serves as an eye guide.

8.2.3. Interaction of gold nanorods with azobenzene containing surfactants with different tail length.

The complexes between gold nanorods and azobenzene containing surfactants $AzoC_6$, $AzoC_8$, $AzoC_{10}$, $AzoC_{12}$ differing in the tail length were prepared by mixing solutions at certain concentrations C(AuNR) and intermediate $C_{Azo} = 0.025 \pm 0.005$ mM. Longitudinal LSPR peak in the absorption spectra of the complexes appeared red-shifted compared to pure gold nanorods. The registered relative red shifts are listed in **Table 8.3**.

Table 8.3. Influence of surfactant tail length on the bathochromic shift in longitudinal plasmonic peak position of gold nanorods in complexes with azobenzene containing surfactants. The listed values (in nm) are the shifts relative to the LSPR of pure gold nanorods.

	C(AuNR)	C_{Azo}, mM	$AzoC_6$	$AzoC_8$	$AzoC_{10}$	$AzoC_{12}$
AuNR-Si1	$0.03\ C_0$	0.03	8.8 ± 2.1	19 ± 1.4	9 ± 1.4	18.5 ± 2.4
AuNR-Si2	$0.1\ C_0$	0.02	5.5 ± 1.8	8.0 ± 1.4	11.0 ± 1.4	-

The origin of LSPR red shift in nanorod-surfactant complexes as compared with pure nanorod suspension is apparently the replacement of dielectric environment around gold nanorods with azobenzene surfactant shell. One can see from **Table 8.3** that the relative red shift increases with surfactant tail length, implying the influence of surfactant hydrophobicity on nanorod-surfactant complex formation. Indeed, for the complexes between AuNR-Si1 and $AzoC_{12}$ surfactant, a pronounced LSPR red shift of 17.0 ± 2.4 nm was registered even at low surfactant concentration $C_{Azo} = 0.004$ mM.

The differences in dielectric properties of the densely packed surfactant shell on gold nanorods between the four azobenzene containing surfactants are likely very small. Therefore, the observed effect of surfactant hydrophobicity can be assigned to the surfactant shell formation, which is facilitated in the case of longer hydrophobic tail. Likely similar to the effect of surfactant concentration, the shell becomes denser and/or becomes thicker at lower C_{Azo} for surfactants with longer tails.

8.3. Thermal cis-trans isomerization of azobenzene surfactant in the presence of gold nanorods

The next experiment tested the acceleration of cis-to-trans thermal isomerization of azobenzene containing surfactant in the presence of gold nanorods. **Figure 8.9** shows absorption spectra of gold nanorods AuNR-Si1 mixed with UV-irradiated azobenzene containing surfactant $AzoC_6$. Spectra were recorded in the dark over time. Temperature increase was registered during the experiment due to spectrophotometer heating.[1] Longitudinal plasmonic maximum of gold nanorods blue-shifted from $\lambda = 794$ nm to $\lambda = 791$ nm upon cis-trans relaxation of surfactant. This effect likely relates to the changes in refractive indices of cis- and trans- surfactant isomers and will be described in more details in the next section. The intensity of the longitudinal plasmonic peak slightly decreased, likely due to a slow sedimentation of gold nanorods. Monoexponential fit of optical density at 376 nm as a function of time $D_{376}(t)$ (similar to Chapter 6) yielded the thermal relaxation time (lifetime of cis-isomer) of cis- azobenzene surfactant $\tau = 22.2 \pm 0.6$ h.

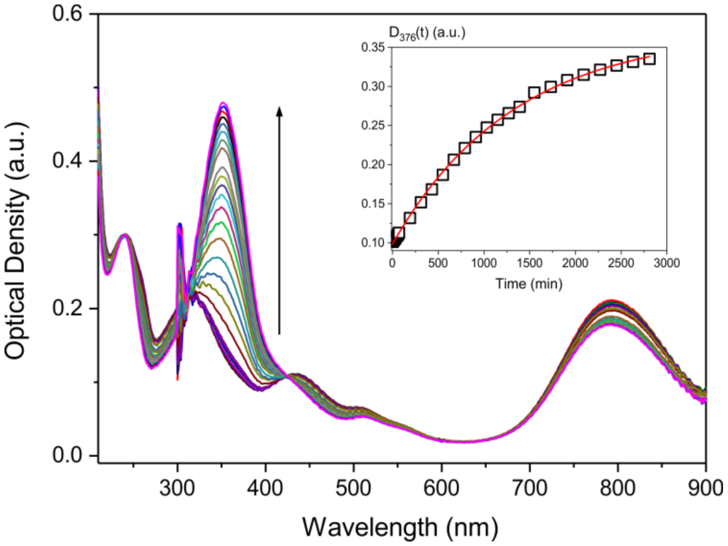

Figure 8.9. UV-Vis absorption spectra of UV-irradiated azobenzene containing surfactant $AzoC_6$ mixed with gold nanorods AuNR-Si1, recorded as a function of time. The inset shows recorded optical density at 376 nm (squares) and its monoexponential fit (red line). Temperature increase was registered during the measurement.

---

[1] This particular experiment was done with the old spectrophotometer Lambda 16 (Perkin Elmer).

The estimated thermal relaxation time of azobenzene surfactant in the presence of gold nanorods is 2.8 times smaller than the relaxation time of surfactant in pure water ($\tau_0 = 62$ h). Most probably, the acceleration of thermal cis-trans isomerization is caused by (i) temperature increase during the experiment, and (ii) the presence of co-solutes, *i. e.* additional electrolytes and stabilizing agents, in gold nanorod suspensions. Indeed, thermal relaxation time of AzoC$_6$ was found to decrease to $\tau_0 = 48$ h even with slight increase in solution ionic strength (5 mM NaCl).[25] The extremely short isomerization time on a minute scale like in the case of gold nanoparticles was not revealed for gold nanorods, what excludes the interaction of azobenzene surfactant cis-isomers with gold surface via adsorbed azo bond, apparently due to protecting silica shell.

8.4. Influence of UV and blue light on the plasmon wavelength of gold nanorods decorated with azobenzene surfactants

Complexes between gold nanorods and azobenzene containing surfactants were prepared at $C_{Azo} \approx 0.03$ mM and subsequently exposed to alternately UV and visible (blue) light. **Figure 8.10** shows two examples of these experiments, for the complexes between AuNR-Si2 and AzoC$_{10}$, and for AuNR-AzoC6 with AzoC$_6$. The results for gold nanorods AuNR-Si1 and AuNR-Si3 essentially reproduce those for AuNR-Si2 and therefore the recorded absorption spectra are not shown.

In **Figure 8.10a**, one can see absorption spectra of gold nanorods AuNR-Si2 without surfactant (black curve), after mixing with surfactant AzoC$_{10}$ (red curve), and after irradiation. After preparation of the complexes, absorption band of azobenzene surfactant appeared in the spectra, showing the maximum at 352 nm. This corresponds to the π-π* band of trans-isomers of AzoC$_{10}$ surfactant. Transverse plasmonic mode of gold nanorods was invariant during the whole experiment, observed at 511 nm. Longitudinal plasmonic maximum experienced red shift by 11 nm (**Table 8.3**), as can be well seen from the inset in **Figure 8.10a**. Spectra after exposure to light overlap, indicating fully reversible light-controlled spectral changes. After irradiation with UV light, corresponding changes in the absorption band of surfactant indicate its trans-cis isomeritation. Simultaneously, longitudinal plasmonic maximum blue-shifted by 3 nm towards the LSPR position of pure gold nanorods. Exposure of the nanorod-surfactant suspension to blue light recovered the predominantly trans- photostationary state of surfactant and longitudinal LSPR wavelength of gold nanorods in complex with AzoC$_{10}$. In AuNR-AzoC6 (**Figure 8.10b**), trans-cis irradiation of AzoC$_6$ surfactant caused shifting and intensity decrease of the nanorod longitudinal plasmonic mode. Probably, every exposure to UV light induced slight aggregation of gold nanorods, thus decreasing the concentration of the dispersed particles in solution. Plasmon peak intensity decrease did not occur in silica-coated gold nanorods. One can see that the absorption maximum of azobenzene containing surfactant has higher intensity in **Figure 8.10b**. This can be due to real surfactant concentration was higher than expected $C_{Azo} = 0.02$ mM, as a result of the AzoC$_6$ presence in the initial AuNR-AzoC6 suspension.

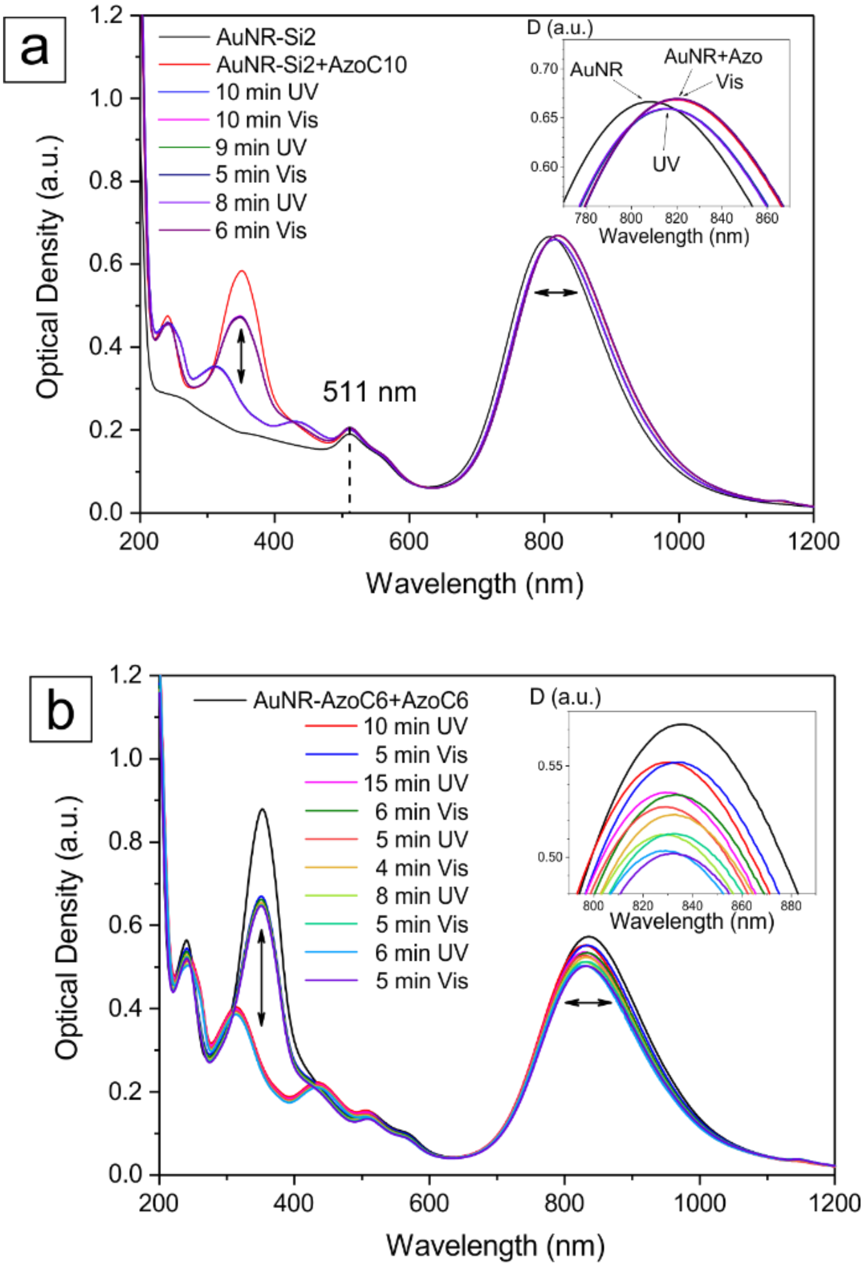

Figure 8.10. UV-Vis-NIR absorption spectra of complexes between gold nanorods and azobenzene containing surfactant after subsequent exposure to UV and blue (Vis) light. The insets show longitudinal peak of gold nanorods at high magnification. (a) Complexes between AuNR-Si2 and azobenzene surfactant AzoC$_{10}$, C(AuNR) = 0.1C$_0$, C$_{Azo}$ = 0.02mM. (b) Gold nanorods AuNR-AzoC6 with added surfactant AzoC$_6$, C(AuNR) = 0.2C$_0$, C$_{Azo}$ = 0.02mM.

Figure 8.11 demonstrates reversible changes in the position of longitudinal plasmonic maximum of gold nanorods in complexes with azobenzene containing surfactants upon photoisomerization. One can see that the spectral changes can be triggered in at least eight UV-Vis irradiation cycles. Data are not shown for AuNR-Si1 in complexes with AzoC$_{10}$, to help Figure reading. These complexes unexpectedly showed the opposite behavior, which might be related to the initial state of surfactant in complexes with gold nanorods, for instance the presence of micelles. Indeed, in Ref. 5 CMC of AzoC$_{10}$ was found to be around 0.07 mM in pure water at room temperature. Accounting for the co-solutes, a reduced CMC value is to be expected. UV light can release individual surfactant molecules from micelles, which then can contribute to the shell around gold nanorods.

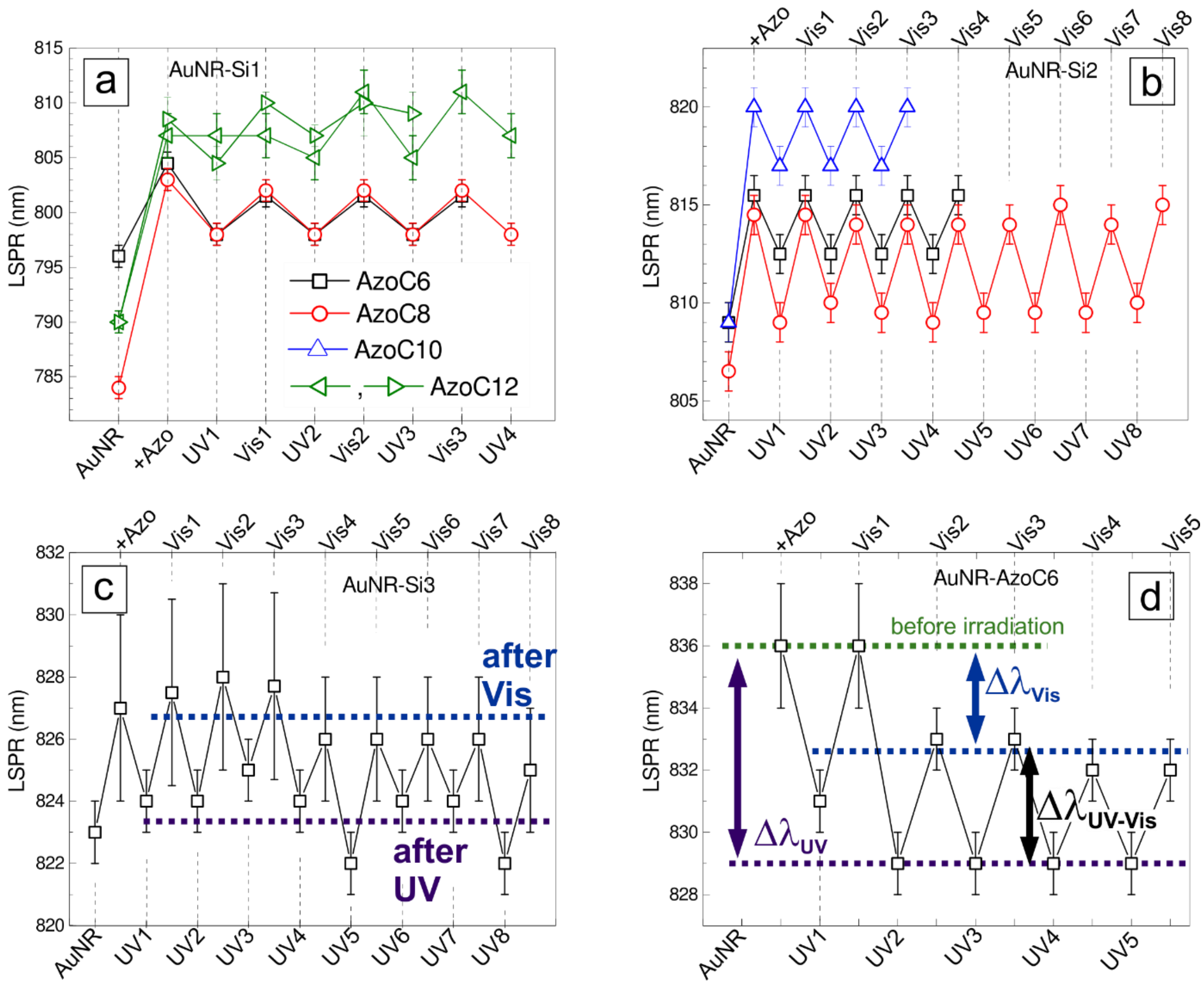

Figure 8.11. Position of longitudinal plasmonic maximum of gold nanorods without surfactant, in complexes with azobenzene containing surfactants, after exposure to UV and blue light. Legend in (a) the top left chart for AuNR-Si1 is applicable to other nanorod batches: (b) AuNR-Si2, (c) AuNR-Si3, (d) AuNR-AzoC6. X-axis shows the events of complex preparation (+Azo), and irradiations with UV and blue (Vis) light. The initial points AuNR correspond to pure gold nanorods. Concentrations of gold nanorods and surfactants were as follows: (a) C(AuNR-Si1) = 0.03 C_0, for $AzoC_6$ and $AzoC_8$ C_{Azo} = 0.03 mM, for $AzoC_{12}$ C_{Azo} = 0.004 mM (—◁—) and C_{Azo} = 0.02 mM (—▷—); (b) C(AuNR-Si2) = 0.1 C_0, for $AzoC_6$ C_{Azo} = 0.03 mM, for $AzoC_8$ and $AzoC_{10}$ C_{Azo} = 0.02 mM; (c) C(AuNR-Si3) = 0.03 C_0, $C_{Azo} \geq 0.1$ mM; (d) C(AuNR-$AzoC_6$) = 0.2 C_0, C_{Azo} = 0.02 mM.

It should be mentioned that for AuNR-Si1 with $AzoC_{12}$ (**Figure 8.11a**, green), the results of two experiments are shown, differing in the surfactant concentration: tringles pointing to the left correspond to low C_{Azo} = 0.004 mM, triangles pointing to the right – to C_{Azo} = 0.02 mM. One can see that LSPR wavelength of gold nanorods could be controlled by light already at low surfactant concentration. The first irradiation cycle of AuNR-Si1 in complexes with $AzoC_{12}$

appeared to be the training cycle, which can be assigned to the process of formation of azobenzene surfactant shell on nanorod surface. In the complexes between AuNR-Si3 and AzoC$_6$ surfactant (**Figure 8.11c**) C_{Azo} = 0.1 mM was higher than in other nanorod-surfactant complexes (C_{Azo} = 0.02 – 0.03 mM) and increased to C_{Azo} = 1 mM in the last three irradiation cycles, *i. e.* one can expect relatively thick azobenzene surfactant shell in these complexes. One can see that such increase in C_{Azo} did not influence the photoresponse of gold nanorods.

Table 8.4 summarizes the observed effect of fine-tuning of LSPR wavelength of gold nanorods by light. Relative photoinduced shifts of LSPR wavelength $\Delta\lambda_{UV}$, $\Delta\lambda_{Vis}$ and $\Delta\lambda_{UV\text{-}Vis}$ were calculated as shown in **Figure 8.11d**.

Table 8.4. Relative photoinduced shift of longitudinal LSPR wavelength of gold nanorods in complexes with azobenzene containing surfactants: (a) average UV-induced shift $\Delta\lambda_{UV}$ relative to the LSPR position in the non-irradiated complexes; (b) average blue-light induced shift $\Delta\lambda_{Vis}$ relative to the non-irradiated complexes; (c) average shift between UV- and Vis- irradiated complexes $\Delta\lambda_{UV\text{-}Vis}$ (absolute values). Negative values in (a) and (b) correspond to blue LSPR shift.

(a)

$\Delta\lambda_{UV}$, nm	AzoC$_6$	AzoC$_8$	AzoC$_{10}$	AzoC$_{12}$
AuNR-Si1	-6.5 ± 1.2	-5.0 ± 1.1	3.5 ± 2.8	-1.7 ± 2.2
AuNR-Si2	-3.0 ± 1.1	-5.0 ± 1.5	-3.0 ± 1.2	-
AuNR-Si3	-2.4 ± 2.8	-	-	-
AuNR-AzoC6	-6.6 ± 2.4	-	-	-

(b)

$\Delta\lambda_{Vis}$, nm	AzoC$_6$	AzoC$_8$	AzoC$_{10}$	AzoC$_{12}$
AuNR-Si1	-3.0 ± 1.2	-1.0 ± 1.2	-0.1 ± 2.8	1.5 ± 2.6
AuNR-Si2	0.0 ± 1.1	-0.2 ± 1.5	0.0 ± 1.2	-
AuNR-Si3	0.5 ± 2.8	-	-	-
AuNR-AzoC6	-2.8 ± 2.6	-	-	-

(c)

$\Delta\lambda_{UV\text{-}Vis}$, nm	AzoC$_6$	AzoC$_8$	AzoC$_{10}$	AzoC$_{12}$
AuNR-Si1	3.5 ± 0.6	4.0 ± 0.6	3.6 ± 0.6	3.7 ± 1.1
AuNR-Si2	3.0 ± 0.5	4.7 ± 0.4	3.0 ± 0.6	-
AuNR-Si3	3.0 ± 0.7	-	-	-
AuNR-AzoC6	4.1 ± 0.7	-	-	-

UV light induced blue shifts of up to 6.6 nm in all nanorod-surfactant complexes, except for the complexes between AuNR-Si1 and AzoC$_{10}$, showing red shift (**Table 8.4a**). The negative values of $\Delta\lambda_{UV}$ imply smaller dielectric constant of the local medium around gold nanorods when azobenzene containing surfactant is in cis-state, compared to trans- conformation. Under blue light, longitudinal plasmon mode of nanorods coincides the LSPR wavelength in non-irradiated complexes almost in all experiments: the values of $\Delta\lambda_{Vis}$ are around zero (**Table 8.4b**). Slightly blue-shifted LSPR wavelengths after exposure to visible light, for instance for the complexes between AuNR-Si1 and AzoC$_6$, may be explained by the photostationary state of surfactant, which was not completely recovered to the predominantly trans- conformation.

The difference between LSPR wavelength of gold nanorod-surfactant complexes in UV and blue light was similar in all experiments, with the all-mean value $\Delta\lambda_{UV\text{-}Vis} = 3.6 \pm 0.3$ nm (**Table 8.4c**). Clear trends related to surfactant concentration, gold nanorod – surfactant ratio, length of surfactant, or nanorod batch were not revealed. The uniform difference in LSPR wavelength in UV and blue light Δλ can be attributed only to the changes in local dielectric environment upon surfactant photoisomerization.

Two interpretations of what happens upon surfactant photoisomerization can be possible. On the one hand, changes in local medium refractive index can be understood in the context of photoinduced changes in dipole moment of surfactant molecules sitting in the shell around gold nanorods. On the other hand, surfactant shell can be destabilized upon UV irradiation, because more bulky and hydrophilic surfactant molecules in cis-conformation can detach from gold nanorods.

Figure 8.12 shows distributions of ς-potential for gold nanorods AuNR-Si1 in complexes with surfactants AzoC$_6$ and AzoC$_8$. Measured ς-potential of gold nanorods had a tendency to be less positive without surfactant and in complexes after UV irradiation ($10 < \varsigma < 25$ mV), and more positive in non-irradiated and Vis-irradiated complexes with surfactant ($30 < \varsigma < 55$ mV). One can see that the distributions of ς-potential appeared bimodal for the complexes with AzoC$_8$. This is likely due to the nonspherical shape of gold nanorods: the theory of the method is well established only for spherical particles. Indeed, DLS size distribution of gold nanorods is bimodal (**Figure 8.12a**), with the modes centered at around 70 nm and 6 nm. In fact, DLS sizes are in a quite good agreement with the dimensions determined by TEM. The bimodality in ς-potential distributions made the quantitative analysis of the surface charge of surfactant-nanorod complexes difficult. Nevertheless, both modes experienced reversible light-induced changes, as illustrated in the plot in **Figure 8.12d**. Considering the average values would not change the conclusion. The complexes with AzoC$_8$ apparently needed one training cycle, assigned to some equilibration of the system, for example disarrangement of micelle-like surfactants structures and/or attachment to gold nanoparticle surface. The registered photoinduced changes in ς-potential indicate that surfactant cis-isomers produced by UV light withdraw from gold nanorod surface, decreasing the particle surface charge to that of pure gold nanorods, and surfactant trans-isomers re-attach to gold nanorods after exposure to blue light, causing the surface ς-potential to increase.

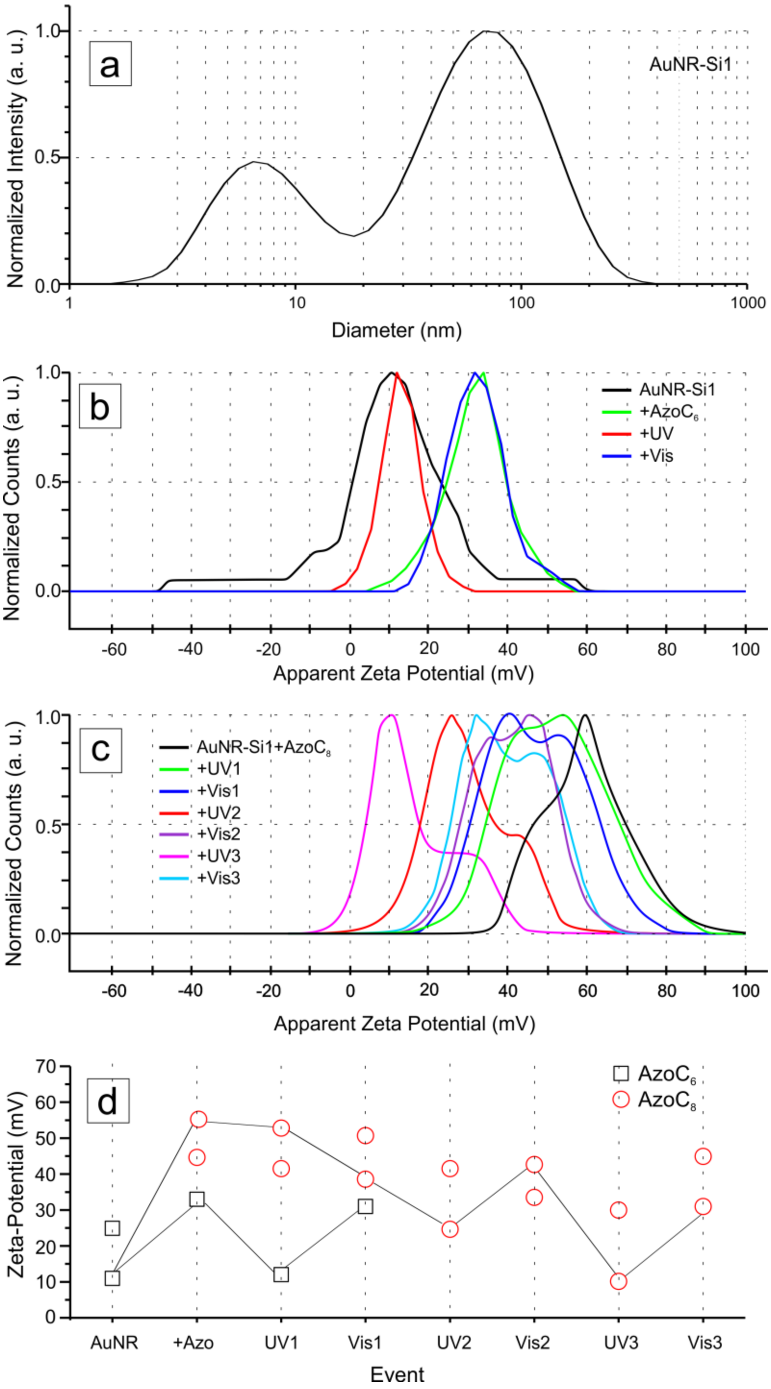

Figure 8.12. (a) Bimodal DLS size distribution for pure gold nanorods AuNR-Si1. (b) Normalized distributions of surface ς-potential of gold nanorods AuNR-Si1 without surfactant and in complexes with surfactant AzoC$_6$ before and after exposure to UV and visible (blue) light (see legend). (c) Normalized distributions of surface ς-potential of the complexes between gold nanorods AuNR-Si1 and azobenzene containing surfactant AzoC$_8$ periodically exposed to UV and visible light (see legend). (d) Surface ς-potential of gold nanorods AuNR-Si1 in complexes with azobenzene containing surfactants AzoC$_6$ (squares) and AzoC$_8$ (circles) as a function of irradiation event. Abscissas are to be read as follows: the initial point AuNR corresponds to pure gold nanorods, +Azo indicates nanorod-surfactant complex preparation, UV and Vis are the complexes exposed to UV and blue light respectively. Both major and minor maxima in ς-potential distributions are shown (open symbols), the main maxima are connected by solid lines. C(AuNR-Si1) = 0.03C$_0$, C_{Azo} = 0.03 mM.

8.5.Discussion

The addition of azobenzene containing surfactant to gold nanorod suspension induced red shift of the longitudinal plasmonic peak in the absorption spectra of gold nanorods and the increase of their surface ς-potential. The value of the LSPR red shift was found to increase with (a) surfactant concentration and (b) surfactant tail length. These effects imply the formation of an azobenzene surfactant shell on gold nanorod surface and thus the alteration of the local dielectric environment. The influence of surfactant tail length is apparently attributed to different surfactant hydrophobicity, which mediates surfactant shell formation on the gold nanorod surface.

The UV irradiation of prepared gold nanorod-surfactant complexes induced blue shift in LSPR wavelength and simultaneous decrease of surface ς-potential toward the values for pure gold nanorods. Subsequent exposure of surfactant-nanorod suspension to blue light returned the LSPR wavelength and surface ς-potential of the complexes to the values for non-irradiated complexes.

Relative LSPR shift between UV- and Vis- irradiated complexes $\Delta\lambda_{\text{UV-Vis}} = 3.6 \pm 0.3$ nm (mean value) appeared to be similar in all prepared suspensions and thus is attributed to the changes in local dielectric properties of the medium upon cis-trans photoisomerization of azobenzene unit within surfactant molecules. Using the registered shift in LSPR wavelength of gold nanorods, one can measure the optical properties of azobenzene containing surfactant shell.

Let's refer to the Equation (1.4) [83] predicting the position of the longitudinal plasmon maximum of gold nanorods with aspect ratio R in the medium with dielectric constant ε_m. It is:

$$\lambda_{max} = (33.34R - 46.31)\varepsilon_m + 472.31.$$

This formula was used to estimate photoreversible changes in the medium refractive index $\Delta n_{UV\text{-}Vis}$, assuming $n = \sqrt{\varepsilon_m}$. The results are shown in **Table 8.5**. The changes in the refractive index perceived by gold nanorods appeared to be very small, with the all-mean value: $\Delta n_{UV\text{-}Vis} = 0.012 \pm 0.002$ nm. Nevertheless, the used gold nanorods were capable of sensing that. It is worth it to comment on the error bars. The overwhelming source of inaccuracy would be the aspect ratio of nanorods, which stayed constant upon exposure to UV and Vis light in our experiments and therefore has been neglected in these simple estimations.

Table 8.5. Photoinduced changes in effective medium refractive index $\Delta n_{\text{UV-Vis}}$ in the complexes between gold nanorods and azobenzene containing surfactants.

$\Delta n_{\text{UV-Vis}}$, RIU	AzoC$_6$	AzoC$_8$	AzoC$_{10}$	AzoC$_{12}$
AuNR-Si1	0.013 ± 0.003	0.015 ± 0.003	-0.013 ± 0.009	0.012 ± 0.005
AuNR-Si2	0.009 ± 0.002	0.015 ± 0.005	0.009 ± 0.003	-
AuNR-Si3	0.008 ± 0.006	-	-	-
AuNR-AzoC6	0.011 ± 0.006	-	-	-

In fact, the local medium around the gold core of the nanorods includes azobenzene containing surfactant along with all compounds remaining in solution after the synthesis and thin silica layer for silica-capped gold nanorods. Thus, the calculated changes in refractive index reflect the properties of the *effective* medium. However, it is interesting to employ the LSPR shift of gold nanorods to estimate the dielectric properties of azobenzene containing surfactant in solution.

Mulvaney *et. al.* [218] adjusted Mie theory to small gold clusters coated with alkanethiolate monolayers, introducing the volume fraction of the shell *g*. Composite gold particles decorated with alkanethiolate SAM in the medium with dielectric constant ε_m were approximated as the spherical gold core with the optical dielectric function ε_{Au} and alkanethiolate shell with the dielectric function ε_s. The environment was assumed non-absorbing and dispersionless. The suggested plasmon resonance condition in dipole approximation is below:

$$\varepsilon_{Au} = -2\varepsilon_s \frac{g\varepsilon_s + (3-g)\varepsilon_m}{(3-2g)\varepsilon_s + 2g\varepsilon_m}$$

Applying the same approach to gold nanorods decorated with azobenzene surfactant shell yields the following plasmon resonance condition:

$$\varepsilon_{Au} = -\chi_i\varepsilon_s \frac{g\varepsilon_s + \varepsilon_m(\chi_i + 1 - g)}{\varepsilon_s\big(1 + \chi_i(1-g)\big) + g\chi_i\varepsilon_m} = -\chi_i\varepsilon_s \frac{\varepsilon_m(\chi_i + 1) + g(\varepsilon_s - \varepsilon_m)}{\varepsilon_s(\chi_i + 1) - g\chi_i(\varepsilon_s - \varepsilon_m)} \qquad (8.1)$$

Here ε_{Au} is the dielectric function of the rod-shaped gold core, ε_s – dielectric constant of the azobenzene surfactant shell, ε_m – dielectric constant of the solvent, χ_i – shape factor, which can be calculated as described in Section 1.2.4. For the studied gold nanorods with mean aspect ratio $R = 3.8$ longitudinal shape factor $\chi_A = 11.4$.

For a thick surfactant shell, $g \rightarrow 1$, and therefore plasmon resonance occurs when $\varepsilon_{Au} = -\chi_i\,\varepsilon_s$. For a thin shell, $g \rightarrow 0$, and $\varepsilon_{Au} = -\chi_i\,\varepsilon_m$.

The volume fraction of the surfactant shell can be found via the volume of a surfactant-decorated particle V(particle) and the volume of the nanorod gold core V(Au core):

$$g = \frac{V(shell)}{V(particle)} = \frac{V(particle) - V(Au\,core)}{V(particle)}$$

Approximating gold nanorods as a cylinder with two half-spheres at the ends (see **Scheme 8.1**), with the gold core of length A and diameter B, decorated with a surfactant layer of thickness d,

$$g = \frac{d}{(\frac{B}{2} + d)^2} \frac{(A-B)(B+d) + B(B+2d) + \frac{4}{3}d^2}{(A-B) + \frac{4}{3}(\frac{B}{2} + d)} \qquad (8.2)$$

Now, let's estimate the refractive index of the studied azobenzene containing surfactants using the results on the complexes between AuNR-Si2 and AzoC$_{10}$. These complexes are chosen because their longitudinal plasmon resonance occurred at the wavelength $\lambda_{SP} = 820$ nm, and real data on gold dielectric constant at this wavelength $\varepsilon_{Au} = -25.7$ are available from Johnson and Christy.[219] Also, these gold nanorods have aspect ratio $R = 3.8$, well matching the all-mean value.

Assuming that the surfactant forms a relatively thick shell under experimental conditions, the simple relation $\varepsilon_{Au} = -\chi_A\, \varepsilon_s$ returns $\varepsilon_s = 2.26$. Neglecting silica capping is likely not dramatic due to its low volume fraction. Since the used azobenzene containing surfactants do not possess absoption at $\lambda > 600$ nm, the refractive index of the surfactant layer can be calculated as $n_s = \sqrt{\varepsilon_s} = 1.504$. Evans *et. al.*[55] suggested that refractive index of azobenzene containing alkanethiol monolayer on gold surface $n \geq 1.5$.

Absorption spectra for gold nanorods AuNR-Si2 without surfactant allow us to estimate the refractive index of the medium. For this, gold dielectric constant at $\lambda = 808$ nm is assumed $\varepsilon_{Au} = -24.7$ based on the plot by Johnson and Christy.[219, 220] The resulting optical parameters of the medium $\varepsilon_m = 2.18$ and $n_m = 1.475$. This n_m value is far from the refractive index of water $n \approx 1.3$. Indeed, the thin silica layer and all additional compounds present in the solution had to be neglected. In fact, they constitute the local media around gold nanorods in the absence of azobenzene surfactant. The found value $n_m = 1.475$ is close to the refractive index of silica $n = 1.456$ reported in Ref. 221.

After exposure of the nanorod-surfactant complexes to UV light, plasmon resonance occurred at $\lambda = 817$ nm. Via the assumed $\varepsilon_{Au} = -25.5$ at this wavelength and calculated ε_s and ε_m, one can find out that the volume fraction of the surfactant shell after UV irradiation $g \approx 0$, *i. e.* indeed cis- surfactant molecules detach gold nanorod surface, in agreement with the results of ς-potential.

Using Equation (8.2) and dimensions in **Table 8.1**, one can find that for AuNR-Si2 $g = 0.96$ at $d = 12$ nm (relatively thick multilayered surfactant shell), and $g = 0.48$ at $d = 3$ nm (assumed to be the thickness of the surfactant bilayer).

Now, let's estimate the refractive index sensitivity of gold nanorods AuNR-Si2 using Equation (1.3) from Section 1.2.5, which was already reminded in Section 8.2.2:

$$\Delta\lambda_{max} = m\Delta n\left(1 - e^{-2d/l}\right)$$

As already estimated in Section 8.2.2, if $d = 12$ nm, $\Delta\lambda_{max} = 0.6\, m\, \Delta n$, assuming decay length $l = 27$ nm. The LSPR red shift upon the formation of nanorod-surfactant complexes $\Delta\lambda_{max} = 12$ nm, changes in the refractive index $\Delta n = n_s - n_m = 0.029$, and thereof the refractive index sensitivity $m = 690$ nm/RIU. This value is in good agreement with that reported in Ref. 222 and significantly higher than reported in Ref. 223 and Ref. 224 for gold nanorods with similar aspect ratios.

In fact, we cannot estimate the thickness of surfactant layer from our experiments. The mechanism when the thin surfactant shell becomes denser with an increase in surfactant concentration and/or tail length may provide similar experimental results. Particularly, accounting for the porosity of silica capping, this speculation should be discussed, although neglecting the silica shell can be crucial in this case. Assuming that a surfactant bilayer with thickness $d = 3$ nm is formed in surfactant-nanorod complexes, $m = 230$ nm/RIU, similar to reported in Ref. 224. This value of m shows high sensitivity of gold nanorods despite silica capping. In this case we cannot estimate dielectric constant of surfactant from $\varepsilon_{Au} = -\chi_A\ \varepsilon_s$, because $g < 1$, but from Equation (8.1) using $g = 0.48$, assumed $\varepsilon_{Au} = -25.7$ and calculated $\varepsilon_m = 2.18$. The resulting parameters of the azobenzene surfactant layer $\varepsilon_s = 2.36$, $n_s = 1.536$. Due to the inhomogeneity of silica capping, lower values of g and consequently higher values of surfactant refractive index are expected. Following the same procedure for AuNR-Si2 in complex with AzoC$_8$, $n_s = 1.493$ is returned assuming a 12-nm thick surfactant shell, and $n_s = 1.512$ in the case of the 3-nm layer formation. Reducing the volume fraction of the decorating surfactant shell to $g = 0.18$ would increase the refractive index of AzoC$_8$ to $n_s = 1.575$. Therefore, depending on the structure of the shell of azobenzene containing surfactant, its estimated refractive index $1.5 \leq n_s \leq 1.6$ from the experiments with gold nanorods AuNR-Si2.

Table 8.6 shows refractive indices of azobenzene containing surfactants calculated from Equation (8.1) using gold dielectric function by Johnson and Christy[219, 220] and LSPR wavelengths of different gold nanorods. The differences in aspect ratio of nanorods were taken into account. The dielectric constants of different surfactants did not differ within error bars when measured using the same batch of gold nanorods. Depending on gold nanorod batch, surfactant refractive indices were found to deviate between $n_s = 1.4$ and $n_s = 1.8$, with the mean value $n_s = 1.6 \pm 0.1$. This value is in a good agreement with the refractive index $n = 1.6$, calculated from ellipsometry measurements of an azobenzene containing polymer thin film,[225] and predicted for 4-nitroazobenzene.[226]

Table 8.6. Estimated optical dielectric constant ε_s and refractive index n_s of azobenzene containing surfactants in near-IR range measured by different gold nanorods.

Complexes		$g = 0$		$g = 1$		$g = 0.5$	
		ε_m	n_m	ε_s	n_s	ε_s	n_s
AuNR-Si1 $\chi_A = 8.6$	AzoC$_6$	2.70	1.64	2.85	1.69	3.01	1.74
	AzoC$_8$			2.83	1.68	2.98	1.73
	AzoC$_{10}$			2.82	1.68	2.94	1.71
	AzoC$_{12}$			2.88	1.70	3.08	1.76
AuNR-Si2 $\chi_A = 11.4$	AzoC$_6$	2.17	1.47	2.22	1.49	2.28	1.51
	AzoC$_8$			2.22	1.49	2.27	1.51
	AzoC$_{10}$			2.26	1.50	2.35	1.53
AuNR-Si3 $\chi_A = 13.2$	AzoC$_6$	1.96	1.40	2.00	1.41	2.03	1.43
AuNR-AzoC6	AzoC$_6$	2.12	1.46	2.29	1.51	2.49	1.58
Mean	-	-	-	2.48 ± ± 0.35	1.57 ± ± 0.11	2.60 ± ± 0.40	1.61 ± ± 0.12

A more detailed information about the surface of gold nanorods, *e.g.* thickness and porosity of the silica capping, would help much to understand the underlying mechanism of interaction with azobenzene containing surfactants, and to clarify the presence of cis- isomers of azobenzene surfactant on gold nanorod surface. At the same time, numerical calculations with a theoretical model accounting for silica capping may be needed to achieve more accuracy the calculated dielectric constants of azobenzene surfactants, and probably reveal the differences in dielectric properties of cis- and trans- isomers. Also, the dielectric function of bulk gold by Johnson and Christy may be inappropriate for gold nanorods due to a lower concentration of free electrons in nanoparticles compared to the bulk material.[203] The collected experimental results predict a successful use of the investigated gold nanorods for sensing in solution due to their high refractive index sensitivity. Furthermore, the results allowed the measurement of the refractive index of azobenzene containing surfactant layers in solution. The practical significance of these findings would be a determination of the refractive index of azobenzene ligands at different irradiation wavelengths (different fractions of cis-isomer) by means of a nanorod plasmonic sensor. In future, the direct measurement of the dielectric function of azobenzene surfactants would verify the assumed interaction mechanism and theoretical approach to the prepared complexes between gold nanorods and azobenzene containing surfactants.

9. Conclusions

The main objective of this work was the study of the complexes between plasmonic nanoparticles and photosensitive azobenzene containing cationic surfactants in water.

First, the optical properties and surface ς-potential of laser ablated gold, silver, palladium, silicon, alloy gold-silver and gold-palladium spherical nanoparticles, as well chemically prepared gold nanorods, were characterized. It was shown that all laser ablated spherical nanoparticles had negative surface charge. Surface ς-potential of gold nanorods appeared positive due to chemical stabilizers. Localized surface plasmon resonance wavelengths were determined for nanoparticles with different shape, size, and composition. Morphology of gold-silver alloy nanoparticles has been revealed using their plasmonic response.

The second and third objectives of the work were the preparation of the complexes between trans-isomers of azobenzene containing cationic surfactants and plasmonic nanoparticles, and investigation of their constitution and photoresponse.

For spherical gold nanoparticles of 10 and 25 nm in diameter, complexes of different constitutions were formed depending on the molar ratio σ between azobenzene containing surfactant and gold surface atoms. It was shown that upon binding to gold nanoparticle surface, surfactant molecules compensated or overcompensated for the nanoparticle charge depending on the molar ratio σ. At $\sigma \approx 0.1$, irreversible self-assembly of gold nanoparticles into nanochains was demonstrated, attributed to the formation of a surfactant monolayer on the gold surface and the particle surface charge neutralization. Gold nanochains possessed the plasmonic coupling mode along with the peak of constituent individual nanoparticles and corresponding blue color of aqueous suspensions. At higher molar ratios σ, gold nanoparticles appeared to be decorated with a bilayer of azobenzene containing surfactant molecules, and thus turned positively charged. Plasmon resonance wavelength of the charged surfactant-decorated gold nanoparticles was similar to that of non-functionalized nanoparticles and exhibited a slight red shift due to the changes in dielectric environment. The color of the suspensions had a pink tone, typical for gold colloids, turning orange at very high molar ratios.

Exposure of gold nanoparticles with the surfactant bilayer on surface to UV light destabilized the surfactant shell due to trans-cis azobenzene isomerization and induced particle nanoaggregation with color changes from pink to blue. The registered plasmonic coupling mode indicated chain morphology of the UV-irradiated gold-surfactant complexes. Complexes between azobenzene containing surfactant in trans- photostationary state with silver and silicon spherical nanoparticles showed similar results, corroborating the proposed complex formation model. These results demonstrate a successful strategy of surface modification of plasmonic nanoparticles with azobenzene photoswitches. The particles decorated with azobenzene surfactant bilayer have potential applications for functionalization of polymers and biopolymers, introducing simultaneously plasmonic and photoswitching properties, as well as opening up the possibility to gain a photocontrol over plasmonic response. Another potential application of azobenzene-modified metal nanoparticles is the photocontrollable self-assembly of plasmonic waveguides. To develop this into a promising technique, this requires further investigations on the alignment of the nanochains formed in solution.

The fourth objective was to study the interaction between cis-isomers of azobenzene containing surfactants and spherical metal nanoparticles. For that, prior to the preparation of the complexes with nanoparticles, solutions of azobenzene containing surfactants were irradiated with UV light. Spherical 10-nm gold nanoparticles showed superior catalytic activity in the subsequent thermal cis-trans isomerization of azobenzenes, which was found to accelerate up to 3500 times compared to pure aqueous solutions.

The study involved a series of azobenzene containing compounds with different chemical structures. Gold has been compared with silver, palladium, silicon, and gold-silver and gold-palladium alloys. The cis-trans thermal isomerization of azobenzenes was found to proceed in at least two steps with different reaction rates in the presence of gold nanoparticles. It was found that the properties of surfactant head group significantly alter the faster isomerization mode. The slower mode was found to depend on the distance between the charged head and the azobenzene unit in the surfactant tail. In a joint project with theoretical chemists, the following electrocatalytic mechanism of the enhanced cis-trans isomerization of azobenzene surfactants in the dark in the presence of nanoparticles has been elucidated. Cis-isomers of azobenzene surfactants adsorb on the particle surface and transfer an electron from the azo bond to the metal surface, so that cis-azobenzene cation radical is formed. In such a cationic radical state, azobenzene cis-trans isomerization is facilitated. Finally, reduction of the trans-azobenzene radical occurs. Gold surface atoms have been suggested to be the catalytic active sites in metal alloy nanoparticles. The theoretical predictions contradict the experimental results for palladium nanoparticles. More detailed theoretical and experimental studies are needed to fully describe the mechanism of azobenzene cis-trans isomerization in the presence of metal nanoparticles.

Finally, plasmon resonance in gold nanorods was to be employed to estimate the dielectric properties of azobenzene surfactants. The last chapter addressed reversible photoinduced isomerization of azobenzene containing surfactants in complexes with gold nanorods. Longitudinal plasmon resonance wavelength and surface zeta-potential of gold nanorods were tracked upon exposure of the complexes to UV and blue light, indicating photoreversible organization of trans- surfactant shell on gold nanorod surface. The concentration and tail length of surfactant molecules influenced their adsorption on nanoparticle surface and suggested shell formation. A modified plasmon resonance condition allowed the estimation of the refractive index of surfactant shell in solution in near-infrared range as $n_s = 1.6 \pm 0.1$. A more detailed study of physico-chemical properties of gold nanorod surfaces, and more sophisticated calculations are needed to estimate surfactant optical parameters employing surface plasmon resonance with a better accuracy. In the future, an experimental measurement of dielectric function of azobenzene surfactants would verify the proposed interaction model and theoretical approach.

10. References

1. Myers, D. *Surfactant science and technology*. (John Wiley & Sons, 2006).
2. Dias, R. S., Dawson, K. & Miguel, M. G. in *DNA Interactions with Polymers and Surfactants* 89–117 (John Wiley & Sons, 2008).
3. Ropers, M. H., Czichocki, G. & Brezesinski, G. Counterion Effect on the Thermodynamics of Micellization of Alkyl Sulfates. *J. Phys. Chem. B* **107,** 5281–5288 (2003).
4. Chatterjee, A., Moulik, S. P., Sanyal, S. K., Mishra, B. K. & Puri, P. M. Thermodynamics of Micelle Formation of Ionic Surfactants: A Critical Assessment for Sodium Dodecyl Sulfate, Cetyl Pyridinium Chloride and Dioctyl Sulfosuccinate (Na Salt) by Microcalorimetric, Conductometric, and Tensiometric Measurements. *J. Phys. Chem. B* **105,** 12823–12831 (2001).
5. Zakrevskyy, Y., Roxlau, J., Brezesinski, G., Lomadze, N. & Santer, S. Photosensitive surfactants: Micellization and interaction with DNA. *J. Chem. Phys.* **140,** 44906 (2014).
6. Santer, S., Kopyshev, A., Donges, J., Yang, H.-K. & Rühe, J. Dynamically Reconfigurable Polymer Films: Impact on Nanomotion. *Adv. Mater.* **18,** 2359–2362 (2006).
7. Schlemmer, C., Betz, W., Berchtold, B., Rühe, J. & Santer, S. The design of thin polymer membranes filled with magnetic particles on a microstructured silicon surface. *Nanotechnology* **20,** 255301 (2009).
8. König, T., Yadavalli, N. S. & Santer, S. Near-Field Induced Reversible Structuring of Photosensitive Polymer Films: Gold Versus Silver Nano-antennas. *Plasmonics* **7,** 535–542 (2012).
9. Zhao, Y. & Ikeda, T. *Smart light-responsive materials: azobenzene-containing polymers and liquid crystals*. (John Wiley & Sons, 2009).
10. Kamenjicki, M., Lednev, I. K. & Asher, S. A. Photoresponsive Azobenzene Photonic Crystals. *J. Phys. Chem. B* **108,** 12637–12639 (2004).
11. Parker, R. M., Gates, J. C., Rogers, H. L., Smith, P. G. R. & Grossel, M. C. Using the photoinduced reversible refractive-index change of an azobenzene co-polymer to reconfigure an optical Bragg grating. *J. Mater. Chem.* **20,** 9118 (2010).
12. Schuh, C., Lomadze, N., Rühe, J., Kopyshev, A. & Santer, S. Photomechanical Degrafting of Azo-Functionalized Poly(methacrylic acid) (PMAA) Brushes. *J. Phys. Chem. B* **115,** 10431–10438 (2011).
13. Lomadze, N., Kopyshev, A., Rühe, J. & Santer, S. Light-Induced Chain Scission in Photosensitive Polymer Brushes. *Macromolecules* **44,** 7372–7377 (2011).
14. Shinkai, S., Matsuo, K., Harada, A. & Manabe, O. Photocontrol of micellar catalyses. *J. Chem. Soc. Perkin Trans. 2* 1261 (1982).
15. Hayashita, T., Kurosawa, T., Miyata, T., Tanaka, K. & Igawa, M. Effect of structural variation within cationic azo-surfactant upon photoresponsive function in aqueous solution. *Colloid Polym. Sci.* **272,** 1611–1619 (1994).
16. Huang, Y. & Kim, D.-H. Light-controlled synthesis of gold nanoparticles using a rigid, photoresponsive surfactant. *Nanoscale* **4,** 6312 (2012).

17. Zakrevskyy, Y., Richter, M., Zakrevska, S., Lomadze, N., von Klitzing, R. & Santer, S. Light-Controlled Reversible Manipulation of Microgel Particle Size Using Azobenzene-Containing Surfactant. *Adv. Funct. Mater.* **22,** 5000–5009 (2012).

18. Rumyantsev, A. M., Santer, S. & Kramarenko, E. Y. Theory of Collapse and Overcharging of a Polyelectrolyte Microgel Induced by an Oppositely Charged Surfactant. *Macromolecules* **47,** 5388–5399 (2014).

19. Richter, M., Zakrevskyy, Y., Eisele, M., Lomadze, N., Santer, S. & von Klitzing, R. Effect of pH, co-monomer content, and surfactant structure on the swelling behavior of microgel-azobenzene-containing surfactant complex. *Polymer* **55,** 6513–6518 (2014).

20. Schimka, S., Lomadze, N., Rabe, M., Kopyshev, A., Lehmann, M., von Klitzing, R., Rumyantsev, A. M., Kramarenko, E. Y. & Santer, S. Photosensitive microgels containing azobenzene surfactants of different charges. *Phys. Chem. Chem. Phys.* **44,** 7686–7708 (2016).

21. Le Ny, A. L. M. & Lee, C. T. Photoreversible DNA condensation using light-responsive surfactants. *J. Am. Chem. Soc.* **128,** 6400–6408 (2006).

22. Sollogoub, M., Guieu, S., Geoffroy, M., Yamada, A., Estévez-Torres, A., Yoshikawa, K. & Baigl, D. Photocontrol of Single-Chain DNA Conformation in Cell-Mimicking Microcompartments. *ChemBioChem* **9,** 1201–1206 (2008).

23. Estévez-Torres, A., Crozatier, C., Diguet, A., Hara, T., Saito, H., Yoshikawa, K. & Baigl, D. Sequence-independent and reversible photocontrol of transcription/expression systems using a photosensitive nucleic acid binder. *Proc. Natl. Acad. Sci. U. S. A.* **106,** 12219–23 (2009).

24. Zakrevskyy, Y., Cywinski, P., Cywinska, M., Paasche, J., Lomadze, N., Reich, O., Löhmannsröben, H.-G. & Santer, S. Interaction of photosensitive surfactant with DNA and poly acrylic acid. *J. Chem. Phys.* **140,** 44907 (2014).

25. Zakrevskyy, Y., Kopyshev, A., Lomadze, N., Morozova, E., Lysyakova, L., Kasyanenko, N. & Santer, S. DNA compaction by azobenzene-containing surfactant. *Phys. Rev. E* **84,** 21909 (2011).

26. Kopyshev, A., Lomadze, N., Feldmann, D., Genzer, J. & Santer, S. Making polymer brush photosensitive with azobenzene containing surfactants. *Polymer* **79,** 65–72 (2015).

27. Kopyshev, A., Galvin, C. J., Patil, R. R., Genzer, J., Lomadze, N., Feldmann, D., Zakrevski, J. & Santer, S. Light-Induced Reversible Change of Roughness and Thickness of Photosensitive Polymer Brushes. *ACS Appl. Mater. Interfaces* **8,** 19175–19184 (2016).

28. Kopyshev, A., Galvin, C. J., Genzer, J., Lomadze, N. & Santer, S. Polymer brushes modified by photosensitive azobenzene containing polyamines. *Polymer* **98,** 421–428 (2016).

29. Sun, Y. L., Mani, N. K., Baigl, D., Gisler, T., Schröder, A. P. & Marques, C. M. Photocontrol of end-grafted lambda-phage DNA. *Soft Matter* **7,** 5578 (2011).

30. Griffiths, J. II. Photochemistry of azobenzene and its derivatives. *Chem. Soc. Rev.* **1,** 481 (1972).

31. Rau, H. in *Photochemistry and photophysics* (ed. J. Rebek) **2,** 119–141 (CRC Press: Boca Raton, FL, 1990).

32. Beharry, A. A., Sadovski, O. & Woolley, G. A. Azobenzene Photoswitching without Ultraviolet Light. *J. Am. Chem. Soc.* **133,** 19684–19687 (2011).

33. Bléger, D., Schwarz, J., Brouwer, A. M. & Hecht, S. *o* -Fluoroazobenzenes as Readily Synthesized Photoswitches Offering Nearly Quantitative Two-Way Isomerization with Visible Light. *J. Am. Chem. Soc.* **134,** 20597–20600 (2012).

34. Yager, K. G. & Barrett, C. J. Novel photo-switching using azobenzene functional materials. *J. Photochem. Photobiol. A Chem.* **182,** 250–261 (2006).

35. Lednev, I. K., Ye, T.-Q., Hester, R. E. & Moore, J. N. Femtosecond Time-Resolved UV−Visible Absorption Spectroscopy of trans -Azobenzene in Solution . *J. Phys. Chem.* **100,** 13338–13341 (1996).

36. Kobayashi, T., Degenkolb, E. O. & Rentzepis, P. M. Picosecond spectroscopy of 1-phenylazo-2-hydroxynaphthalene. *J. Phys. Chem.* **83,** 2431–2434 (1979).

37. Satzger, H., Spörlein, S., Root, C., Wachtveitl, J., Zinth, W. & Gilch, P. Fluorescence spectra of trans- and cis-azobenzene - Emission from the Franck-Condon state. *Chem. Phys. Lett.* **372,** 216–223 (2003).

38. Fischer, E., Frankel, M. & Wolovsky, R. Wavelength Dependence of Photoisomerization Equilibria in Azocompounds. *J. Chem. Phys.* **23,** 1367 (1955).

39. Hartley, G. S. The Cis-form of Azobenzene. *Nature* **140,** 281 (1937).

40. Kumar, G. S. & Neckers, D. C. Photochemistry of azobenzene-containing polymers. *Chem. Rev.* **89,** 1915–1925 (1989).

41. de Lange, J. J., Robertson, J. M. & Woodward, I. X-Ray Crystal Analysis of Trans-Azobenzene. *Proc. R. Soc. A* **171,** 398–410 (1939).

42. Klajn, R. Immobilized azobenzenes for the construction of photoresponsive materials. *Pure Appl. Chem.* **82,** 2247–2279 (2010).

43. Kasha, M. Energy Transfer Mechanisms and the Molecular Exciton Model for Molecular Aggregates. *Radiat. Res.* **20,** 55–70 (1963).

44. Kunitake, T., Okahata, Y., Shimomura, M., Yasunami, S. & Takarabe, K. Formation of stable bilayer assemblies in water from single-chain amphiphiles. Relationship between the amphiphile structure and the aggregate morphology. *J. Am. Chem. Soc.* **103,** 5401–5413 (1981).

45. Bandara, H. M. D. & Burdette, S. C. Photoisomerization in different classes of azobenzene. *Chem. Soc. Rev.* **41,** 1809–1825 (2012).

46. Tamai, N. & Miyasaka, H. Ultrafast Dynamics of Photochromic Systems. *Chem. Rev.* **100,** 1875–1890 (2000).

47. Lamarre, L. & Sung, C. S. P. Studies of physical aging and molecular motion by azochromophoric labels attached to the main chains of amorphous polymers. *Macromolecules* **16,** 1729–1736 (1983).

48. Norman, L. L. & Barrett, C. J. Solution Properties of Self-Assembled Amphiphilic Copolymers Determined by Isomerization Spectroscopy. *J. Phys. Chem. B* **106,** 8499–8503 (2002).

49. Wu, A. & Talham, D. R. Photoisomerization of Azobenzene Chromophores in Organic/Inorganic Zirconium Phosphonate Thin Films Prepared Using a Combined

Langmuir−Blodgett and Self-Assembled Monolayer Deposition. *Langmuir* **16,** 7449–7456 (2000).

50. Wang, R., Iyoda, T., Jiang, L., Tryk, D. A., Hashimoto, K. & Fujishima, A. Structural investigation of azobenzene-containing self-assembled monolayer films. *J. Electroanal. Chem.* **438,** 213–219 (1997).

51. Moldt, T., Brete, D., Przyrembel, D., Das, S., Goldman, J. R., Kundu, P. K., Gahl, C., Klajn, R. & Weinelt, M. Tailoring the Properties of Surface-Immobilized Azobenzenes by Monolayer Dilution and Surface Curvature. *Langmuir* **31,** 1048–1057 (2015).

52. Wolf, M. & Tegeder, P. Reversible molecular switching at a metal surface: A case study of tetra-tert-butyl-azobenzene on Au(111). *Surf. Sci.* **603,** 1506–1517 (2009).

53. Muntwiler, M., Lindstrom, C. D. & Zhu, X.-Y. Delocalized electron resonance at the alkanethiolate self-assembled monolayer⁄Au(111) interface. *J. Chem. Phys.* **124,** 81104 (2006).

54. Zhang, J., Whitesell, J. K. & Fox, M. A. Photoreactivity of Self-assembled Monolayers of Azobenzene or Stilbene Derivatives Capped on Colloidal Gold Clusters. *Chem. Mater.* **13,** 2323–2331 (2001).

55. Evans, S., Johnson, S. & Ringsdorf, H. Photoswitching of azobenzene derivatives formed on planar and colloidal gold surfaces. *Langmuir* **14,** 6436–6440 (1998).

56. Weidner, T., Bretthauer, F., Ballav, N., Motschmann, H., Orendi, H., Bruhn, C., Siemeling, U. & Zharnikov, M. Correlation between the Molecular Structure and Photoresponse in Aliphatic Self-Assembled Monolayers with Azobenzene Tailgroups. *Langmuir* **24,** 11691–11700 (2008).

57. El Garah, M., Palmino, F. & Cherioux, F. Reversible Photoswitching of Azobenzene-Based Monolayers Physisorbed on a Mica Surface. *Langmuir* **26,** 943–949 (2010).

58. Pace, G., Ferri, V., Grave, C., Elbing, M., von Hanisch, C., Zharnikov, M., Mayor, M., Rampi, M. A. & Samori, P. Cooperative light-induced molecular movements of highly ordered azobenzene self-assembled monolayers. *Proc. Natl. Acad. Sci.* **104,** 9937–9942 (2007).

59. Nakagawa, M., Watase, R. & Ichimura, K. Spatially Controlled Photoisomerizability of Azobenzene Moieties in Langmuir-Blodgett Monolayers of Ion-Paired Macrocyclic Amphiphiles. *Mol. Cryst. Liq. Cryst. Sci. Technol. Sect. A. Mol. Cryst. Liq. Cryst.* **344,** 113–118 (2000).

60. Shin, K. & Shin, E.-J. Photoresponsive Azobenzene-modified Gold Nanoparticle. *Bull. Korean Chem. Soc.* **29,** 1259–1262 (2008).

61. Klajn, R., Wesson, P. J., Bishop, K. J. M. & Grzybowski, B. A. Writing Self-Erasing Images using Metastable Nanoparticle 'Inks'. *Angew. Chemie Int. Ed.* **48,** 7035–7039 (2009).

62. Manna, A., Chen, P.-L., Akiyama, H., Wei, T.-X., Tamada, K. & Knoll, W. Optimized Photoisomerization on Gold Nanoparticles Capped by Unsymmetrical Azobenzene Disulfides. *Chem. Mater.* **15,** 20–28 (2003).

63. Sadler, J. L. & Bard, A. J. Electrochemical reduction of aromatic azo compounds. *J. Am. Chem. Soc.* **90,** 1979–1989 (1968).

64. Neta, P. & Levanon, H. Spectrophotometric study of the radicals produced by the

reduction of syn- and anti-azobenzene. *J. Phys. Chem.* **81,** 2288–2292 (1977).

65. Laviron, E. & Mugnier, Y. A study of the isomerization of cis-azobenzene anion radical in dimethylformamide. *J. Electroanal. Chem. Interfacial Electrochem.* **93,** 69–73 (1978).

66. Goulet-Hanssens, A., Utecht, M., Mutruc, D., Titov, E., Schwarz, J., Grubert, L., Bléger, D., Saalfrank, P. & Hecht, S. Electrocatalytic Z → E Isomerization of Azobenzenes. *J. Am. Chem. Soc.* **139,** 335–341 (2017).

67. Kreibig, U. & Vollmer, M. *Optical Properties of Metal Clusters*. (Springer, 1995).

68. Sonntag, M. D., Klingsporn, J. M., Zrimsek, A. B., Sharma, B., Ruvuna, L. K. & Van Duyne, R. P. Molecular plasmonics for nanoscale spectroscopy. *Chem. Soc. Rev.* **43,** 1230–1247 (2014).

69. Lal, S., Link, S. & Halas, N. J. Nano-optics from sensing to waveguiding. *Nat. Photonics* **1,** 641–648 (2007).

70. Kawata, S., Inouye, Y. & Verma, P. Plasmonics for near-field nano-imaging and superlensing. *Nat. Photonics* **3,** 388–394 (2009).

71. Anker, J. N., Hall, W. P., Lyandres, O., Shah, N. C., Zhao, J. & Van Duyne, R. P. Biosensing with plasmonic nanosensors. *Nat. Mater.* **7,** 442–453 (2008).

72. Daniel, M.-C. & Astruc, D. Gold Nanoparticles: Assembly, Supramolecular Chemistry, Quantum-Size-Related Properties, and Applications toward Biology, Catalysis, and Nanotechnology. *Chem. Rev.* **104,** 293–346 (2004).

73. Willets, K. A. & Van Duyne, R. P. Localized Surface Plasmon Resonance Spectroscopy and Sensing. *Annu. Rev. Phys. Chem.* **58,** 267–297 (2007).

74. Maier, S. A. *Plasmonics: Fundamentals and Applications*. (Springer, 2007).

75. Long, Y.-T. & Jing, C. *Springer Briefs in Molecular Science: Localized Surface Plasmon Resonance Based Nanobiosensors*. (Springer, 2014).

76. Kelly, K. L., Coronado, E., Zhao, L. L. & Schatz, G. C. The Optical Properties of Metal Nanoparticles: The Influence of Size, Shape, and Dielectric Environment. *J. Phys. Chem. B* **107,** 668–677 (2003).

77. Bohren, C. F. & Huffman, D. R. *Absorption and Scattering of Light by Small Particles*. (1983).

78. Willets, K. & Van Duyne. Localized Surface Plasmon Resonance Spectroscopy and Sensing. *Suppl. Mater. Annu. Rev. Phys. Chem* **58,** 267–97 (2007).

79. Link, S. & El-Sayed, M. A. Shape and size dependence of radiative, non-radiative and photothermal properties of gold nanocrystals. *Int. Rev. Phys. Chem.* **19,** 409–453 (2000).

80. Jain, P. K., Lee, K. S., El-Sayed, I. H. & Mostafa A. El-Sayed. Calculated Absorption and Scattering Properties of Gold Nanoparticles of Different Size, Shape, and Composition: Applications in Biological Imaging and Biomedicine. *J. Phys. Chem. B* **110,** 7238–7248 (2006).

81. Mie, G. Beiträge zur Optik trüber Medien, speziell kolloidaler Metallösungen. *Ann. Phys.* **25,** 377–445 (1908).

82. Underwood, S. & Mulvaney, P. Effect of the Solution Refractive Index on the Color of Gold Colloids. *Langmuir* **10,** 3427–3430 (1994).

83. Link, S. & El-Sayed, M. A. Spectral Properties and Relaxation Dynamics of Surface

Plasmon Electronic Oscillations in Gold and Silver Nanodots and Nanorods. *J. Phys. Chem. B* **103,** 8410–8426 (1999).

84. Jensen, T., Kelly, L., Lazarides, A. & Schatz, G. C. Electrodynamics of Noble Metal Nanoparticles and Nanoparticle Clusters. *J. Clust. Sci.* **10,** 295–317 (1999).

85. Sönnichsen, C., Franzl, T., Wilk, T., Von Plessen, G. & Feldmann, J. Plasmon resonances in large noble-metal clusters. *New J. Phys.* **4,** 93.1-93.8 (2002).

86. Sönnichsen, C., Franzl, T., Wilk, T., Von Plessen, G., Feldmann, J., Wilson, O. & Mulvaney, P. Drastic Reduction of Plasmon Damping in Gold Nanorods. *Phys. Rev. Lett.* **88,** 77402 (2002).

87. Hövel, H., Fritz, S., Hilger, A., Kreibig, U. & Vollmer, M. Width of cluster plasmon resonances: Bulk dielectric functions and chemical interface damping. *Phys. Rev. B* **48,** 18178–18188 (1993).

88. Raschke, G., Kowarik, S., Franzl, T., Sonnichsen, C., Klar, T. A., Feldmann, J., Nichtl, A. & Kurzinger, K. Biomolecular Recognition Based on Single Gold Nanoparticle Light Scattering. *Nano Lett.* **3,** 935–938 (2003).

89. Amendola, V. & Meneghetti, M. Size Evaluation of Gold Nanoparticles by UV−vis Spectroscopy. *J. Phys. Chem. C* **113,** 4277–4285 (2009).

90. Schönauer, D., Quinten, M. & Kreibig, U. Precursor-states of percolation in quasi-fractal many-particle-systems. *Zeitschrift für Phys. D Atoms, Mol. Clust.* **12,** 527–532 (1989).

91. Satoh, N., Hasegawa, H., Tsujii, K. & Kimura, K. Photoinduced Coagulation of Au Nanocolloids. *J. Phys. Chem.* **98,** 2143–2147 (1994).

92. Vance, F. W., Lemon, B. I. & Hupp, J. T. Enormous Hyper-Rayleigh Scattering from Nanocrystalline Gold Particle Suspensions. **102,** 10091–10093 (1998).

93. Wustholz, K. L., Henry, A.-I., McMahon, J. M., Freeman, R. G., Valley, N., Piotti, M. E., Natan, M. J., Schatz, G. C. & Duyne, R. P. Van. Structure−Activity Relationships in Gold Nanoparticle Dimers and Trimers for Surface-Enhanced Raman Spectroscopy. *J. Am. Chem. Soc.* **132,** 10903–10910 (2010).

94. Jain, P. K., Huang, W. & El-Sayed, M. A. On the Universal Scaling Behavior of the Distance Decay of Plasmon Coupling in Metal Nanoparticle Pairs: A Plasmon Ruler Equation. *Nano Lett.* **7,** 2080–2088 (2007).

95. Rechberger, W., Hohenau, A., Leitner, A., Krenn, J. R., Lamprecht, B. & Aussenegg, F. R. Optical properties of two interacting gold nanoparticles. *Opt. Commun.* **220,** 137–141 (2003).

96. Maier, S. A., Kik, P. G. & Atwater, H. A. Observation of coupled plasmon-polariton modes in Au nanoparticle chain waveguides of different lengths: Estimation of waveguide loss. *Appl. Phys. Lett.* **81,** 1714–1716 (2002).

97. Maier, S. A., Kik, P. G. & Atwater, H. A. Optical pulse propagation in metal nanoparticle chain waveguides. *Phys. Rev. B* **67,** 205402 (2003).

98. Cortie, M. B. & Mcdonagh, A. M. Synthesis and Optical Properties of Hybrid and Alloy Plasmonic Nanoparticles. **111,** 3713–3735 (2011).

99. Ferrando, R., Jellinek, J. & Johnston, R. L. Nanoalloys: From Theory to Applications of Alloy Clusters and Nanoparticles. *Chem. Rev.* **108,** 845–910 (2008).

100. Lide, D. in *CRC handbook of chemistry and physics* (eds. Haynes, W. M., Lide, D. R. & Bruno, T. J.) 12–123 (CRC Press, 2016).

101. Kuladeep, R., Jyothi, L., Alee, K. S., Deepak, K. L. N. & Narayana Rao, D. Laser-assisted synthesis of Au-Ag alloy nanoparticles with tunable surface plasmon resonance frequency. *Opt. Mater. Express* **2,** 161 (2012).

102. Compagnini, G., Messina, E., Puglisi, O. & Nicolosi, V. Laser synthesis of Au/Ag colloidal nano-alloys: Optical properties, structure and composition. *Appl. Surf. Sci.* **254,** 1007–1011 (2007).

103. Sánchez-Ramírez, J. F., Pal, U., Nolasco-Hernández, L., Mendoza-Álvarez, J. & Pescador-Rojas, J. A. Synthesis and Optical Properties of Au-Ag Alloy Nanoclusters with Controlled Composition. *J. Nanomater.* **2008,** 1–9 (2008).

104. Papavassiliou, G. C. Surface plasmons in small Au-Ag alloy particles. *J. Phys. F Met. Phys.* **6,** L103–L105 (1976).

105. S. Link, Z. L. Wang & M. A. El-Sayed. Alloy Formation of Gold−Silver Nanoparticles and the Dependence of the Plasmon Absorption on Their Composition. *J. Phys. Chem. B* **103,** 3529–3533 (1999).

106. Rioux, D. & Meunier, M. Seeded Growth Synthesis of Composition and Size-Controlled Gold–Silver Alloy Nanoparticles. *J. Phys. Chem. C* **119,** 13160–13168 (2015).

107. Shore, M. S., Wang, J., Johnston-Peck, A. C., Oldenburg, A. L. & Tracy, J. B. Synthesis of Au(Core)/Ag(Shell) Nanoparticles and their Conversion to AuAg Alloy Nanoparticles. *Small* **7,** 230–234 (2011).

108. Villa, A., Dimitratos, N., Chan-Thaw, C. E., Hammond, C., Veith, G. M., Wang, D., Manzoli, M., Prati, L. & Hutchings, G. J. Characterisation of gold catalysts. *Chem. Soc. Rev.* **45,** 4953–4994 (2016).

109. Mahl, D., Diendorf, J., Ristig, S., Greulich, C., Li, Z.-A., Farle, M., Köller, M. & Epple, M. Silver, gold, and alloyed silver–gold nanoparticles: characterization and comparative cell-biologic action. *J. Nanoparticle Res.* **14,** 1153 (2012).

110. Peng, Z., Spliethoff, B., Tesche, B., Walther, T. & Kleinermanns, K. Laser-Assisted Synthesis of Au−Ag Alloy Nanoparticles in Solution. *J. Phys. Chem. B* **110,** 2549–2554 (2006).

111. Papagiannouli, I., Aloukos, P., Rioux, D., Meunier, M. & Couris, S. Effect of the Composition on the Nonlinear Optical Response of Au $_x$ Ag $_{1-x}$ Nano-Alloys. *J. Phys. Chem. C* **119,** 6861–6872 (2015).

112. Kracker, M., Worsch, C. & Rüssel, C. Optical properties of palladium nanoparticles under exposure of hydrogen and inert gas prepared by dewetting synthesis of thin-sputtered layers. *J. Nanoparticle Res.* **15,** 1594 (2013).

113. Sugawa, K., Tahara, H., Yamashita, A., Otsuki, J., Sagara, T., Harumoto, T. & Yanagida, S. Refractive Index Susceptibility of the Plasmonic Palladium Nanoparticle: Potential as the Third Plasmonic Sensing Material. *ACS Nano* **9,** 1895–1904 (2015).

114. Liu, H. B., Pal, U., Medina, A., Maldonado, C. & Ascencio, J. A. Structural incoherency and structure reversal in bimetallic Au − Pd nanoclusters. *Phys. Rev. B* **71,** 75403 (2005).

115. Turkevich, J. Colloidal Gold. Part II. *Gold Bull.* **18,** 125–131 (1985).

116. Harada, M., Asakura, K. & Toshima, N. Catalytic Activity and Structural Analysis of Polymer-Protected Au/Pd Bimetallic Clusters Prepared by the Successive Reduction of HAuCl4 and PdCl2. *J. Phys. Chem. B* **97,** 5103–5114 (1993).

117. Scott, R. W. J., Wilson, O. M., Oh, S.-K., Kenik, E. A. & Crooks, R. M. Bimetallic Palladium-Gold Dendrimer-Encapsulated Catalysts. *J. Am. Chem. Soc.* **126,** 15583–15591 (2004).

118. Nutt, M. O., Hughes, J. B. & Wong, M. S. Designing Pd-on-Au Bimetallic Nanoparticle Catalysts for Trichloroethene Hydrodechlorination. *Environ. Sci. Technol.* **39,** 1346–1353 (2005).

119. Kan, C., Cai, W., Li, C., Zhang, L. & Hofmeister, H. Ultrasonic synthesis and optical properties of Au/Pd bimetallic nanoparticles in ethylene glycol. *J. Phys. D. Appl. Phys.* **36,** 1609–1614 (2003).

120. Weitz, D. A., Huang, J. S., Lin, M. Y. & Sung, J. Limits of the Fractal Dimension for Irreversible Kinetic Aggregation of Gold Colloids. *Phys. Rev. Lett.* **54,** 1416–1419 (1985).

121. Lin, M. Y., Lindsay, H. M., Weitz, D. A., Ball, R. C., Klein, R. & Meakin, P. Universality in colloid aggregation. *Nature* **339,** 360–362 (1989).

122. Lin, M. Y., Lindsay, H. M., Weitz, D. A., Ball, R. C., Klein, R. & Meakin, P. Universal reaction-limited colloid aggregation. *Phys. Rev. A* **41,** 2005–2020 (1990).

123. Lin, M. Y., Lindsay, H. M., Weitz, D. A., Klein, R., Ball, R. C. & Meakin, P. Universal diffusion-limited colloid aggregation. *J. Phys. Condens. Matter* **2,** 3093–3113 (1990).

124. Taylor, R. W., Lee, T.-C., Scherman, O. A., Esteban, R., Aizpurua, J., Huang, F. M., Baumberg, J. J. & Mahajan, S. Precise Subnanometer Plasmonic Junctions for SERS within Gold Nanoparticle Assemblies Using Cucurbit[*n*]uril 'Glue'. *ACS Nano* **5,** 3878–3887 (2011).

125. Esteban, R., Taylor, R. W., Baumberg, J. J. & Aizpurua, J. How Chain Plasmons Govern the Optical Response in Strongly Interacting Self-Assembled Metallic Clusters of Nanoparticles. *Langmuir* **28,** 8881–8890 (2012).

126. Herrmann, L. O., Valev, V. K., Tserkezis, C., Barnard, J. S., Kasera, S., Scherman, O. A., Aizpurua, J. & Baumberg, J. J. Threading plasmonic nanoparticle strings with light. *Nat. Commun.* **5,** 442–453 (2014).

127. Yang, Y., Matsubara, S., Nogami, M. & Shi, J. Controlling the aggregation behavior of gold nanoparticles. *Mater. Sci. Eng. B* **140,** 172–176 (2007).

128. Lin, S., Li, M., Dujardin, E., Girard, C. & Mann, S. One-Dimensional Plasmon Coupling by Facile Self-Assembly of Gold Nanoparticles into Branched Chain Networks. *Adv. Mater.* **17,** 2553–2559 (2005).

129. Muto, H., Yamada, K., Miyajima, K. & Mafuné, F. Estimation of Surface Oxide on Surfactant-Free Gold Nanoparticles Laser-Ablated in Water. *J. Phys. Chem. C* **111,** 17221–17226 (2007).

130. Hasegawa, H., Satoh, N., Tsujii, K. & Kimura, K. Fractal analysis of the coalescence process of Au nano-meter particles dispersed in 2-propanol. *Zeitschrift für Phys. D Atoms, Mol. Clust.* **20,** 325–327 (1991).

131. Klajn, R., Bishop, K. J. M. & Grzybowski, B. A. Light-controlled self-assembly of

reversible and irreversible nanoparticle suprastructures. *Proc. Natl. Acad. Sci. U. S. A.* **104,** 10305–9 (2007).

132. Köhntopp, A., Dabrowski, A., Malicki, M. & Temps, F. Photoisomerisation and ligand-controlled reversible aggregation of azobenzene-functionalised gold nanoparticles. *Chem. Commun.* **50,** 10105 (2014).

133. Manna, D., Udayabhaskararao, T., Zhao, H. & Klajn, R. Orthogonal Light-Induced Self-Assembly of Nanoparticles using Differently Substituted Azobenzenes. *Angew. Chemie Int. Ed.* **54,** 12394–12397 (2015).

134. Lee, J.-W. & Klajn, R. Dual-responsive nanoparticles that aggregate under the simultaneous action of light and CO2. *Chem. Commun.* **51,** 2036–2039 (2015).

135. Kundu, P. K., Samanta, D., Leizrowice, R., Margulis, B., Zhao, H., Börner, M., Udayabhaskararao, T., Manna, D. & Klajn, R. Light-controlled self-assembly of non-photoresponsive nanoparticles. *Nat. Chem.* **7,** 646–652 (2015).

136. Samanta, D. & Klajn, R. Aqueous Light-Controlled Self-Assembly of Nanoparticles. *Adv. Opt. Mater.* **4,** 1373–1377 (2016).

137. Astruc, D. *Nanoparticles and catalysis*. (Wiley-VCH, 2008).

138. Bond, G. C., Louis, C. & Thompson, D. T. *Catalysis by Gold*. **6,** (Imperial College Press, 2006).

139. Haruta, M., Kobayashi, T., Sano, H. & Yamada, N. Novel Gold Catalysts for the Oxidation of Carbon Monoxide at a Temperature far Below 0 °C. *Chem. Lett.* **16,** 405–408 (1987).

140. Zhang, Y., Cui, X., Shi, F. & Deng, Y. Nano-Gold Catalysis in Fine Chemical Synthesis. *Chem. Rev.* **112,** 2467–2505 (2011).

141. Astruc, D., Lu, F. & Aranzaes, J. R. Nanoparticles as Recyclable Catalysts: The Frontier between Homogeneous and Heterogeneous Catalysis. *Angew. Chemie Int. Ed.* **44,** 7852–7872 (2005).

142. Hashmi, A. S. K. & Hutchings, G. J. Gold Catalysis. *Angew. Chemie Int. Ed.* **45,** 7896–7936 (2006).

143. Zahmakıran, M. & Özkar, S. Metal nanoparticles in liquid phase catalysis; from recent advances to future goals. *Nanoscale* **3,** 3462 (2011).

144. Hervés, P., Pérez-Lorenzo, M., Liz-Marzán, L. M., Dzubiella, J., Lu, Y. & Ballauff, M. Catalysis by metallic nanoparticles in aqueous solution: model reactions. *Chem. Soc. Rev.* **41,** 5577 (2012).

145. Mahmoud, M. A., Garlyyev, B. & El-Sayed, M. A. Determining the Mechanism of Solution Metallic Nanocatalysis with Solid and Hollow Nanoparticles: Homogeneous or Heterogeneous. *J. Phys. Chem. C* **117,** 21886–21893 (2013).

146. Studer, A. & Curran, D. P. The electron is a catalyst. *Nat. Chem.* **6,** 765–773 (2014).

147. Henglein, A. Small-particle research: physicochemical properties of extremely small colloidal metal and semiconductor particles. *Chem. Rev.* **89,** 1861–1873 (1989).

148. Ung, T., Giersig, M., Dunstan, D. & Mulvaney, P. Spectroelectrochemistry of Colloidal Silver. *Langmuir* **13,** 1773–1782 (1997).

149. Carregal-Romero, S., Pérez-Juste, J., Hervés, P., Liz-Marzán, L. M. & Mulvaney, P.

Colloidal Gold-Catalyzed Reduction of Ferrocyanate (III) by Borohydride Ions: A Model System for Redox Catalysis. *Langmuir* **26,** 1271–1277 (2010).

150. Gu, S., Wunder, S., Lu, Y., Ballauff, M., Fenger, R., Rademann, K., Jaquet, B. & Zaccone, A. Kinetic Analysis of the Catalytic Reduction of 4-Nitrophenol by Metallic Nanoparticles. *J. Phys. Chem. C* **118,** 18618–18625 (2014).

151. An, K. & Somorjai, G. A. Size and Shape Control of Metal Nanoparticles for Reaction Selectivity in Catalysis. *ChemCatChem* **4,** 1512–1524 (2012).

152. Burda, C., Chen, X., Narayanan, R. & El-Sayed, M. A. Chemistry and Properties of Nanocrystals of Different Shapes. *Chem. Rev.* **105,** 1025–1102 (2005).

153. Lin, C., Tao, K., Hua, D., Ma, Z. & Zhou, S. Size Effect of Gold Nanoparticles in Catalytic Reduction of p-Nitrophenol with NaBH4. *Molecules* **18,** 12609–12620 (2013).

154. Fenger, R., Fertitta, E., Kirmse, H., Thünemann, A. F. & Rademann, K. Size dependent catalysis with CTAB-stabilized gold nanoparticles. *Phys. Chem. Chem. Phys.* **14,** 9343 (2012).

155. Zeng, J., Zhang, Q., Chen, J. & Xia, Y. A Comparison Study of the Catalytic Properties of Au-Based Nanocages, Nanoboxes, and Nanoparticles. *Nano Lett.* **10,** 30–35 (2010).

156. Narayanan, R. & El-Sayed, M. A. Shape-Dependent Catalytic Activity of Platinum Nanoparticles in Colloidal Solution. *Nano Lett.* **4,** 1343–1348 (2004).

157. Hvolbæk, B., Janssens, T. V. W., Clausen, B. S., Falsig, H., Christensen, C. H. & Nørskov, J. K. Catalytic activity of Au nanoparticles. *Nano Today* **2,** 14–18 (2007).

158. Nelayah, J., Kociak, M., Stéphan, O., García de Abajo, F. J., Tencé, M., Henrard, L., Taverna, D., Pastoriza-Santos, I., Liz-Marzán, L. M. & Colliex, C. Mapping surface plasmons on a single metallic nanoparticle. *Nat. Phys.* **3,** 348–353 (2007).

159. Sardar, R., Funston, A. M., Mulvaney, P. & Murray, R. W. Gold Nanoparticles: Past, Present, and Future. *Langmuir* **25,** 13840–13851 (2009).

160. Zinchenko, A., Taniguchi, S. & Murata, S. Size-Dependent Catalytic Activity of Gold Nanoparticles in DNA Hydrogels. *Macromol. Symp.* **358,** 106–111 (2015).

161. Lu, Y., Yu Mei, Marc Schrinner, Ballauff, M., Michael W. Möller & Breu, J. In Situ Formation of Ag Nanoparticles in Spherical Polyacrylic Acid Brushes by UV Irradiation. (2007).

162. Wunder, S., Polzer, F., Lu, Y., Mei, Y. & Ballauff, M. Kinetic Analysis of Catalytic Reduction of 4-Nitrophenol by Metallic Nanoparticles Immobilized in Spherical Polyelectrolyte Brushes. *J. Phys. Chem. C* **114,** 8814–8820 (2010).

163. Lu, Y., Proch, S., Schrinner, M., Drechsler, M., Kempe, R. & Ballauff, M. Thermosensitive core-shell microgel as a ‘nanoreactor’ for catalytic active metal nanoparticles. *J. Mater. Chem.* **19,** 3955 (2009).

164. Lopez-Sanchez, J. A., Dimitratos, N., Hammond, C., Brett, G. L., Kesavan, L., White, S., Miedziak, P., Tiruvalam, R., Jenkins, R. L., Carley, A. F., Knight, D., Kiely, C. J. & Hutchings, G. J. Facile removal of stabilizer-ligands from supported gold nanoparticles. *Nat. Chem.* **3,** 551–556 (2011).

165. Kim, C. & Lee, H. Change in the catalytic reactivity of Pt nanocubes in the presence of different surface-capping agents. *Catal. Commun.* **10,** 1305–1309 (2009).

166. Niu, Z. & Li, Y. Removal and Utilization of Capping Agents in Nanocatalysis. *Chem. Mater.* **26,** 72–83 (2014).

167. Borodko, Y., Humphrey, S. M., Tilley, T. D., Frei, H. & Somorjai, G. A. Charge-transfer interaction of poly(vinylpyrrolidone) with platinum and rhodium nanoparticles. *J. Phys. Chem. C* **111,** 6288–6295 (2007).

168. Carregal-Romero, S., Buurma, N. J., Pérez-Juste, J., Liz-Marzán, L. M. & Hervés, P. Catalysis by Au@pNIPAM Nanocomposites: Effect of the Cross-Linking Density. *Chem. Mater.* **22,** 3051–3059 (2010).

169. Wu, S., Dzubiella, J., Kaiser, J., Drechsler, M., Guo, X., Ballauff, M. & Lu, Y. Thermosensitive Au-PNIPA Yolk-Shell Nanoparticles with Tunable Selectivity for Catalysis. *Angew. Chemie Int. Ed.* **51,** 2229–2233 (2012).

170. Wu, S., Kaiser, J., Drechsler, M., Ballauff, M. & Lu, Y. Thermosensitive Au-PNIPA yolk-shell particles as 'nanoreactors' with tunable optical properties. *Colloid Polym. Sci.* **291,** 231–237 (2013).

171. Lawrence, R. L., Scola, B., Li, Y., Lim, C.-K., Liu, Y., Prasad, P. N., Swihart, M. T. & Knecht, M. R. Remote Optically Controlled Modulation of Catalytic Properties of Nanoparticles through Reconfiguration of the Inorganic/Organic Interface. *ACS Nano* **10,** 9470–9477 (2016).

172. Gu, S., Kaiser, J., Marzun, G., Ott, A., Lu, Y., Ballauff, M., Zaccone, A., Barcikowski, S. & Wagener, P. Ligand-free Gold Nanoparticles as a Reference Material for Kinetic Modelling of Catalytic Reduction of 4-Nitrophenol. *Catal. Letters* **145,** 1105–1112 (2015).

173. Kalekar, A. M., Kumar, K., Sharma, K., Luwang, M. N. & Sharma, G. K. Catalytic activity of bare and porous palladium nanostructures in the reduction of 4-nitrophenol. *RSC Adv.* **6,** 11911–11920 (2016).

174. Shiju, N. R. & Guliants, V. V. Recent developments in catalysis using nanostructured materials. *Appl. Catal. A Gen.* **356,** 1–17 (2009).

175. Notar Francesco, I., Fontaine-Vive, F. & Antoniotti, S. Synergy in the Catalytic Activity of Bimetallic Nanoparticles and New Synthetic Methods for the Preparation of Fine Chemicals. *ChemCatChem* **6,** 2784–2791 (2014).

176. Shi, J. On the Synergetic Catalytic Effect in Heterogeneous Nanocomposite Catalysts. *Chem. Rev.* **113,** 2139–2181 (2013).

177. Liu, J. H., Wang, A. Q., Chi, Y. S., Lin, H. P. & Mou, C. Y. Synergistic effect in an Au-Ag alloy nanocatalyst: CO oxidation. *J. Phys. Chem. B* **109,** 40–43 (2005).

178. Endo, T., Yoshimura, T. & Esumi, K. Synthesis and catalytic activity of gold–silver binary nanoparticles stabilized by PAMAM dendrimer. *J. Colloid Interface Sci.* **286,** 602–609 (2005).

179. Slater, T. J. A., Macedo, A., Schroeder, S. L. M., Burke, M. G., O'Brien, P., Camargo, P. H. C. & Haigh, S. J. Correlating Catalytic Activity of Ag–Au Nanoparticles with 3D Compositional Variations. *Nano Lett.* **14,** 1921–1926 (2014).

180. Crole, D. A., Freakley, S. J., Edwards, J. K. & Hutchings, G. J. Direct synthesis of hydrogen peroxide in water at ambient temperature. *Proc. R. Soc. A Math. Phys. Eng. Sci.* **472,** 20160156 (2016).

181. Wei, X., Yang, X.-F., Wang, A.-Q., Li, L., Liu, X.-Y., Zhang, T., Mou, C.-Y. & Li, J. Bimetallic Au–Pd Alloy Catalysts for N $_2$ O Decomposition: Effects of Surface Structures on Catalytic Activity. *J. Phys. Chem. C* **116,** 6222–6232 (2012).

182. Hayashi, N., Sakai, Y., Tsunoyama, H. & Nakajima, A. Development of Ultrafine Multichannel Microfluidic Mixer for Synthesis of Bimetallic Nanoclusters: Catalytic Application of Highly Monodisperse AuPd Nanoclusters Stabilized by Poly(*N* -vinylpyrrolidone). *Langmuir* **30,** 10539–10547 (2014).

183. Sarina, S., Bai, S., Huang, Y., Chen, C., Jia, J., Jaatinen, E., Ayoko, G. A., Bao, Z. & Zhu, H. Visible light enhanced oxidant free dehydrogenation of aromatic alcohols using Au–Pd alloy nanoparticle catalysts. *Green Chem.* **16,** 331–341 (2014).

184. Kaiser, J., Leppert, L., Welz, H., Polzer, F., Wunder, S., Wanderka, N., Albrecht, M., Lunkenbein, T., Breu, J., Kümmel, S., Lu, Y. & Ballauff, M. Catalytic activity of nanoalloys from gold and palladium. *Phys. Chem. Chem. Phys.* **14,** 6487 (2012).

185. Kaiser, J., Szczerba, W., Riesemeier, H., Reinholz, U., Radtke, M., Albrecht, M., Lu, Y. & Ballauff, M. The structure of AuPd nanoalloys anchored on spherical polyelectrolyte brushes determined by X-ray absorption spectroscopy. *Faraday Discuss.* **162,** 45 (2013).

186. Gu, S., Lu, Y., Kaiser, J., Albrecht, M. & Ballauff, M. Kinetic analysis of the reduction of 4-nitrophenol catalyzed by Au/Pd nanoalloys immobilized in spherical polyelectrolyte brushes. *Phys. Chem. Chem. Phys.* **17,** 28137–28143 (2015).

187. Léonard, E., Mangin, F., Villette, C., Billamboz, M. & Len, C. Azobenzenes and catalysis. *Catal. Sci. Technol.* **6,** 379–398 (2016).

188. Wei, Y., Han, S., Kim, J., Soh, S. & Grzybowski, B. A. Photoswitchable Catalysis Mediated by Dynamic Aggregation of Nanoparticles. *J. Am. Chem. Soc.* **132,** 11018–11020 (2010).

189. Yoon, J. H. & Yoon, S. Photoisomerization of azobenzene derivatives confined in gold nanoparticle aggregates. *Phys. Chem. Chem. Phys.* **13,** 12900–12905 (2011).

190. Hallett-Tapley, G. L., D'Alfonso, C., Pacioni, N. L., McTiernan, C. D., González-Béjar, M., Lanzalunga, O., Alarcon, E. I. & Scaiano, J. C. Gold nanoparticle catalysis of the cis–trans isomerization of azobenzene. *Chem. Commun.* **49,** 10073 (2013).

191. Nachtigall, O., Kördel, C., Urner, L. H. & Haag, R. Photoresponsive Switches at Surfaces Based on Supramolecular Functionalization with Azobenzene-Oligoglycerol Conjugates. *Angew. Chemie Int. Ed.* **53,** 9669–9673 (2014).

192. Simoncelli, S. & Aramendía, P. F. Mechanistic insight into the Z–E isomerization catalysis of azobenzenes mediated by bare and core–shell gold nanoparticles. *Catal. Sci. Technol.* **5,** 2110–2116 (2015).

193. Titov, E., Lysyakova, L., Lomadze, N., Kabashin, A. V., Saalfrank, P. & Santer, S. Thermal Cis-to-Trans Isomerization of Azobenzene-Containing Molecules Enhanced by Gold Nanoparticles: An Experimental and Theoretical Study. *J. Phys. Chem. C* **119,** 17369–17377 (2015).

194. Dumont, D., Galstian, T. V, Senkow, S. & Ritcey, A. M. Liquid Crystal Photoalignment using New Photoisomerisable Langmuir-Blodgett Films. *Mol. Cryst. Liq. Cryst.* **375,** 341–352 (2002).

195. Venancio-Marques, A., Bergen, A., Rossi-Gendron, C., Rudiuk, S. & Baigl, D. Photosensitive Polyamines for High-Performance Photocontrol of DNA Higher-Order

Structure. *ACS Nano* **8,** 3654–3663 (2014).

196. Schimka, S., Santer, S., Mujkić-Ninnemann, N. M., Bléger, D., Hartmann, L., Wehle, M., Lipowsky, R. & Santer, M. Photosensitive Peptidomimetic for Light-Controlled, Reversible DNA Compaction. *Biomacromolecules* **17,** 1959–1968 (2016).

197. Kabashin, A. V & Meunier, M. Synthesis of colloidal nanoparticles during femtosecond laser ablation of gold in water. *J. Appl. Phys.* **94,** 7941 (2003).

198. Kabashin, A. V & Meunier, M. Femtosecond laser ablation in aqueous solutions: a novel method to synthesize non-toxic metal colloids with controllable size. *J. Phys. Conf. Ser.* **59,** 354–359 (2007).

199. Besner, S., Kabashin, A. V & Meunier, M. Fragmentation of colloidal nanoparticles by femtosecond laser-induced supercontinuum generation. *Appl. Phys. Lett.* **89,** 233122 (2006).

200. Besner, S., Kabashin, A. V & Meunier, M. Two-step femtosecond laser ablation-based method for the synthesis of stable and ultra-pure gold nanoparticles in water. *Appl. Phys. A* **88,** 269–272 (2007).

201. Maximova, K., Aristov, A., Sentis, M. & Kabashin, A. V. Size-controllable synthesis of bare gold nanoparticles by femtosecond laser fragmentation in water. *Nanotechnology* **26,** 65601 (2015).

202. Sylvestre, J., Poulin, S., Kabashin, A. V, Sacher, E., Meunier, M., Luong, J. H. T., Montre, Ä. P. De & Postale, C. Surface Chemistry of Gold Nanoparticles Produced by Laser Ablation in Aqueous Media. *J. Phys. Chem. B* **108,** 16864–16869 (2004).

203. Mitzscherling, S., Cui, Q., Koopman, W. & Bargheer, M. Dielectric function of two-phase colloid–polymer nanocomposite. *Phys. Chem. Chem. Phys.* **17,** 29465–29474 (2015).

204. Lysyakova, L., Lomadze, N., Neher, D., Maximova, K., Kabashin, A. V. & Santer, S. Light-Tunable Plasmonic Nanoarchitectures Using Gold Nanoparticle–Azobenzene-Containing Cationic Surfactant Complexes. *J. Phys. Chem. C* **119,** 3762–3770 (2015).

205. Israelachvili, J. N. in *Intermolecular and Surface Forces* 291–340 (Academic Press, 2011).

206. Intartaglia, R., Bagga, K., Brandi, F., Das, G., Genovese, A., Di Fabrizio, E. & Diaspro, A. Optical Properties of Femtosecond Laser-Synthesized Silicon Nanoparticles in Deionized Water. *J. Phys. Chem. C* **115,** 5102–5107 (2011).

207. Allen, F. G. & Gobeli, G. W. Work Function, Photoelectric Threshold, and Surface States of Atomically Clean Silicon. *Phys. Rev.* **127,** 150–158 (1962).

208. Seidl, M., Meiwes-Broer, K. -H. & Brack, M. Finite-size effects in ionization potentials and electron affinities of metal clusters. *J. Chem. Phys.* **95,** 1295–1303 (1991).

209. Zhang, Y., Pluchery, O., Caillard, L., Lamic-Humblot, A.-F., Casale, S., Chabal, Y. J. & Salmeron, M. Sensing the Charge State of Single Gold Nanoparticles via Work Function Measurements. *Nano Lett.* **15,** 51–55 (2015).

210. Zhou, L. & Zachariah, M. R. Size resolved particle work function measurement of free nanoparticles: Aggregates vs. spheres. *Chem. Phys. Lett.* **525–526,** 77–81 (2012).

211. Alloway, D. M., Graham, A. L., Yang, X., Mudalige, A., Colorado, R., Wysocki, V. H., Pemberton, J. E., Randall Lee, T., Wysocki, R. J. & Armstrong, N. R. Tuning the

Effective Work Function of Gold and Silver Using ω-Functionalized Alkanethiols: Varying Surface Composition through Dilution and Choice of Terminal Groups. *J. Phys. Chem. C* **113,** 20328–20334 (2009).

212. Michaelson, H. B. The work function of the elements and its periodicity. *J. Appl. Phys.* **48,** 4729–4733 (1977).

213. Nikoobakht, B. & El-Sayed, M. A. Evidence for Bilayer Assembly of Cationic Surfactants on the Surface of Gold Nanorods. *Langmuir* **17,** 6368–6374 (2001).

214. Pastoriza-Santos, I., Pérez-Juste, J. & Liz-Marzán, L. M. Silica-Coating and Hydrophobation of CTAB-Stabilized Gold Nanorods. *Chem. Mater.* **18,** 2465–2467 (2006).

215. Perez-Juste, J., Pastoriza-Santos, I., Liz-Marzan, L. & Mulvaney, P. Gold nanorods: Synthesis, characterization and applications. *Coord. Chem. Rev.* **249,** 1870–1901 (2005).

216. Tian, L., Chen, E., Gandra, N., Abbas, A. & Singamaneni, S. Gold Nanorods as Plasmonic Nanotransducers: Distance-Dependent Refractive Index Sensitivity. *Langmuir* **28,** 17435–17442 (2012).

217. Jain, P. K., Eustis, S. & El-Sayed, M. A. Plasmon Coupling in Nanorod Assemblies: Optical Absorption, Discrete Dipole Approximation Simulation, and Exciton-Coupling Model. *J. Phys. Chem. B* **110,** 18243–18253 (2006).

218. Templeton, A. C., Pietron, J. J., Murray, R. W. & Mulvaney, P. Solvent Refractive Index and Core Charge Influences on the Surface Plasmon Absorbance of Alkanethiolate Monolayer-Protected Gold Clusters. *J. Phys. Chem. B* **104,** 564–570 (2000).

219. Johnson, P. B. & Christy, R. W. Optical Constants of the Noble Metals. *Phys. Rev. B* **6,** 4370–4379 (1972).

220. Polyanskiy, M. N. Refractive index database. *https://refractiveindex.info*

221. Philipse, A. . & Vrij, A. Preparation and properties of nonaqueous model dispersions of chemically modified, charged silica spheres. *J. Colloid Interface Sci.* **128,** 121–136 (1989).

222. Yu, C. & Irudayaraj, J. Quantitative evaluation of sensitivity and selectivity of multiplex nanoSPR biosensor assays. *Biophys. J.* **93,** 3684–92 (2007).

223. Mayer, K. M., Lee, S., Liao, H., Rostro, B. C., Fuentes, A., Scully, P. T., Nehl, C. L. & Hafner, J. H. A Label-Free Immunoassay Based Upon Localized Surface Plasmon Resonance of Gold Nanorods. *ACS Nano* **2,** 687–692 (2008).

224. Chen, H., Kou, X., Yang, Z., Ni, W. & Wang, J. Shape- and Size-Dependent Refractive Index Sensitivity of Gold Nanoparticles. *Langmuir* **24,** 5233–5237 (2008).

225. Haberjoh, J. P. Bachelor Thesis 'Ellipsometrische Untersuchung der Photoisomerisation von Azobenzenen in Lösung und Polymerfilmen'. (University of Potsdam, Germany, 2016).

226. https://www.scbt.com/scbt/product/4-nitroazobenzene-2491-52-3.

11. Abbreviations

CMC – critical micelle concentration

CTAB – cetyltrimethylammonium bromide

SAM – self-assembled monolayer

LSPR – localized surface plasmon resonance

SERS – surface-enhanced Raman spectroscopy

RLCA – reaction-limited colloidal aggregation

DLCA – diffusion-limited colloidal aggregation

TEM – transmission electron microscopy

EDX – energy-dispersive X-ray spectroscopy

SEM – scanning electron microscopy

AFM – atomic force microscopy

DLS – dynamic light scattering

UV – ultraviolet

Vis – visible

NIR – near-infrared

DMSO - dimethylsulfoxide

C_{Azo} – concentration of azobenzene surfactant

DFT – density functional theory

RIU – refractive index unit

12. Acknowledgement

I sincerely thank my principal supervisor Prof. Dr. Svetlana Santer for all the life lessons I had to learn during my work, my second supervisor Prof. Dr. Dieter Neher for lots of support on my stony way, and my current post-doctoral supervisor Dr. Karl Kratz for unrelated yet immeasurable support during finishing this thesis.

I appreciate a lot the work of my referees PD Dr. Marina Grenzer and Prof. Dr. Ilko Bald.

I am grateful to all my collaborators: Dr. Yuriy Ryabchikov and back in 2013 a PhD student Ksenia Maximova from the group of Prof. Dr. Andrei Kabashin at the Aix-Marseille University in France, Dr. Alexey Kucherik and Dr. Stella Kutrovskaya at the Vladimir State University in Russia, Dr. Qianling Cui, who worked in the group of Prof. Bargheer at the University of Potsdam in the past, for the preparation of nanoparticles; Evgenii Titov, who has recently achieved his doctoral degree under the supervision of Prof. Dr. Peter Saalfrank at the University of Potsdam, for theoretical calculations; Dr. Yuriy Ryabchikov, Dr. Claudia Prietzel in the group of Prof. Dr. Joachim Kötz at the University of Potsdam, and Dr. Zdravko Kochovski in the group of Dr. Yan Lu at the Humboldt University in Berlin, as well as Dr. Markus Wollgarten at Helmholtz Zentrum Berlin of Materials and Energy for TEM micrographs, and the group of Prof. Dr. Zoya Ignatova at the University of Hamburg for the linearization of plasmid DNA.

My thanks also go to my former colleagues Dr. Nino Lomadze for the synthesis of azobenzene compounds, Dr. Alexey Kopyshev for support, Dr. Nataraja Sekhar Yadavalli, who was a PhD student during my work, and Selina Schimka for helpful discussions, as well as to my new colleagues Dr. Matthias Heuchel and Stephen Quinn, and the whole two groups at the University of Potsdam and at the Helmholtz-Center Geesthacht for the warm working atmosphere.

Last but not least, my gratitude goes to „Koordinationsbüro für Chancengleichheit” at the University of Potsdam for financial support, Dr. Renate Schmidt and my husband Bastian Kruck for holding me in the hardest times, and my whole family and friends, especially Michael Seiler, for their empathy.

13. Appendix

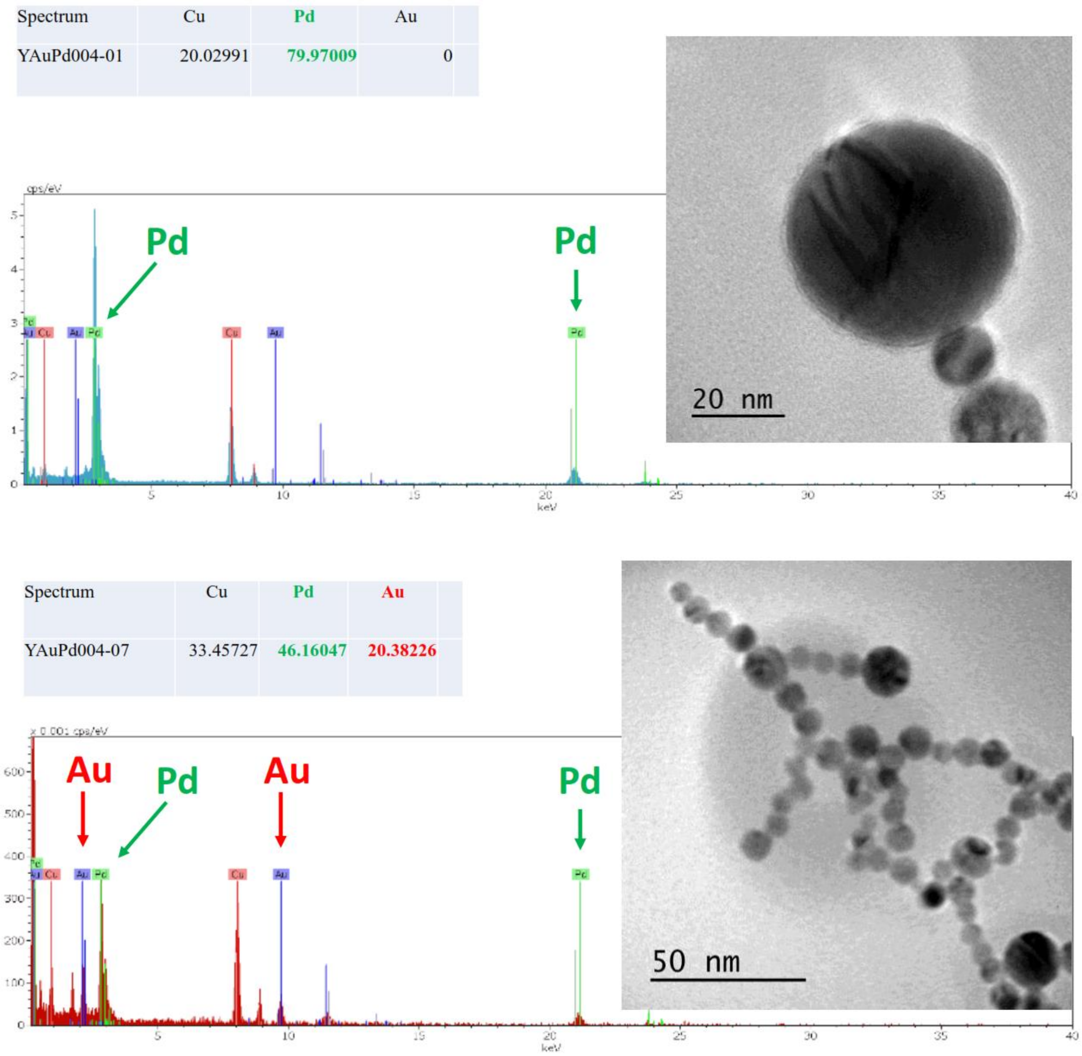

Spectrum	Cu	Pd	Au
YAuPd004-01	20.02991	79.97009	0

Spectrum	Cu	Pd	Au
YAuPd004-07	33.45727	46.16047	20.38226

Figure Appendix-13.1. TEM micrographs (right) and corresponding EDX spectra (left) of alloy gold-palladium nanoparticle suspension. (Data of Dr. Ryabchikov)

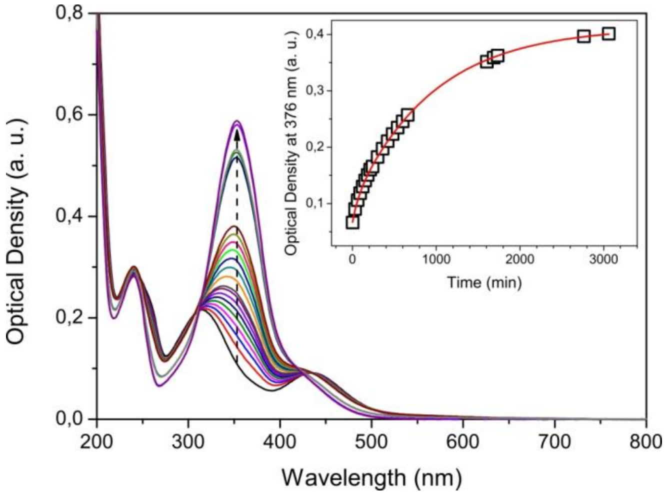

Figure Appendix-13.2. Absorption spectra over time of UV irradiated azobenzene containing surfactant AzoC$_6$ in the presence of palladium nanoparticles. The inset shows time dependency of optical density at 376 nm (squares) and its exponential fit (red line).

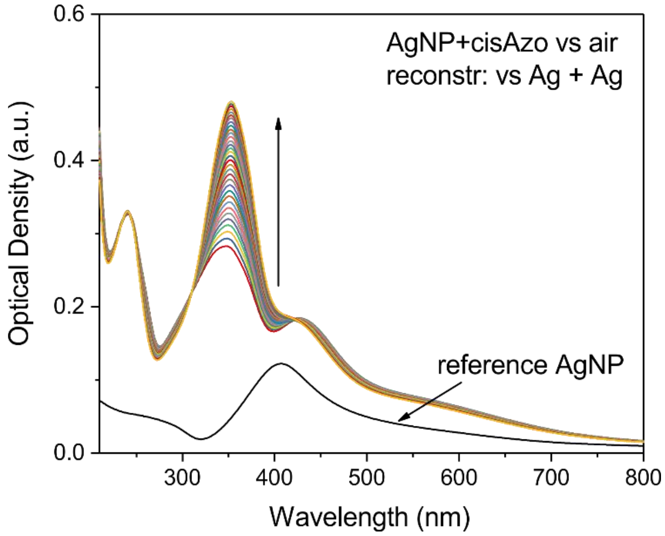

Figure Appendix-13.3. Time-dependent absorption spectra of UV irradiated azobenzene containing surfactant AzoC$_6$ in the presence of silver nanoparticles prepared at Aix-Marseille University. The spectra were recorded versus air. Black line shows the spectrum of reference silver nanoparticles in water of the same concentration C_{Ag} = 0.075 mM.

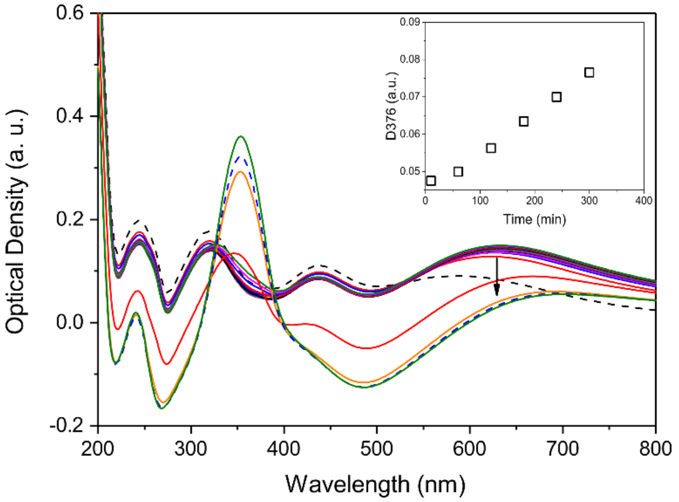

Figure Appendix-13.4. Periodically recorded absorption spectra of UV-irradiated azobenzene containing surfactant AzoC$_6$ mixed with silicon nanoparticles SiNP Ar, recorded versus SiNP Ar aqueous colloid. The inset shows optical density over time within the first five hours before precipitation.

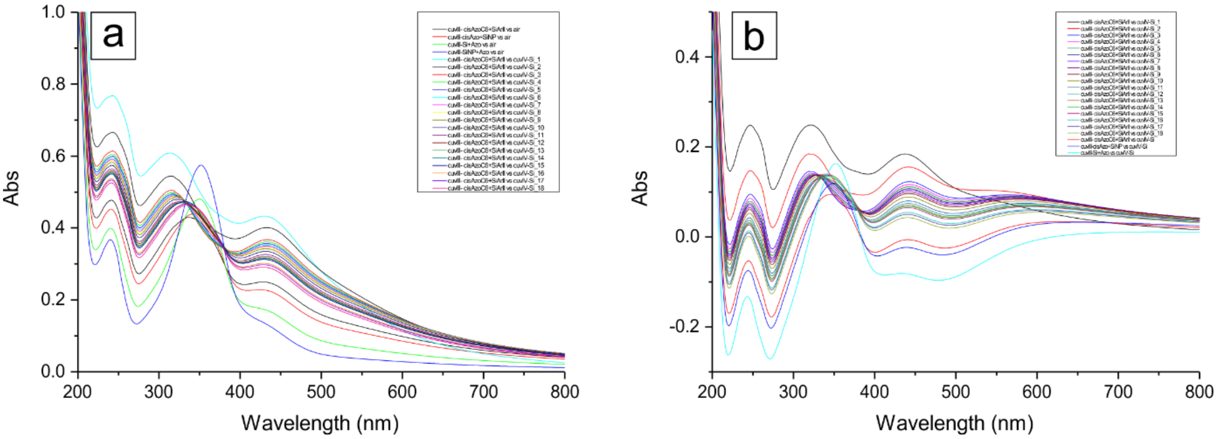

Figure Appendix-13.5. Periodically recorded absorption spectra of UV-irradiated azobenzene containing surfactant AzoC$_6$ mixed with silicon nanoparticles SiNP Ar II, recorded versus air (a) and reference SiNP Ar II aqueous colloid (b).